Ontwikkeling van een dynamische eindige differentiemethode voor Large-Eddy Simulatie

Development of a Dynamic Finite Difference Method for Large-Eddy Simulation

Dieter Fauconnier

Promotor: prof. E. Dick
Proefschrift ingediend tot het behalen van de graad van
Doctor in de Ingenieurswetenschappen: Werktuigkunde-Elektrotechniek

Vakgroep Mechanica van Stroming, Warmte en Verbranding
Voorzitter: prof. dr. ir. R. Sierens
Faculteit Ingenieurswetenschappen
Academiejaar 2008-2009

UNIVERSITEIT GENT

ISBN 978-90-8578-235-3
NUR 978,928
Wettelijk depot: D/2008/10.500/55

Promotor: prof. E. Dick

Vakgroep Mechanica van Stroming, Warmte en Verbranding
Sint-Pietersnieuwstraat 41
B-9000 Gent
België

This research was funded by a Ph.D grant of the Institute for the Promotion of Innovation through Science and Technology in Flanders (IWT-Vlaanderen).

Le savant n'étudie pas la nature parce que cela est utile; il l'étudie parce qu'il y prend plaisir et il y prend plaisir parce qu'elle est belle. Si la nature n'était pas belle, elle ne vaudrait pas la peine d'être connue, la vie ne vaudrait pas la peine d'être vécue. Je ne parle pas ici, bien entendu, de cette beauté qui frappe les sens, de la beauté des qualités et des apparences ; non que j'en fasse fi, loin de là, mais elle n'a rien à faire avec la science; je veux parler de cette beauté plus intime qui vient de l'ordre harmonieux des parties, et qu'une intelligence pure peut saisir.

Poincaré, Jules Henri

Acknowledgments

I wish to express my sincere gratitude to all those people who guided and supported me in many ways, during the past four years of my PhD.

First of all, I thank my promotor prof. Erik Dick, not only for giving me the opportunity to realise this project, but also for the intellectual freedom to explore scientific *terra incognita*. I consider his excellent guidance and expertise as essential for successfully accomplishing this dissertation. His enthusiasm certainly encouraged me to seek continuously for new solutions to new problems.

I would also like to thank my senior colleague and supervisor dr. Chris De Langhe, who managed to *streamline* my often rudimentary thoughts on turbulence, modeling and mathematics. The innumerable profound discussions have contributed substantially to a broader and more refined understanding about the *art* of scientific research.

Further, I want to express my gratitude to all my colleagues for the good atmosphere at work. Especially, I thank Pieter Rauwoens, not only for instructing me on the house-code, but also for the various inspiring conversations. I am also very grateful to Yves Maenhout, for taking care of all hardware and software problems during my PhD.

Above all, I thank my partner Stefanie for her unconditional support, patience and motivation throughout the past four years, despite my often silent and grumpy moods.

Finally, I thank my parents and my sisters Ann and Kaat, for everything they have done for me the past 27 years. I am especially indebted to my parents for their commitment to give me an excellent education and for their confidence and unconditional support during my lifetime.

Dankwoord

Ik wens mijn oprechte dank uit te spreken aan allen die me gedurende de voorbije vier jaar begeleid en gesteund hebben in mijn doctoraatsonderzoek.

Ten eerste, bedank ik mijn promotor prof. Erik Dick, niet enkel omwille van de kans die hij me geboden heeft dit project te verwezenlijken, maar tevens voor de intellectuele vrijheid bij het verkennen van wetenschappelijk *terra incognita*. Ik beschouw zijn uitstekende begeleiding en expertise als essentieel in het succesvol beëindigen van dit proefschrift. Zijn enthousiasme inspireerde me om voortdurend te zoeken naar nieuwe oplossingen voor nieuwe problemen.

Voorts wens ik ook mijn collega en begeleider dr. Chris De Langhe te bedanken, die erin slaagde mijn vaak rudimentaire gedachten m.b.t. turbulentie, modellering en wiskunde te *stroomlijnen*. De talloze diepgaande gesprekken hebben alvast bijgedragen tot een breder en meer verfijnd inzicht in de *kunst* van het wetenschappelijk onderzoek.

Ook wil ik mijn dank betuigen aan al mijn collega's voor de goede sfeer op het werk. In het bijzonder dank ik Pieter Rauwoens, niet alleen om me doorheen de huiscode te gidsen, maar ook voor de diverse inspirerende gesprekken. Tevens ben ik Yves Maenhout dank verschuldigd voor het tijdig verhelpen van alle hardware- en softwareproblemen.

Bovenal, bedank ik mijn partner Stefanie voor haar onvoorwaardelijke steun, geduld en motivatie in de afgelopen vier jaar, ondanks mijn vaak zwijgzame en kribbige gemoedstoestand.

Tot slot, dank ik mijn ouders en mijn zussen Ann en Kaat, voor alles wat ze voor mij gedaan hebben de voorbije 27 jaar. In het bijzonder ben ik mijn ouders heel wat dank verschuldigd voor hun toewijding in mijn opvoeding, alsook voor hun vertrouwen en onvoorwaardelijke steun gedurende mijn leven.

Synopsis

Since the earliest numerical calculation of Lewis Fry Richardson almost a century ago, the role of Computational Fluid Dynamics (CFD) has evolved from an *expensive* research tool which is confined to academic environments, into an important instrument for industrial design and development. For example, Computational Fluid Dynamics has become indispensable for the design of compact heat exchangers, since it offers a flexible and cost-effective tool for parametric investigations, detailed analysis of complex and critical flow phenomena *etcetera*, in contrast to expensive and time-consuming experiments [76]. The continuing development of modern computer technology, obviously played an utterly important role in this evolution. However, despite the enormous increase of computational power in the last three decades, Computational Fluid Dynamics still encounters limitations today. For instance, the Direct Numerical Simulation (DNS) of turbulent flows is still prohibitively expensive for industrial applications, due to the enormous amount of grid cells required to resolve the finest vortex motions in the turbulent flow. However, almost since the early days of Computational Fluid Dynamics, various approaches and strategies have been developed to overcome the excessive grid requirements of DNS. In particular Large-Eddy Simulation (LES), a technique that relies on resolving only the dominant large-scale flow features and modeling the dynamic influence of the unresolved small-scale features, is evolving in recent years into a mature simulation technique for turbulent flows, with the potential to combine cost effectiveness with accuracy [61].

In the past decades, the necessity for numerical quality in Direct Numerical Simulations and especially Large-Eddy Simulations of turbulent flows, has been recognized by many researchers [32, 49, 19, 4]. In a properly resolved Direct Numerical Simulation, the smallest resolved scales are located far into the dissipation range. Since these scales have only a very small energy-content in comparison with the largest resolved scales in the flow, they are often considered to have a negligible influence on the mean flow statistics. In a Large-Eddy Simulation, however, where only the most important large scale structures are resolved, the smallest resolved scales are part of the inertial subrange such that they contain relatively more energy than those in the dissipation range. Hence, the smallest resolved scales in Large-Eddy Simulation are not negligible and have a significant influence on the evolution of the LES-flow. The accuracy with which these small scales are described is therefore expected to be important. In order to reduce the computational costs, it is

highly desirable in LES to resolve as much scales as possible on a given computational grid. In order to accomplish this, the numerical method requires sufficient accuracy for all scales. This ensure that the magnitudes of the discretization errors remain smaller than the magnitude of the modeled unresolved scales of motion [32]. However, if the accuracy of the numerical method cannot be guaranteed, the amount of resolved small-scale structures must be reduced in order to control the discretization errors. Hence, in order to resolve the same amount of scales as before, a much finer computational grid is required. This is often prohibitively expensive for most three-dimensional LES computations of industrial applications.

In order to obtain better numerical accuracy, it is common practice in Computational Fluid Dynamics to use classic high-order finite difference schemes that are based on a specific truncation of the Taylor series. These methods involve finite difference approximations that achieve a certain formal asymptotic order of accuracy for the approximation of the largest scales in the flow. Although this may be sufficient for very well resolved Direct Numerical Simulations, it is not necessarily the optimal strategy for Large-Eddy Simulation. Indeed, for extremely well resolved Direct Numerical Simulations, in which the smallest significant scales of motion are several times larger than the size of the computational grid, the Taylor series of the finite difference approximations converge rapidly due to small contributions of the higher derivatives. Hence, the classical Taylor-based asymptotic numerical techniques that rely on such a fast convergence of the Taylor series, may suffice for such Direct Numerical Simulations. However, for Large-Eddy Simulation and even for some Direct Numerical Simulations, the size of the smallest resolved scales is typically in the order of the grid spacing and are thus only marginally resolved. Hence, the contributions of the higher derivatives in the truncation terms of the Taylor series become much more important, slowing down the convergence of the Taylor series and thus leading to significant numerical errors. Therefore, it is much more advantageous to minimize all contributions in the Taylor series in order to obtain good global accuracy for all resolved scales. In other words, the global truncation error, that represents all scales, should be minimized instead of focusing on the highest possible accuracy for only the largest scales in the flow. The advantages of such an approach were already discovered in 1993 by Tam *et al.* [79] in the field of computational aero-acoustics. Indeed, the accurate simulation of propagating waves requires high-performance finite difference methods. Despite the fact that other researchers followed this cost-effective and highly accurate strategy for various applications [45, 37, 2, 6], the use of *optimized* finite difference schemes did yet not become a standard technique in the world of Large-Eddy Simulation.

In the present dissertation a family of *dynamic* finite difference methods is developed, which succeed in minimizing the global discretization error on the solution in *real time* during the calculation. This strategy allows to obtain always a *(nearly) optimal* numerical method that corresponds to the flow characteristics at that time. The approach implies that the intrinsic characteristics of this finite difference method vary during the simulation in such a way that the global numerical error is always

minimized.
The construction of these dynamic finite difference approximations relies on the determination of an optimal value for the preceding coefficient in the leading order truncation term by means of a *sampling-based dynamic procedure*. Although the sampling-based dynamic procedure was originally proposed in [89, 88, 22, 46] for the determination of the model coefficients in Large-Eddy Simulation, it is used in this work in a new, alternative way in order to determine the optimal stencil coefficients in the finite difference approximation. By comparing the Taylor series expansions of any basic finite difference approximation on two different grid resolutions, the method allows to extract a nearly optimal value for the leading order coefficient, provided that a blending factor f is predefined, which regulates the sensitivity of the procedure to the small scales in the resolved flow. Adopting a *characteristic* energy spectrum of the resolved flow field, a one-off calibration procedure was proposed to retrieve the optimal value of the blending factor. This optimal value of the blending factor is expected to be robust and applicable for a large range of turbulent flows.
Although the dynamic schemes share similarities with the *prefactored* Dispersion-Relation Preserving schemes of e.g. Tam *et al.* [79], Kim *et al.* [45] and many others [37, 2, 6], their behaviour is more refined. Indeed, the stencil-coefficients of the developed dynamic finite difference approximations are *dynamically adapted* during the simulation through the dynamic coefficient, which is determined according to the resolved flow field. In case of DNS resolution, i.e. if the small-scale structures are represented by sufficient amount of grid nodes on the grid, the dynamic schemes reduce to the standard Taylor-based finite difference schemes with optimal formal asymptotic order of accuracy. When going to LES resolution, the schemes seamlessly adapt to Dispersion-Relation Preserving schemes. This could be particularly interesting for transient developing flows, or in case of grid refinement studies with fixed filter width.

The developed dynamic finite difference approximations were extensively and rigorously tested for Large-Eddy Simulation. For a first quality assessment, a simpler problem than the Large-Eddy Simulation of three-dimensional Navier-Stokes turbulence is considered. Following the work of Love [54], Das *et al.* [20] and de Stefano *et al.* [21], the one-dimensional *viscous Burgers' equation* with periodic boundary conditions is selected as a less complicated but eligible alternative to the Navier-Stokes equations. Similar to the Navier-Stokes equations, Burgers' equation contains a quadratic nonlinear term and it exhibits an inertial range in the energy spectrum, as in real turbulence.
Secondly, the performance of the dynamic finite difference schemes is examined for the Large-Eddy Simulation of the three-dimensional *Taylor-Green vortex flow*. The Taylor-Green vortex flow is perhaps one of the simplest prototype systems in which to study the breakdown-process of large-scale vortices into successively smaller ones and may be interpreted as transition into turbulence. The selected flow is therefore very well suited in the current quality assessment on the dynamic finite difference

approximations.

In the present work, two types of dynamic finite difference methods were considered. The *linear* dynamic finite difference methods contain a spatially averaged constant dynamic coefficient such that the resulting finite difference approximations remain unaltered in the spatial domain. On the other hand, the *nonlinear* dynamic finite difference methods contain a spatially varying dynamic coefficient, such that the resulting finite difference approximations differ from node to node. The results obtained from both studies clearly demonstrate the high potential of the *linear* dynamic finite difference methods. On the other hand, the *nonlinear* variant showed rather poor results and was concluded to be inappropriate for LES. The linear dynamic schemes systematically recover the accuracy of the standard asymptotic high-order finite difference schemes, provided that all scales of motion in the flow field are well-resolved on the computational grid. This implicates that they adapt according to the smooth solution of the flow, focusing on maximum accuracy of the largest resolved scales. Obviously, this is an advantage over the Dispersion-Relation Preserving schemes which remain suboptimal for those solutions, since they are designed a priori for non-smooth solutions on the computational grid.
Once the resolution becomes marginal and thus inadequate to resolve accurately all scales of motion in the laminar or turbulent flow, the linear dynamic schemes adjust the dynamic coefficient according to the resolved scales on the computational grid. The sensitivity with which the linear dynamic schemes respond to small scale information in the physical spectrum is predefined by the blending factor f. More specifically, the magnitude of the Taylor series that determines the truncation error is minimized. As soon as the flow is fully turbulent and the energy spectrum exhibits an inertial range, both the linear dynamic finite difference schemes and the static Dispersion-Relation Preserving schemes perform very similar.

In conclusion, the family of linear dynamic finite difference methods that is developed in the present dissertation, provides a very useful and viable tool for numerically accurate Large-Eddy Simulations of turbulent flows, since these schemes have the intrinsic ability to adapt their characteristics optimally to the resolved flow physics with respect to the computational grid.

Synopsis

Sinds de eerste numerieke stromingsberekening van Lewis Fry Richardson, bijna een eeuw geleden, is de rol van numerieke stromingsmechanica geëvolueerd van een relatief duur onderzoeksinstrument dat beperkt was tot academische omgevingen, tot een uitermate belangrijk hulpmiddel voor industrieel ontwerp en ontwikkeling. Zo is bijvoorbeeld numerieke stromingsmechanica een onontbeerlijk instrument geworden in het ontwerpproces van ondermeer compacte warmtewisselaars, gezien de enorme flexibiliteit en kostefficiëntie voor het uitvoeren van parameterstudies zowel als voor het gedetailleerd analyseren van ingewikkelde en kritische stromingspatronen. Daarmee is numerieke stromingsmechanica een betrouwbaar alternatief voor de dure en tijdrovende experimenten die vroeger aan het ontwerp voorafgingen [76]. De voortdurende ontwikkeling van de moderne computertechnologie speelde uiteraard een zeer belangrijke rol in deze evolutie. Echter, ondanks de enorme toename in computerkracht, de voorbije drie decennia, botst de numerieke stromingsmechanica nog steeds aan tegen de beperkingen van de huidige computertechnologie. Zo is bijvoorbeeld Directe Numerieke Simulatie (DNS) van turbulente stromingen een nog steeds onbetaalbare methode voor toepassing in industriële omgevingen, omwille van het enorme aantal benodigde rekenpunten voor het berekenen van de allerkleinste wervels in de turbulente stroming. Echter, reeds sinds het ontstaan van numerieke stromingsmechanica, werden verscheidene technieken en strategieën ontwikkeld die toelaten het aantal rekenpunten drastisch te beperken. In het bijzonder de Simulatie van Grote Wervels, of in het jargon *Large-Eddy Simulation* (LES), evolueert de laatste jaren tot een volwaardige simulatietechniek voor turbulente stromingen, waarbij kosteneffectiviteit en nauwkeurigheid gecombineerd worden [61]. Deze techniek steunt op het oplossen van enkel de meest dominante en grootschalige wervels in de stroming terwijl de invloed van de onbekende kleinschalige wervels gemodelleerd dient te worden.

In de afgelopen decennia erkenden vele onderzoekers de noodzaak om de numerieke kwaliteit van Directe Numerieke Simulaties en vooral voor Large-Eddy Simulaties voor turbulente stromingen te waarborgen [32, 49, 19, 4]. In zeer goed geresolveerde Directe Numerieke Simulatie, bevinden de kleinst berekende wervelstructuren zich ver in het dissipatiebereik van het energiespectrum. Aangezien deze structuren slechts een zeer kleine energie-inhoud hebben in vergelijking met de grootste schalen in de stromingsoplossing, wordt hun invloed op de gemiddelde stromingsstatistieken vaak verwaarloosbaar verondersteld. Echter, voor Large-Eddy Simulatie, waar al-

leen de belangrijkste grootschalige structuren worden berekend, maken de kleinste schalen deel uit van het inertiële subbereik zodat zij relatief meer energie bevatten dan deze in het dissipatiebereik. Daarom zijn de kleinst geresolveerde schalen vaak niet meer verwaarloosbaar en hebben zij een significante invloed op de evolutie van de LES-stroming. Bijgevolg kan men verwachten dat de nauwkeurigheid waarmee deze kleine schalen weergegeven worden belangrijk is. Om de computationele kosten enigszins te beperken, is het bovendien wenselijk in LES om zoveel mogelijk fysische wervelstructuren te berekenen op een bepaald rekenrooster. Om hieraan tegemoet te komen, dient de numerieke methode voldoende nauwkeurig te zijn voor alle structuren, zodat de grootte van de discretisatiefouten kleiner blijft dan de grootte van de gemodelleerde wervelstructuren [32]. Indien echter de nauwkeurigheid van de numerieke methode niet kan worden gegarandeerd, dient men de hoeveelheid berekende kleinschalige structuren op het rekenrooster te reduceren, zodat de discretisatiefouten beperkt blijven. Dit betekent tevens dat voor het bepalen van dezelfde hoeveelheid fysische wervelinformatie als voorheen, een veel fijner rekenrooster vereist is. Dit is vaak onbetaalbaar voor driedimensionale Large-Eddy Simulaties van turbulente stromingen, vooral in industriële toepassingen.

Om een aanvaardbare numerieke nauwkeurigheid te waarborgen, worden in numerieke stromingsmechanica typisch klassieke eindige differentiemethoden aangewend die gebaseerd zijn op een truncatie van de Taylorreeks. Dergelijke methoden maken gebruik van eindige differentiebenaderingen die gekenmerkt worden door een bepaalde formele asymptotische orde van nauwkeurigheid met betrekking tot de grootste wervelstructuren in de stroming. Hoewel dergelijke methoden volstaan voor zeer goed geresolveerde Directe Numerieke Simulaties, is het niet noodzakelijk een optimale strategie voor Large-Eddy Simulaties. Immers, voor extreem goed geresolveerde Directe Numerieke Simulaties waarbij de kleinste wervelstructuren vele malen groter zijn dan de resolutie van het rekenrooster, convergeert de Taylorreeks in de eindige differentiebenaderingen relatief snel wegens de kleine bijdragen van de hogere afgeleiden. Daarom volstaan de klassieke asymptotische numerieke methoden, aangezien ze net steunen op dergelijke snelle convergentie van de Taylorreeks. Voor Large-Eddy Simulatie of zelfs voor sommige Directe Numerieke Simulaties echter, is de grootte van de kleinste schalen typisch van dezelfde orde als de roosterresolutie zodat ze slechts marginaal geresolveerd zijn. Bijgevolg zijn de bijdragen van de hogere afgeleiden in de truncatietermen van de Taylorreeks veel belangrijker zodat de convergentie van de Taylor reeks vertraagt en relatief grote numerieke fouten kunnen ontstaan. Het minimaliseren van alle bijdragen in de afgeknotte Taylorreeks is daarom veel voordeliger aangezien een dergelijke strategie leiden tot een globale nauwkeurigheidsverbetering voor alle berekende wervelstructuren in de stroming. Dit houdt in dat de globale numerieke fouten voor alle wervels samen geminimaliseerd worden in plaats van het behalen van een zo hoog mogelijke nauwkeurigheid voor enkel de grootste wervels in de stroming. Het enorme potentieel van een dergelijke aanpak werd reeds ontdekt in 1993 door Tam *et al.* [79] in het gebied van de numerieke aero-akoestiek. Net als in Large-Eddy Simulatie vereist de accurate

simulatie van golfvoortplanting immers hoog performante eindige differentiebenaderingen. Ondanks het feit dat andere onderzoekers deze kosteneffectieve en zeer nauwkeurige strategie aanwendden voor verscheidene doeleinden [45, 37, 2, 6], groeide het gebruik van dergelijke *geoptimaliseerde* eindige differentiemethoden niet uit tot een standaard techniek in de wereld van LES.

In het huidige proefschrift wordt een familie van *dynamische* eindige differentiemethoden ontwikkeld, die de globale discretisatie fout op de stromingsoplossing in *real-time* minimaliseren tijdens de simulatie. Deze strategie maakt het mogelijk om steeds een *(bijna) optimale* numerieke methode te waarborgen, in overeenstemming met de karakteristieken van de stromingsoplossing op dat moment. De aanpak houdt in dat de intrinsieke eigenschappen van de voorgestelde eindige differentiemethode variëren tijdens de simulatie, zodanig dat de globale numerieke fout steeds minimaal is.
De constructie van deze dynamische eindige differentiebenaderingen steunt op de bepaling van een optimale waarde voor de coëfficiënt van de leidende afknottingsterm in de Taylorreeks, door middel van de *sampling-based dynamische procedure*. Niettegenstaande de sampling-based dynamische procedure oorspronkelijk voorgesteld werd in [89, 88, 22, 46] ter bepaling van de model coëfficiënt in Large-Eddy Simulatie, wordt de methode in dit werk op een nieuwe, alternatieve wijze aangewend ter bepaling van de optimale stencil coëfficiënten in het eindige differentieschema. Door de de Taylor reeks van eender welke eindige differentiebenadering op twee verschillende resoluties van het rekenrooster te vergelijken, maakt de methode het mogelijk om een bijna optimale waarde voor de coëfficiënt te bepalen, op voorwaarde dat een mengfactor f vooraf wordt opgegeven. Deze factor regelt slechts de gevoeligheid van de dynamische procedure aan de kleinschalige informatie in de stroming. Op basis van een *karakteristiek* energiespectrum van de stroming, wordt een eenmalige procedure voorgesteld om de optimale waarde van deze mengfactor te bepalen. Deze optimale waarde voor de blending factor wordt voldoende robuust verondersteld en is dus toepasbaar voor een brede verzameling van turbulent stromingen.
Hoewel de dynamische schema's een aantal gelijkenissen vertonen met de *Dispersie-Relatie-Behoudende* schema's van bijvoorbeeld Tam *et al.* [79], Kim *et al.* [45] en vele anderen [37, 2, 6], is hun gedrag meer verfijnd. Immers, de coëfficiënten van deze ontwikkelde dynamische eindige differentiebenaderingen worden op *dynamische* wijze aangepast tijdens de simulatie door middel van één enkele *dynamische coëfficiënt*. Deze laatste wordt bepaald op basis van de berekende stromingsoplossing en het bijhorende energie spectrum. In het geval van DNS-resolutie, i.e. bij voldoende roosterpunten om de kleinste wervelstructuren nauwkeurig weer te geven op het rekenrooster, reduceren de dynamische schema's zich tot de standaard Taylor-gebaseerde eindige differentiebenaderingen, die gekenmerkt worden door een optimale formele en asymptotische orde van nauwkeurigheid. Indien de simulatie naar LES-resolutie overschakelt, passen de schema's zich naadloos en optimaal aan. Dergelijke eigenschap kan bijzonder interessant zijn voor de berekening van ontwikkelende en transitionele stromingen, of voor roosterverfijning studies waarbij de

breedte van de LES-filter gefixeerd wordt.

De ontwikkelde dynamische eindige differentiebenaderingen worden verder uitvoerig getest voor Large-Eddy Simulaties van karakteristieke turbulente stromingen. Voor een eerste beoordeling van hun kwaliteit, wordt een vereenvoudigd modelprobleem voor driedimensionale Navier-Stokes turbulentie beschouwd. Naar het voorbeeld van Love [54], Das *et al.* [20] en de Stefano *et al.* [21], wordt de eendimensionale *viskeuze Burgers' vergelijking* met periodische randvoorwaarden geselecteerd als eenvoudiger, maar geschikt alternatief voor de Navier-Stokes vergelijkingen. Net als de Navier-Stokes vergelijkingen, bevat Burgers' vergelijking een niet-lineaire kwadratische term, en vertoont het typische Burgers' energiespectrum een duidelijke inertiële zone gelijkend op dat van een realistisch turbulent spectrum.
Vervolgens worden de prestaties van de dynamische eindige differentiemethoden onderzocht voor Large-Eddy Simulatie van de driedimensionale *Taylor-Green wervelstroming*. De Taylor-Green wervelstroming is wellicht één van de eenvoudigste prototypesystemen waarin het fundamentele afbraakproces van grootschalige wervels in steeds kleinere wervels, kan worden bestudeerd en kan daarom beschouwd worden als representatief voor transitionele stromingen. De geselecteerde stroming is dus goeds geschikt voor de beoogde kwaliteitsbeoordeling van de dynamische eindige differentiebenaderingen.

In het huidige werk, werden twee types van dynamische eindige differentiemethoden beschouwd. The *lineaire* dynamische differentiemethoden bevatten een ruimtelijk gemiddelde constante dynamische coëfficiënt zodat the resulterende eindige differentiebenadering niet veranderd in het ruimtelijke domein. Anderzijds bevatten de *niet-lineaire* dynamische differentiemethoden een ruimtelijk variërende coëfficiënt, zodat de resulterende eindige differentiebenaderingen wijzigen van punt tot punt in het domein. De bekomen resultaten in beide studies illustreren duidelijk het grote potentieel van de dynamische *lineaire* eindige differentiemethoden. De *niet-lineaire* variant daarentegen, leidt slechts tot povere resultaten en werden ongeschikt bevonden voor LES. De *lineaire* dynamische schema's bereiken systematisch de nauwkeurigheid van de asymptotische hogere orde eindige differentiemethoden, op voorwaarde dat alle wervels in de stroming door voldoende roosterpunten weergegeven zijn op het rekenrooster. Dit impliceert dat dergelijke schema's zich aanpassen aan het reguliere stromingspatroon, zodat maximale nauwkeurigheid van de grootste wervels bekomen wordt. De dynamische schema's blijken in deze situaties voordeliger dan de *Dispersie-Relatie Behoudende* schema's. Deze laatste zijn immers suboptimaal voor dergelijke reguliere stromingspatronen, aangezien ze ontworpen werden voor irreguliere stromingsoplossingen op rekenrooster.
Indien echter de wervels in de laminaire of turbulente stroming met onvoldoende roosterpunten worden voorgesteld om de nauwkeurigheid te waarborgen, passen de *lineaire* dynamische schema's zich aan via de dynamische coëfficiënt, in overeenstemming met de eigenschappen van de stromingsoplossing op het rekenrooster. De gevoeligheid waarmee de lineaire dynamische schema's reageren op kleinschalige informatie in het spectrum is vooraf bepaald door de mengfactor f. Bovendien is de

grootte van de numerieke fout minimaal. Zodra de stroming volledig turbulent wordt en het energiespectrum een inertiëel bereik vertoont, is de performantie van de dynamische lineaire eindige differentie schema's en dat van de statische *Dispersie-Relatie Behoudende* zeer vergelijkbaar.

Kortom, de familie van lineaire dynamische eindige differentiemethoden die ontwikkeld werd in dit proefschrift, biedt een zeer nuttig en waardevol instrument voor nauwkeurige LES-simulaties van turbulente stromingen, omwille van hun intrinsiek vermogen zich optimaal aan te passen aan de fysische kenmerken van de stroming in relatie tot het rekenrooster.

Contents

List of Figures

List of Tables

Nomenclature

The notation that is used throughout this dissertation, is enlisted hereafter in the following order: Acronyms, Greek Symbols, Operator Symbols and Roman Symbols. The page on which the symbol first appears, is indicated in the right column.

Acronyms

CFD	Computational Fluid Dynamics	2
CFL	Courant-Friederichs-Lewy	158
CPU	Central Processing Unit	32
DNS	Direct Numerical Simulation	4
DRP	Dispersion-relation preserving	166
FLOPS	Floating Point Operations	32
LES	Large-Eddy Simulation	4
RAM	Random access memory	32
EDQNM	Eddy-Damped Quasi-Normal Markovian	92

Greek Symbols

α	Filter cutoff ratio	52
α	Ratio of the sampling wavenumbers	103
α	Slope of the energy spectrum	141
α_j	Coefficients of the Runge-Kutta method	81
α_j	Ratio of the sampling wavenumbers in direction j	103
α_l	Implicit coefficient of a finite difference approximation	65
β_j	Explcit coefficient of a finite difference approximation	61
$\boldsymbol{\beta}$	Kernel of explicit stencil coefficients	64
$\delta(x)$	Dirac delta distribution	18
$\delta^3(\mathbf{x})$	Three-dimensional Dirac delta distribution	23
Δt	Time increment or time step	30
Δ	Grid spacing in one dimension	18
Δ_c	Filter width	38
δ_{ij}	Kronecker delta	48
$\boldsymbol{\Delta}$	Array of grid spacings in each direction	18
ϵ	Infinitesimal number	18

ω_η	Temporal frequency of the Kolmogorov scales	31
ω_{max}	Temporal Nyquist frequency	31
Ω_{kl}	Rotation tensor	49
ξ	Dual coordinate indication of x	22
ζ	Ratio of the grid spacing to the Kolmogorov length	29

Operator Symbols

$\|\cdot\|$	Magnitude or absolute value	11
$\mathscr{C}(\overline{u}_i)$	Continuity operator	98
$\Im(\cdot)$	Imaginary part of a complex number	82
$\lim_{\phi\to\epsilon}$	Limit as the quantity ϕ tend to infinitesimal value ϵ	61
$\|\cdot\|_q$	The vector norm of order q	165
$\widehat{\phi}$	Fourier transform of a variable ϕ	11
$\overline{(\cdot)}$	Primary filter	36
$\mathscr{O}\left(\Delta^k\right)$	Order of accuracy k in grid spacing Δ	63
$\widetilde{(\cdot)}$	Sampled variable on grid resolution κ_{max}/α	102
$\widetilde{(\cdot)}$	Secondary filter	52
$(\cdot)^<$	Resolved part of the interactions	46
$(\cdot)^>$	Unresolved part of the interactions	46
$(\cdot)''$	Smallest resolved part of a variable	54
$(\cdot)'$	Unresolved part of a variable	43
∂	Domain boundary surface	106
$\Re(\cdot)$	Real part of a complex number	82
$*$	Convolution operator	24
$\langle . \rangle$	Spatial averaging operator	53
$\langle . \rangle$	Statistical averaging operator	13
$\widehat{\phi}^*$	Complex conjugate of Fourier variable ϕ	13
$\mathscr{F}\{\cdot\}$	Fourier operator	11
$\circ$	Symbol that denotes: "Operates on"	20
$\overline{(\cdot)}$	Sampled variable on grid resolution κ_{max}	19
$\mathscr{S}^{\mathbf{\Delta}}$	Three-dimensional Sampling operator	23
$\mathscr{S}^{\Delta}$	Sampling operator	20

Roman Symbols

c	Artificial speed of sound	88
C^π	Dynamic coefficient of the continuity equation	101
C_k	Kolmogorov constant	15
C_s	Smagorinsky constant	50
C_i^σ	Dynamic coefficient of the Navier-Stokes equation	101
$c_{k,n}$	Taylor coefficient of the n^{th} derivative	100
$c_{k,n}^*$	Theoretical value of the Taylor coefficient of the n^{th} derivative	99

$c_{k,n}^{dyn}$	Dynamic coefficient	120
$\mathscr{D}\left(\Delta^k\right)$	Dissipator of order k	89
$\mathscr{E}$	Error	118
$\mathbf{e}_i$	Unit vector in the i^{th} coordinate direction	11
$E\left(\kappa,t\right)$	Characteristic one-dimensional energy spectrum function	14
$E\left(\boldsymbol{\kappa},t\right)$	Energy spectrum in three-dimensional Fourier space	13
f	Blending factor	104
$F_\eta\left(\kappa,t\right)$	Function to determine shape of the dissipation range	16
$F_e\left(\kappa,t\right)$	Function to determine shape of the energy containing range	16
f_{opt}	Optimal blending factor	140
f_{opt}^*	Asymptotic value of the optimal blending factor	146
$\mathscr{G}\left(x\right)$	Filter function	36
$\mathscr{G}\left(\mathbf{x},\Delta_c\right)$	Homogeneous sharp cutoff filter kernel	43
$\mathrm{H}\left(x\right)$	Heaviside function	38
$\mathscr{H}$	Helicity	192
i	Imaginary unit	11
$\mathbf{k}$	Vector of coordinate indices	18
$k\left(t\right)$	Total kinetic energy as function of time	13
k_r	Resolved kinetic energy	209
$\mathscr{L}_{ij}$	Resolved turbulent stress tensor	53
$\mathscr{L}_i^\sigma$	Vectorial Leonard term in Navier-Stokes equations	103
$\mathscr{L}$	Leonard term in the dynamic schemes	118
$\mathscr{L}^\pi$	Scalar Leonard term in continuity equation	103
$\mathscr{L}$	Length of the computational box	11
L	Integral length scale	17
L_{11}	Longitudinal integral length scale	17
$L_{2,\phi}$	L_2-norm on the variable ϕ	111
$\mathscr{M}_{ij}$	Resolved model stress tensor	53
$\mathscr{M}_i^\sigma$	Vectorial model term in Navier-Stokes equations	103
$\mathscr{M}$	Modeled truncation term in the dynamic schemes	118
$\mathscr{M}^\pi$	Scalar model term in continuity equation	103
$\mathscr{N}\left(\overline{u}_i,\overline{p}\right)$	Navier Stokes operator	81
$\mathbf{N}$	Array of grid nodes in each direction	18
N	Number of nodes in one dimension	23
N_t	Number of time steps	32
$\mathscr{P}_{jk}\left(\boldsymbol{\kappa}\right)$	Projection tensor	12
$p\left(\mathbf{x},t\right)$	Pressure field	10
Q	Vortex criterion parameter	199
q	Indication of the implicit stencil width $2q+1$	65
Re	Reynolds number	10
Re_λ	Reynolds number based on Taylor microscale	17
Re_L	Reynolds number based on integral length scale	17
r	Indication of the explicit stencil width $2r+1$	61

S	Strain rate magnitude	50
S_{kl}	Strain rate tensor	49
t	Time	10
$T(\boldsymbol{\kappa}, t)$	Rate of energy transfer	13
$T_{x \to \xi}$	Coordinate transformation operator	22
$\overline{u}_i^*$	Predictor velocity for pressure correction	90
$\mathbf{u}(\mathbf{x}, t)$	Eulerian instantaneous velocity field vector	10
$u_j(\mathbf{x}, t)$	Eulerian instantaneous velocity component	10
$\mathscr{W}(\kappa)$	Spectral weighting function	93
$\mathbf{x}$	Cartesian coordinate vector	10
x_j	Cartesian coordinate component	10

If we knew what we're doing, it wouldn't be called research would it?

Einstein, Albert

1 Introduction

1.1 Large-Eddy Simulation: a modern strategy in Computational Fluid Dynamics

"Imagine a large hall like a theatre, except that the circles and galleries go right round through the space usually occupied by the stage. The walls of this chamber are painted to form a map of the globe. The ceiling represents the north polar regions, England is in the gallery, the tropics in the upper circle, Australia on the dress circle and the Antarctic in the pit.

A myriad computers[1] *are at work upon the weather of the part of the map where each sits, but each computer attends only to one equation or part of an equation. The work of each region is coordinated by an official of higher rank. Numerous little "night signs" display the instantaneous values so that neighboring computers can read them. Each number is thus displayed in three adjacent zones so as to maintain communication to the North and South on the map.*

From the floor of the pit a tall pillar rises to half the height of the hall. It carries a large pulpit on its top. In this sits the man in charge of the whole theatre; he is surrounded by several assistants and messengers. One of his duties is to maintain a uniform speed of progress in all parts of the globe. In this respect he is like the conductor of an orchestra in which the instruments are slide-rules and calculating machines. But instead of waving a baton he turns a beam of rosy light upon any region that is

[1] i.e. people who do computations.

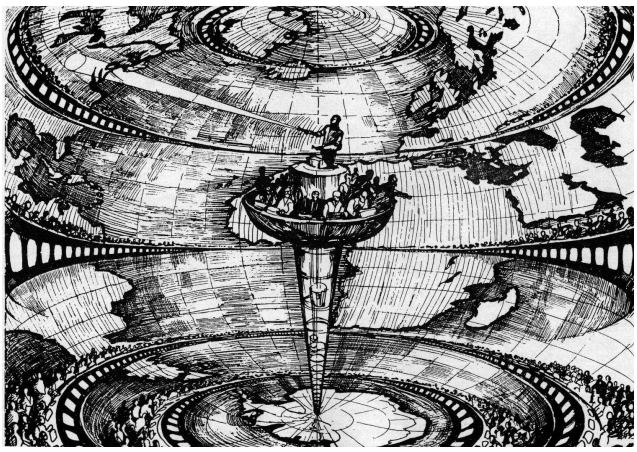

Figure 1.1: Richardsons' Forecast Factory. Artist impression by A. Lannerback, in Dagens Nyheter, Stockholm [57].

running ahead of the rest, and a beam of blue light upon those who are behindhand.

Four senior clerks in the central pulpit are collecting the future weather as fast as it is being computed, and dispatching it by pneumatic carrier to a quiet room. There it will be coded and telephoned to the radio transmitting station. Messengers carry piles of used computing forms down to a storehouse in the cellar.

In a neighboring building there is a research department, where they invent improvements. But there is much experimenting on a small scale before any change is made in the complex routine of the computing theatre. In a basement an enthusiast is observing eddies in the liquid lining of a huge spinning bowl, but so far the arithmetic proves the better way. In another building are all the usual financial, correspondence and administrative offices. Outside are playing fields, houses, mountains and lakes, for it was thought that those who compute the weather should breathe of it freely."

The previous fanciful literary fragment was extracted from the book *Weather Prediction by Numerical Process*, published in 1922 by the famous English mathematician and meteorologist Lewis Fry Richardson [73, 57].[2] Although the fantastic and ambitious proposal of a *forecast factory* (see Figure 1.1) seems grotesque today, it may be considered as the earliest numerical weather prediction system that relied on a very rudimentary form of Computational Fluid Dynamics (CFD). In Richardson's proposal, the atmosphere that covers the globe was divided into $120 \times 100 \times 5$ grid cells in which the primitive differential equations,[3] used at that time, were

[2] Note that Richardson is also well-known for his extrapolation formula.

[3] Besides the continuity equation and the thermal energy equation, these primitive equations consists of a form of the Navier-Stokes equations that describe hydrodynamical flow on the surface

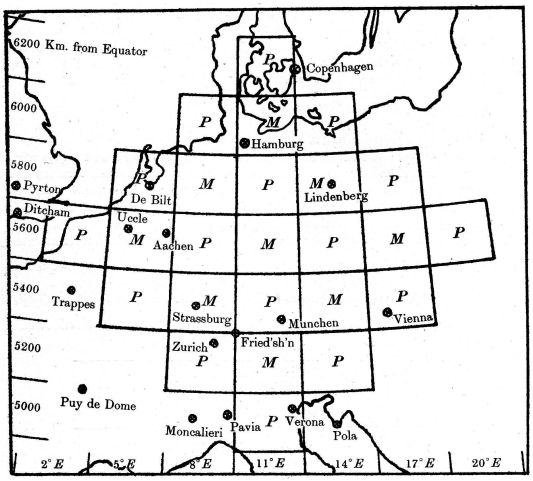

Figure 1.2: The earliest CFD calculation of Lewis Fry Richardson. Grid used by Richardson for his forecast of the weather of May 20^{th} 1910. The pressure was specified at points denoted P, and the momentum at points denoted M. The prediction was confined to the calculation of the initial tendencies at the P-point near Munich and the M-point directly to the north. Source Lynch [57].

solved manually using finite difference approximations. Despite the fact that the method devised by Richardson was utterly impractical at the time of its publication, he demonstrated its application by carrying out a trial forecast of the weather on May 20^{th} 1910 *ab initio* from data taken at 7am. The original computational grid used by Richardson is displayed in Figure 1.2. Although the results of this trial forecast failed dramatically due to smoothing of the data, a recent study showed that the *corrected* forecast turns out to be essentially accurate which was a remarkable achievement considering the calculations were done by hand [57].

Since the earliest numerical calculation of Richardson almost a century ago, the role of Computational Fluid Dynamics has evolved from an *academic* research tool which was confined to the laboratory, into an important instrument for industrial design and development. For example, Computational Fluid Dynamics has become indispensable for the design of compact heat exchangers, since it offers a flexible and cost-effective tool for parametric investigations and detailed analysis of complex and critical flow phenomena, in contrast to expensive and time-consuming experiments [76]. The continuing development of modern computer technologies, obviously played a very important role in this evolution. However, despite the enormous increase of computational power in the last three decades, Computational Fluid Dynamics still encounters limitations today. For instance, the Direct Nu-

of a sphere under the assumption that vertical motion is much smaller than horizontal motion (hydrostasis) and that the fluid layer depth is small compared to the radius of the sphere.

merical Simulation (DNS) of turbulent flows at high Reynolds numbers is still prohibitively expensive for industrial applications, due to the enormous amount of computational resources required to resolve the finest vortex motions in the turbulent flow. However, almost since the early days of Computational Fluid Dynamics, various approaches and strategies have been developed to overcome the excessive grid requirements of DNS. In particular Large-Eddy Simulation (LES) is evolving in recent years into a mature simulation technique for turbulent flows, with the potential to combine cost effectiveness with accuracy [61]. This technique relies on resolving only the dominant large-scale flow features, whereas the dynamic influence of the unresolved small-scale features on the evolution of the large ones must be taken into account by a model. Despite the plenitude of advanced subgrid models that were designed, the earliest model proposed by Joseph Smagorinsky in 1963 [78], survived the test of time and became the most widespread model in Large-Eddy Simulation. In 1991, Germano *et al.* [30], proposed a supplementary *dynamic procedure* in order to determine the coefficient in Smagorinsky's model, which was till then often treated as an arbitrary coefficient. This major breakthrough made the *dynamic* Smagorinsky model one of the most popular models for Large-Eddy Simulation, due to its robustness and acceptable accuracy in various flows. Although the dynamic Smagorinsky models significantly improved the accuracy and reliability of Large-Eddy Simulations, several researchers began to understand since the early nineties, that the global accuracy of Large-Eddy Simulations was not only liable to the performance of the adopted models, but also to the numerical method used to solve the LES-equations. In particular the numerical errors, related to the discretization technique used to solve the partial differential equations, may affect the quality of the smallest resolved scales in the Large-Eddy Simulation, eventually leading to a nonlinear accumulation of numerical errors and modeling errors in the simulation. This is briefly discussed in the next section.

1.2 Motivation and Objectives

In the past decades, the necessity for numerical quality in Direct Numerical Simulations and Large-Eddy Simulations of turbulent flows, has been recognized by many researchers [32, 49, 19, 4]. In a very well resolved Direct Numerical Simulation, the smallest resolved scales are located far into the dissipation range. Since these scales have only a very small energy-content in comparison with the largest resolved scales in the flow, they are often considered to have a negligible influence on the mean flow statistics. In a Large-Eddy Simulation, however, where only the most important large scale structures are resolved, the smallest resolved scales are part of the inertial subrange such that they contain relatively more energy than those in the dissipation range. Hence, the smallest resolved scales in Large-Eddy Simulation are not negligible and have a significant influence on the evolution of the LES-flow. The accuracy with which these small scales are described is therefore expected to be important. In order to reduce the computational costs, it is highly desirable in LES to resolve as much scales as possible on a given computational grid. In order to accom-

plish this, the adopted numerical method requires sufficient accuracy for all scales in order to ensure that the magnitudes of the discretization errors remain smaller than the magnitude of the modeled unresolved scales of motion [32]. However, if the accuracy of the numerical method cannot be guaranteed, the amount of resolved scales must be reduced in order to control the discretization errors. Hence, in order to resolve the same amount of scales as before, a much finer computational grid is required. This is often prohibitively expensive for most three-dimensional LES computations of industrial applications. Furthermore, the dynamic Smagorinsky model strongly relies on the smallest resolved scales in LES. Hence, accurate resolution of the small-scales should result in a more correct application of the model. Obviously, good numerical quality for an affordable LES is vital for accurate flow prediction as it directly influences resolved scales of motion as well as subgrid modeling.

In order to obtain better numerical accuracy, it is common practice in Computational Fluid Dynamics to use classic high-order central schemes based on the truncation of the Taylor series. This approach leads to finite difference approximations that achieve a certain formal asymptotic order of accuracy for the approximation of the largest scales in the flow. Although this may be sufficient for very well resolved Direct Numerical Simulations, it is not necessarily the optimal strategy for Large-Eddy Simulation. Indeed, for extremely well resolved Direct Numerical Simulations, in which the smallest significant scales of motion are several times larger then the size of the computational grid, the Taylor series of the finite difference approximations converge rapidly due to small contributions of the higher derivatives. Hence, the classical Taylor-based asymptotic numerical techniques that rely on fast convergence of the Taylor series, generally suffice for those flows. However, for Large-Eddy Simulation and even for some Direct Numerical Simulations, the size of the smallest resolved scales is typically in the order of the grid spacing and are thus only marginally resolved. Hence, the contributions of the higher derivatives in the truncation terms of the Taylor series become much more important, slowing down the convergence of the Taylor series and thus leading to significant numerical errors. Therefore, it would be much more advantageous to minimize all contributions in the Taylor series to obtain good overall performance for all resolved scales of fluid motion. In other words, one tries to minimize the global truncation error for all scales instead of focusing on obtaining the highest possible accuracy for only the largest scales of motion. This useful point of view was already recognized by Tam *et al.* [79] in 1993 in the field of computational aero-acoustics, where accurate simulation of propagating waves requires high-performance finite difference approaches. Despite the fact that other researchers followed this cost-effective and highly accurate strategy [45, 37, 2, 6], the use of *optimized* finite difference schemes did not yet become a standard technique in the world of Large-Eddy Simulation.

The main objective of the present dissertation is the design of a *dynamic* finite difference method which minimizes the global discretization error on the solution in

real time during the calculation. Such a strategy would allow one to always obtain a *(nearly) optimal* numerical method that corresponds to the flow characteristics at that time. Such an approach implies that the intrinsic characteristics of this finite difference method vary during the simulation in such a way that the global numerical error is always minimized. The proposed methodology is expected to provide improved quality and more flexibility in general numerical simulations, and may be particularly advantageous for Large-Eddy Simulations.

1.3 Outline of the present dissertation

Chapter 2 is devoted to the fundamental description of the motion of incompressible Newtonian fluids. Through a fundamental mathematical and physical study of the governing Navier-Stokes equations, the different scales of motion in both laminar and turbulent fluid flows are characterized. This allows one to assess the minimal requirements for Direct Numerical Simulation of homogeneous and isotropic turbulence and leads to a clear understanding of the encountered limitations which form the motivation for Large-Eddy Simulation.

In Chapter 3, the mathematical framework for Large-Eddy simulation is introduced, together with Smagorinsky's subgrid model that accounts for the unresolved scales. Moreover, two more advanced modeling techniques are discussed, namely the dynamic procedure and multiscale modeling, which improve the performance of the standard subgrid model. Finally, the sensitivity of both techniques to the numerics is explained, introducing at the same time the basic problem description of this dissertation.

The standard numerical methods, used to approximate the partial differential equations for DNS and LES, are introduced in Chapter 4. Most important, an appraisal is given of the standard finite difference approximations for Large-Eddy Simulation. It is argued that these standard approximations with formal order of accuracy may not be optimal in the context of LES, and that *optimized* finite difference approximations might be more advantageous. Ultimately the motivation and objectives for this dissertation are explained.

Based on the motivations and objectives discussed in Chapter 4, a first attempt to illustrate the ability of the *sampling-based dynamic procedure* in order to obtain improved numerical accuracy is demonstrated. Using Taylor series expansion, an analytical formulation for the exact truncation error in the Navier-Stokes equations and the continuity equation is derived. By taking a modified leading order truncation term into account, a *model-formulation* for the truncation errors is developed, which will allow to minimize the global truncation error by means of a *dynamic coefficient*. Finally, the concept is evaluated for a two-dimensional steady laminar flow in a lid-driven cavity at a Reynolds number $\mathrm{Re} = 400$.

Chapter 6 forms the core of this dissertation, and is devoted to the mathematical construction of a family of dynamic low-dispersive finite difference approximations

for the partial derivatives. An explicit and implicit family of dynamic low-dispersive finite difference approximations is constructed by combining Taylor series expansions on two different grid resolutions. The accuracy of the constructed schemes is analyzed in Fourier space using modified wavenumbers. The relation of the dynamic schemes with the Dispersion-Relation-Preserving scheme of Tam *et al.* [79] and the Dispersion-Relation-Preserving compact Padé scheme of Kim *et al.* [45] is then demonstrated.

The designed dynamic finite difference approximations are extensively tested in the Large-Eddy Simulation of Burgers' turbulence in Chapter 7 and in the Large-Eddy Simulation of the Taylor-Green vortex flow in Chapter 8. Both cases are considered well suited for an extensive quality assessment of the constructed dynamic schemes.

The main conclusions of this work are formulated in Chapter 9, whereas some future developments are proposed in Chapter 10.

When I meet God, I am going to ask Him two questions: Why relativity? And why turbulence? I really believe he will have an answer for the first.

Heisenberg, Werner

2

The Navier-Stokes equations

The present chapter is devoted to the fundamental description of the motion of incompressible Newtonian fluids.[1] Considering the fluid to be a continuous medium rather than a collection of individual molecules, the physical laws of fluid motion describe the conservation of mass and momentum. This is mathematically expressed by a set of partial differential equations called the Navier-Stokes equations. Since the Navier-Stokes equations are nonlinear, analytical solutions do not exist[2] and numerical simulation is the only alternative. Through a mathematical and physical dimensional analysis of these equations, the different scales of motion in both laminar and turbulent fluid flows are characterized. This allows to assess the minimal requirements for Direct Numerical Simulation (DNS) of the Navier-Stokes equations and leads to a clear understanding of the mathematical problem and the encountered limitations which form the basis of this dissertation.

2.1 The Navier-Stokes equations

Consider an incompressible viscous fluid with unit density described by the velocity field $\mathbf{u}(\mathbf{x}, t)$ in a reference Cartesian coordinate system $\mathbf{x} \in \mathbb{R}^3$ such that $\mathbf{u}(\mathbf{x}, t) = [u_1(x_1, x_2, x_3, t), u_2(x_1, x_2, x_3, t), u_3(x_1, x_2, x_3, t)]$. This velocity field is governed by the set of partial differential equations comprising the continuity and

[1] Newtonian fluids are characterized by a shear stress which is linearly proportional to the velocity gradient in the direction perpendicular to the plane of shear.

[2] Unless substantially simplified flows are considered.

the Navier-Stokes equations

$$\frac{\partial u_i}{\partial x_i} = 0 \tag{2.1}$$

$$\frac{\partial u_i}{\partial t} + u_j \frac{\partial u_i}{\partial x_j} = -\frac{\partial p}{\partial x_i} + \nu \frac{\partial^2 u_i}{\partial x_j^2}, \tag{2.2}$$

where ν denotes the kinematic molecular viscosity and $p = p(\mathbf{x}, t)$ denotes the kinematic pressure field.[3] These equations must be supplemented by initial conditions and boundary conditions in order to obtain a well-posed mathematical problem.

The inertial force, represented by the nonlinear term in (2.2), is responsible for the destabilization of large flow structures. As a consequence, large vortex structures break up into successively smaller and smaller ones. This cascading mechanism continues until the viscous force becomes dominant and the smallest eddies are dissipated into heat due to the viscosity. The Reynolds number is defined as $\mathrm{Re} = \frac{\mathscr{U}\mathscr{L}}{\nu}$, where $\mathscr{U}$ denotes a representative velocity of the flow and $\mathscr{L}$ denotes a characteristic size of the geometry. It represents the ratio of the inertial force to the viscous force and provides an indication of the number of scales in the flow. In case of laminar flows, where the Reynolds numbers are rather low, the number of scales is limited due to the predominant viscous force, resulting in a smooth and stable flow pattern. However, in case of turbulent flows, which are characterized by high Reynolds numbers, the inertial force is dominant leading to an unstable chaotic flow pattern that contains an entire spectrum of scales of motion.

Since the cascade is statistically accompanied with a transfer of energy from large scales to smaller ones, before being dissipated by the viscosity, a further study of the scale interactions and the corresponding *energy cascade* seems obligatory in order to have a better understanding of the nature of laminar and turbulent flows. In the following section the equations (2.1), (2.2) and (2.3) are transformed to Fourier space in order to obtain the evolution equation of the different scales in terms of Fourier modes. This allows to derive the balance equation for the kinetic energy of the flow, given in Section 2.3.

[3] Since the set of equations (2.1)-(2.2) is sufficient to describe the motion of an incompressible fluid, the pressure field $p = p(\mathbf{x}, t)$ is determined solely by the velocity field $\mathbf{u}(\mathbf{x}, t)$. Taking the divergence of the momentum equations (2.2) and imposing the continuity equation (2.1) leads to the elliptic Poisson equation

$$\frac{\partial^2 p}{\partial x_i^2} = -\frac{\partial u_i}{\partial x_j}\frac{\partial u_j}{\partial x_i}. \tag{2.3}$$

It should be appreciated that satisfaction of this Poisson equation is a necessary and sufficient condition for the solenoidal velocity field to remain solenoidal [70].

2.2 Spectral representation

Consider the Navier-Stokes equations supplemented with periodic boundary conditions, such that the resulting periodic velocity field $\mathbf{u}(\mathbf{x},t)$ is confined to a cubical domain $\Omega = 0 \leq x_j \leq \mathscr{L}$ where

$$\mathbf{u}(\mathbf{x}+\mathscr{L}\mathbf{e}_i,t) = \mathbf{u}(\mathbf{x},t), \quad i=1,2,3 \tag{2.4}$$

in which $\mathbf{e}_i$ denotes the unit vector in the i^{th} coordinate direction. Due to the periodicity, the velocity field can be represented as a three-dimensional Fourier series of a set of orthogonal basic functions $e^{i\boldsymbol{\kappa}\mathbf{x}} = \cos(\boldsymbol{\kappa}\mathbf{x}) + i\sin(\boldsymbol{\kappa}\mathbf{x})$, i.e.

$$\mathbf{u}(\mathbf{x},t) = \sum_{\boldsymbol{\kappa}} \widehat{\mathbf{u}}(\boldsymbol{\kappa},t)\, e^{i\boldsymbol{\kappa}\mathbf{x}}, \tag{2.5}$$

where $\boldsymbol{\kappa} = [\kappa_1,\kappa_2,\kappa_3] \in \mathbb{R}^3$ denotes the wavenumber vector with magnitude $\kappa = |\boldsymbol{\kappa}|$. The Fourier coefficients $\widehat{\mathbf{u}}(\boldsymbol{\kappa},t)$ are determined by the Fourier transform $\mathscr{F}\{.\}$ such that

$$\widehat{\mathbf{u}}(\boldsymbol{\kappa},t) = \mathscr{F}\{\mathbf{u}(\mathbf{x},t)\}. \tag{2.6}$$

A more fundamental description of Fourier transformations and their properties is given in Appendix A. Following Pope [70], the equation for the evolution of the Fourier modes $\widehat{\mathbf{u}}(\boldsymbol{\kappa},t)$ is obtained by applying the operator $\mathscr{F}\{.\}$ term by term to the Navier-Stokes equations (2.2), leading to

$$\frac{d}{dt}\widehat{u}_j(\boldsymbol{\kappa},t) + i\kappa_k \mathscr{F}\{u_j(\mathbf{x},t)\,u_k(\mathbf{x},t)\} = -i\kappa_j\widehat{p}(\boldsymbol{\kappa},t) - \nu\kappa^2\widehat{u}_j(\boldsymbol{\kappa},t), \tag{2.7}$$

where $\widehat{p}(\boldsymbol{\kappa},t) = \mathscr{F}\{p(\mathbf{x},t)\}$. The Fourier coefficients of the pressure can be obtained by applying operator $\mathscr{F}\{.\}$ to the Poisson equation (2.3) such that

$$\widehat{p}(\boldsymbol{\kappa},t) = -\frac{\kappa_j\kappa_k}{\kappa^2}\mathscr{F}\{u_j(\mathbf{x},t)\,u_k(\mathbf{x},t)\} = -\frac{\kappa_k\kappa_l}{\kappa^2}\mathscr{F}\{u_k(\mathbf{x},t)\,u_l(\mathbf{x},t)\}. \tag{2.8}$$

Equation (2.7) is then simplified as

$$\begin{aligned}\frac{d}{dt}\widehat{u}_j(\boldsymbol{\kappa},t) &= -i\kappa_l\left(\delta_{jk} - \frac{\kappa_j\kappa_k}{\kappa^2}\right)\mathscr{F}\{u_k(\mathbf{x},t)\,u_l(\mathbf{x},t)\} - \nu\kappa^2\widehat{u}_j(\boldsymbol{\kappa},t) &(2.9)\\ &= -i\kappa_l\mathscr{P}_{jk}(\boldsymbol{\kappa})\,\mathscr{F}\{u_k(\mathbf{x},t)\,u_l(\mathbf{x},t)\} - \nu\kappa^2\widehat{u}_j(\boldsymbol{\kappa},t), &(2.10)\end{aligned}$$

in which $\mathscr{P}_{jk}(\boldsymbol{\kappa})$ is the projection tensor.[4] Following Pope [70], the nonlinear convective term in expression (2.10) is evaluated as

$$\mathscr{F}\left\{u_k(\mathbf{x},t)\,u_l(\mathbf{x},t)\right\} = \mathscr{F}\left\{\left[\sum_{\boldsymbol{\kappa}'}\widehat{u}_k\left(\boldsymbol{\kappa}',t\right)e^{i\boldsymbol{\kappa}'.\mathbf{x}}\right]\left[\sum_{\boldsymbol{\kappa}''}\widehat{u}_l\left(\boldsymbol{\kappa}'',t\right)e^{i\boldsymbol{\kappa}''.\mathbf{x}}\right]\right\} \tag{2.11}$$

$$= \sum_{\boldsymbol{\kappa}'}\sum_{\boldsymbol{\kappa}''}\widehat{u}_k\left(\boldsymbol{\kappa}',t\right)\widehat{u}_l\left(\boldsymbol{\kappa}'',t\right)\mathscr{F}\left\{e^{i(\boldsymbol{\kappa}'+\boldsymbol{\kappa}'').\mathbf{x}}\right\} \tag{2.12}$$

$$= \sum_{\boldsymbol{\kappa}'}\sum_{\boldsymbol{\kappa}''}\widehat{u}_k\left(\boldsymbol{\kappa}',t\right)\widehat{u}_l\left(\boldsymbol{\kappa}'',t\right)\delta_{\boldsymbol{\kappa},\boldsymbol{\kappa}'+\boldsymbol{\kappa}''} \tag{2.13}$$

$$= \sum_{\boldsymbol{\kappa}'}\widehat{u}_k\left(\boldsymbol{\kappa}',t\right)\widehat{u}_l\left(\boldsymbol{\kappa}-\boldsymbol{\kappa}',t\right). \tag{2.14}$$

By substitution of this result into the equation for the evolution of the spectral velocity (2.10), one obtains the deterministic set of ordinary differential equations

$$\frac{d}{dt}\widehat{u}_j(\boldsymbol{\kappa},t) = -i\kappa_l\mathscr{P}_{jk}(\boldsymbol{\kappa})\sum_{\boldsymbol{\kappa}'}\widehat{u}_k\left(\boldsymbol{\kappa}',t\right)\widehat{u}_l\left(\boldsymbol{\kappa}-\boldsymbol{\kappa}',t\right) - \nu\kappa^2\widehat{u}_j(\boldsymbol{\kappa},t). \tag{2.15}$$

The nonlinear convective term is non-local in wavenumber space since it involves *triadic interactions* between wavenumber vectors $\boldsymbol{\kappa}$, $\boldsymbol{\kappa}'$ and $\boldsymbol{\kappa}''$, such that $\boldsymbol{\kappa}'+\boldsymbol{\kappa}''=\boldsymbol{\kappa}$. This means that each scale or eddy in the flow interacts with all other scales. The various scale-interactions statistically result into smaller eddies, characterized by higher wavenumber vectors. Once the scales are small enough, the inertial effects become negligible in contrast to the dominant viscous effects. Hence, in the final period of decay the small scales evolve almost independently of all others and decay exponentially with time at the rate $\nu\kappa^2$ [70]. In case of laminar flows, the triadic interactions are rather limited due to the non-negligible viscous effects, whereas for turbulence, the plenitude of nonlinear triadic interactions determines the chaotic[5] behaviour of the flow. In the next section the role of the triadic interactions and the viscous damping in the energy cascade is examined.

2.3 THE ENERGY CASCADE

Formulating the energy cascade in terms of Fourier modes is advantageous since it provides a clear quantification of the energy of the different Fourier modes as well as an explicit expression for the energy transfer between the different modes, which determines the energy cascade [70].

[4] The operator $\mathscr{P}_{jk}$ projects the nonlinear force vector onto a plane normal to $\boldsymbol{\kappa}$, expressing thus the continuity constraint $\boldsymbol{\kappa}\cdot\widehat{\mathbf{u}}=0$.

[5] Remark that chaotic turbulent motions do not imply any randomness, since they obey the laws of physics rather than coincidence. The chaos is therefore said to be deterministic.

2.3.1 The evolution of kinetic energy

In order to analyze the energy cascade, involving the energy transfer between the different modes, the evolution equation for the kinetic energy of the Fourier modes is derived from the evolution equation of the spectral velocity (2.15). The kinetic energy spectrum of the Fourier modes is defined as

$$E(\boldsymbol{\kappa},t)=\frac{1}{2}\left\langle \widehat{u}_j(\boldsymbol{\kappa},t)\,\widehat{u}_j^*(\boldsymbol{\kappa},t)\right\rangle, \tag{2.16}$$

where $\widehat{u}_j^*(\boldsymbol{\kappa},t)=\widehat{u}_j(-\boldsymbol{\kappa},t)$ denotes the complex conjugate of the velocity field and $\langle . \rangle$ denotes the statistical ensemble average over all realizations of the velocity field. Multiplication of the evolution equation (2.15) with the complex conjugated velocity field $\widehat{u}_j^*(\boldsymbol{\kappa},t)$ and averaging over different realizations leads to

$$\frac{d}{dt}E(\boldsymbol{\kappa},t)=T(\boldsymbol{\kappa},t)-2\nu\kappa^2E(\boldsymbol{\kappa},t), \tag{2.17}$$

where

$$T(\boldsymbol{\kappa},t)=\kappa_l\mathscr{P}_{jk}(\boldsymbol{\kappa})\,\Re\left\{-i\sum_{\boldsymbol{\kappa}'}\left\langle \widehat{u}_j^*(\boldsymbol{\kappa},t)\,\widehat{u}_k(\boldsymbol{\kappa}',t)\,\widehat{u}_l(\boldsymbol{\kappa}-\boldsymbol{\kappa}',t)\right\rangle\right\}, \tag{2.18}$$

representing the rate of energy transfer between different modes. In case of a statistically isotropic flow[6] in a periodic box, it can be verified that the global balance of the energy transfer is zero, i.e. $\sum_{\boldsymbol{\kappa}}T(\boldsymbol{\kappa},t)=0$. In the absence of external energy sources that vary in time, the change in kinetic energy of the Fourier modes only depends on the exchange of energy between the different modes and the loss of kinetic energy due to viscous dissipation. Since the large eddies tend to break up into smaller ones, the energy transfer acts mainly in the direction from larger scales (low wavenumber modes) toward smaller scales (higher wavenumber modes). The total amount of kinetic energy in the flow is defined as

$$k(t) = \sum_{\boldsymbol{\kappa}}E(\boldsymbol{\kappa},t) \tag{2.19}$$

$$= \frac{1}{16\pi^3}\iiint_{-\infty}^{\infty}\langle u_i(\mathbf{x},t)\,u_i(\mathbf{x},t)\rangle\,d\mathbf{x}, \tag{2.20}$$

whereas the total rate of dissipation is defined as

$$\varepsilon(t) = \sum_{\boldsymbol{\kappa}}2\nu\kappa^2E(\boldsymbol{\kappa},t) \tag{2.21}$$

$$= \frac{2}{8\pi^3}\iiint_{-\infty}^{\infty}\left\langle \nu\frac{\partial u_i}{\partial x_j}(\mathbf{x},t)\,\frac{\partial u_i}{\partial x_j}(\mathbf{x},t)\right\rangle d\mathbf{x}. \tag{2.22}$$

[6] Turbulence flows are defined as statistically isotropic if the velocity field is statistically invariant under all spatial transformations, i.e. translation, rotation and reflection.

Note that both expressions for the kinetic energy (2.19) and (2.20), and both expressions for the dissipation rate (2.21) and (2.22) are identical due to *Parseval's theorem* explained in Appendix A.

2.3.2 The energy spectrum

Consider a homogeneous isotropic flow field $\mathbf{u}(\mathbf{x},t)$ that remains invariant under spatial transformations and thus does not contain any preferential direction. Under this assumption, it is possible to obtain a characteristic energy spectrum function $E(\kappa,t) \in \mathbb{R}$ by removing all directional information from the energy spectrum $E(\boldsymbol{\kappa},t) \in \mathbb{R}^3$. The information about the direction of the Fourier modes is removed by integrating $E(\boldsymbol{\kappa},t)$ over all wavenumbers $\boldsymbol{\kappa}$ with magnitude $\kappa = |\boldsymbol{\kappa}|$. Following Pope [70], the energy spectrum $E(\boldsymbol{\kappa},t)$ is considered for further analysis as the analytical counterpart of the discrete energy spectrum.[7] Removing the directional information from $E(\boldsymbol{\kappa},t)$ is mathematically translated as integrating $E(\boldsymbol{\kappa},t)$ over a spherical surface $\mathscr{S}(\kappa)$ with radius κ

$$E(\kappa,t) = \oint E(\boldsymbol{\kappa},t)\, d\mathscr{S}(\kappa) = \iiint_{\boldsymbol{\kappa}} E(\boldsymbol{\kappa},t)\, \delta(|\boldsymbol{\kappa}|-\kappa)\, d\boldsymbol{\kappa}. \tag{2.24}$$

The expressions for the kinetic energy and the dissipation rate are straightforwardly obtained from previous equation

$$k(t) = \int_0^\infty E(\kappa,t)\, d\kappa, \tag{2.25}$$

$$\varepsilon(t) = \int_0^\infty 2\nu\kappa^2 E(\kappa,t)\, d\kappa. \tag{2.26}$$

Since the energy spectrum function $E(\kappa,t)$ represents the energy content of the different characteristic scales in a statistically isotropic flow, it is fully determined by the inertial effects (related to energy transfer) and viscous effects (related to energy dissipation) and thus by the Reynolds number. As a consequence, the shape of the energy spectrum and the number of scales is different for laminar and turbulent flow regimes. In the following section, the characteristic form of the turbulent energy spectrum is examined, and the difference with the spectrum related to laminar flows is briefly discussed.

[7] The analytical energy spectrum is readily obtained from the discrete energy spectrum by

$$E(\overline{\boldsymbol{\kappa}},t) = \sum_{\boldsymbol{\kappa}} \delta(\overline{\boldsymbol{\kappa}}-\boldsymbol{\kappa})\, E(\boldsymbol{\kappa},t), \tag{2.23}$$

where $\overline{\boldsymbol{\kappa}}$ is the continuous wavenumber vector.

2.3.3 Turbulence: Kolmogorov's law

It has since long been recognized that for a sufficiently high Reynolds number Re (see e.g. Figure 2.1), turbulent flows are characterized by a universal behaviour. As mentioned before, the large eddy structures, represented by low wavenumbers, break up due to inertial effects into successively smaller and smaller eddies until the smallest eddies are finally dissipated by viscous effects. This breakdown of large structures into smaller ones is accompanied with a transfer of kinetic energy from large to smaller eddies until this energy is dissipated by the molecular viscosity. It is exactly this energy cascade and dissipation mechanism that obeys a universal law. In 1941 Kolmogorov [47] published a general theory on the local structure of turbulence. Besides the *energy-containing range* which contains the largest, most energetic and anisotropic scales, Kolmogorov distinguished a second *universal equilibrium range* of smaller turbulent scales down the cascade. These small eddies are considered locally isotropic, flow independent and in quasi equilibrium since the directional information of the large scales is quickly lost in the cascade. Furthermore, this universal equilibrium range is classified into two subranges, i.e. the *inertial subrange* and the *dissipation (sub)range*. The scales in the dissipation range are responsible for almost the entire dissipation since they experience significant viscous damping. The smallest scales of significance in this range, called the Kolmogorov scales are characterized by the length scale

$$\eta\left(t\right) = \left(\frac{\nu^3}{\varepsilon\left(t\right)}\right)^{\frac{1}{4}}. \tag{2.27}$$

In contrast to the dissipation range, the inertial subrange is mostly determined by inertial effects whereas the viscous effects are negligible. Kolmogorov postulated that the motions in the inertial subrange have a universal form which is uniquely determined by the rate of dissipation ε and their length scale, independently of the viscosity (*the second similarity hypothesis*). Based on dimensional analysis, the energy spectrum in the inertial subrange is given by

$$E\left(\kappa, t\right) = C_k \varepsilon\left(t\right)^{\frac{2}{3}} \kappa^{-\frac{5}{3}}, \tag{2.28}$$

where C_k is the universal Kolmogorov constant and is measured to be approximately $C_k = 1.5$. Figure 2.1 demonstrates the normalized energy spectrum at various Reynolds numbers. For an arbitrary high Reynolds number Re (Figure 2.1), the energy containing range, inertial subrange and dissipation range are indicated. Notice the $-5/3$-inertial range scaling and the dissipation range where the energy spectrum decays exponentially. However, for decreasing values of the Reynolds number (e.g. $\frac{\mathrm{Re}}{4}, \frac{\mathrm{Re}}{16}, \frac{\mathrm{Re}}{64}$), the number of scales is reduced due to increasing influence of the viscous effects such that the inertial range behaviour tends to disappear. Once the energy containing range converts immediately into the dissipation range (e.g. $\frac{\mathrm{Re}}{64}$), the shape of the energy spectrum may be considered as characteristic for laminar

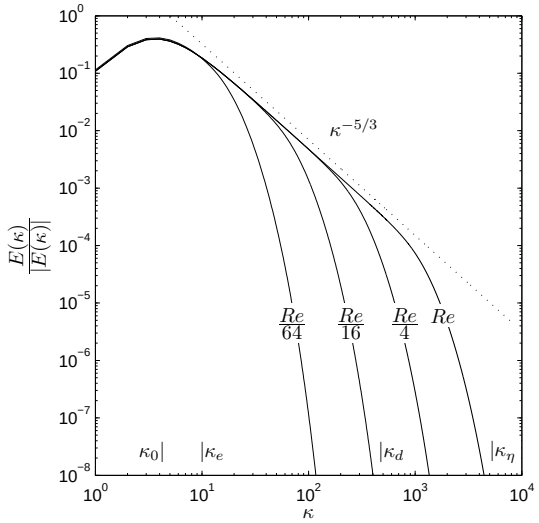

Figure 2.1: The normalized energy spectrum. For arbitrary high Reynolds numbers (Re) one can distinguish the energy containing range $\kappa \leq \kappa_e$, the inertial subrange $\kappa_e \leq \kappa \leq \kappa_d$ and the dissipation range $\kappa_d \leq \kappa \leq \kappa_\eta = \frac{2\pi}{\eta}$.

flows. Summarizing, turbulent flows are thus characterized by their inertial range scaling in contrast to laminar flows where the inertial range is absent. According to Pope [70], the entire energy spectrum function can be modeled by extending the Kolmogorov spectrum (2.28) with two non-dimensional functions as

$$E(\kappa, t) = C_k \varepsilon(t)^{\frac{2}{3}} \kappa^{-\frac{5}{3}} F_e(\kappa, t) F_\eta(\kappa, t). \tag{2.29}$$

The function $F_e(\kappa, t)$ determines the shape of the energy containing range and tends to unity for large κ. Similarly, $F_\eta(\kappa, t)$ determines the shape of the dissipation range and tends to unity for small κ. Several prescriptions are known for both functions, but they generally contain some parameters which are tuned to fit the experimental data. Note that $F_e(\kappa, t)$ cannot be captured easily in a universal expression as it is dominated by the large-scale flow characteristics and thus related to the specific geometry. For a complete description of these functions, the reader is referred to [70, 74].

2.3.4 Homogeneous Isotropic Turbulence

Before advancing to the discussion about numerical simulations of turbulent flows and their computational requirements, some definitions are needed concerning the different length scales of eddies in homogeneous isotropic turbulence [70]. For

isotropic turbulence, one defines the *longitudinal integral length scale* L_{11} as

$$L_{11}(t) = \frac{3\pi}{4k(t)} \int_0^\infty \frac{E(\kappa, t)}{\kappa} d\kappa, \tag{2.30}$$

which represents the largest relevant longitudinal length scales in the flow. Another measure which is roughly related to the largest relevant length scales is defined as

$$L(t) = \frac{k(t)^{3/2}}{\varepsilon(t)}. \tag{2.31}$$

At high Reynolds numbers Re, the length scale ratio L_{11}/L tends asymptotically to the value 0.43, although this ratio significantly increases for lower Reynolds numbers. The *(transversal) Taylor microscale*, defined from the relations

$$\lambda_g(t) = \sqrt{15\nu \frac{k(t)}{\varepsilon(t)}} \tag{2.32}$$

$$= \sqrt{10}\eta(t)^{2/3} L(t)^{1/3}, \tag{2.33}$$

is intermediate in size between the Kolmogorov length scale η and the length scale L. This well-defined quantity is often used in later analysis.
Further, it is possible to define different Reynolds numbers based on the different length scale-definitions, which are mutually related by

$$\mathrm{Re}_L(t) = \frac{\sqrt{k(t)}L(t)}{\nu} = \frac{k(t)^2}{\nu\varepsilon(t)} \tag{2.34}$$

$$= \frac{3}{20}\mathrm{Re}_\lambda^2 \approx \frac{6}{20}\mathrm{Re}. \tag{2.35}$$

These definitions will be used further in the next section.

2.4 Direct Numerical Simulation of Turbulence

Direct numerical simulation (DNS) consists in solving the *discrete* Navier-Stokes equations[8] numerically on a computational grid, resolving all the scales of motion, including the smallest Kolmogorov scales. Although the DNS approach is straightforward and unrivaled in accuracy, it is appreciated from the previous fundamental study that the resolution requirements become prohibitively expensive with increasing number of scales which is proportional to the Reynolds number.

[8]Supplemented with a set of boundary conditions appropriate to the flow.

The present section is initiated with a rigorous mathematical description of discretization, referred to as *sampling*. The properties related to this mathematical operation form the fundamentals of the *finite difference* framework which is the subject of this dissertation. By means of some of these properties one is allowed to make a well-considered realistic estimation of the resolution requirements for the DNS of homogeneous isotropic turbulence and to appraise the involved computational effort. The resulting conclusions motivate the use of more affordable approaches such as *Large-Eddy Simulation* (LES), where only the largest energetic scales are resolved, modeling the influence of the small dissipative scales on the evolution of the large ones.

2.4.1 The Sampling operator

Solving the Navier-Stokes equations numerically involves the consistent *projection* of the velocity field $\mathbf{u}(\mathbf{x}, t)$ and the governing Navier-Stokes equations from the continuum spatial domain $\Omega \subset \mathbb{R}^3$ with Cartesian coordinates $\mathbf{x} \in \mathbb{R}^3$ to the discrete spatial domain $\Omega^{\Delta} \subset \mathbb{R}^3$ with discrete equispaced Cartesian coordinates $\mathbf{x_k} = [x_1(\mathbf{k}), x_2(\mathbf{k}), x_3(\mathbf{k})] \in \mathbb{R}^3$, and $\mathbf{k} = [k_1, k_2, k_3] \in \mathbb{N}^3$ the index vector. Let $\mathbf{N} = [N_1, N_2, N_3]$ represent the number of grid nodes in each direction such that $0 \leq k_j \leq N_j$, $j = 1, 2, 3$ and let $\boldsymbol{\Delta} = [\Delta_1, \Delta_2, \Delta_3]$ give the uniform grid spacing in each direction. Further the temporal dimension t is considered implicitly without any loss of generality.[9] This projection requires now the definition of a mathematical *sampling function*, operating between continuum and discrete space. Following Bracewell [7], definition 2.4.1 introduces the mathematical operator that describes the sampling process in a one-dimensional space $\mathbb{R}$.

Definition 2.4.1 (***Dirac comb*** $\text{ш}(x)$, $x \in \mathbb{R}$)**.** Let $\delta(x)$, $x \in \mathbb{R}$ be the *Dirac delta distribution*,[10] then the *Dirac comb* or *Shah function* $\text{ш}(x)$ is defined as an infinite series of Dirac distributions

$$\text{ш}(x) = \sum_{k=-\infty}^{\infty} \delta(x - k), \tag{2.38}$$

[9] Note that temporal discretization can be described equivalently, however, since it is straightforward it will not be explicitly discussed.

[10] The Dirac delta distribution may be defined as

$$\delta(x) = \lim_{q \to 0} \left[\frac{1}{q\sqrt{\pi}} e^{-x^2/q^2} \right] = \begin{cases} 0 & x \neq 0 \\ \infty & x = 0 \end{cases}, \tag{2.36}$$

and satisfies the condition

$$\int_{-\infty}^{\infty} \delta(x)\, dx = \int_{-\epsilon}^{\epsilon} \delta(x)\, dx = 1, \quad \epsilon > 0. \tag{2.37}$$

normalized as

$$\int_{k-\frac{1}{2}}^{k+\frac{1}{2}} \text{ш}\,(x)\,dx = 1. \tag{2.39}$$

If the scale of x is compressed by a factor $a > 0$, thus reducing the original unit area of the pulses with a factor a, then the strength of the pulses also needs to be reduced by the factor a. The rescaled Dirac comb then reads

$$\text{ш}\,(ax) = \frac{1}{a}\sum_{k=-\infty}^{\infty} \delta\left(x - \frac{k}{a}\right). \tag{2.40}$$

In analogy with the Dirac distribution, the Dirac comb is a *generalized function*[11] whose definition and properties rely on the integral expression

$$\int_{k-\frac{1}{2}}^{k+\frac{1}{2}} \text{ш}\,(x)\,g\,(x)\,dx, \tag{2.41}$$

where $g\,(x)$ is any differentiable test function which is continuous at k, $\forall k$. By means of integral (2.41), some important properties of the Dirac comb are discussed, that are relevant for nonlinear differential equations such as the Navier-Stokes equations.

i. Consider the test function $g\,(x) = u\,(x)$ and the scaling factor $a = 1/\Delta$, then

$$\begin{aligned} \overline{u}\,(x) &= \frac{1}{\Delta}\text{ш}\left(\frac{x}{\Delta}\right)u\,(x) && (2.42)\\ &= \sum_{k=-\infty}^{\infty} \delta\,(x - k\Delta)\,u\,(x) && (2.43)\\ &= \sum_{k=-\infty}^{\infty} \delta\,(x - x_k)\,u\,(x_k)\,, && (2.44) \end{aligned}$$

is the *discontinuous* sampled function represented by a modulated Dirac comb in $\mathbb{R}$ such that $\overline{u}\,(x \neq x_k) = 0$ and $\overline{u}\,(x = x_k) = u\,(x_k)$. The *discrete* sampled function is then defined by the integral (2.41) leading to

$$\overline{u}\,(x_k) = \int_{x_k-\frac{\Delta}{2}}^{x_k+\frac{\Delta}{2}} \overline{u}\,(x)\,dx. \tag{2.45}$$

[11] A generalized function can be defined as the limit of a class of distribution functions such that an ideal function is obtained [70].

Due to this sampling property, the Dirac comb is considered to be a mathematical operator that defines the discretization process. Note that the Dirac comb is an idempotent operator, such that

$$\frac{1}{\Delta}\text{Ш}\left(\frac{x}{\Delta}\right)\left[\frac{1}{\Delta}\text{Ш}\left(\frac{x}{\Delta}\right)u(x)\right] = \frac{1}{\Delta}\text{Ш}\left(\frac{x}{\Delta}\right)u(x) = \overline{u}(x). \tag{2.46}$$

Before continuing, a shorthand notation for the sampling operation is introduced. Hence, the *sampling operator* $\mathscr{S}^{\Delta}$ is defined as

$$\mathscr{S}^{\Delta}\circ u(x) = \overline{u}(x), \tag{2.47}$$
$$\mathscr{S}^{\Delta}\circ\mathscr{S}^{\Delta}\circ u(x) = \mathscr{S}^{\Delta}\circ u(x) = \overline{u}(x), \ (\textit{Idempotency}), \tag{2.48}$$

where $\circ$ denotes "operating on".

ii. Assume the test function $g(x) = u(x)\,v(x)$ with $v(x) \in \mathbb{R}$ continuous at x_k, $\forall k$. The argument of the integral (2.41) is then evaluated as

$$\frac{1}{\Delta}\text{Ш}\left(\frac{x}{\Delta}\right)u(x)\,v(x)\,dx = \sum_{k=-\infty}^{\infty}\delta(x-x_k)\,u(x)\,v(x) \tag{2.49}$$
$$= \sum_{k=-\infty}^{\infty}\delta(x-x_k)\,u(x_k)\,v(x_k) \tag{2.50}$$
$$= \overline{u}(x)\,\overline{v}(x), \tag{2.51}$$

and further

$$\int_{x_k-\frac{\Delta}{2}}^{x_k+\frac{\Delta}{2}}\frac{1}{\Delta}\text{Ш}\left(\frac{x}{\Delta}\right)u(x)\,v(x)\,dx = \overline{u}(x_k)\,\overline{v}(x_k). \tag{2.52}$$

This result proves the commutativity of the Dirac comb or sampling operator with the product of two continuous functions, and can be expressed as

$$\mathscr{S}^{\Delta}\circ[u(x)\,v(x)] = \left[\mathscr{S}^{\Delta}\circ u(x)\right]\left[\mathscr{S}^{\Delta}\circ v(x)\right], \ (\textit{Commutativity}). \tag{2.53}$$

iii. In contrast to the product-commutation (2.51), the Dirac comb does not commute with the spatial derivatives. Therefore, consider the test function $g(x) = \frac{\partial u(x)}{\partial x}$ where the continuous partial derivative is typically defined as

$$\frac{\partial u(x)}{\partial x} = \lim_{\Delta\to\epsilon}\frac{u(x+\Delta)-u(x-\Delta)}{2\Delta}, \quad \epsilon = 0. \tag{2.54}$$

In order for the limit to exist, the function $u(x)$ must be necessarily continuous. Hence, the argument of integral (2.41), given by expression

$$\frac{1}{\Delta}\text{ш}\left(\frac{x}{\Delta}\right)\frac{\partial u(x)}{\partial x} = \frac{1}{\Delta}\text{ш}\left(\frac{x}{\Delta}\right)\left[\lim_{\Delta\to\epsilon}\frac{u(x+\Delta)-u(x-\Delta)}{2\Delta}\right], \tag{2.55}$$

obviously differs from expression

$$\begin{aligned}\frac{1}{\Delta}\text{ш}\left(\frac{x}{\Delta}\right)\frac{\partial u(x)}{\partial x} &\neq \lim_{\Delta\to\epsilon}\sum_{k=-\infty}^{\infty}\delta(x-x_k)\frac{u(x+\Delta)-u(x-\Delta)}{2\Delta} &(2.56)\\ &\neq \lim_{\Delta\to\epsilon}\frac{\overline{u}(x+\Delta)-\overline{u}(x-\Delta)}{2\Delta}. &(2.57)\end{aligned}$$

Indeed, since $\overline{u}(x)$ is by definition a discontinuous function, the limit does not exist any longer. Therefore, the definition of the derivative cannot be satisfied, unless approximatively. A possible *finite difference* approximation for the partial derivative may now be defined by evaluating the integral (2.41) such that

$$\begin{aligned}\int_{x_k-\frac{\Delta}{2}}^{x_k+\frac{\Delta}{2}}\frac{1}{\Delta}\text{ш}\left(\frac{x}{\Delta}\right)\frac{\partial u(x)}{\partial x}dx &\approx \frac{\overline{u}(x_k+\Delta)-\overline{u}(x_k-\Delta)}{2\Delta} &(2.58)\\ &\approx \frac{\overline{u}(x_{k+1})-\overline{u}(x_{k-1})}{2\Delta} &(2.59)\\ &\approx \frac{\delta\overline{u}(x)}{\delta x}, &(2.60)\end{aligned}$$

where $\delta = \mathscr{S}^{\Delta}\circ\partial$ in short hand notation. Since finite difference approximations are the subject of this dissertation a more extensive discussion is given in the following chapters.

iv. The Fourier transform of the Dirac comb, which is a periodic function with period Δ such that $\text{ш}(x+\Delta) = \text{ш}(x), \forall x$, appears to be another Dirac comb [7] since

$$\begin{aligned}\mathscr{F}\left\{\frac{1}{\Delta}\text{ш}\left(\frac{x}{\Delta}\right)\right\} &= \mathscr{F}\left\{\sum_{k=-\infty}^{\infty}\delta(x-x_k)\right\} &(2.61)\\ &= \sum_{k=-\infty}^{\infty}\mathscr{F}\{\delta(x-x_k)\} &(2.62)\\ &= \frac{1}{2\pi}\sum_{k=-\infty}^{\infty}e^{-i\kappa x_k} &(2.63)\\ &= \frac{1}{\Delta}\sum_{k=-\infty}^{\infty}\delta(\kappa-k\kappa_s) = \frac{1}{2\pi}\text{ш}\left(\frac{\kappa}{\kappa_s}\right), &(2.64)\end{aligned}$$

where $\kappa_s = \frac{2\pi}{\Delta}$ denotes the sampling wavenumber determined by the grid spacing. In the next section, this property is used to obtain the Fourier transform of the sampled velocity field $\overline{u}(x)$. The conclusions from this Fourier analysis will prove to be very important since they determine the computational requirements of a Direct Numerical Simulation.

In the previous, the Dirac comb and its properties were considered in case of a uniform grid spacing, leading thus to uniform sampling. Nevertheless, the concept of sampling can easily be extended to computational grids with a *non-uniform grid spacing*. Assume a well chosen transformation function $T_{x\to\xi}$ which transforms the function $g(x)$ from physical space $x \in \mathbb{R}$ to a corresponding computational space $\xi \in \mathbb{R}$, such that

$$\xi = T_{x\to\xi}(x) \tag{2.65}$$

and thus,

$$g(\xi) = g(T_{x\to\xi}(x)). \tag{2.66}$$

Hence, the non-uniform sampling operation on $g(x)$ in physical space $x \in \mathbb{R}$ is equivalent with the uniform sampling of the transformed function $g(\xi)$ in computational space $\xi \in \mathbb{R}$, before transforming it back to physical space. It is emphasized that the properties of function $g(\xi)$ may differ from those related to $g(x)$. It may be clear that all previously defined properties of the sampling operator remain valid under this transformation. For instance, using the chain rule for differentiation, the derivatives in physical space are now approximated as

$$\overline{\frac{\partial u(x)}{\partial x}} = \int_{\xi_k-\frac{\Delta}{2}}^{\xi_k+\frac{\Delta}{2}} \frac{1}{\Delta} \text{ш}\left(\frac{\xi}{\Delta}\right) \frac{\partial u(\xi)}{\partial \xi} d\xi \overline{\frac{\partial \xi(x)}{\partial x}} \tag{2.67}$$

$$= \int_{\xi_k-\frac{\Delta}{2}}^{\xi_k+\frac{\Delta}{2}} \frac{1}{\Delta} \text{ш}\left(\frac{\xi}{\Delta}\right) \frac{\partial u(\xi)}{\partial \xi} d\xi \overline{\frac{\partial x(\xi)}{\partial \xi}}^{-1} \tag{2.68}$$

$$\approx \frac{\delta \overline{u}(\xi)}{\delta \xi} \overline{\frac{\partial x(\xi)}{\partial \xi}}^{-1}. \tag{2.69}$$

In the following, only uniform grids are considered, avoiding unnecessary complexity. In order to discretize the continuous velocity field $\mathbf{u}(\mathbf{x})$, $\mathbf{x} \in \mathbb{R}^3$, it is necessary to extend definition (2.4.1) to $\mathbb{R}^3$.

Definition 2.4.2 (***Dirac comb*** $\text{Ш}(\mathbf{x}), \mathbf{x} \in \mathbb{R}^3$**).** The *Dirac comb* in $\text{Ш}(\mathbf{x}), \mathbf{x} \in \mathbb{R}^3$ is defined as the product of one-dimensional Shah functions

$$\text{Ш}(\mathbf{x}) = \prod_{j=1}^{3} \text{ш}(x_j) = \sum_{\mathbf{k}=-\infty}^{\infty} \delta^3(\mathbf{x} - \mathbf{k}), \tag{2.70}$$

where the Dirac delta distribution $\delta^3(\mathbf{x})$ is given by

$$\delta^3(\mathbf{x}) = \prod_{j=1}^{3} \delta(x_j), \; x_j \in \mathbb{R}. \tag{2.71}$$

Further, $\text{Ш}(\mathbf{x})$ is normalized as

$$\iiint_{\mathbf{k}-\frac{\mathbf{1}}{\mathbf{2}}}^{\mathbf{k}+\frac{\mathbf{1}}{\mathbf{2}}} \text{Ш}(\mathbf{x})\, d\mathbf{x} = 1. \tag{2.72}$$

Assume a vector of scaling coefficients $\mathbf{a} = [a_1, a_2, a_3]$, then the rescaled Dirac comb in $\mathbb{R}^3$ is given by

$$\text{Ш}(\mathbf{ax}) = \prod_{j=1}^{3} \text{ш}(a_j x_j) = \prod_{j=1}^{3} \left[\frac{1}{a_j} \sum_{\mathbf{k}=-\infty}^{\infty} \delta\left(x_j - \frac{k_j}{a_j} \right) \right]. \tag{2.73}$$

It can be understood that all properties, i.e. idempotency (2.46), product commutation (2.51), non-commutativity with derivatives and finally the Fourier transform, are maintained for multi-dimensional fields and their application is straightforward. The short hand notation for the three-dimensional sampling operator is given by $\mathscr{S}^{\mathbf{\Delta}} \circ \mathbf{u}(\mathbf{x}) = \mathscr{S}^{\Delta_1} \circ \mathscr{S}^{\Delta_2} \circ \mathscr{S}^{\Delta_3} \circ \mathbf{u}(\mathbf{x})$.

2.4.2 Aliasing: the Nyquist-Shannon theorem

In order to avoid unnecessary complications, a uniform computational grid is considered with an equal number of nodes in every direction such that $N = N_j$ and $\Delta = \Delta_j$ for $j = 1, 2, 3$. It was shown in Section 2.3.3 that the smallest eddies in a homogeneous isotropic flow are characterized by the Kolmogorov wavenumber $\kappa_\eta = \frac{2\pi}{\eta}$. This implies that the Fourier modes at wavenumbers $\kappa > \kappa_\eta$ have no significant energy as can be seen from Figure 2.1. Hence, the velocity field $\mathbf{u}(\mathbf{x})$ is considered to be a band-limited field, as it contains only energy in the wavenumber-band $0 \leq \kappa \leq \kappa_\eta$. In this section, the consequences of the sampling operation on the band-limited velocity $\mathbf{u}(\mathbf{x})$ and the corresponding energy spectrum are examined.

The Fourier transform of the discontinuous sampled velocity field $\overline{\mathbf{u}}(\mathbf{x},t)$ is obtained by

$$\begin{aligned}
\widehat{\overline{\mathbf{u}}}(\boldsymbol{\kappa}) &= \mathscr{F}\left\{\frac{1}{\Delta^3}\text{Ш}\left(\frac{\mathbf{x}}{\boldsymbol{\Delta}}\right)\mathbf{u}(\mathbf{x},t)\right\} && (2.74)\\
&= \mathscr{F}\left\{\frac{1}{\Delta^3}\text{Ш}\left(\frac{\mathbf{x}}{\boldsymbol{\Delta}}\right)\right\} * \mathscr{F}\{\mathbf{u}(\mathbf{x},t)\} \quad \textit{(Convolution theorem)} && (2.75)\\
&= \frac{1}{8\pi^3}\text{Ш}\left(\frac{\boldsymbol{\kappa}}{\kappa_s}\right) * \widehat{\mathbf{u}}(\boldsymbol{\kappa},t) && (2.76)\\
&= \frac{1}{\Delta^3}\sum_{\mathbf{k}=-\infty}^{\infty}\widehat{\mathbf{u}}(\boldsymbol{\kappa}-\mathbf{k}\kappa_s,t). && (2.77)
\end{aligned}$$

Apparently, due to the convolution of $\widehat{\mathbf{u}}(\boldsymbol{\kappa},t)$ with the Dirac Comb,[12] the Fourier modes $\widehat{u}(\boldsymbol{\kappa},t)$ are infinitely replicated in every direction of the wavenumber space at every integer multiple k_j of the sampling wavenumber $\kappa_s = \frac{2\pi}{\Delta}$. These replicas are called images. Analogously, the energy spectrum of the sampled velocity field $\overline{E}(\boldsymbol{\kappa},t)$, is obtained as

$$\begin{aligned}
\overline{E}(\boldsymbol{\kappa},t) &= \frac{1}{2}\widehat{\overline{\mathbf{u}}}(\boldsymbol{\kappa},t)\,\widehat{\overline{\mathbf{u}}}^*(\boldsymbol{\kappa},t) && (2.79)\\
&= \frac{1}{2}\left\{\frac{1}{\Delta^3}\sum_{\mathbf{k}=-\infty}^{\infty}\widehat{\mathbf{u}}(\boldsymbol{\kappa}-\mathbf{k}\kappa_s,t)\right\}\left\{\frac{1}{\Delta^3}\sum_{\mathbf{k}=-\infty}^{\infty}\widehat{\mathbf{u}}^*(\boldsymbol{\kappa}-\mathbf{k}\kappa_s,t)\right\} && (2.80)\\
&= \frac{1}{2\Delta^6}\sum_{\mathbf{k}=-\infty}^{\infty}\widehat{\mathbf{u}}(\boldsymbol{\kappa}-\mathbf{k}\kappa_s,t)\,\widehat{\mathbf{u}}^*(\boldsymbol{\kappa}-\mathbf{k}\kappa_s,t) && (2.81)\\
&= \frac{1}{\Delta^6}\sum_{\mathbf{k}=-\infty}^{\infty}E(\boldsymbol{\kappa}-\mathbf{k}\kappa_s,t), && (2.82)
\end{aligned}$$

which is a series of repeated and shifted energy spectra. Since the considered flow is isotropic, the sampled energy spectrum function $\overline{E}(\kappa,t)$ is obtained by integrating the energy spectrum $\overline{E}(\boldsymbol{\kappa},t)$ over spherical shells (2.24), removing any directional information. If the wavenumber-shift characterized by κ_s is sufficiently large, equation (2.82) shows that the neighboring spectra coexist without interference. However, the adjacent images of the spectrum, e.g. $\overline{E}(\kappa,t)$ and $\overline{E}(\kappa+\kappa_s,t)$ overlap if the wavenumber-shift is too small. This is illustrated in Figure 2.2. Due to the summation in equation (2.82) the energy of the overlapping Fourier modes is combined such that an energy pile-up is observed at the tail of the original energy spectrum as if the tail-energy is mirrored around the intersection. It may be

[12]

$$\frac{1}{8\pi^3}\text{Ш}\left(\frac{\boldsymbol{\kappa}}{\kappa_s}\right) * \widehat{\mathbf{u}}(\boldsymbol{\kappa}) = \frac{1}{8\pi^3}\text{ш}\left(\frac{\kappa_1}{\kappa_s}\right) * \left[\text{ш}\left(\frac{\kappa_2}{\kappa_s}\right) * \left[\text{ш}\left(\frac{\kappa_3}{\kappa_s}\right) * \widehat{\mathbf{u}}(\boldsymbol{\kappa},t)\right]\right]. \quad (2.78)$$

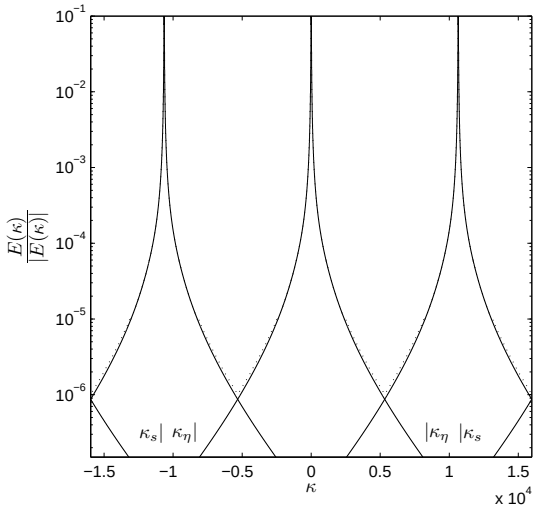

Figure 2.2: The principle of aliasing. The energy spectrum overlaps with two neighboring spectrum-images, both shifted with sampling wavenumber κ_s. The resulting energy spectrum contains an energy pile-up at the end of the spectrum $(\cdots)$.

clear from Figure 2.3 that the energy pile-up becomes significant once the inertial ranges start to overlap. This phenomenon, called *aliasing*, results from the fact that the eddies smaller than the grid spacing cannot be seen on the computational grid. These small scales, corresponding to high wavenumbers, are erroneously represented or *aliased* as larger eddies corresponding to lower wavenumbers. The sufficient and necessary condition that precludes aliasing is derived by imposing the constraint

$$\kappa_\eta < \kappa_s - \kappa_\eta, \tag{2.83}$$

resulting in

$$\kappa_\eta < \frac{\kappa_s}{2} = \frac{\pi}{\Delta} = \kappa_{max}. \tag{2.84}$$

The wavenumber κ_{max}, which indicates the smallest motion that can be represented on the computational grid, is called the *Nyquist-frequency* and (2.84) forms the basis for the *Nyquist-Shannon Sampling Theorem*.[13] Aside from the fact that no wavenumber-information is lost if the Nyquist criterion $\kappa_\eta < \kappa_{max}$ is satisfied, the Nyquist-Shannon theorem states that under this condition, the original velocity field $\mathbf{u}(\mathbf{x})$ can be entirely reconstructed from the sampled field $\overline{\mathbf{u}}(\mathbf{x})$. The reconstruction involves the use of a reconstruction filter that extracts the original spectrum, removing the images. In physical space, the reconstruction filter is given by the *sine*

[13] Named after the Swedish physicist Harry Nyquist and the American mathematician Claude Elwood Shannon.

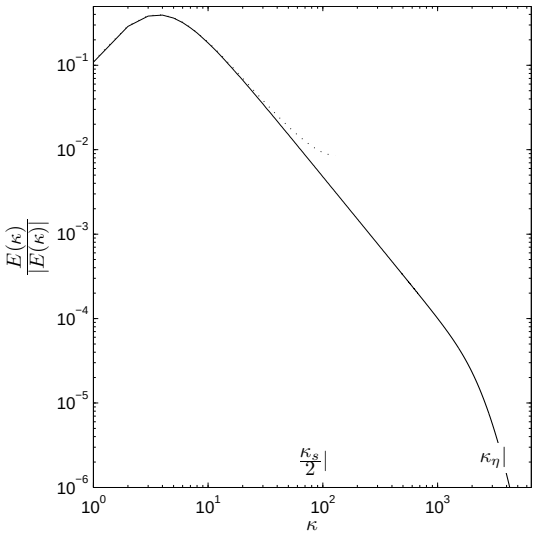

Figure 2.3: Aliased energy spectrum. The significant energy pile-up at tail of the energy spectrum $(\cdots)$ is due to the interfering spectrum-images.

cardinal or *sinc*[14] function such that

$$\mathbf{u}(\mathbf{x},t) = \left[\prod_{j=1}^{3} 2\pi \,\mathrm{sinc}\left(\kappa_s x_j\right)\right] * \overline{\mathbf{u}}(\mathbf{x},t)\,. \tag{2.85}$$

In summary, this fundamental study indicates that Direct Numerical Simulation requires the use of a computational grid with maximum resolution $\kappa_{max} = \frac{\pi}{\Delta}$ on which the smallest Kolmogorov scales can be resolved, i.e. $\kappa_\eta < \kappa_{max}$. Hence, the required number of nodes N is related to the size of the Kolmogorov motions η and thus to the Reynolds number Re. In Section 2.4.4, the relation between N and the Reynolds number Re is deduced, based on scaling properties of turbulent flows in combination with the Nyquist criterion. However, this first requires a projection of the Navier-Stokes equations from continuum space to discrete space as well as a projection of continuum time to discrete time, the latter discretization being analogous to the former.

2.4.3 The discrete Navier-Stokes equations

Spatial discretization is obtained by applying the sampling operator $\mathscr{S}^{\mathbf{\Delta}} = \mathscr{S}^{\Delta_{x_1}} \circ \mathscr{S}^{\Delta_{x_2}} \circ \mathscr{S}^{\Delta_{x_3}}$ to the continuity equation (2.1) and the Navier-Stokes equations (2.2). This operation results in a projection from the continuum spatial domain $\Omega \subset \mathbb{R}^3$ with Cartesian coordinates $\mathbf{x} \in \mathbb{R}^3$ to the discrete spatial domain $\Omega^\Delta \subset \mathbb{R}^3$ with discrete equispaced Cartesian coordinates $\mathbf{x_k} = [x_1(\mathbf{k}), x_2(\mathbf{k}), x_3(\mathbf{k})] \in \mathbb{R}^3$,

[14] The sine cardinal function is defined as $\mathrm{sinc}(x) = \frac{\sin(x)}{x}$.

and $\mathbf{k} = [k_1, k_2, k_3] \in \mathbb{N}^3$ the index vector. Let $\mathbf{N} = [N_1, N_2, N_3]$ represent the number of grid nodes in each direction such that $0 \leq k_j \leq N_j$, $j = 1, 2, 3$ and let $\boldsymbol{\Delta} = [\Delta_1, \Delta_2, \Delta_3]$ give the uniform grid spacing in each direction. Further, the sampling operator $\mathscr{S}^{\Delta_t}$ projects the Navier-Stokes equations (2.2) from continuum time $t \in \mathbb{R}$ to discrete time $t_n \in \mathbb{R}$, $n \in \mathbb{N}$ where Δt denotes the time interval. Using properties (2.45),(2.51) and (2.59), the discrete continuity and the Navier-Stokes equations are then written as

$$\frac{\delta \overline{u}_i}{\delta x_i} = \Pi^{\Delta} \tag{2.86}$$

$$\frac{\delta \overline{u}_i}{\delta t} + \overline{u}_j \frac{\delta \overline{u}_i}{\delta x_j} = -\frac{\delta \overline{p}}{\delta x_i} + \nu \frac{\delta^2 \overline{u}_i}{\delta x_j^2} + \Sigma_i^{\Delta}, \tag{2.87}$$

where the pressure field is described by the discrete Poisson equation.[15] Due to the non-commutativity of the sampling operator $\mathscr{S}^{\Delta}$ with the spatial partial derivatives, *truncation errors* arise in the continuity equation, the momentum equations and the Poisson equation,[16] which are formally given by the relations

$$\Pi^{\Delta} = \frac{\delta \overline{u}_i}{\delta x_i} - \overline{\frac{\partial u_i}{\partial x_i}} \tag{2.90}$$

$$\Sigma_i^{\Delta} = \overline{u}_j \left(\frac{\delta \overline{u}_i}{\delta x_j} - \overline{\frac{\partial u_i}{\partial x_j}} \right) + \left(\frac{\delta \overline{p}}{\delta x_i} - \overline{\frac{\partial p}{\partial x_i}} \right) - \nu \left(\frac{\delta^2 \overline{u}_i}{\delta x_j^2} - \overline{\frac{\partial^2 u_i}{\partial x_j^2}} \right). \tag{2.91}$$

Since at this point, the exact expressions for the truncation errors Π^{Δ}, Σ_i^{Δ} (and Λ^{Δ}) are not essential in the further discussions, their definitions are postponed. Further, the grid spacing Δ_j in each direction is assumed just small enough, such that the Kolmogorov scales are resolved correctly on the computational grid and the Nyquist criterion $\kappa_{max} > \kappa_\eta$ is satisfied for the projected velocity field $\overline{\mathbf{u}}(\mathbf{x}_k, t)$. If $\kappa_{max} \approx \kappa_\eta$, the evaluation of the nonlinear term $\overline{u}_i \overline{u}_j$ leads to the creation of Fourier modes in the wavenumber range $\kappa_\eta \leq \kappa \leq 2\kappa_\eta$ and thus the Nyquist criterion is violated. Despite the fact that the nodal values of $\overline{u}_i \overline{u}_j$ are exact in physical space, the aliasing errors occur as soon as a spatial interpolation of these nodal values is applied. Such interpolations are intrinsically assumed in finite difference approximations e.g. used in the evaluation of the nonlinear force $\frac{\delta \overline{u}_i \overline{u}_j}{\delta x_j}$ (see Chapter

[15] The discrete Poisson equation is given by

$$\frac{\delta^2 \overline{p}}{\delta x_i^2} = -\frac{\delta \overline{u}_i}{\delta x_j} \frac{\delta \overline{u}_j}{\delta x_i} + \Lambda^{\Delta}. \tag{2.88}$$

[16] The truncation error of the Poisson equation is given by

$$\Lambda^{\Delta} = \left(\frac{\delta^2 \overline{p}}{\delta x_i^2} - \overline{\frac{\partial^2 p}{\partial x_i^2}} \right) + \left(\frac{\delta \overline{u}_i}{\delta x_j} \frac{\delta \overline{u}_j}{\delta x_i} - \overline{\frac{\partial u_i}{\partial x_j}} \, \overline{\frac{\partial u_j}{\partial x_i}} \right). \tag{2.89}$$

4). Due to these interpolations, the Fourier modes in the wavenumber range $\kappa_\eta \leq \kappa \leq 2\kappa_\eta$ are aliased to erroneous modes in the wavenumber range $0 \leq \kappa \leq \kappa_{max}$.[17] In principle, aliasing is avoided if $\kappa_\eta < \frac{1}{2}\kappa_{max}$. However, Orszag [67] showed, that if $\kappa_\eta < \frac{2}{3}\kappa_{max}$, all the aliases satisfy $\kappa_{alias} > \frac{2}{3}\kappa_{max}$. In other words, all aliasing errors appear in the region $\kappa_\eta < \frac{2}{3}\kappa_{max} < \kappa \leq \kappa_{max}$, where they are immediately dissipated by the viscous effects, whereas the range of interest $0 \leq \kappa \leq \kappa_\eta$ is not polluted by aliasing. Thus, in order to have a mathematical and physical consistent DNS simulation, the grid spacing must be chosen such that $\kappa_{max} > \frac{3}{2}\kappa_\eta$.

2.4.4 Computational requirements for DNS

With the conclusions of the previous sections, the relation between the number of nodes and the Reynolds number Re for homogeneous isotropic turbulence can be derived. Following Pope [70], the number of nodes in each direction of the computational grid is determined by the relation

$$N = 2\frac{\kappa_{max}}{\kappa_0} = 2\frac{\kappa_{max}\eta}{\kappa_0 L_{11}}\left(\frac{L_{11}}{L}\right)\left(\frac{L}{\eta}\right) \tag{2.92}$$

where $\kappa_0 = \frac{2\pi}{\mathscr{L}}$ denotes the largest energy containing scales, localized at the peak of the energy spectrum. The ratio L/η can immediately be expressed as function of the Taylor Reynolds number using relations (2.31) and (2.27) such that

$$\frac{L}{\eta} = \mathrm{Re}_L^{\frac{3}{4}} = \left(\frac{3}{20}\right)^{\frac{3}{4}} \mathrm{Re}_\lambda^{\frac{3}{2}}. \tag{2.93}$$

Further, the ratio L_{11}/L is determined by the length scale definitions (2.30) and (2.31). This ratio can be expressed as function of the Taylor Reynolds number Re_λ, by using the model spectrum (2.29). As mentioned before, L_{11}/L tends to the asymptotic value of 0.43 for large Reynolds numbers Re_λ, but this ratio increases significantly for decreasing Re_λ, as seen in Figure 2.4. Since it will turn out that Direct Numerical Simulation is only affordable at low Re_λ, this behaviour should be included for further application in this work. In order to obtain a simple relationship between L_{11}/L and Re_λ, a curve fitting of the exact profile in [70] is preferred. A curve fitting of the form

$$\frac{L_{11}}{L} \approx \frac{\alpha}{\mathrm{Re}_\lambda} + \beta, \tag{2.94}$$

in which $\alpha = 12$ and $\beta = 0.43$ was found to lead to a fairly good approximation as shown in Figure 2.4. Finally, for homogeneous isotropic turbulence, the lower limit

[17] More specific, two wavenumbers κ' and κ'' interact to give $\kappa = \kappa' + \kappa''$ and their aliases $\kappa_{alias} = \kappa' + \kappa'' \pm 2k\kappa_{max}, \forall k > 0$.

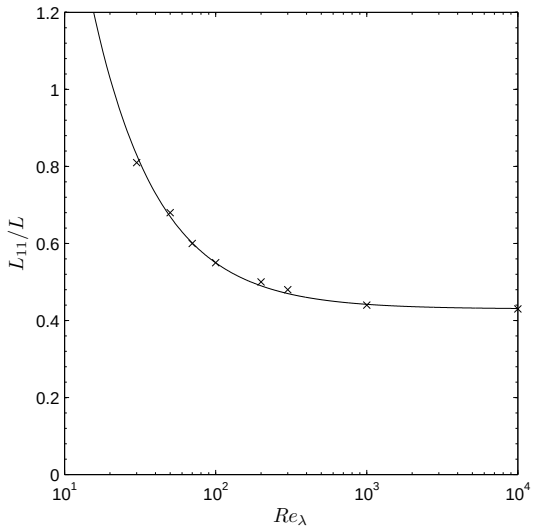

Figure 2.4: DNS grid requirements. The ratio of the longitudinal integral length scale to $L = k^{3/2}/\varepsilon$ as a function of the Taylor Reynolds number Re_λ. Curve fitting $(\cdots)$ of Pope's results obtained with the model spectrum $(\times)$ [70].

of the domain size $\mathscr{L}$ is constrained as eight times the longitudinal integral length scale or $\mathscr{L} = 8L_{11}$ [70], such that

$$\kappa_0 L_{11} = \frac{\pi}{4}. \tag{2.95}$$

Substitution of the length scale ratios (2.93), (2.94) and (2.95) into equation (2.92) results in

$$N \approx \frac{8}{\pi}\left(\frac{3}{20}\right)^{\frac{3}{4}}(\kappa_{max}\eta)\left(\frac{12}{\mathrm{Re}_\lambda} + 0.43\right)\mathrm{Re}_\lambda^{\frac{3}{2}}, \tag{2.96}$$

where the ratio $\kappa_{max}\eta$ remains the only degree of freedom left. Obviously, the choice of $\kappa_{max}\eta$ is related to the discussion concerning aliasing. Defining the ratio of the grid spacing to the Kolmogorov length as

$$\zeta = \frac{\Delta}{\eta} = \frac{\pi}{\kappa_{max}\eta} = \frac{1}{2}\frac{\kappa_\eta}{\kappa_{max}}, \tag{2.97}$$

then aliasing is prevented if $\zeta = \frac{1}{3}$, as discussed above [67]. However, Pope [70] suggests a value $\zeta = \frac{\pi}{1.5} \approx 2.1$, based on the observations that the dissipation spectrum is very small beyond $\kappa_{max}\eta = 1.5$ and that η underestimates the size of the dissipative motions. Hence, aliasing errors are assumed negligible. Relation (2.96) for the required number of nodes N in each direction and the total number

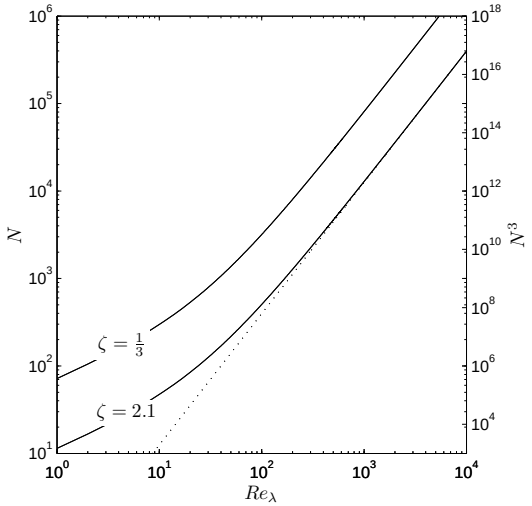

Figure 2.5: DNS grid requirements. The number of nodes N (and N^3) required for DNS of homogeneous isotropic turbulence for two choices of $\zeta = \frac{\kappa_\eta}{2\kappa_{max}}$, (—). High-Reynolds asymptote for $L_{11}/L = 0.43$ and $\zeta = 2.1$, $(\cdots)$.

of nodes N^3 as function of Re_λ is illustrated in Figure 2.5. Remark that a fully resolved DNS simulation ($\zeta = \frac{1}{3}$) requires approximately six times the number of nodes N of the marginally resolved DNS ($\zeta = 2.1$), such that the computational cost of the total simulation will increase with a factor 216, probably with only little gain in accuracy.

Similarly, in order to obtain an accurate time-advancement of the Navier-Stokes equations, the time increment Δt is necessarily smaller than the smallest time scale defined by $\tau_\eta = \sqrt{\nu/\varepsilon} = \eta^2/\nu$, which is related to the Kolmogorov length scales. Suppose a predefined time scale ratio θ

$$\frac{\Delta t}{\tau_\eta} = \theta, \tag{2.98}$$

Assume that the length and velocity scales of the initial flow are of order 1, such that the Reynolds number is written as $\mathrm{Re} \approx \frac{1}{\nu}$,[18] then the time step is obtained by

$$\Delta t = \theta\tau_\eta = \theta\frac{\eta^2}{\nu} \tag{2.99}$$

$$\approx \frac{\theta}{2}\eta^2\mathrm{Re} \approx \theta\eta^2\mathrm{Re}_\lambda^2, \tag{2.100}$$

[18] This assumption is based on the definition of the Taylor-Green vortex flow by *Brachet et al.* [8] which is considered for DNS further in this dissertation.

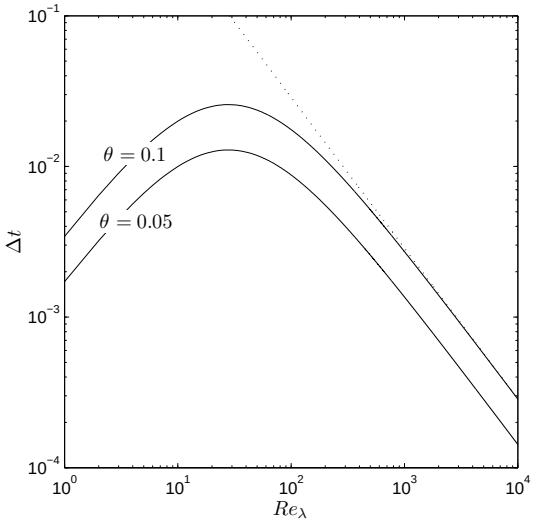

Figure 2.6: DNS time step requirements. The increment of the time required for accurate time advancement in DNS of homogeneous isotropic turbulence as function of $\theta = \frac{\Delta t}{\tau_\eta}$, (—). High-Reynolds asymptote for $L_{11}/L = 0.43$ and $\theta = 0.1$, $(\cdots)$.

and further developed as

$$\Delta t \approx \frac{\theta}{2}\left(\frac{\eta}{L}\right)^2\left(\frac{L}{L_{11}}\right)^2\left(\frac{L_{11}\kappa_0}{\kappa_0}\right)^2 \mathrm{Re}_\lambda^2 \tag{2.101}$$

$$\approx \frac{\theta}{2}\frac{\pi^2}{16}\left(\frac{\eta}{L}\right)^2\left(\frac{L}{L_{11}}\right)^2 \mathrm{Re}_\lambda^2 \tag{2.102}$$

$$\approx \frac{\theta}{2}\frac{\pi^2}{16}\left(\frac{20}{3}\right)^{\frac{3}{2}}\left\{\frac{\mathrm{Re}_\lambda}{(12+0.43\mathrm{Re}_\lambda)^2}\right\}. \tag{2.103}$$

The Nyquist criterion for the temporal discretization imposes that the frequency of the Kolmogorov scales $\omega_\eta = \frac{2\pi}{\tau_\eta}$ should be smaller than the Nyquist frequency $\omega_{max} = \frac{\pi}{\Delta t}$, such that $\omega_\eta < \omega_{max}$ and $\theta < \frac{1}{2}$. Moreover, the exact value of θ depends on the accuracy of the adopted numerical method for discrete time advancement of the solution. Typically 2^{nd} - up to 4^{th} -order accurate low-storage *Runge-Kutta* methods are used. In general, these methods guarantee accurate time stepping if the temporal variation of the physical phenomena is sufficiently small in comparison with the time step e.g. $\omega_\eta \leq \frac{1}{5}\omega_{max}$, such that $\theta \leq 0.1$ as suggested by Pope [70]. Expression (2.103) for the time increment Δt as function of Re_λ is illustrated in Figure 2.6.

Although Figures 2.5 and 2.6 indicate that the computational requirements increase rapidly with the Reynolds number, no direct information is provided about the corresponding computational costs. Therefore, a fair quantitative estimation of

Re_λ	Re_L	Re	N	N^3	N_t	Memory	CPU_1	CPU_2	CPU_3
25	94	313	105	1.1×10^6	156	64 Mb	25.4 s	4.20 s	0.20 ms
50	375	1250	218	1.0×10^7	169	576 Mb	4.14 min	40.9 s	1.70 ms
100	1500	5000	505	1.3×10^8	228	7 Gb	1.16 h	11.5 min	28.6 ms
250	9375	31250	1735	5.2×10^9	430	292 Gb	3.70 d	14.7 h	2.20 s
500	37500	125000	4661	1.0×10^{11}	776	6 Tb	4.30 m	21.4 d	1.30 min
1000	150000	500000	12834	2.1×10^{12}	1472	118 Tb	14.1 y	2.30 y	50.5 min

Table 2.1: Hypothetical Estimation of computational effort for DNS of isotropic turbulence at various Reynolds numbers. The number of nodes N and N^3 ($\zeta = 2.1$); the number of time steps N_t to calculate 1s of the flow ($\theta = 0.025$); The lower bound of the memory; the CPU-time for three contemporary computing systems: *Single core Intel Pentium 4 Prescott* 3.6*GHz at* 7 *GigaFLOPS* (CPU_1)*; 2× Quad-core Intel Xeon X5355* 2.66*GHz at* 42.56 *GigaFLOPS (Ghent University)* (CPU_2)*; IBM* Roadrunner*(USA) with 6912 dual-core AMD Opteron processors at* 1.026 *PetaFLOPS* (CPU_3).

the computational effort, required to perform a Direct Numerical Simulation of e.g. 1 second of a homogeneous isotropic turbulent flow, seems useful. Following [70], the necessary time to compute 1 second of the flow, is mainly determined by the number of floating-point operations and thus proportional to product of the number of nodes N^3 and the number of time steps $N_t = \frac{1}{\Delta t}$.[19] Using equations (2.96) and (2.103) this yields

$$N^3 N_t = \frac{N^3}{\Delta t} = \frac{\left(\frac{8}{\pi}\left(\frac{3}{20}\right)^{\frac{3}{4}} \frac{\pi}{\zeta}\left(\frac{12}{\mathrm{Re}_\lambda} + 0.43\right)\mathrm{Re}_\lambda^{\frac{3}{2}}\right)^3}{\frac{\theta}{2}\frac{\pi^2}{16}\left(\frac{20}{3}\right)^{\frac{3}{2}}\left\{\frac{\mathrm{Re}_\lambda}{(12+0.43\mathrm{Re}_\lambda)^2}\right\}} \tag{2.104}$$

$$= \frac{16384}{\pi^2}\left(\frac{3}{20}\right)^{\frac{15}{4}} \frac{1}{\zeta^3\theta}\left(12\mathrm{Re}_\lambda^{\frac{1}{2}} + 0.43\mathrm{Re}_\lambda^{\frac{11}{2}}\right) \tag{2.105}$$

Suppose that 10^3 floating point operations (FLOPS) per mode per time step are needed. Further, the storage of a double precision value requires 8 bytes, such that the memory requirements per scalar variable are given by $8N^3$ bytes.[20] Table 2.1 gives an overview of the CPU-time and memory requirements, obtained by relation (2.105), for three contemporary computer systems: a classic personal computer with single core Intel Pentium 4, a Quad-core Intel Xeon server and finally the world's fastest supercomputer *Roadrunner*.[21] Since the overall computational time increases as $\mathrm{Re}_\lambda^{11/2}$ and the memory storage increase with $\mathrm{Re}_\lambda^{9/2}$, the results obviously indicate that a sufficiently resolved DNS ($\zeta = 2.1$) becomes prohibitively expensive for fully

[19] Here, Euler time stepping is assumed involving one iteration per time increment. In case of multi-stage Runge-Kutta methods, several iterations are involved per time increment such that N_t should be multiplied with the number of stages.

[20] Remark that for incompressible flows, at least 7 variables ($\mathbf{u}$, $\mathbf{x}$ and p) are stored in the random access memory (RAM), neglecting intermediate calculation variables.

[21] It is assumed that all processors are used in the computation.

developed turbulent flows with a clear inertial range, at Reynolds numbers $\mathrm{Re}_\lambda > 100$.

2.4.5 Motivation for Large-Eddy Simulation

It is useful to retrieve a distribution of the computational effort over the different scales in a Direct numerical simulation of isotropic turbulence. An estimation of the involved costs for resolving the scales in the dissipation range, i.e. $\kappa_d\eta \approx 0.1 \leq \kappa\eta$ [70], is determined by the ratio of the nodes required to resolve scales outside the dissipation range N_{out}, over the total number of nodes N. With equation (2.96) the percentage of computational nodes required to resolve the dissipation range is obtained by

$$1 - \frac{N_{out}^3}{N^3} = 1 - \left(\frac{\kappa_d\eta}{\kappa_{max}\eta}\right)^3 = \frac{10^3\pi^3 - \zeta^3}{10^3\pi^3} \tag{2.106}$$

such that for $\zeta = 2.1$, 99.97% of the wavenumber modes are in the dissipation range (99.99% if $\zeta = 1/3$). In other words, only 0.03% (0.01%) of the wavenumbers are used for resolving the scales in the inertial subrange and the energy containing range, whereas these scales contain more then 80% of the kinetic energy and are thus considered most important. The enormous computational efforts to resolve mainly the insignificant dissipative scales motivate the use of more affordable approaches. A viable alternative is Large-Eddy simulation (LES), where only the largest scales are resolved, neglecting the smallest dissipative scales which are part of the dissipation range. Although the latter technique is the subject of the next chapter, a rough estimation is given for the computational costs involved. Assume that only the largest scales in the energy containing range and the inertial range are resolved on the computational grid such that $\kappa_{max}\eta \leq \kappa_d\eta \approx 0.1$ [70]. The required number of nodes N^3 for LES is then reduced with a factor $1/3.10^{-4} \approx 3.10^3$ in comparison with DNS. At very high Reynolds numbers, the number of gridnodes in a Direct Numerical Simulation of homogeneous isotropic turbulence scales as $N \propto \mathrm{Re}_\lambda^{3/2}$ whereas the number of time steps scales as $N_t \propto \mathrm{Re}_\lambda \propto N^{2/3}$. Hence, the number of time steps required in LES is reduced with a factor $\left(1/3.10^{-4}\right)^{2/9} \approx 6$ in comparison with DNS. In conlusion, the computational time for LES, which is proportional to the total number of floating point operations N^3N_t, is roughly 20000 times less than in case of DNS. Moreover the memory requirements reduce with a factor 3.10^3 since they are proportional to N^3.

By a model is meant a mathematical construct which, with the addition of certain verbal interpretations, describes observed phenomena. The justification of such a mathematical construct is solely and precisely that it is expected to work.

Von Neumann, John

3

Large-Eddy Simulation

The philosophy of Large-Eddy simulation (LES) is to resolve only the largest unsteady and flow specific turbulent motions, which are part of the energy containing range or the inertial subrange and represent approximately 80% of the kinetic energy. Since the important main features of the flow are resolved, the LES solution is believed to provide a statistically accurate prediction of the mean flow. As discussed in Chapter 2, the gain in computational effort for LES is substantial in comparison with Direct Numerical Simulation, since the smallest dissipative eddies, responsible for approximately 99% of the grid requirements in DNS, are not resolved.

Since the smallest dissipative motions remain unresolved in LES, their effect on the resolved scales requires proper modeling. According to the Kolmogorov hypotheses, these scales are considered to be locally isotropic, universal and in quasi equilibrium, since the directional information of the large scales gets lost in the cascade. Hence, models that account for these scales are based on universal scaling behaviour and are therefore supposed to be flow independent.

The present chapter introduces the mathematical framework for Large-Eddy Simulation that is maintained in this dissertation and describes the standard, and most popular subgrid model that accounts for the unresolved scales. Moreover, two more advanced modeling techniques are discussed, which tend to improve the performance of the standard subgrid model. Finally, the sensitivity of both techniques to the numerics is explained, introducing at the same time the basic problem description of this dissertation.

3.1 PHILOSOPHY OF LARGE-EDDY SIMULATION

According to the Nyquist-Shannon theorem (Sections 2.4.2 and 2.4.3), the discretization of the turbulent velocity field $\mathbf{u}(\mathbf{x},t)$ and the governing Navier-Stokes equations requires a extremely fine computational grid with $\kappa_\eta \leq \frac{2}{3}\kappa_{max} = \frac{2\pi}{3\Delta}$ in order to avoid aliasing. Since the purpose of LES is to resolve only the largest and most important motions of turbulence on an affordable computational grid $\kappa_{max} \ll \kappa_\eta$, discretization of the velocity field $\mathbf{u}(\mathbf{x},t)$ and the governing equations demands an appropriate *filtering operation* that reduces the number of scales (wavenumbers) in the velocity field $\mathbf{u}(\mathbf{x},t)$, satisfying the Nyquist criterion. However, filtering the Navier-Stokes equations induces a *residual-stress tensor* that expresses the effects of the small unresolved scales on the large resolved scales and which requires modeling.

3.1.1 FILTER DEFINITION

Filtering of the velocity field $\mathbf{u}(\mathbf{x},t)$, $\mathbf{x} \in \mathbb{R}^3$ and the governing Navier-Stokes equations involves a restriction of the flow's spectral content in continuum space $\mathbb{R}^3$.[1] Although this restriction requires the definition of a mathematical *filtering operation* in $\mathbb{R}^3$, this operator is first examined in one-dimensional space $\mathbb{R}$.

Definition 3.1.1 (***Filtering operation in*** $\mathbb{R}$ **).** The filtering operation is defined as the convolution of the velocity field $u(x,t)$, $x \in \mathbb{R}$ with a *filter function* $\mathscr{G}(x)$, $x \in \mathbb{R}$. Following Pope's notation [70], the convolution is expressed by

$$\overline{u}(x,t) = \mathscr{G}(x) * u(x,t) = \int \mathscr{G}(x,\xi)\, u(x-\xi,t)\, d\xi, \tag{3.1}$$

where $\mathscr{G}(x,\xi)$ is called the *filter kernel*, and $\overline{u}(x,t)$ denotes the filtered velocity field.[2] Further, $\mathscr{G}(x,\xi)$ is normalized as

$$\int \mathscr{G}(x,\xi)\, d\xi = 1, \quad \forall x \in \mathbb{R}. \tag{3.2}$$

The filter kernel $\mathscr{G}(x,\xi)$ is called homogeneous if $\mathscr{G}(x,\xi) = \mathscr{G}(\xi)$ is independent of the spatial position x in the unbounded domain $x \in [-\infty,\infty]$.

In the following only homogeneous filter kernels are considered. The dual definition in Fourier space is now obtained by taking the Fourier transform of equation (3.1) and applying the convolution theorem such that

$$\widehat{\overline{u}}(\kappa,t) = \widehat{\mathscr{G}}(\kappa)\, \widehat{u}(\kappa,t), \quad \widehat{\mathscr{G}}(\kappa) = 2\pi \mathscr{F}\{\mathscr{G}(x)\}. \tag{3.3}$$

[1] Note that spatial filtering, automatically induces an implicit temporal filtering, since it is possible to associate a characteristic time scale with each characteristic length scale [74]. As a consequence, the required time step Δt, determined by the time scale of the smallest resolved eddies, is significantly larger for LES than for DNS. Nevertheless, since time filtering is merely a consequence of spatial filtering, it is not treated explicitly in the further discussion.

[2] Remark that in this chapter, $\overline{u}$ denotes the filtered velocity field instead of the sampled velocity field.

Obviously, the filtering operation results into a modification of the magnitude of each individual Fourier mode $\widehat{u}(\kappa, t)$. In order to ensure the appropriate behaviour of the filter, three important constraints are imposed [74].

i. *Conservation of constants.* Assume $u(x,t) = u(t)$, then

$$\overline{u}(t) = u(t). \tag{3.4}$$

This constraint is guaranteed by the normalization condition (3.2), which reads $\widehat{\mathscr{G}}(0) = 1$ in Fourier space.

ii. *Linearity.* Assume $u(x,t)$ and $v(x,t)$, then

$$\overline{u(x,t) + v(x,t)} = \overline{u}(x,t) + \overline{v}(x,t), \tag{3.5}$$

which follows automatically from definition (3.1).

iii. *Commutation with partial derivation.* Assume the partial derivative $\frac{\partial u(x,t)}{\partial x}$, then

$$\overline{\frac{\partial u(x,t)}{\partial x}} = \frac{\partial \overline{u}(x,t)}{\partial x}. \tag{3.6}$$

This commutation constraint is guaranteed for homogeneous convolution filters defined in an unbounded domain $x \in [-\infty, \infty]$. However, in case of non-homogeneous filters $\mathscr{G}(x,\xi)$, e.g. with variable filter width in bounded domains, (3.6) is not satisfied. Hence, commutation errors arise which are formally expressed as

$$\frac{\partial \overline{u}(x,t)}{\partial x} - \overline{\frac{\partial u(x,t)}{\partial x}} = \int \frac{\partial \mathscr{G}(x,\xi)}{\partial x} u(x-\xi,t)\, d\xi. \tag{3.7}$$

Nevertheless, since these commutation errors are beyond the scope of this dissertation, the reader is referred to e.g. Ghosal *et al.* [33], van der Bos *et al.* [81] and Geurts *et al.* [31] for further information thereon.

Aside from these imposed constraints, general convolution filters are characterized by three additional properties:

iv. Convolution filters are generally not idempotent, i.e. they do not satisfy

$$\overline{\overline{u}}(x,t) \neq \overline{u}(x,t). \tag{3.8}$$

Only filter kernels $\widehat{\mathscr{G}}(\kappa)$ that consists of a Heaviside function such that $\left[\widehat{\mathscr{G}}(\kappa)\right]^2 = \widehat{\mathscr{G}}(\kappa)$, satisfy (3.8) and are thus idempotent. A homogeneous filter which consists of a Heaviside function is called an orthogonal operator.

	$\mathscr{G}(\xi)$	$\widehat{\mathscr{G}}(\kappa)$
Box	$\frac{1}{\Delta_c}\mathrm{H}\left(\frac{\Delta_c}{2}-\lvert\xi\rvert\right)$	$\frac{\sin\left(\frac{\pi\kappa}{2\kappa_c}\right)}{\frac{\pi\kappa}{2\kappa_c}}$
Gaussian	$\sqrt{\frac{6}{\pi\Delta_c^2}}\,e^{-\left(\frac{6\xi^2}{\Delta_c^2}\right)}$	$e^{-\left(\frac{\pi^2\kappa^2}{24\kappa_c^2}\right)}$
Sharp cutoff	$\frac{\sin\left(\frac{\pi\xi}{\Delta_c}\right)}{\frac{\pi\xi}{\Delta_c}}$	$\mathrm{H}\left(\kappa_c-\lvert\kappa\rvert\right)$

Table 3.1: Three classical homogeneous filter functions $\mathscr{G}(x)$. The non-projective Box filter kernel $\mathscr{G}(\xi)$ is local in physical space, but has a non-local transfer function $\widehat{\mathscr{G}}(\kappa)$. Instead, the non-projective Gaussian filter kernel has both non-local kernel $\mathscr{G}(\xi)$ and a non-local transfer function $\widehat{\mathscr{G}}(\kappa)$. Finally, the sharp cutoff filter is a projective filter, which has a non-local kernel $\mathscr{G}(\xi)$ but a local transfer function $\widehat{\mathscr{G}}(\kappa)$.

v. Convolution filters are not necessarily projective. A filter is called projective if no inverse filtering operation can be defined. Hence, projective filtering induces an irremediable loss of information, whereas non-projective filtering implies that the filtering can be interpreted as a change of variable with no loss of information [74]. This property is utterly important in the context of aliasing, since in order to rigorously avoid aliasing, the Fourier modes at $\kappa \geq \kappa_{max}$ must be annihilated. Obviously, only projective filters satisfy this requirement exactly, whereas non-projective filters only reduce the magnitude of these modes without forcing them exactly to zero. Moreover, if the projective filter is idempotent, then the magnitude of modes $\kappa \leq \kappa_{max}$ remains unaltered.

vi. Finally, general convolution filters do not commute with the product operator. Consider e.g. $u(x,t)$ and $v(x,t)$, then

$$\overline{u(x,t)\,v(x,t)} \neq \overline{u}(x,t)\,\overline{v}(x,t)\,. \tag{3.9}$$

Obviously, property (3.9) will be responsible for the appearance of a commutation error on the nonlinear term in the filtered Navier-Stokes equations. The commutation error takes the form of a *residual-stress* tensor which represents the effect of the smallest unresolved scales on the large resolved scales. This is subject of the discussion in Section 3.2.

Consider the filter width Δ_c corresponding with the cutoff wavenumber $\kappa_c = \frac{\pi}{\Delta_c}$. The three classical and most commonly used filters types are defined in Table 3.1, and their characteristics are illustrated in Figure 3.1. Although the box filter is local in physical space, i.e. the kernel $\mathscr{G}(\xi) = 0$, $\forall\,\lvert\xi\rvert > \frac{\Delta_c}{2}$, its transfer function $\widehat{\mathscr{G}}(\kappa)$ is non-local because the sine cardinal function only converges to zero at $\kappa \to \infty$.

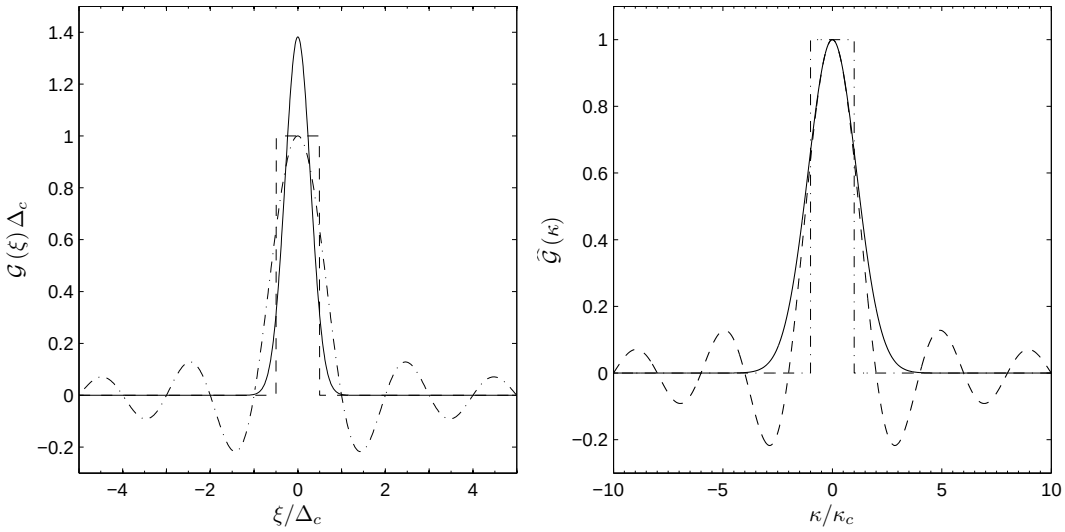

Figure 3.1: Three classical filter functions. Left: convolution kernel $\mathscr{G}(\xi)$. **Right:** transfer function $\widehat{\mathscr{G}}(\kappa)$. Box filter $(---)$; Gaussian filter $(—)$; Sharp cutoff filter $(-\cdot-\cdot)$.

Moreover, it does not satisfy property (3.8) and is thus not a projecting filter. On the other hand, the sharp cutoff filter displays exactly the opposite behaviour. $\mathscr{G}(\xi)$ is non-local in physical space whereas its transfer function $\widehat{\mathscr{G}}(\kappa)$ remains localized. This filter satisfies property (3.8) such that it is a projective filter. Finally, the Gaussian filter is non-local, both in spectral and physical space and does not satisfy the idempotency property (3.8). Since both the box and Gaussian filters have a non-local transfer function $\widehat{\mathscr{G}}(\kappa)$ and are not projective, the filtered velocity field $\overline{u}(x,t)$ still contains the original number of Fourier modes, although with altered magnitude. Therefore, the filter operation can be inverted to obtain $u(x,t)$ from $\overline{u}(x,t)$. In contrast, the sharp cutoff filter forces the Fourier modes above the cutoff wavenumber κ_c to zero, which is an irreversible operation. Moreover, the sharp cutoff filter precludes aliasing whereas the Gaussian and the box filter do not.
In order to filter the continuous velocity field $\mathbf{u}(\mathbf{x},t)$, $\mathbf{x} \in \mathbb{R}^3$, it is necessary to extend the filter definition (3.1.1) to $\mathbb{R}^3$. However, this definition is not unique and one can define an *anisotropic filter*, whose properties may differ in each spatial direction, as well as an *isotropic filter* whose properties are independent of any spatial direction [70].

Definition 3.1.2 (***Filtering operation in*** $\mathbb{R}^3$ **).** The *anisotropic* homogeneous filter definition in $\mathbb{R}^3$ is obtained by tensorizing the mono-dimensional filter kernels through multiplication such that

$$\overline{\mathbf{u}}(\mathbf{x},t) = \mathscr{G}(\mathbf{x}) * \mathbf{u}(\mathbf{x},t) = \prod_{j=1}^{3} \mathscr{G}(x_j) * \mathbf{u}(\mathbf{x},t), \tag{3.10}$$

whereas the *isotropic* homogeneous filter definition in $\mathbb{R}^3$ is obtained by symmetrizing the mono-dimensional filter kernels such that

$$\overline{\mathbf{u}}(\mathbf{x},t) = \mathscr{G}(|\mathbf{x}|) * \mathbf{u}(\mathbf{x},t), \quad |\mathbf{x}| = \sqrt{x_1^2 + x_2^2 + x_3^2}. \tag{3.11}$$

For instance, in case of the sharp-cutoff filter, the anisotropic filter definition results in a cuboidal transfer function, whereas the isotropic definition leads to a spherical transfer function.[3,4]
Although in the literature the adopted definition is rarely clarified, it appears that the anisotropic definition is widely used in combination with finite difference methods whereas the isotropic definition is commonly used for (pseudo-)spectral methods. Moreover, the isotropic filter definition seems more physical when considering homogeneous isotropic turbulence, whereas from a mathematical point of view the anisotropic filter definition is favoured. Since the three-dimensional Dirac comb (definition 2.4.2) is constructed as the product of three independent one-dimensional Dirac functions, each Cartesian direction may be discretized differently, as long as the Nyquist criterion corresponding to that direction is satisfied. Hence, this suggests independent filtering in each Cartesian direction which is equivalent to anisotropic filtering. In this work, anisotropic filtering is used for solving the Navier-Stokes equations whereas isotropic filtering is adopted for post-processing the solution and the related energy spectra.

3.1.2 The filtered energy spectrum

The effects of the filtering operation on the velocity field $\mathbf{u}(\mathbf{x},t)$ are most clearly demonstrated by examining the filtered energy spectrum. This allows to distinguish the most appropriate *theoretical* filter to deduce the LES-equations with. Consider the homogeneous isotropic turbulent velocity field $\mathbf{u}(\mathbf{x},t)$ and its energy spectrum defined as

$$E(\boldsymbol{\kappa},t) = \frac{1}{2}\left\langle \widehat{u}_j(\boldsymbol{\kappa},t)\,\widehat{u}_j^*(\boldsymbol{\kappa},t)\right\rangle. \tag{3.12}$$

The energy spectrum of the filtered velocity field $\overline{\mathbf{u}}(\mathbf{x},t)$ is then calculated using relation (3.3) as

$$\begin{aligned}
\overline{E}(\boldsymbol{\kappa},t) &= \frac{1}{2}\left\langle \widehat{\overline{u}}_j(\boldsymbol{\kappa},t)\,\widehat{\overline{u}}_j^*(\boldsymbol{\kappa},t)\right\rangle && (3.13)\\
&= \widehat{\mathscr{G}}(\boldsymbol{\kappa})\,\widehat{\mathscr{G}}^*(\boldsymbol{\kappa})\,\frac{1}{2}\left\langle \widehat{u}_j(\boldsymbol{\kappa},t)\,\widehat{u}_j^*(\boldsymbol{\kappa},t)\right\rangle && (3.14)\\
&= \widehat{\mathscr{G}}(\boldsymbol{\kappa})\,\widehat{\mathscr{G}}^*(\boldsymbol{\kappa})\,E(\boldsymbol{\kappa},t). && (3.15)
\end{aligned}$$

[3] Note that for the box filter, the anisotropic definition results in a cuboidal averaging volume is whereas the isotropic definition gives a spherical averaging volume.

[4] In principle, it is possible to imagine yet another filter definition intermediate to the anisotropic and isotropic one, such that an ellipsoid transfer function (sharp cutoff filter) or an ellipsoid averaging volume (box filter) is obtained.

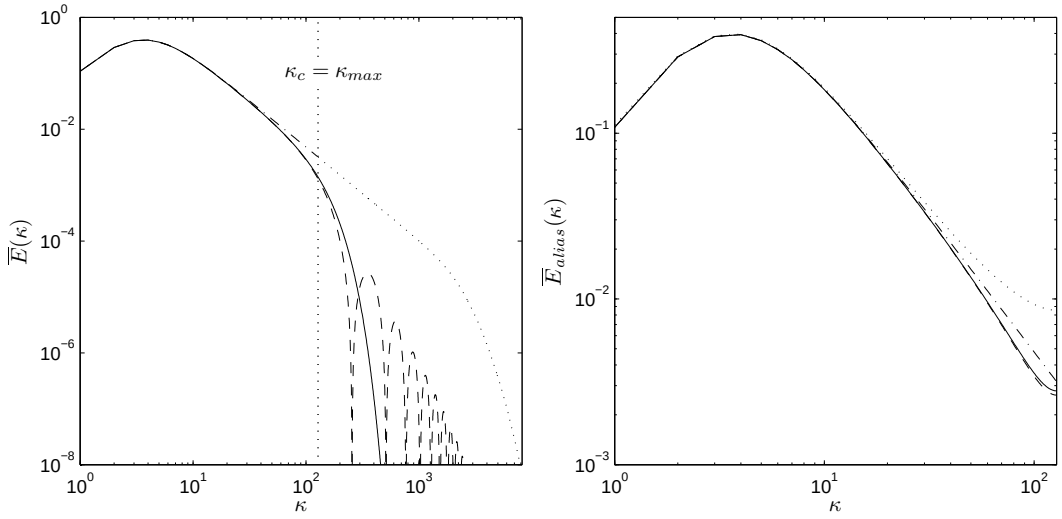

Figure 3.2: The filtered energy spectrum. Left: filtered spectrum $\overline{E}(\kappa, t)$. **Right:** the aliased spectrum $\overline{E}_{alias}(\kappa, t)$. Box filter (– – –); Gaussian filter (—); Sharp cutoff filter (– · –); Unfiltered spectrum (· · ·).

Integration over spherical shells results then into the filtered energy spectrum function

$$\overline{E}(\kappa, t) = \iiint_{\boldsymbol{\kappa}} \widehat{\mathscr{G}}(\boldsymbol{\kappa}) \widehat{\mathscr{G}}^*(\boldsymbol{\kappa}) E(\boldsymbol{\kappa}, t) \delta(|\boldsymbol{\kappa}| - \kappa) d\boldsymbol{\kappa} \tag{3.16}$$

$$= \left|\widehat{\mathscr{G}}(\kappa)\right|^2 E(\kappa, t). \tag{3.17}$$

The filtered energy spectrum function is shown in Figure 3.2 for the box filter, the Gaussian filter and the sharp cutoff filter. First, it is noticed that only the sharp cutoff filter annihilates the wavenumber modes beyond the cutoff wavenumber κ_c whereas the box filter and the Gaussian filter merely damp these wavenumber modes. As a consequence, aliasing appears as soon as the box-filtered or Gaussian-filtered velocity field is discretized, since the Nyquist criterion is not rigorously satisfied. These aliasing errors result in the energy pile-up demonstrated in Figure 3.2, at the tail of the energy spectrum. Moreover, unlike the sharp cutoff filter which leaves the wavenumber modes $\kappa < \kappa_c$ unharmed, the box filter and the Gaussian filter tend to attenuate the energy of the Fourier modes near the cutoff. Based on these observations, one defines the *subfilter scales* and the *subgrid scales* [16]. The term *subfilter scales* indicates the turbulent motions at $\kappa < \kappa_c$, that are removed or damped due to imperfect smooth filtering.[5] In principle these scales can be recovered by inverting the filter operation, or they may be approximated by modeling. Remark that these subfilter scales do not exist in case of the sharp Fourier filter. The term

[5]Note that the aliased scales are not covered by this terminology.

subgrid scales indicates all scales $\kappa > \kappa_c$ that cannot be seen on the computational grid and thus cannot be recovered, even if the adopted filter operation is smooth. This emphasizes that the DNS solution can never be reconstructed from the LES solution.

3.1.3 FILTER SELECTION

At this point, the selection of a theoretical filter is required in order to derive the LES-equations. The goal of LES is to reproduce the dynamics and statistics of the filtered DNS solution as accurately as possible, by resolving only the high energetic large scale features (corresponding to ideally 80% of the total kinetic energy) in the flow on a relatively coarse grid, while neglecting the low-energy small scales. Although there are ongoing discussions favoring smooth reconstructable filters over the projective unreconstructable filters and vice versa [21, 23, 24, 25, 26], the rigorous mathematical constraint imposed by the Nyquist criterion impels a projective filter since it precludes aliasing. Therefore, the sharp cutoff filter is favoured in this dissertation in order to derive the LES-equations. Below, the most important properties of the sharp cutoff filter are summarized [21, 70].

i. Since the sharp cutoff filter is a projector, the filtered velocity field $\widehat{\overline{\mathbf{u}}}(\boldsymbol{\kappa}, t)$ is represented with complete accuracy by a finite set of wavenumber modes $\kappa < \kappa_c$.

ii. As a consequence, the filtered velocity field $\widehat{\overline{\mathbf{u}}}(\boldsymbol{\kappa}, t)$ provides no direct information about the residual motions. Moreover, the velocity fluctuations $\left(1 - \widehat{\mathscr{G}}(\boldsymbol{\kappa})\right) \widehat{\mathbf{u}}(\boldsymbol{\kappa}, t)$ do not contain resolved wave number modes [21]. Hence, no subfilter scales arise and no additional defiltering or modeling is needed to reconstruct these scales.

iii. In contrast to smooth filters, the issues related to modeling and resolution are separate for the cutoff filter. This feature will prove very important in this dissertation where the numerical errors and modeling errors are separated.

iv. Inevitably, when using sharp cutoff filters, the *Gibbs-phenomenon* can arise due to the truncation of an infinite Fourier series. This phenomenon causes wiggles in the filtered velocity field (also called ringing) and is closely related to the smoothness of the original velocity field. Smooth velocity fields described by rapidly converging Fourier series with rapidly decaying Fourier coefficients $\widehat{\mathbf{u}}(\boldsymbol{\kappa}, t)$, are less liable to the Gibbs-phenomenon when filtered, whereas irregular velocity fields, described by very slowly converging Fourier series with slowly decaying Fourier coefficients $\widehat{\mathbf{u}}(\boldsymbol{\kappa}, t)$, display significant ringing. This means that sharp cutoff filtering of a turbulent velocity field possibly induces the Gibbs-phenomenon if the cutoff wavenumber κ_c lies in the inertial subrange

where the Fourier coefficients only decay with $\kappa^{-5/3}$.[6,7]

v. Finally, it is possible to interpret the box filter and the Gaussian filter as certain approximations to the sharp cutoff filter. Indeed, the box filter does have a local support in physical space in contrast to the sharp cutoff filter. Although the Gaussian filter is non-local in physical space, it can be considered quasi-local since the magnitude decays exponentially in space.

3.2 The filtered Navier-Stokes equations

The governing equations for the Large-Eddy Simulation are obtained by applying the convolution filter $\mathscr{G}(\mathbf{x})$ to the Navier-Stokes equations. In the previous section, the sharp cutoff filter was favoured, since it rigorously precludes aliasing as imposed by the Nyquist criterion.
Consider the homogeneous sharp cutoff filter denoted by $\mathscr{G}(\mathbf{x}, \Delta_c)$ in physical space or $\widehat{\mathscr{G}}(\boldsymbol{\kappa}, \kappa_c)$ in spectral space. The cutoff wavenumber $\kappa_c = \frac{\pi}{\Delta_c}$ is assumed constant and remains unspecified *pro tempore*. The velocity field is then decomposed as

$$\mathbf{u}(\mathbf{x}, t) = \overline{\mathbf{u}}(\mathbf{x}, t) + \mathbf{u}'(\mathbf{x}, t) \tag{3.18}$$

where $\overline{\mathbf{u}}(\mathbf{x}, t)$ denotes the *low-pass* filtered velocity field (large scales) and $\mathbf{u}'(\mathbf{x}, t)$ denotes the *high-pass* filtered velocity field (small scales) such that

$$\widehat{\overline{\mathbf{u}}}(\boldsymbol{\kappa}, t) = \widehat{\mathscr{G}}(\boldsymbol{\kappa}, \kappa_c)\, \widehat{\mathbf{u}}(\boldsymbol{\kappa}, t), \quad 0 \leq \kappa \leq \kappa_c \tag{3.19}$$

$$\widehat{\mathbf{u}}'(\boldsymbol{\kappa}, t) = \left[1 - \widehat{\mathscr{G}}(\boldsymbol{\kappa}, \kappa_c)\right] \widehat{\mathbf{u}}(\boldsymbol{\kappa}, t), \quad \kappa_c \leq \kappa \leq \kappa_\eta \tag{3.20}$$

3.2.1 The filtered equations in physical space

Since the sharp cutoff filter is assumed homogeneous, i.e. with uniform filter width, the filter operation commutes with the partial derivatives according to equation 3.6. The filtered continuous Navier-Stokes equations (2.1) and (2.2) are then obtained as

$$\frac{\partial \overline{u}_i}{\partial x_i} = 0 \tag{3.21}$$

$$\frac{\partial \overline{u}_i}{\partial t} + \frac{\partial \overline{u_i u_j}}{\partial x_j} = -\frac{\partial \overline{p}}{\partial x_i} + \nu \frac{\partial^2 \overline{u}_i}{\partial x_j^2}, \tag{3.22}$$

[6] If the cutoff lies in the dissipation range the ringing would be less severe since the Fourier coefficients $\widehat{\mathbf{u}}(\boldsymbol{\kappa}, t)$ decay exponentially.

[7] Due to the non-positiveness of the sharp cutoff filter function, i.e. $\mathscr{G}(x) \geq 0$ is not strictly satisfied, the residual stress tensor and the related subgrid kinetic energy, which is often used for subgrid modeling, are not guaranteed to be positive definite [86]. Therefore, it might be necessary to ensure the realizability of the solution by using and additional smoothing filter in order to control or eliminate these oscillations. Nevertheless, this regularization action may be considered as a part of the physical modeling.

Type	Contribution	Wavenumber range
Resolved	$\overline{\overline{u}_i\overline{u}_j}$	$\lvert\boldsymbol{\kappa}\rvert < \kappa_c$
Cross	$\overline{u_i'\overline{u}_j} + \overline{\overline{u}_i u_j'}$	$\lvert\boldsymbol{\kappa}'\rvert \geq \kappa_c$ and $\lvert\boldsymbol{\kappa}\rvert < \kappa_c$
Reynolds	$\overline{u_i'u_j'}$	$\lvert\boldsymbol{\kappa}'\rvert \geq \kappa_c$

Table 3.2: Various stress contributions. One can distinguish the resolved stress contributions due to resolved scale-interactions, the Cross stress contributions due to interactions between resolved scales κ and unresolved scales κ' and the Reynolds stress contributions due to unresolved scale-interactions. Note that every type contributes in $0 \leq \lvert\boldsymbol{\kappa}\rvert < \kappa_c$.

where $\overline{p}\,(\mathbf{x}, t)$ denotes the filtered pressure field. Although the filter operation does not commute with the product operator, as shown in equation (3.9), the nonlinear term must be expressed as function of the filtered velocity field $\overline{\mathbf{u}}\,(\mathbf{x}, t)$ in order to solve equation (3.22). However, substitution of the decomposed velocity field (3.18) into the nonlinear term results in

$$\frac{\partial \overline{u}_i}{\partial t} + \frac{\partial \overline{\overline{u}_i\overline{u}_j}}{\partial x_j} + \frac{\partial \overline{\tau}_{ij}}{\partial x_j} \quad = \quad -\frac{\partial \overline{p}}{\partial x_i} + \nu \frac{\partial^2 \overline{u}_i}{\partial x_j^2}, \tag{3.23}$$

where the commutation error or the *residual-stress* tensor is formally expressed as $\overline{\tau}_{ij} = \overline{u_i u_j} - \overline{\overline{u}_i\overline{u}_j}$. Formulation (3.23) is typically known as the *doube decomposition*. Using definition (3.18) the residual-stress tensor is further developed as

$$\overline{\tau_{ij}} = \overline{u_i u_j} - \overline{\overline{u}_i\overline{u}_j} = \overline{u_i'\overline{u}_j} + \overline{\overline{u}_i u_j'} + \overline{u_i'u_j'}, \tag{3.24}$$

where $\overline{u_i'\overline{u}_j} + \overline{\overline{u}_i u_j'}$ represents the contribution of the interactions between the unresolved scales and the resolved scales, whereas $\overline{u_i'u_j'}$ represents the contribution of the interactions between unresolved scales. Table 3.2 gives an overview of the different stresses [70, 74]. Since the Cross stress contributions and the Reynolds stress contributions in $\overline{\tau}_{ij}$ are not exclusively defined in terms of the resolved velocity field, equation (3.23) is *unclosed*. Closure is achieved by modeling the residual stress tensor, i.e. expressing it in terms of the resolved velocity field, such that the (3.23) can be solved. This is subject of Section 3.3.

In the previous discussion, the cutoff wavenumber was deliberately left undetermined since its value is imposed by the adopted discretization. Consider the uniform computational grid with the grid spacing Δ corresponding to the *grid cutoff wavenumber* $\kappa_{max} = \frac{\pi}{\Delta}$ on which the equations are discretized. In order to control aliasing due to the nonlinear stress $\overline{u}_i\overline{u}_j$ evaluation, Orszag [67] proved that the filter cutoff wavenumber $\kappa_c = \frac{\pi}{\Delta_c}$ should at least satisfy $\kappa_c = \frac{2}{3}\kappa_{max}$. Hence, the aliasing errors are restricted to the scales in the range $\kappa > \frac{2}{3}\kappa_{max}$ which are eliminated by the *explicit* filtering operation on the resolved stress $\overline{\overline{u}_i\overline{u}_j}$. Moreover, the explicit filtering

guarantees that the velocity field on the next time step is restricted to $\kappa < \frac{2}{3}\kappa_{max}$. However, this explicit filtering operation is most commonly not performed, and one obtains the *triple decomposition* by rearranging equation (3.23) as

$$\frac{\partial \overline{u}_i}{\partial t} + \frac{\partial \overline{u}_i \overline{u}_j}{\partial x_j} + \frac{\partial \overline{\tau}_{ij}}{\partial x_j} + \frac{\partial \tau^l_{ij}}{\partial x_j} = -\frac{\partial \overline{p}}{\partial x_i} + \nu \frac{\partial^2 \overline{u}_i}{\partial x_j^2}, \tag{3.25}$$

where $\tau^l_{ij} = \overline{\overline{u}_i \overline{u}_j} - \overline{u}_i \overline{u}_j$ denotes the *Leonard* stresses. This formulation implies that a residual stress model is required for $\overline{\tau}_{ij} + \tau^l_{ij}$ in order to cancel exactly the contributions in the range $\kappa > \frac{2}{3}\kappa_{max}$, which is extremely difficult, if not impossible [70]. Nevertheless, the triple decomposition is most commonly preferred since it requires less computational effort. Moreover, equation (3.25) is guaranteed to be *Galilean invariant*[8] regardless the adopted filter definition or residual stress model, whereas equation (3.23) is only Galilean invariant if the filter is orthogonal or if the invariance error of the filtered nonlinear term is exactly compensated by the invariance error of the residual stress model. An extensive discussion on this topic can be found in Meyers *et al.* [63]. Since in Section 3.1.3 the sharp cutoff filter was considered to be the most relevant and mathematical consistent filter definition for the current LES philosophy, Galilean invariance is theoretically guaranteed for both the double decomposition as well as the triple decomposition. Although the sharp cutoff filter is necessarily approximated in most realistic numerical simulations, preserving Galilean invariance is considered merely a discretization problem rather then a conceptual problem related to the double decomposition. Hence, the philosophy of Large-Eddy simulation with the double decomposition, involving the explicit filtering, is preferred in this dissertation.

3.2.2 The filtered equations in spectral space

In order to construct an appropriate model for the residual stresses, it is necessary to understand the effect of the unresolved scales on the resolved flow field. Therefore, the energy transfer between the resolved and unresolved scales in the spectral energy balance is examined. This requires first the formulation of the filtered Navier-Stokes equations in Fourier space. Following Pope [70], the evolution equation of the filtered Fourier modes is obtained by multiplying equation (2.15) with the sharp cutoff filter kernel $\widehat{\mathscr{G}}(\boldsymbol{\kappa}, \kappa_c) = \mathrm{H}(\kappa_c - |\boldsymbol{\kappa}|)$ leading to

$$\frac{d}{dt}\widehat{\overline{u}}_j(\boldsymbol{\kappa}, t) = -i\kappa_l \mathscr{P}_{jk}(\boldsymbol{\kappa}) \sum_{\boldsymbol{\kappa}'} \widehat{\mathscr{G}}(\boldsymbol{\kappa}, \kappa_c)\, \widehat{u}_k(\boldsymbol{\kappa}', t)\, \widehat{u}_l(\boldsymbol{\kappa} - \boldsymbol{\kappa}', t) - \nu\kappa^2 \widehat{\overline{u}}_j(\boldsymbol{\kappa}, t) \tag{3.26}$$

The closure problem arises because the nonlinear term in (3.26) includes unknown Fourier coefficients $\widehat{\mathbf{u}}(\boldsymbol{\kappa}', t)$ and $\widehat{\mathbf{u}}(\boldsymbol{\kappa} - \boldsymbol{\kappa}', t)$. Hence, the equations need closure

[8] The solution of the governing equations is said to be Galilean invariant if it remains the same in different inertial frames.

by expressing the nonlinear term as function of the resolved Fourier modes and to model the remaining unresolved interactions. The spectral LES-equations with double decomposition are written as

$$\frac{d}{dt}\widehat{\overline{u}}_j(\boldsymbol{\kappa},t) = F_j^{<}(\boldsymbol{\kappa},t) + F_j^{>}(\boldsymbol{\kappa},t) - \nu\kappa^2\widehat{\overline{u}}_j(\boldsymbol{\kappa},t), \tag{3.27}$$

where $F_j^{<}(\boldsymbol{\kappa},t)$ represents the resolved triadic interactions

$$F_j^{<}(\boldsymbol{\kappa},t) = -i\kappa_l \mathscr{P}_{jk}(\boldsymbol{\kappa}) \sum_{\boldsymbol{\kappa}'} \widehat{\mathscr{G}}(\boldsymbol{\kappa},\kappa_c)\, \widehat{\overline{u}}_k\left(\boldsymbol{\kappa}',t\right) \widehat{\overline{u}}_l\left(\boldsymbol{\kappa}-\boldsymbol{\kappa}',t\right), \tag{3.28}$$

and $F_j^{>}(\boldsymbol{\kappa},t)$ represents the unresolved triadic interactions

$$F_j^{>}(\boldsymbol{\kappa},t) = -i\kappa_l \mathscr{P}_{jk}(\boldsymbol{\kappa}) \sum_{\mathbf{max}(\boldsymbol{\kappa}',\boldsymbol{\kappa}-\boldsymbol{\kappa}')\geq\kappa_\mathbf{c}} \widehat{\mathscr{G}}(\boldsymbol{\kappa},\kappa_c)\, \widehat{u}_k\left(\boldsymbol{\kappa}',t\right) \widehat{u}_l\left(\boldsymbol{\kappa}-\boldsymbol{\kappa}',t\right). \tag{3.29}$$

Obviously, the unresolved triadic interactions, that involve the cross stresses and Reynolds stresses, need to be modeled.

3.2.3 Spectral energy balance in LES

The energy spectrum of the filtered velocity field is defined in analogy with Section 3.1.2 as

$$\overline{E}(\boldsymbol{\kappa},t) \;=\; \widehat{\mathscr{G}}(\boldsymbol{\kappa},\kappa_c)^2\, E(\boldsymbol{\kappa},t) = \widehat{\mathscr{G}}(\boldsymbol{\kappa},\kappa_c)^2 \left\langle \frac{1}{2}\widehat{u}_j(\boldsymbol{\kappa},t)\, \widehat{u}_j^*(\boldsymbol{\kappa},t) \right\rangle. \tag{3.30}$$

With this definition the spectral energy balance equation is derived by multiplying (3.27) with $\widehat{\overline{u}}_j^*(\boldsymbol{\kappa},t)$ and averaging over all realizations, leading to

$$\frac{d\overline{E}(\boldsymbol{\kappa},t)}{dt} = -2\nu\boldsymbol{\kappa}^2\overline{E}(\boldsymbol{\kappa},t) + T^{<}(\boldsymbol{\kappa},t) + T^{>}(\boldsymbol{\kappa},t), \tag{3.31}$$

where the rate of energy transfer due to the resolved triadic interactions is given by

$$T^{<}(\boldsymbol{\kappa},t) = -i\kappa_l \mathscr{P}_{jk}(\boldsymbol{\kappa}) \sum_{\boldsymbol{\kappa}'} \widehat{\mathscr{G}}(\boldsymbol{\kappa},\kappa_c) \left\langle \widehat{\overline{u}}_k\left(\boldsymbol{\kappa}',t\right) \widehat{\overline{u}}_l\left(\boldsymbol{\kappa}-\boldsymbol{\kappa}',t\right) \widehat{\overline{u}}_j^*(\boldsymbol{\kappa},t) \right\rangle, \tag{3.32}$$

and the rate of gain of energy from the unresolved triadic interactions is defined as

$$T^{>}(\boldsymbol{\kappa},t) = -i\kappa_l \mathscr{P}_{jk}(\boldsymbol{\kappa}) \sum_{\mathbf{max}(\boldsymbol{\kappa}',\boldsymbol{\kappa}-\boldsymbol{\kappa}')\geq\kappa_\mathbf{c}} \widehat{\mathscr{G}}(\boldsymbol{\kappa},\kappa_c) \left\langle \widehat{u}_k\left(\boldsymbol{\kappa}',t\right) \widehat{u}_l\left(\boldsymbol{\kappa}-\boldsymbol{\kappa}',t\right) \widehat{\overline{u}}_j^*(\boldsymbol{\kappa},t) \right\rangle \tag{3.33}$$

Because the total energy of the resolved triadic interactions is conserved, summation of equation (3.31) over all wavenumbers results in

$$\frac{d\overline{k}}{dt} = -\overline{\varepsilon} + \sum_{\kappa} T^{>}(\boldsymbol{\kappa}, t), \tag{3.34}$$

where the final term represents the net transfer of energy from the resolved scales to the unresolved scales and vice versa. $\sum_{\kappa} T^{>}(\boldsymbol{\kappa}, t)$ is predominantly negative corresponding to a drain of energy from the resolved interactions (*forward scatter*), but positive values of $\sum_{\kappa} T^{>}(\boldsymbol{\kappa}, t)$ can appear, corresponding to an energy injection from the unresolved interactions to the resolved interactions (*backscatter*). Although it is not considered in this work, Leslie *et al.* [51] showed that the backscatter can be quite significant. Since the effect of the unresolved interactions is mainly dissipative, $\sum_{\kappa} T^{>}(\boldsymbol{\kappa}, t)$ is most commonly modeled in analogy with the molecular dissipation, i.e.

$$T^{>}(\boldsymbol{\kappa}, t) = -2\nu_e^q(\kappa, \kappa_c)\,\boldsymbol{\kappa}^{2q}\overline{E}(\boldsymbol{\kappa}, t), \quad q \in \mathbb{N}^+, \tag{3.35}$$

where $\nu_e(\kappa, \kappa_c)$ denotes the *eddy viscosity* and q is typically unity, although other choices are possible.[9] The basic idea behind the eddy-viscosity concept is that scales of motions of given size, are acted on by smaller scales as if the latter were an augmentation of the molecular viscosity [48].[10] Assuming the Kolmogorov spectrum, Kraichnan [48] showed that for homogeneous isotropic turbulence, the eddy-viscosity $\nu_e(\kappa, \kappa_c)$, which depends on the wavenumber magnitude κ and the cutoff wavenumber κ_c in the inertial subrange, is given by

$$\nu_e(\kappa, \kappa_c) = \frac{\gamma}{12}\sqrt{C_k}\varepsilon^{\frac{1}{3}}\kappa_c^{-\frac{4}{3}}, \tag{3.36}$$

where C_k denotes the Kolmogorov constant and γ is a numerical constant. Although expression (3.36) gives a fairly good approximation of the theoretical eddy-viscosity in case $\kappa \ll \kappa_c$, ν_e rises sharply as κ approaches κ_c displaying the so-called *cusped behaviour*. This is demonstrated in Figure 3.3.

3.3 Subgrid modeling

From the previous section it was learned that the effect of the unresolved scales of motion is generally dissipative in nature. Moreover, under the assumption that this dissipative effect is similar to the molecular dissipation mechanism, the eddy-viscosity concept was introduced. Starting from the general expression of the eddy-viscosity concept in physical space, the *Smagorinsky model* for the residual stresses

[9] For $q = 2, 3, 4\cdots$, one obtains so-called *hyper-viscosity* models.

[10] This hypothesis is also known as the Boussinesq hypothesis.

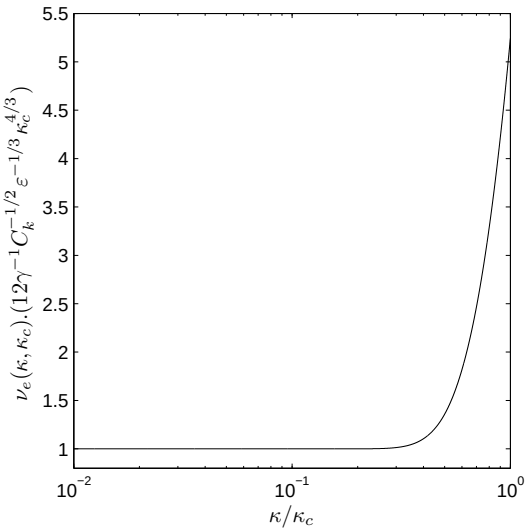

Figure 3.3: The cusped behaviour of the spectral eddy-viscosity. For $\kappa < 0.5\kappa_c$, $\nu_e(\kappa, \kappa_c)$ is within 15% of its assymptotic value and theses scales contribute approximately 25% of the total energy drain. About 50% of the total energy drain comes from scales at $\kappa > 0.75\kappa_c$ [48].

is discussed in the present section. This simple eddy-viscosity model is most commonly used in Large-Eddy simulations and therefore quite important. Furthermore, the *dynamic procedure* and the *multi-scale modeling technique* are introduced as improvements of the Smagorinsky model.

3.3.1 A TENSORIAL EDDY-VISCOSITY MODEL

Consider the residual-stress tensor $\overline{\tau}_{ij} = \overline{u_i u_j} - \overline{\overline{u_i}\,\overline{u_j}}$. If the exact description of the large scale pressure is not required, the trace of $\overline{\tau}_{ij}$ may be added to the pressure, which is then calculated in order to ensure the incompressibility. Hence, the *anisotropic* residual-stress tensor is defined as

$$\overline{\tau}^a_{ij} = \overline{\tau}_{ij} - \frac{1}{3}\overline{\tau}_{kk}\delta_{ij} = \overline{u_i u_j} - \overline{\overline{u_i}\,\overline{u_j}} - \frac{1}{3}\left(\overline{u_k u_k} - \overline{\overline{u_k}\,\overline{u_k}}\right)\delta_{ij}, \tag{3.37}$$

where the *Kronecker delta* δ_{ij} denotes the identity tensor. The *isotropic* residual stress is included in the modified filtered pressure as

$$\overline{\mathrm{p}} = \overline{p} + \frac{1}{3}\overline{\tau}_{kk}, \tag{3.38}$$

which is solved from the Poisson equation. Obviously, only the anisotropic tensor $\overline{\tau}^a_{ij}$ requires modeling. Since the dissipative effect of the unresolved scales on the resolved scales is considered to be similar to the viscous dissipation, the eddy-viscosity concept intrinsically assumes that the anisotropic residual-stress tensor is

determined by the velocity gradients of the resolved flow field. Following Carati *et al.* [13], a tensorial relation for the stress as a function of the resolved velocity gradients in an anisotropic system is written as

$$\tau_{ij}^{a} = \nu_{ijkl}\overline{S}_{kl} + \mu_{ijkl}\overline{\Omega}_{kl}, \tag{3.39}$$

where the symmetric resolved strain tensor $\overline{S}_{kl}$ and the anti-symmetric resolved rotation tensor $\overline{\Omega}_{kl}$ are given respectively by

$$\overline{S}_{kl} = \frac{1}{2}\left(\frac{\partial \overline{u}_k}{\partial x_l} + \frac{\partial \overline{u}_l}{\partial x_k}\right), \quad \overline{\Omega}_{kl} = \frac{1}{2}\left(\frac{\partial \overline{u}_k}{\partial x_l} - \frac{\partial \overline{u}_l}{\partial x_k}\right), \tag{3.40}$$

whereas ν_{ijkl} and μ_{ijkl} denote two 4^{th} -rank eddy-viscosity tensors each formally determined by 81 independent parameters. However, based on the tensor symmetry properties of $\overline{\tau}_{ij}$, $\overline{S}_{kl}$ and $\overline{\Omega}_{kl}$, Carati *et al.* [13] showed that

$$\nu_{ijkl} = \nu_{jikl} \tag{3.41}$$
$$\nu_{ijkl} = \nu_{ijlk} \tag{3.42}$$
$$\nu_{iikl} = 0 \tag{3.43}$$
$$\nu_{ijkk} = 0, \tag{3.44}$$

such that ν_{ijkl} is described by only 25 independent parameters, whereas

$$\mu_{ijkl} = \mu_{jikl} \tag{3.45}$$
$$\mu_{ijkl} = -\mu_{ijlk} \tag{3.46}$$
$$\mu_{iikl} = 0, \tag{3.47}$$

such that μ_{ijkl} is determined by only 15 independent parameters. Moreover, these viscosity tensors may be simplified further, by using the symmetries of the flow. Carati *et al.* [13] and Abba *et al.* [1] constructed anisotropic tensorial eddy-viscosity models, but since this topic will not be addressed further in this dissertation, the reader is referred to their work.

For homogeneous isotropic turbulence, no preferential directions exist, and ν_{ijkl} can be further reduced to

$$\nu_{ijkl} = -\nu_e\left(\delta_{ik}\delta_{jl} + \delta_{il}\delta_{jk} - \frac{2}{3}\delta_{ij}\delta_{kl}\right), \tag{3.48}$$

whereas $\mu_{ijkl} = 0$. By substitution of (3.48) into expression (3.39), the linear eddy-viscosity model is obtained as

$$\tau_{ij}^{a} = -2\nu_e\overline{S}_{ij}. \tag{3.49}$$

This model is equivalent with the spectral eddy-viscosity model (3.35) for $q = 1$. Since turbulent flows are generally anisotropic, it is appreciated that the linear isotropic eddy-viscosity model is only a rough approximation. Nevertheless, this model is most frequently used in Large-Eddy Simulations.

3.3.2 The Smagorinsky model

In analogy with the expression of the spectral eddy-viscosity (3.36), the eddy-viscosity in physical space is proportional to the dissipation rate ε and the cutoff length Δ_c such that

$$\nu_e = \frac{\gamma}{12}\frac{\sqrt{C_k}}{\pi^{4/3}}\varepsilon^{\frac{1}{3}}\Delta_c^{\frac{4}{3}}. \tag{3.50}$$

Since the rate of energy transfer ε is usually not directly accessible in LES, Smagorinsky [78] proposed to identify ε in the inertial range (assuming an infinite Reynolds number and thus neglecting the molecular viscosity) with the dissipation of the unresolved scales, by invoking the local-equilibrium hypothesis.[11] This hypothesis further implies that the dissipation of the unresolved scales of motion is assumed to be in equilibrium with the production of the subgrid kinetic energy. Following Sagaut [74] and Leslie *et al.* [51], it is preferred in the current framework of homogeneous isotropic turbulence to perform the reasoning on statistical averages rather than on the local values in the physical space as originally proposed by Smagorinsky [78]. Hence, the local-equilibrium assumption translates into

$$\varepsilon \approx \left\langle -\tau_{ij}^a\,\overline{S_{ij}}\right\rangle = \left\langle \nu_e \overline{S}^2\right\rangle \approx \nu_e \left\langle \overline{S}^2\right\rangle. \tag{3.51}$$

Here, $\overline{S} = \sqrt{2\overline{S_{ij}}\,\overline{S_{ij}}}$ denotes the filtered strain rate magnitude. Substitution of relation (3.51) into expression (3.50) results in

$$\nu_e = C_s^2\Delta_c^2\left\langle \overline{S}^2\right\rangle^{1/2}, \tag{3.52}$$

where the Smagorinsky constant C_s is determined by

$$C_s = \frac{1}{\pi^2}\left(\frac{\gamma}{12}\sqrt{C_k}\right)^{3/2}, \tag{3.53}$$

Lilly [52] calculated the C_s slightly different and found the generally accepted standard value $C_s \approx 0.17$. Although the eddy-viscosity in Smagorinsky's subgrid model (3.52) is meant to be an ensemble averaged quantity in the framework of isotropic turbulence, i.e. averaged over time and space, it is often used in its spatial and temporal localized formulation in order to be more adaptable to the flow being calculated. However, there is no particular justification for this local use of relations that are on average true for the whole, since they only ensure that the energy transfers through the cutoff are expressed correctly on the average, and not locally [74].

[11] The local-equilibrium hypothesis assumes that the flow is in constant spectral equilibrium such that no accumulation of energy occurs in the energy spectrum. This implies an instantaneous response of all scales in the cascade to sudden changes in the energy flux.

Nevertheless, the Smagorinsky residual-stress or *subgrid* model for LES with the double decomposition is expressed as

$$\overline{\tau}^a_{ij} = -2C_s^2\Delta_c^2\overline{\overline{S}\,\overline{S}_{ij}}. \tag{3.54}$$

Muschinski [66] interpreted the LES equations as the equations of motion of a hypothetical turbulent non-Newtonian fluid, called the *LES fluid*. Then, *the Smagorinsky fluid* is by definition the LES fluid that is specified by the Smagorinsky closure and corresponds with a hypothetical shear-thickening fluid, since the Smagorinsky viscosity (3.52) is proportional to the strain rate magnitude. Whereas in the Navier-Stokes equations the molecular viscosity is a fluid property and the dissipation length (i.e. Kolmogorov length scale) is the free variable, in a Smagorinsky fluid, the dissipation length is the fluid property and the viscosity is variable.
Since the Smagorinsky model is derived for Large-Eddy simulation of turbulent flows at an infinite Reynolds number, that is with a filter cutoff in the inertial range, its application to finite Reynolds numbers or non-equilibrium flows is not completely justified. It has since long been recognized that the Smagorinsky-Lilly coefficient C_s, is actually not a constant but depends on the position of the cutoff wavenumber in the spectrum, more specific on the ratio Δ_c/η and L/Δ_c.

i. At low Reynolds numbers, when the cutoff wavenumber lies into the far dissipation range, i.e. $\Delta_c/\eta \to 1$, Voke [84] and Meneveau *et al.* [58] showed that the value of the Smagorinsky-Lilly coefficient decreases with increasing Δ_c/η, and vanishes if $\Delta_c/\eta \approx 1$. This implies that in the dissipation range, the Smagorinsky viscosity experiences a more rapid decrease with Δ_c than the inertial range scaling with $\Delta_c^{4/3}$. Therefore, the constant Smagorinsky model is too dissipative for low-Reynolds number flows, transitional flows and even near boundaries.

ii. Equivalently, Meyers *et al.* [64] showed that if the cutoff length approaches the integral length scale, i.e. $L/\Delta_c \approx 1$, the Smagorinsky-Lilly coefficient becomes dependent of this ratio. Hence, the Smagorinsky-Lilly model requires relatively large ratios of L/Δ_c in order to obtain *scale separation* such that the coefficient is L/Δ_c-independent. If L/Δ_c is too small, the model significantly affects the large-scale structures.

Recently, Meyers *et al.* [64] succeeded to derive a universal expression for C_s that depends on the ratio L/Δ_c and the Reynolds number (and thus implicitly on Δ_c/η), by using Pope's model energy spectrum (2.29) and accounting for the shape of the filter. An alternative approach to obtain the appropriate model coefficient C_s is the *dynamic procedure* by Germano *et al.* [30]. This technique tends to capture the scaling behaviour of C_s with Δ_c/η such that C_s vanishes for $\Delta_c/\eta \approx 1$. Another popular technique to remedy the deficiencies of the constant coefficient Smagorinsky model, is the *scale separation* or *multi-scale* approach, which restricts the model to the smallest resolved scales only. Both techniques are discussed hereafter.

3.3.3 Dynamic Procedure

The dynamic procedure by Germano *et al.* [30] is an elegant mathematical tool that allows to measure the model coefficient by using information from the resolved scales. More specific, it minimizes the error associated with the specific eddy-viscosity assumption in the model considered [74]. Hence the procedure is not restricted to the Smagorinsky formulation, but can be applied to more general formulations such as (3.50) [14, 90].
Consider the primary sharp cutoff LES filter $\mathscr{G}(\mathbf{x}) = \mathscr{G}(\mathbf{x}, \kappa_c)$ which is characterized by the cutoff wavenumber $\kappa_c = \frac{\pi}{\Delta_c} = \frac{2}{3}\kappa_{max}$, κ_{max} being the cutoff wavenumber of the computational grid with grid spacing Δ. The filtered velocity field, denoted by the overbar $\bar{\cdot}$, is then defined as

$$\overline{\mathbf{u}}(\mathbf{x}, t) = \mathscr{G}(\mathbf{x}, \kappa_c) * \mathbf{u}(\mathbf{x}, t). \tag{3.55}$$

Using this definition, the LES-equations with double decomposition (3.23) are obtained, in which the filtered nonlinear term is expressed as function of the filtered velocity field and the residual stress model $\overline{\tau}^a_{ij}(\Delta_c)$, i.e.

$$\overline{u_i u_j} = \overline{\overline{u}_i \overline{u}_j} + \overline{\tau}_{ij}(\Delta_c). \tag{3.56}$$

Further, consider a second *self-similar* filter $\mathscr{G}(\mathbf{x}, \lambda_c)$ which has the same shape of the primary filter but with a different cutoff wavenumber $\lambda_c = \kappa_c/\alpha$, $\alpha \in \mathbb{N}^+$ [15]. Since the sharp cutoff filter is orthogonal and projective, the *double filtered* velocity field, denoted by $\widetilde{\bar{\cdot}}$ is then given by

$$\widetilde{\mathbf{u}}(\mathbf{x}, t) = \widetilde{\overline{\mathbf{u}}}(\mathbf{x}, t) = \mathscr{G}(\mathbf{x}, \lambda_c) * \overline{\mathbf{u}}(\mathbf{x}, t). \tag{3.57}$$

Application of this secondary filtering operation to the LES-equations (3.23) results in the *double filtered* LES-equations with double decomposition, where the filtered nonlinear term is expressed in analogy with (3.56) as

$$\widetilde{\overline{u_i u_j}} = \widetilde{\overline{\overline{u}_i \overline{u}_j}} = \widetilde{\overline{u}}_i \widetilde{\overline{u}}_j + \widetilde{\tau}_{ij}(\alpha\Delta_c). \tag{3.58}$$

However, the left hand side of (3.58) is readily obtained by filtering expression (3.56) resulting in

$$\widetilde{\overline{u_i u_j}} = \widetilde{\overline{\overline{u}_i \overline{u}_j}} = \widetilde{\overline{u}_i \overline{u}_j} + \widetilde{\tau}_{ij}(\Delta_c). \tag{3.59}$$

Identifying equations (3.58) and (3.59) finally leads to a set of 9 equations

$$\mathscr{L}_{ij} = \widetilde{\overline{u}_i \overline{u}_j} - \widetilde{\overline{u}}_i \widetilde{\overline{u}}_j = \widetilde{\tau}_{ij}(\alpha\Delta_c) - \widetilde{\tau}_{ij}(\Delta_c), \tag{3.60}$$

which is called the *Germano identity*. Notice that for LES with the double decomposition, the Leonard stresses are given by $\mathscr{L}_{ij} = \widetilde{\overline{u}_i \overline{u}_j} - \widetilde{\overline{u}}_i \widetilde{\overline{u}}_j$, whereas for LES with

the triple decomposition the Leonard stresses would yield $\mathscr{L}_{ij} = \widetilde{\overline{u}_i \overline{u}_j} - \widetilde{u}_i \widetilde{u}_j$. With the Smagorinsky model for the anisotropic part of the residual stress[12]

$$\overline{\tau}^a_{ij} = \overline{\tau}_{ij} - \frac{1}{3}\overline{\tau}_{kk}\delta_{ij} = -2C_s^2 \Delta_c^2 \overline{\overline{S}\,\overline{S}_{ij}}, \tag{3.61}$$

the Germano identity yields

$$\begin{aligned} \mathscr{L}_{ij} - \frac{1}{3}\mathscr{L}_{kk}\delta_{ij} &= \widetilde{\tau}^a_{ij}(\alpha\Delta_c) - \widetilde{\tau}^a_{ij}(\Delta_c) && (3.62)\\ &= C_s^2 \left[2\Delta_c^2 \widetilde{\overline{S}\,\overline{S}_{ij}} - 2(\alpha\Delta_c)^2 \widetilde{\widetilde{S}\widetilde{S}_{ij}} \right], && (3.63) \end{aligned}$$

or in short hand notation

$$\mathscr{L}^a_{ij} = C_s^2 \mathscr{M}_{ij}. \tag{3.64}$$

Relation (3.64) determines a set of 9 linear equations, of which only 5 are independent [70]. In principle, one could replace C_s^2 by a specific *fourth-rank* tensor in which 9 model coefficients (5 independent) could be calculated from this set of equations, determining the effective filter width for each residual stress component. This is reminiscent to the tensorial eddy-viscosity concept. Nevertheless, in practice only one coefficient is obtained from the 5 independent equations. Lilly [53] proposed to extract C_s by minimizing the mean-square error

$$\mathscr{E} = \left\langle \left(\mathscr{L}^a_{ij} - C_s^2 \mathscr{M}_{ij} \right)^2 \right\rangle, \tag{3.65}$$

where $\langle . \rangle$ denotes the spatial averaging over all homogeneous directions. Finally, differentiation with respect to C_s^2 yields

$$C_s^2 = \frac{\langle \mathscr{L}^a_{ij} \mathscr{M}_{ij} \rangle}{\langle \mathscr{M}_{ij} \mathscr{M}_{ij} \rangle}. \tag{3.66}$$

Although the dynamic procedure is considered to be a standard technique, some important implicit assumptions require attention. In order to obtain expression (3.64), the Smagorinsky coefficient is necessarily assumed independent of the (cut-off) wavenumber in the interval $[\lambda_c, \kappa_c]$ such that $C_s(\alpha\Delta_c/\eta) = C_s(\Delta_c/\eta)$. Hence, $C_s(\Delta_c/\eta)$ is approximated by the dynamic procedure as a piecewise constant function. Although this *self-similarity* assumption is quite reasonable if the cutoff wavenumbers κ_c and λ_c lie in the inertial subrange and if the value of α is small, it becomes less justified for cutoff wavenumbers in the dissipation range (or energy containing range), or if α is large. Meneveau *et al.* [58] suggested to adopt an explicit

[12] The isotropic stress is accounted for in the modified pressure.

function for $C_s(\Delta_c/\eta)$ in order to remedy this deficiency. Nevertheless, the traditional dynamic procedure seems to perform quite well and typically a *filter width ratio* $\alpha = 2$ is adopted. Furthermore, to preserve the mathematical consistency, C_s must be a constant in order to bring it outside the filtering operator in the evaluation of $\widetilde{\overline{\tau}}^a_{ij}(\Delta_c) = \widetilde{\tau}^a_{ij}(\Delta_c)$ in (3.59). This constraint is usually not respected in practical simulations. In order to keep the mathematical inconsistency minimal, one should at least guarantee the smoothness of the Smagorinsky coefficient.

3.3.4 MULTISCALE MODELING

It was argued by Hughes *et al.* [40, 41] that many shortcomings of the Smagorinsky based approaches are associated with their inability to successfully differentiate between large and small scales (scale separation), especially when L/Δ_c is too small. Hence, they suggested to perform a scale separation *ab initio*, by segregating the resolved scales into *largest resolved scales* and *smallest resolved scales*, by an orthogonal projective filtering operator. Under the assumption that the distant triadic interactions, i.e. interactions between the largest resolved scales and the residual scales, have a negligible influence on the large scale dynamics, only the contributions of the local triadic interactions are modeled.
Consider again the sharp cutoff filter $\mathscr{G}(\mathbf{x}, \lambda_c)$ with cutoff wavenumber $\lambda_c = \kappa_c/\alpha, \alpha \in \mathbb{N}^+$. Since $\mathscr{G}(\mathbf{x}, \lambda_c)$ is an orthogonal projective filter, the *resolved* velocity field $\overline{\mathbf{u}}$ is decomposed as

$$\overline{\mathbf{u}}(\mathbf{x}, t) = \widetilde{\mathbf{u}}(\mathbf{x}, t) + \mathbf{u}''(\mathbf{x}, t), \tag{3.67}$$

where $\widetilde{\mathbf{u}}(\mathbf{x}, t) = \widetilde{\overline{\mathbf{u}}}(\mathbf{x}, t)$ indicates the largest resolved scales and $\mathbf{u}''(\mathbf{x}, t)$ denotes the smallest resolved scales, such that

$$\widehat{\widetilde{\mathbf{u}}}(\boldsymbol{\kappa}, t) = \widehat{\mathscr{G}}(\boldsymbol{\kappa}, \lambda_c)\,\widehat{\mathbf{u}}(\boldsymbol{\kappa}, t), \quad 0 \le \kappa \le \lambda_c \tag{3.68}$$

$$\widehat{\mathbf{u}}''(\boldsymbol{\kappa}, t) = \left[1 - \widehat{\mathscr{G}}(\boldsymbol{\kappa}, \lambda_c)\right]\widehat{\mathscr{G}}(\boldsymbol{\kappa}, \kappa_c)\,\widehat{\mathbf{u}}(\boldsymbol{\kappa}, t), \quad \lambda_c \le \kappa \le \kappa_c. \tag{3.69}$$

In principle, the LES-equations (3.23) are then formally decomposed into the large scale equations for $\widetilde{\mathbf{u}}(\mathbf{x}, t)$ and the small scale equations for $\mathbf{u}''(\mathbf{x}, t)$ yielding[13]

$$\frac{\partial \widetilde{u}_i}{\partial t} + \frac{\partial \widetilde{\overline{u}_i \overline{u}_j}}{\partial x_j} = -\frac{\partial \widetilde{p}}{\partial x_i} + \nu \frac{\partial^2 \widetilde{u}_i}{\partial x_j^2} \tag{3.70}$$

$$\frac{\partial u_i''}{\partial t} + \frac{\partial (\overline{u}_i \overline{u}_j)''}{\partial x_j} + \frac{\partial \overline{\tau}''_{ij}}{\partial x_j} = -\frac{\partial p''}{\partial x_i} + \nu \frac{\partial^2 u_i''}{\partial x_j^2}, \tag{3.71}$$

where $(.)''$ denotes the *band-pass* filtering in the range $\lambda_c \le \kappa < \kappa_c$. Since the distant triadic interactions are neglected, the large scale equations are closed. Nevertheless,

[13] In practice, the sum of both equations is solved.

the small scale equations remain unclosed and require a model for the residual stresses due to local interactions. Hughes *et al.* [40, 41] proposed to close the residual stress tensor $\overline{\tau}''_{ij}$ by an eddy-viscosity model of the Smagorinsky type. Three such closures are typically adopted [38], i.e. the *large-small*, the *all-small* and the *small-small*, respectively defined as

$$\overline{\tau}''_{ij} = -2C^2_{s,1}\Delta^2_c \left(\widetilde{S}S''_{ij}\right)'', \tag{3.72}$$

$$\overline{\tau}''_{ij} = -2C^2_{s,2}\Delta^2_c \left(\overline{S}S''_{ij}\right)'', \tag{3.73}$$

$$\overline{\tau}''_{ij} = -2C^2_{s,3}\Delta^2_c \left(S''S''_{ij}\right)'', \tag{3.74}$$

in which the eddy-viscosity is calculated using respectively the largest resolved scales, the smallest resolved scales, and the sum of both,[14] whereas the strain rate tensor is only calculated on the small-scale field. Further, the total residual stress model is projected again to the small scale velocity field due to the band-pass filter $(.)''$. The model constant $C_{s,i}, i = 1, 2, 3$ is evaluated analogously as done by Lilly [52], although here, both cutoff wavenumbers need to be accounted for. This results in the expressions

$$C_{s,3} = C_s \frac{\kappa_c}{\lambda_c}\left[\left(\frac{\kappa_c}{\lambda_c}\right)^{4/3} - 1\right]^{-4/3}, \tag{3.75}$$

for the *small-small* closure, and

$$C_{s,1} = C_s \frac{\kappa_c}{\lambda_c}\left[\left(\frac{\kappa_c}{\lambda_c}\right)^{4/3} - 1\right]^{-1/2}, \tag{3.76}$$

for the *large-small* closure [40]. It can be verified that these constants are larger than the standard Smagorinsky coefficient $C_s \approx 0.17$.

Although good results were obtained, mainly due to the absence of the dissipation on the largest resolved scales, some concerns about the multi-scale approach need to be addressed. Several studies by e.g. Eyink [25] and Domaradzki *et al.* [23, 24] confirm that the energy transfer is mainly dominated by contributions of local triadic interactions since cancellation occurs among significant contributions from nonlocal interactions. Although these findings seem to support the multi-scale approach which attempts to model merely the contributions from local triadic interactions, Sagaut *et al.* [75] observed a significant pile-up in the energy spectrum in the range $0 \leq \kappa < \lambda_c$, near the cutoff wavenumber λ_c. This phenomenon arises in the current multi-scale formalism since the energy drain due to the distant triadic interactions, is neglected. This agrees with the analysis of Kraichnan [48], who found that the

[14] Remark that these choices are *ad hoc* rather than based on physical considerations.

distant triadic interactions can be responsible for 25% of the energy drain. Sagaut *et al.* [75] noticed that the energy accumulation increased due to the excessive dissipation of the multi-scale models in the range $\lambda_c \leq \kappa < \kappa_c$. This was interpreted as a bottleneck effect due to the substantial decrease of the energy drain in the forward energy cascade. These results are confirmed by the study of Hughes *et al.* [42], who found that the energy transfers from the low-wavenumber part of the spectrum to the unresolved scales is underestimated by the multi-scale models, in contrast to the dynamic Smagorinsky model. In order to alleviate the energy pile-up, Sagaut *et al.* [75] suggested to replace the orthogonal projective sharp cutoff filter, by a non-orthogonal smooth filter which is non-local in Fourier space. Hence, the most important part of the distant interactions, contributing to the energy transfer is taken into account. However, the use of a non-orthogonal smooth filter in order to perform the scale separation, undermines the philosophy of the multi-scale approach since the locality assumption is abandonned. Indeed, Vreman [85], showed that for non-orthogonal smooth filter operators, the multi-scale residual stress model reduces to a hyperviscosity model (corresponding to expression (3.35) for $q > 1$). Nevertheless, the application of hyperviscosity models, and by consequence multi-scale models with non-orthogonal operators, appears to be advantageous since they tend to approximate better the cusped behaviour (Figure 3.3) whereas excessive dissipation of the small scales is avoided. Moreover combination of these models with the dynamic procedure leads to very good results, although application of the *Germano procedure* to the framework of multi-scale modeling with orthogonal projections is not straightforward. In order to preserve the consistency of the procedure, the double filtered equations are necessarily derived from the small scale equations (3.71) whereas the test filter of the procedure should have a cutoff within the narrow band $[\lambda_c, \kappa_c]$. In practice, however, one directly applies the dynamic coefficient otained with the traditional Smagorinsky model to the multiscale models, altough this is not entirely justified [38].

3.3.5 Concluding Remarks

In the current dissertation, the dynamic Smagorinsky model is preferred in order to account for the unresolved interactions in the Large-Eddy Simulation with double decomposition. This choice is motivated by the fact that this model does not require the *ad hoc* definition of model constants since it adapts the magnitude of the dissipation to the resolved physics of the flow. Only the test filter for the dynamic procedure must be predefined, but has only a limited influence on the models' performance. In contrast, the multiscale technique requires the choice of a specific closure-variant and the corresponding model constants. Moreover, the scale separation filter must be determined *ad hoc* although it entirely determines the success of the multiscale approach. Finally, all multiscale models leads to significant energy pile-up in combination with the sharp cutoff filter.

3.4 Implications toward numerical methods

In the past decades, the necessity for numerical quality in Direct Numerical Simulations (DNS) and Large-Eddy Simulations (LES) of turbulent flows has been recognized by many researchers (e.g. Ghosal [32], Kravchenko *et al.* [49], Moin *et al.* [19] and Berland *et al.* [4]). In a very well resolved Direct Numerical Simulation, the smallest resolved scales are located far into the dissipation range. Since these scales have only a very small energy-content in comparison with the largest resolved scales in the flow, they are often considered to have a negligible influence on the mean flow statistics. In a Large-Eddy Simulation, however, where only the most important large scale structures are resolved, the smallest resolved scales are part of the inertial subrange such that they contain relatively more energy than those in the dissipation range. Hence, the smallest resolved scales in Large-Eddy Simulation are not negligible and have a significant influence on the evolution of the LES-flow. The accuracy with which these small scales are described is therefore expected to be important. In order to reduce the computational costs, it is highly desirable in LES to maximize the ratio between the physical resolution and the grid resolution κ_c/κ_{max}. As mentioned before this ratio is limited to the value $\kappa_c/\kappa_{max} = 2/3$ by the Nyquist criterion [67]. Therefore, the adopted numerical method requires sufficient accuracy for all scales in the range $0 \leq \kappa < \kappa_c$ in order to ensure that the magnitudes of the discretization errors (defined in Section 2.4.3) remain smaller than the magnitude of the modeled residual force of the unresolved scales of motion [32, 19, 4]. However, if the accuracy of the numerical method is not guaranteed, the ratio κ_c/κ_{max} must be reduced in order to control the discretization errors. In order to resolve the same amount of scales to a fixed cutoff wavenumber κ_c, the grid cutoff wavenumber κ_{max}, which is proportional with the number of grid nodes, needs to be increased. This is most often prohibitively expensive for most three-dimensional LES computations. Moreover, subgrid modeling techniques such as the dynamic procedure or multi-scale modeling strongly rely on the smallest resolved scales in LES. Accurate resolution of the small-scales should result in correct application of these subgrid models. Obviously, good numerical quality for an affordable LES is vital for accurate flow prediction as it may influence the resolved physics as well as the subgrid modeling.

Truth is much too complicated to allow anything but approximations.

Von Neumann, John

4 Numerical method

In the previous chapters, the governing equations for DNS and LES were introduced. A rigorous mathematical description of the discretization concept was given (see Chapter 2), resulting in the definition of a *sampling operator*. This operator projects the set of analytical equations to a set of discrete equations which can be resolved numerically. It was shown in Section 2.4.1 that the sampling operator gives rise to a commutation error when applied to the partial derivatives. Hence, the partial derivatives of the discrete velocity field need to be approximated since they cannot be obtained exactly.

In the present chapter, the standard *explicit* and *implicit central Finite Difference approximations* for the spatial derivatives are introduced and their accuracy is examined through Fourier analysis. Since the sharp cutoff filter, which is selected as the theoretical filter that appears in the LES-equations with double decomposition, is non-local in physical space, a localized approximation of this filter kernel is required for numerical simulations. Although in this dissertation, the sharp cutoff filtering is performed in Fourier space, the derivation of finite difference approximations for this filter is briefly discussed.

Next, the temporal discretization by *Runge-Kutta methods* is introduced as well as two *algorithms* that are used to solve the discrete equations. In particular the discretizations of the nonlinear and viscous terms in the Navier-Stokes equations as well as the discretization of the Poisson equation are discussed.

Finally, an appraisal is given of the standard finite difference approximations in Large-Eddy Simulation. It is argued that these standard approximations with formal order of accuracy may not be ideal in the context of LES, and that so-called *optimized* finite difference approximations might be more advantageous. In this

context the motivation for this dissertation is then explained.

4.1 SPATIAL DISCRETIZATION BY FINITE DIFFERENCES

In this dissertation, the *regular structured grid system* is considered, which is a tessellation of the Euclidean space by congruent rectangles or rectilinear cuboid elements. A two-dimensional[1] regular structured grid is illustrated in Figure 4.1. In such a regular grid system, the velocity components u_j, $j = 1, 2, 3$ and the pressure p are stored in the same nodes at the vertices of the tessellations. Moreover, the discretization of the Navier-Stokes equations and the Poisson equation are also centered at these nodes. The regular grid system is the most natural and unambiguous system in combination with finite differences. In the following, only one-dimensional uniform grids are considered.[2]

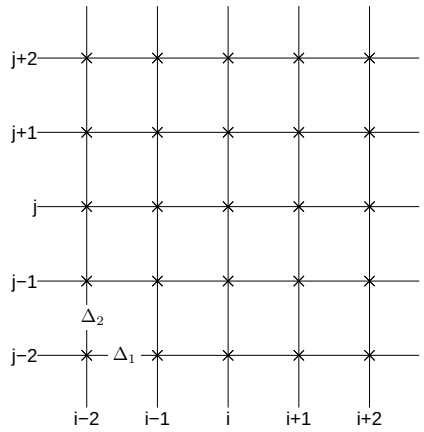

Figure 4.1: A regular 2-dimensional uniform grid. The velocity components $u_j, j = 1, 2$ and the pressure p are stored in the same nodes ($\times$) which are identified by the index-pair (i, j). The grid spacing is defined by the vector $\boldsymbol{\Delta} = [\Delta_1, \Delta_2]$.

In Section 2.4.1 the Dirac comb or sampling operator $\mathscr{S}^{\boldsymbol{\Delta}}$ was defined as the mathematical operator with which the partial differential equations are discretized. It was shown that this sampling operator does not commute with the partial derivatives, since the analytical definition of the derivative is no longer valid in case of discontinuous sampled variables. As a consequence, some approximation for the definition of these partial derivatives must be found, taking into account the finite grid spacing. The obtained *finite difference* approximation is characterized by a specific *order of accuracy*, which depends on the adopted definition of the derivative. This is further discussed.

[1] The three-dimensional regular grid system is a straightforward extension of this.

[2] As discussed in Section 2.4.1, the extension to multi-dimensional spaces or non-uniform Cartesian grids is straightforward. Recall that the latter uses an analytical of discrete mapping between a uniform grid and a non-uniform grid.

4.1.1 Explicit Finite Difference approximations

Consider a one-dimensional uniform grid with discrete equispaced Cartesian coordinates $x_i \in \mathbb{R}$, $i \in \mathbb{N}$ such that the grid spacing $\Delta = x_{i+1} - x_i = x_i - x_{i-1}$. Then the definition of the n^{th} partial derivative of a *continuous* variable $u(x,t)$, $x \in \mathbb{R}$, evaluated in a node x_i, is given by

$$\frac{\partial^n u}{\partial x^n}(x_i) = \lim_{\Delta \to \epsilon} \left[\frac{1}{\Delta^n} \sum_{j=-r}^{r} \beta_j u\left(x_{i+j}\right) \right], \quad \epsilon = 0, \tag{4.1}$$

where β_j denotes a set of weighting coefficients and $2r$ is the number of neighbouring nodes involved in the specific definition. The *stencil width* of the scheme is $2r+1$. Remark that the continuity of $u(x,t)$ in $x = x_i$ is a necessary condition for the limit in (4.1) to exist since both $\lim_{\Delta \to 0^-}$ and $\lim_{\Delta \to 0^+}$ must exist and be equal. However, continuity is a *necessary* but not a *sufficient* condition for differentiability. Requiring the function $u(x,t)$ to be *Lipschitz continuous* in $x = x_i$ is a sufficient condition since it limits how fast the continuous function $u(x,t)$ may change in $x = x_i$.[3] If $u(x,t)$, is an *infinitely differentiable* function, $u(x_{i+j}) = u(x_i + j\Delta)$ can be expanded in a *Taylor series* about x_i, i.e.

$$u(x_i + j\Delta) = \sum_{q=0}^{\infty} \frac{(j\Delta)^q}{q!} \frac{\partial^q u}{\partial x^q}(x_i), \quad \forall j. \tag{4.2}$$

Substitution of (4.2) into (4.1) then yields

$$\frac{\partial^n u}{\partial x^n}(x_i) = \lim_{\Delta \to \epsilon} \left[\sum_{q=0}^{\infty} \left(\sum_{j=-r}^{r} \frac{\beta_j j^q}{q!} \right) \Delta^{q-n} \frac{\partial^q u}{\partial x^q}(x_i) \right], \quad \epsilon = 0. \tag{4.3}$$

The set of $2r+1$ weighting coefficients β_j can now be obtained by identifying the first $q = 2r+1$ terms on the right-hand side of (4.3) with those at the left-hand side. Hence, a set of $2r+1$ equations for $2r+1$ unknown coefficients must be resolved. This translates into the matrix equation

$$\begin{bmatrix} \frac{(-r)^0}{0!} & \cdots & \frac{(j)^0}{0!} & \cdots & \frac{(r)^0}{0!} \\ \vdots & & \vdots & & \vdots \\ \frac{(-r)^n}{n!} & \cdots & \frac{(j)^n}{n!} & \cdots & \frac{(r)^n}{n!} \\ \vdots & & \vdots & & \vdots \\ \frac{(-r)^{2r}}{(2r)!} & \cdots & \frac{(j)^{2r}}{(2r)!} & \cdots & \frac{(r)^{2r}}{(2r)!} \end{bmatrix} \begin{bmatrix} \beta_{-r} \\ \vdots \\ \beta_0 \\ \vdots \\ \beta_r \end{bmatrix} = \begin{bmatrix} 0 \\ \vdots \\ 1 \\ \vdots \\ 0 \end{bmatrix}. \tag{4.4}$$

[3] Weisstein, Eric W. "Derivative." From MathWorld–A Wolfram Web Resource. http://mathworld.wolfram.com/Derivative.html

n	β_{-5}	β_{-4}	β_{-3}	β_{-2}	β_{-1}	β_0	β_1	β_2	β_3	β_4	β_5	k
1					$-\frac{1}{2}$	0	$\frac{1}{2}$					2
				$\frac{1}{12}$	$-\frac{2}{3}$	0	$\frac{2}{3}$	$-\frac{1}{12}$				4
			$-\frac{1}{60}$	$\frac{3}{20}$	$-\frac{3}{4}$	0	$\frac{3}{4}$	$-\frac{3}{20}$	$\frac{1}{60}$			6
		$\frac{1}{280}$	$-\frac{4}{105}$	$\frac{1}{5}$	$-\frac{4}{5}$	0	$\frac{4}{5}$	$-\frac{1}{5}$	$\frac{4}{105}$	$-\frac{1}{280}$		8
	$-\frac{1}{1260}$	$\frac{5}{504}$	$-\frac{5}{84}$	$\frac{5}{21}$	$-\frac{5}{6}$	0	$\frac{5}{6}$	$-\frac{5}{21}$	$\frac{5}{84}$	$-\frac{5}{504}$	$\frac{1}{1260}$	10

Table 4.1: Explicit finite difference approximations. Explicit finite difference approximation of order k for the 1^{st} derivative.

Obviously, $n < 2r + 1$ is a necessary condition in order to have a square, invertible matrix. Examining the specific structure of the matrix in (4.4) reveals that the resulting set of coefficients must be *symmetric* for even values of n, whereas for odd values of n, the coefficients are *anti-symmetric*, i.e.

$$\beta_{j-w} = \beta_{j+w}, \quad \forall w \in [1, r], \forall n \in 2\mathbb{N} \tag{4.5}$$

$$\beta_{j-w} = -\beta_{j+w}, \quad \forall w \in [1, r], \forall n \in 2\mathbb{N} + 1. \tag{4.6}$$

As a consequence, expression (4.3) reduces to an even power series in Δ. Moreover, for $n \in 2\mathbb{N}$, all derivatives in series (4.3) are even, whereas for $n \in 2\mathbb{N} + 1$ all derivatives are odd. It may also be obvious from (4.4) that the first $q < 2r + 1$, $\forall q \neq n$ terms in expression (4.3) vanish exactly, regardless the value of Δ. However, the remaining terms for which $q \geq 2r + 1$, vanish only if $\epsilon \equiv 0$. As shown in Section (2.4.1), this is no longer satisfied in discrete space where $\epsilon > 0$, since the sampling operator transforms the continuous field $u(x)$ to a discontinuous field $\overline{u}(x)$ in discrete space. Substitution of expression (4.1) into (4.3) and applying the sampling operator finally yields (with $q = k' + n$),

$$\overline{\frac{\partial^n u}{\partial x^n}}(x_i) = \frac{\delta^n \overline{u}}{\delta x^n}(x_i) - \sum_{k'=k}^{\infty} \left(\sum_{j=-r}^{r} \frac{\beta_j j^{k'+n}}{(k'+n)!} \right) \Delta^k \overline{\frac{\partial^{k'+n} u}{\partial x^{k'+n}}}(x_i), \tag{4.7}$$

where the *finite difference approximation* of the partial derivative is defined as

$$\frac{\delta^n \overline{u}}{\delta x^n}(x_i) = \frac{1}{\Delta^n} \sum_{j=-r}^{r} \beta_j \overline{u}(x_{i+j}), \tag{4.8}$$

and the series' initial index is determined by

$$k = \begin{cases} 2r + 1 - n & \forall n \in 2\mathbb{N} + 1 \\ 2r + 2 - n & \forall n \in 2\mathbb{N} \end{cases}. \tag{4.9}$$

n	β_{-5}	β_{-4}	β_{-3}	β_{-2}	β_{-1}	β_0	β_1	β_2	β_3	β_4	β_5	k
2					1	-2	1					2
				$-\frac{1}{12}$	$\frac{4}{3}$	$-\frac{5}{2}$	$\frac{4}{3}$	$-\frac{1}{12}$				4
			$\frac{1}{90}$	$-\frac{3}{20}$	$-\frac{3}{2}$	$-\frac{49}{18}$	$\frac{3}{2}$	$-\frac{3}{20}$	$\frac{1}{90}$			6
		$-\frac{1}{560}$	$\frac{8}{315}$	$-\frac{1}{5}$	$\frac{8}{5}$	$-\frac{205}{72}$	$\frac{8}{5}$	$-\frac{1}{5}$	$\frac{8}{315}$	$-\frac{1}{560}$		8
	$\frac{1}{3150}$	$-\frac{2}{403}$	$\frac{5}{126}$	$-\frac{5}{21}$	$\frac{5}{3}$	$-\frac{1086}{371}$	$\frac{5}{3}$	$-\frac{5}{21}$	$\frac{5}{126}$	$-\frac{2}{403}$	$\frac{1}{3150}$	10

Table 4.2: Explicit finite difference approximations. Explicit finite difference approximation of order k for the 2^{nd} derivative.

The remaining series expansion in (4.7), called the *truncation error*, is convergent and vanishes only when $\Delta \to 0$, whereas the first term of the truncation error is the *leading order truncation term*. Moreover, the finite difference approximation (4.8) is said to have a formal *order of accuracy k*, denoted as $\mathscr{O}\left(\Delta^k\right)$. Since $\sum_{j=-r}^{r} \frac{\beta_j j^{k'+n}}{(k'+n)!} = 0$, $\forall k' \in 2\mathbb{N}+1$, the truncation error is an even power-series in Δ. Tables 4.1, 4.2 and 4.3 give an overview of several finite difference approximations with various orders of accuracy for different derivatives. These approximations are frequently used throughout this dissertation.

When the $(k+n)^{th}$ derivative in the leading order truncation term in equation (4.7) is symmetrically discretized, a finite difference approximation of order $\mathscr{O}\left(\Delta^{k+2}\right)$ is obtained for the n^{th} derivative. Successive discretization of each new leading order truncation term with (4.7), finally results in the discrete series expansion for the n^{th} derivative

$$\overline{\frac{\partial^n u}{\partial x^n}}\left(x_i\right) = \sum_{k=0}^{\infty} \gamma_k \Delta^k \frac{\delta^{k+n}\overline{u}}{\delta x^{k+n}}\left(x_i\right), \tag{4.10}$$

where the coefficients γ_k are obtained from the combination of the various factors $\sum_{j=-r}^{r} \frac{\beta_j j^{k'+n}}{(k'+n)!}$. Since the sum of two convergent series is again convergent, the remaining truncation series after each successive discretization of the leading order truncation term in (4.7) is also convergent. This implies that the successive discretization process eventually forces the remaining leading order truncation term to zero. Hence, expression (4.10) is also convergent. Moreover, the right hand side series of expression (4.10) converges to the n^{th} partial derivative at the left hand side, when the number of grid nodes goes to infinity (which is equivalent of forcing $\Delta \to 0$), provided that $\overline{u}\left(x\right)$ is sampled with a sampling wavenumber lower than the Nyquist wavenumber such that it contains the same spectral information as the infinitely differentiable function $u\left(x\right)$. When the finite difference approximation (4.8) is interpreted as a convolution of the sampled field $\overline{u}\left(x\right)$ with a convolution kernel

n	β_{-5}	β_{-4}	β_{-3}	β_{-2}	β_{-1}	β_0	β_1	β_2	β_3	β_4	β_5	k
3				$-\frac{1}{2}$	1	0	-1	$\frac{1}{2}$				2
4				1	-4	6	-4	1				2
5			$-\frac{1}{2}$	2	$-\frac{5}{2}$	0	$\frac{5}{2}$	-2	$\frac{1}{2}$			2
6			1	-6	15	-20	15	-6	1			2
7		$-\frac{1}{2}$	3	-7	7	0	-7	7	-3	$\frac{1}{2}$		2
8		1	-8	28	-56	70	-56	28	-8	1		2

Table 4.3: Explicit finite difference approximations. Explicit finite difference approximation of order $k = 2$ for higher derivatives.

$\boldsymbol{\beta}$ that has finite support, i.e.

$$\frac{\delta^n \overline{u}}{\delta x^n}(x_i) = \boldsymbol{\beta}|_{-r}^{r} * \overline{u}(x), \tag{4.11}$$

equation (4.10) can be written as the convolution of the sampled field $\overline{u}(x)$ with a convolution kernel $\boldsymbol{\beta}$ that has an infinite stencil support, or

$$\overline{\frac{\partial^n u}{\partial x^n}}(x) = \lim_{r\to\infty} \boldsymbol{\beta}|_{-r}^{r} * \overline{u}(x). \tag{4.12}$$

As shown in Chapter 2, it follows from the Nyquist-Shannon theorem (Section 2.4.2) that

$$u(x) = 2\pi \operatorname{sinc}(\kappa_s x) * \overline{u}(x), \quad \kappa_s = \frac{2\pi}{\Delta}. \tag{4.13}$$

Thus, the n^{th} partial derivative is obtained from the previous expression as

$$\frac{\partial^n u(x)}{\partial x^n} = 2\pi \frac{\partial^n}{\partial x^n} [\operatorname{sinc}(\kappa_s x)] * \overline{u}(x). \tag{4.14}$$

Comparison of equations (4.12) and (4.14) suggests that the finite difference approximation of the n^{th} derivative converges to the n^{th} derivative of the sine cardinal function if the stencil support $2r + 1$ tends to infinity, i.e.

$$\lim_{r\to\infty} \boldsymbol{\beta}|_{-r}^{r} = 2\pi \frac{\partial^n}{\partial x^n} [\operatorname{sinc}(\kappa_s x)]. \tag{4.15}$$

This property is proven in Section 4.1.3. Taking this observation into consideration, it might be advantageous to construct finite difference operators by using *truncated* or *windowed* sinc-functions with compact stencil support. However, these *spectral difference methods* are not discussed in this dissertation.

4.1.2 Implicit Finite Difference approximations

The previous section was devoted to the construction of general explicit finite difference approximations. Although the explicit approximations are straightforward and easy to implement, they have the drawback that the stencil width, and thus the computational effort, increases proportional with the order of accuracy, i.e $k = 2r$. Therefore, Lele [50] introduced the *implicit* or *compact* finite difference approximations with compact stencil support. The definition of the implicit finite difference approximation of the n^{th} partial derivative in a node x_i, is written as

$$\lim_{\Delta\to\epsilon}\sum_{l=-q}^{q}\alpha_l\frac{\partial^n u}{\partial x^n}\left(x_{i+l}\right)=\lim_{\Delta\to\epsilon}\sum_{j=-r}^{r}\frac{\beta_j}{\Delta^n}u\left(x_{i+j}\right),\quad \epsilon=0. \tag{4.16}$$

Consider, in analogy with (4.2) the Taylor series expansion of $u\left(x_{i+j}\right)=u\left(x_i+j\Delta\right)$, respectively $\frac{\partial^n u}{\partial x^n}\left(x_{i+l}\right)=\frac{\partial^n u}{\partial x^n}\left(x_i+l\Delta\right)$ about x_i

$$u\left(x_i+j\Delta\right) = \sum_{k=0}^{\infty}\frac{\left(j\Delta\right)^k}{k!}\frac{\partial^k u}{\partial x^k}\left(x_i\right),\quad \forall j, \tag{4.17}$$

$$\frac{\partial^n u}{\partial x^n}\left(x_i+l\Delta\right) = \sum_{k'=0}^{\infty}\frac{\left(l\Delta\right)^{k'}}{k'!}\frac{\partial^{k'+n} u}{\partial x^{k'+n}}\left(x_i\right),\quad \forall l. \tag{4.18}$$

Substitution of expressions(4.17) and (4.18) into the definition (4.16) and assuming $k'=k-n$ then yields (for $\Delta\to 0$),

$$\sum_{k=n}^{\infty}\left(\sum_{l=-q}^{q}\frac{\alpha_l l^{k-n}}{(k-n)!}\right)\Delta^{k-n}\frac{\partial^k u}{\partial x^k}\left(x_i\right)=\sum_{k=0}^{\infty}\left(\sum_{j=-r}^{r}\frac{\beta_j j^k}{k!}\right)\Delta^{k-n}\frac{\partial^k u}{\partial x^k}\left(x_i\right). \tag{4.19}$$

Obviously the $2q+1$ weighting coefficients α_j and the $2r+1$ weighting coefficients β_j, are obtained by matching the Taylor series coefficients in (4.19). Hence, a set of $2r+2q+2$ equations for as much unknown coefficients must be resolved. When $z=2r+2q+1$, this translates into the matrix equation

$$\begin{bmatrix} 0 & \cdots & 0 & -\frac{(-r)^0}{0!} & \cdots & -\frac{(r)^0}{0!} \\ \vdots & & \vdots & \vdots & & \vdots \\ 0 & \cdots & 0 & -\frac{(-r)^{n-1}}{(n-1)!} & \cdots & -\frac{(r)^{n-1}}{(n-1)!} \\ \frac{(-q)^0}{0!} & \cdots & \frac{(q)^0}{0!} & -\frac{(-r)^n}{n!} & \cdots & -\frac{(r)^n}{n!} \\ \vdots & & \vdots & \vdots & & \vdots \\ \frac{(-q)^{z-n}}{(z-n)!} & \cdots & \frac{(q)^{z-n}}{(z-n)!} & -\frac{(j)^z}{(z)!} & \cdots & -\frac{(r)^z}{(z)!} \end{bmatrix}\begin{bmatrix} \alpha_{-q} \\ \vdots \\ \alpha_q \\ \beta_{-r} \\ \vdots \\ \beta_r \end{bmatrix}=\begin{bmatrix} 0 \\ \vdots \\ 0 \\ 0 \\ \vdots \\ 1 \end{bmatrix}, \tag{4.20}$$

where the final equation determines the coefficient of the leading order truncation term, here chosen as unity, and $n\leq z$ is a necessary condition in order to have a

n	α_0	$\alpha_{\pm1}$	$\alpha_{\pm2}$	β_{-3}	β_{-2}	β_{-1}	β_0	β_1	β_2	β_3	k
1	1	$\frac{1}{4}$				$-\frac{3}{4}$	0	$\frac{3}{4}$			4
	1	$\frac{1}{3}$			$-\frac{1}{36}$	$-\frac{14}{18}$	0	$\frac{14}{18}$	$\frac{1}{36}$		6
	1	$\frac{4}{9}$	$\frac{1}{36}$		$-\frac{25}{216}$	$-\frac{40}{54}$	0	$\frac{40}{54}$	$\frac{25}{216}$		8
	1	$\frac{3}{8}$		$-\frac{1}{480}$	$-\frac{1}{20}$	$-\frac{25}{32}$	0	$\frac{25}{32}$	$\frac{1}{20}$	$\frac{1}{480}$	8
	1	$\frac{1}{2}$	$\frac{1}{20}$	$-\frac{1}{600}$	$-\frac{101}{600}$	$-\frac{17}{24}$	0	$\frac{17}{24}$	$\frac{101}{600}$	$\frac{1}{600}$	10

Table 4.4: Implicit finite difference approximations. Padé-type finite difference approximation of order k for the 1^{st} derivative.

square, invertible matrix.[4] Examination of the specific structure of the matrix in (4.20) reveals that

$$\beta_{j-w} = \beta_{j+w}, \quad \forall w \in [1,r]\,,\ \forall n \in 2\mathbb{N} \tag{4.21}$$

$$\beta_{j-w} = -\beta_{j+w}, \quad \forall w \in [1,r]\,,\ \forall n \in 2\mathbb{N}+1, \tag{4.22}$$

whereas

$$\alpha_{l-w} = \alpha_{l+w}, \quad \forall w \in [1,q]\,,\ \forall n \in \mathbb{N}. \tag{4.23}$$

As a consequence, the truncation error is an even power-series in Δ which contain only even derivatives if $n \in 2\mathbb{N}$, whereas for $n \in 2\mathbb{N}+1$ it contains only odd derivatives. Finally, the *implicit* finite difference approximation for the n^{th} derivative reads

$$\sum_{l=-q}^{q} \alpha_l \overline{\frac{\partial^n u}{\partial x^n}}\,(x_{i+l}) = \sum_{j=-r}^{r} \frac{\beta_j}{\Delta^n} \overline{u}\,(x_{i+j}) - \sum_{k'=k}^{\infty} \left(\sum_{l=-q}^{q} \frac{\alpha_l l^{k'}}{(k')!} - \sum_{j=-r}^{r} \frac{\beta_j j^{k'+n}}{(k'+n)!} \right) \Delta^{k'} \frac{\partial^{k'+n} u}{\partial x^{k'+n}}\,(x_i)\,, \tag{4.24}$$

where the order of accuracy k is given by

$$k = \begin{cases} 2r+2q+1-n & \forall n \in 2\mathbb{N}+1 \\ 2r+2q+2-n & \forall n \in 2\mathbb{N} \end{cases}. \tag{4.25}$$

These implicit or compact finite difference schemes are often referred to in literature as *Padé* schemes. Tables 4.4 and 4.5 give an overview of the most common

[4] Note that the coefficient matrix (4.20) may be ill-conditioned leading to a nearly singular matrix. Nevertheless, balancing techniques exist to improve the condition number of this matrix.

n	α_0	$\alpha_{\pm1}$	$\alpha_{\pm2}$	β_{-3}	β_{-2}	β_{-1}	β_0	β_1	β_2	β_3	k
2	1	$\frac{1}{10}$				$\frac{6}{5}$	$-\frac{12}{5}$	$\frac{6}{5}$			4
	1	$\frac{2}{11}$			$\frac{3}{44}$	$\frac{12}{11}$	$-\frac{51}{22}$	$\frac{12}{11}$	$\frac{3}{44}$		6
	1	$\frac{117}{401}$	$\frac{23}{2358}$		$\frac{310}{1572}$	$\frac{320}{393}$	$-\frac{265}{131}$	$\frac{320}{393}$	$\frac{310}{1572}$		8
	1	$\frac{9}{38}$		$-\frac{23}{6840}$	$\frac{17}{190}$	$\frac{147}{152}$	$-\frac{1801}{855}$	$\frac{147}{152}$	$\frac{17}{190}$	$-\frac{23}{6840}$	8
	1	$\frac{334}{899}$	$\frac{43}{1798}$	$\frac{79}{16182}$	$\frac{173}{899}$	$\frac{1065}{1798}$	$-\frac{2211}{1400}$	$\frac{1065}{1798}$	$\frac{173}{899}$	$\frac{79}{16182}$	10

Table 4.5: Implicit finite difference approximations. Padé-type finite difference approximation of order k for the 2^{nd} derivative.

Padé approximations for the 1^{st} and 2^{nd} derivative. Note that the k^{th}-order Padé approximation (4.24) can be reformulated as

$$\sum_{l=-q}^{q} \alpha_l \overline{\frac{\partial^n u}{\partial x^n}}\,(x_{i+l}) = \sum_{j=0}^{k-2q} \beta'_j \Delta^j \frac{\delta^{j+n}\overline{u}}{\delta x^{j+n}}\,(x_i) - \sum_{k'=k}^{\infty} \left(\sum_{l=-q}^{q} \frac{\alpha_l l^{k'}}{(k')!} - \sum_{j=-r}^{r} \frac{\beta_j j^{k'+n}}{(k'+n)!} \right) \Delta^{k'} \frac{\partial^{k'+n} u}{\partial x^{k'+n}}\,(x_i)\,, \quad (4.26)$$

in which the derivatives $\frac{\delta^{j+n}\overline{u}}{\delta x^{j+n}}\,(x_i)$ are approximated with a 2^{nd} -order explicit finite difference approximation. Hence, the explicit finite difference approximation can be interpreted as a particular case of the implicit approximation with $q = 0$. Although the discussed implicit finite difference schemes have a compact stencil support, in contrast to the explicit schemes, the implicit part has to be solved by inverting the left-hand side matrix in (4.24), leading to an increase of the computational cost. Nevertheless, this may be worthwhile due to the improved accuracy in comparison with the explicit schemes, which is demonstrated in next section. The inversion is typically done iteratively using the well-known LU-decomposition or Cholesky-decomposition technique [59].[5]

4.1.3 Fourier analysis

Although the *order of accuracy* k indicates how fast the truncation series of the finite difference approximation converges to zero when $\Delta \to 0$, no direct information is retrieved about the *accuracy* itself. Therefore, the explicit and implicit finite difference approximations are examined in Fourier space in order to obtain an indication of the accuracy for each Fourier mode. The Fourier analysis provides an effective way to quantify the resolution characteristics of the difference approximations, and will prove very useful for unambiguously assessing the quality of all

[5]Note that for Cholesky-decomposition, the original matrix must be symmetric and positive-definite.

approximations, as well as for further optimization of the difference schemes [50]. In analogy with the expression of the Fourier transformation of the analytical n^{th} derivative

$$\mathscr{F}\left\{\frac{\partial^n u}{\partial x^n}\right\} = (i\kappa)^n \widehat{u}, \tag{4.27}$$

one can define the Fourier transform of a general finite difference approximation as

$$\mathscr{F}\left\{\frac{\delta^n \overline{u}}{\delta x^n}\right\} = \left(i\kappa'_n\right)^n \widehat{\overline{u}}, \tag{4.28}$$

where κ'_n denotes the *modified wavenumber*. The transfer function $\widehat{\mathscr{G}}(\kappa)$ of the finite difference operator is then defined as the ratio of (4.28) to (4.27), or

$$\widehat{\mathscr{G}}(\kappa) = \frac{{\kappa'_n}^n}{\kappa^n}. \tag{4.29}$$

The modified wavenumber and the transfer function reflect the error of the discrete approximation for a single Fourier mode with relative wavenumber κ/κ_{max}. The real part of the modified wavenumber κ'_n represents *dispersion errors* that affect the phase speed of different wave components, whereas the imaginary part represents *dissipation errors* that affect the amplitude of the wave components. Since the dissipation errors are absent for symmetric finite difference approximations, the latter are favoured for Large-Eddy Simulation in order to avoid excessive damping of the small scale structures. The modified wavenumber of a finite difference scheme is obtained by substituting the discrete wave $\overline{u}(x_{i+j}) = e^{i\kappa(x_i+j\Delta)}$ into the finite difference approximations (4.8) or (4.24). Since the explicit difference approximation can be interpreted as a particular case of the implicit difference approximation for $q = 0$, the general expression for the modified wavenumber is given by

$${\kappa'_n}^n(\kappa) = \frac{1}{i^n}\frac{\sum_{j=-r}^{r} \beta_j e^{i\kappa j\Delta}}{\sum_{l=-q}^{q} \alpha_l e^{i\kappa l\Delta}}. \tag{4.30}$$

Using the symmetry properties of the coefficients β_j and α_l, depending on the parity of n, and by means of the definitions

$$\sin(a\kappa\Delta) = \frac{e^{ia\Delta\kappa} - e^{-ia\Delta\kappa}}{2i}, \tag{4.31}$$

$$\cos(a\kappa\Delta) = \frac{e^{ia\Delta\kappa} + e^{-ia\Delta\kappa}}{2}, \tag{4.32}$$

the expression (4.30) can be split into

$$\kappa_n'^{\,n}(\kappa) = \frac{\sum_{j=1}^{r} \beta_j' \sin(j\kappa\Delta)}{\sum_{l=0}^{q} \alpha_l' \cos(l\kappa\Delta)}, \quad \forall n \in 2\mathbb{N}+1 \tag{4.33}$$

$$\kappa_n'^{\,n}(\kappa) = \frac{\sum_{j=0}^{r} \beta_j' \cos(j\kappa\Delta)}{\sum_{l=0}^{q} \alpha_l' \cos(l\kappa\Delta)}, \quad \forall n \in 2\mathbb{N}, \tag{4.34}$$

where the coefficients β_0' are determined by

$$\beta_0' = \frac{\beta_0}{i^{n-1}}, \quad \forall n \in 2\mathbb{N}+1, \tag{4.35}$$

$$\beta_0' = \frac{\beta_0}{i^{n}}, \quad \forall n \in 2\mathbb{N}, \tag{4.36}$$

and β_j' by

$$\beta_j' = \frac{2\beta_j}{i^{n-1}}, \quad \forall n \in 2\mathbb{N}+1,\ \forall j > 0 \tag{4.37}$$

$$\beta_j' = \frac{2\beta_j}{i^{n}}, \quad \forall n \in 2\mathbb{N},\ \forall j > 0, \tag{4.38}$$

whereas α_l' are obtained by

$$\alpha_0' = \alpha_0, \quad \forall n \tag{4.39}$$

$$\alpha_l' = 2\alpha_l, \quad \forall n,\ \forall l > 0. \tag{4.40}$$

Note that in case of the explicit finite difference approximations the denominator reduces to unity, i.e. $q = 0$ and $\alpha_0 = 1$. A selection of modified wavenumbers for explicit and implicit finite difference approximations for the 1^{st} and 2^{nd} derivative is depicted in Figures 4.2 and 4.3.

As mentioned before, the dispersion errors in central difference approximation, represented by the real part of the modified wavenumber, affect the phase speed of each Fourier mode. In multi-dimensional problems the phase errors related to the adopted finite difference approximation also appear in the form of anisotropy [50]. Indeed, the finite difference approximations induce not only different phase speeds for different Fourier modes, but also for different orientations of these modes. Following Lele [50], the anisotropic Fourier mode propagation on a two-dimensional

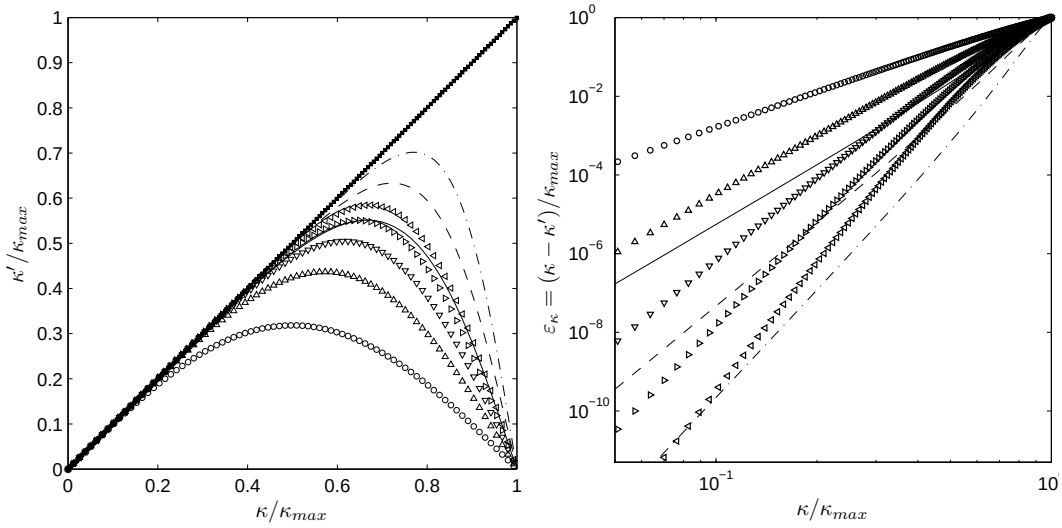

Figure 4.2: Modified wavenumbers of finite difference approximations. The modified wavenumber $\kappa_1'(\kappa)$ (**left**) and the normalized dispersion error (**right**) for the 1^{st} derivative: 2^{nd} ($\circ$), 4^{th} ($\triangle$), 6^{th} ($\triangledown$), 8^{th} ($\triangleright$), 10^{th} ($\triangleleft$) -order explicit approximations, and 4^{th} (——), 6^{th} (– – –), 8^{th} ($-\cdot-\cdot$) order Padé approximations.

computational grid, is represented by the transfer function

$$\widehat{\mathscr{G}}(\kappa,\phi) = \frac{\cos(\phi)\,\kappa_n'(\kappa\cos(\phi)) + \sin(\phi)\,\kappa_n'(\kappa\sin(\phi))}{\kappa}, \tag{4.41}$$

where ϕ denotes the angle between the propagation direction and the first Cartesian direction x_1. Figures 4.4 and 4.5 show $\widehat{\mathscr{G}}(\kappa,\phi)$ for a selection of implicit and explicit finite difference approximations for the 1^{st} derivative.

Since the modified wavenumbers κ_n' converge to the exact wavenumber κ with increasing order of accuracy, the corresponding transfer functions (4.29) converge in this limit to the Heaviside function such that

$$\lim_{k\to\infty} \widehat{\mathscr{G}}(\kappa) = \mathrm{H}(\kappa - \kappa_{max}), \tag{4.42}$$

where k denotes the order of accuracy, determined by the number of nodes in the difference approximation. This is displayed in Figure 4.6. By definition the previous expression implies that

$$\widehat{u}(x) = \lim_{k\to\infty} \widehat{\mathscr{G}}(\kappa)\,\widehat{\overline{u}}(x) = \mathrm{H}(\kappa - \kappa_{max})\,\widehat{\overline{u}}(x), \tag{4.43}$$

such that the inverse Fourier transform yields

$$u(x) = 2\pi\,\mathrm{sinc}(2\kappa_{max}x) * \overline{u}(x). \tag{4.44}$$

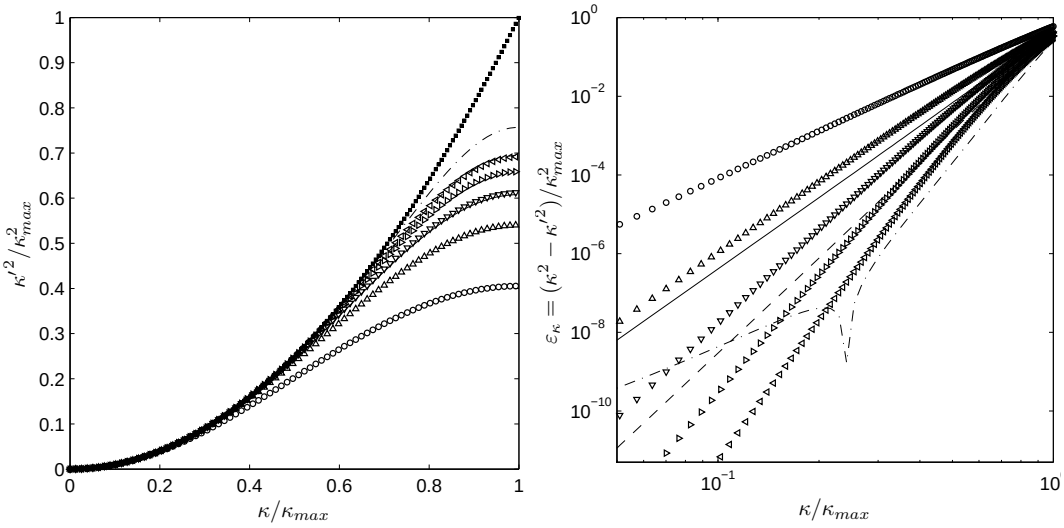

Figure 4.3: Modified wavenumbers of finite difference approximations. The modified wavenumber ${\kappa'_2}^2(\kappa)$ (**left**) and the normalized dispersion error (**right**) for the 2^{nd} derivative: : 2^{nd} ($\circ$), 4^{th} ($\triangle$), 6^{th} ($\triangledown$), 8^{th} ($\triangleright$), 10^{th} ($\triangleleft$) -order explicit approximations, and 4^{th} (——), 6^{th} ($---$), 8^{th} ($-\cdot-\cdot$) -order Padé approximations.

Hence, each finite difference approximation is equivalent with the analytical derivative of a polynomial interpolation function which converges to the exact sine cardinal interpolation function that follows from the Nyquist-Shannon theorem, if the order of accuracy tends to infinity. This conclusion corresponds with the previously obtained expression (4.14). However, in reality, the stencil support is always finite. As a consequence, the finite difference approximations of the partial derivatives induce an implicit filtering of the velocity field and the corresponding energy spectrum. In order to minimize this effect, higher order finite difference approximations are favoured over lower order approximations in delicate numerical computations such as Large-Eddy Simulation. Moreover, it may be clear that explicit filtering of the nonlinear term in an LES formulation with double decomposition is certainly advantageous, since the Fourier modes in the range $\frac{2}{3}\kappa_{max} \leq \kappa \leq \kappa_{max}$, which are mostly affected by the numerics, are eliminated. Since only the reliable scales are preserved whereas the unreliable scales are removed, the accuracy of the simulation should improve. This is confirmed by the work of Lund *et al.* [56, 55], Gullbrand *et al.* [35, 36], Brandt *et al.* [9, 10] and recently Berland *et al.* [4], who found that explicit filtering in LES, allows to reduce the numerical errors since the dispersion errors, dissipation errors and various commutation errors in the high-wavenumber region are eliminated from the solution.

Note that it is possible to mimic finite difference approximations by transforming the velocity field $u(x)$ to Fourier space, multiplying it with the modified wavenum-

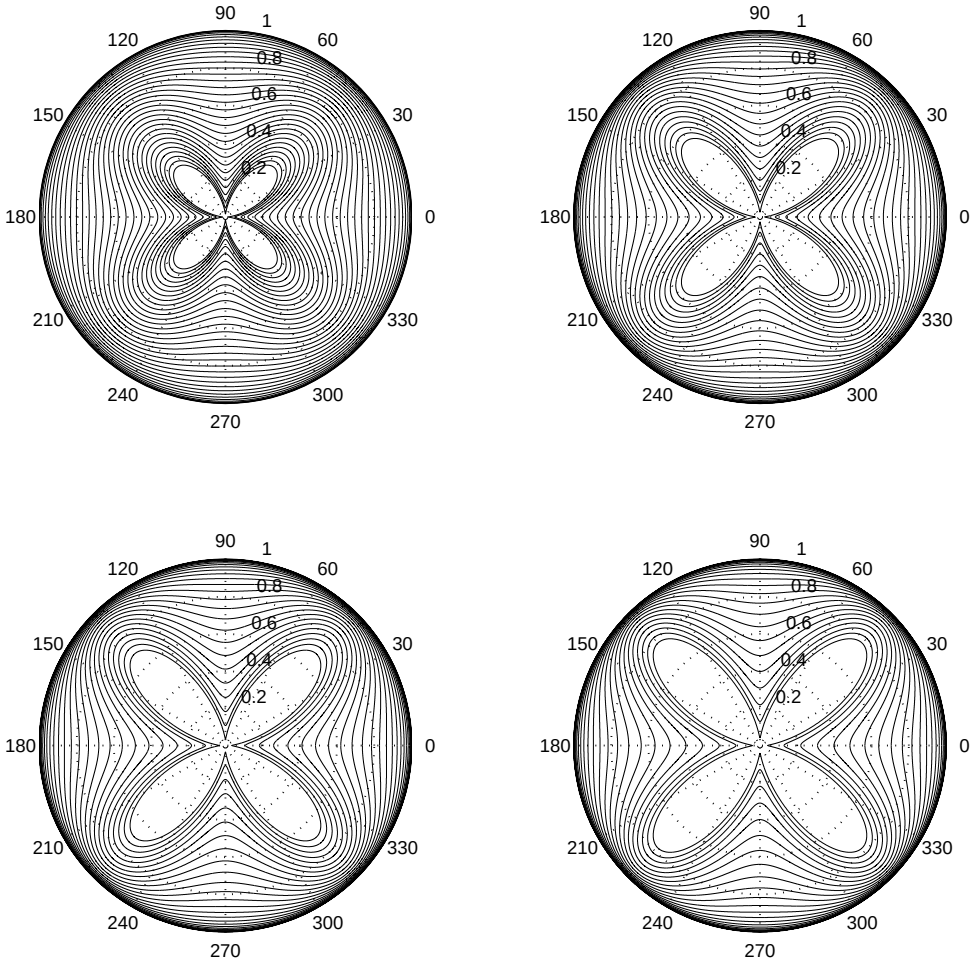

Figure 4.4: Polar plot of the phase speed anisotropy of the 1^{st} derivative. Transfer function $\mathscr{G}(\kappa, \phi)$ indicating the anisotropy induced by the 2^{nd} - (**upper left**), 4^{th} - (**upper right**), 6^{th} - (**lower left**) and 8^{th} - (**lower right**) order explicit finite difference approximation.

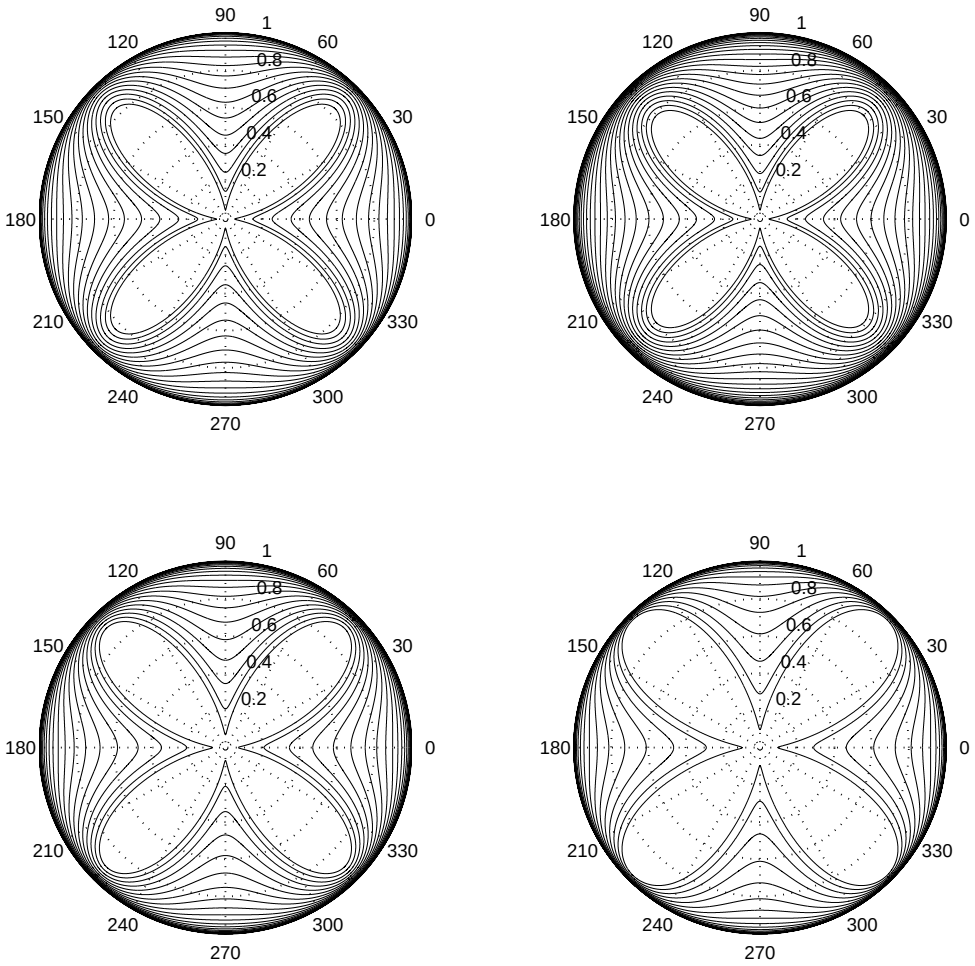

Figure 4.5: Polar plot of the phase speed anisotropy of the 1^{st} derivative. Transfer function $\widehat{\mathscr{G}}(\kappa, \phi)$ indicating the anisotropy induced by the 10^{th} -order explicit finite difference approximation (**upper left**) and the 4^{th} - (**upper right**), 6^{th} - (**lower left**) and 8^{th} - (**lower right**) order implicit finite difference approximations.

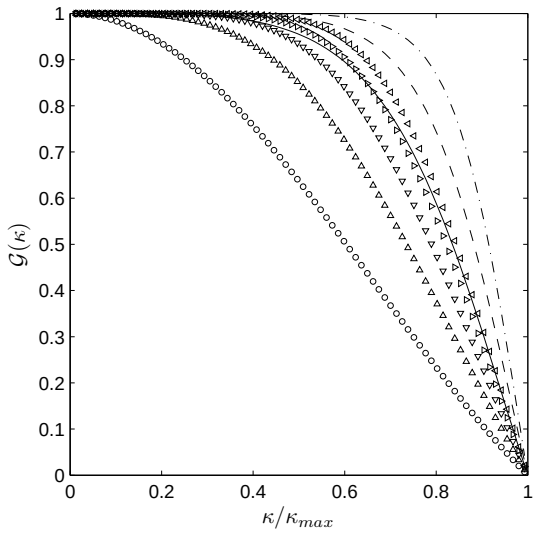

Figure 4.6: Transfer function for various finite difference approximations. The transfer function $\widehat{\mathscr{G}}(\kappa)$ of the 1^{st} derivative.

ber, as in expression (4.28), and transforming it back to physical space. Although this technique is restricted to periodic domains only, it is used in this dissertation as a fast and practical tool to perform various finite difference calculations.

4.1.4 FINITE DIFFERENCE FILTERS

In this dissertation, the sharp cutoff filter is advocated as the optimal explicit filter in the context of Large-Eddy simulation with the double decomposition. However, since the *sinc* kernel is non-local in physical space, its implementation would require an infinite number of nodes in the computational domain. Therefore, the sharp cutoff filter needs to be approximated in order to be applicable for numerical computations. In analogy with the partial derivatives, various explicit and implicit finite difference approximations for the sharp-cutoff filter are constructed. Considering again the explicit approximations as a particular case of the implicit approximations, the general *symmetric* k^{th}-order finite difference approximation of a filter [50, 83] is defined as

$$\sum_{l=-q}^{q} \alpha_l \widetilde{\phi}\left(x_{i+l}\right) = \sum_{j=-r}^{r} \beta_j \phi\left(x_{i+j}\right) + \mathscr{O}\left(\Delta^k\right), \tag{4.45}$$

where $\widetilde{\phi}(x)$ denotes a filtered discrete variable in $\mathbb{R}$. It is advantageous to design the filters in Fourier space in order to control directly the spectral characteristics of the

n	m	α_0	$\alpha_{\pm1}$	$\alpha_{\pm2}$	$\alpha_{\pm3}$	β_0	$\beta_{\pm1}$	$\beta_{\pm2}$	$\beta_{\pm3}$	$\beta_{\pm4}$
3	1	1				$\frac{47}{72}$	$\frac{35}{144}$	$-\frac{11}{144}$	$\frac{1}{144}$	
1	1	$\frac{2}{3}$	$\frac{1}{6}$			$\frac{1}{2}$	$\frac{1}{4}$			
3	1	$\frac{5}{6}$	$\frac{1}{12}$			$\frac{7}{12}$	$\frac{1}{4}$	$-\frac{1}{24}$		
5	3	$\frac{49}{120}$	$\frac{13}{60}$	$\frac{19}{240}$		$\frac{11}{30}$	$\frac{119}{480}$	$\frac{1}{15}$	$\frac{1}{480}$	
7	5	$\frac{205}{624}$	$\frac{43}{192}$	$\frac{41}{416}$	$\frac{11}{832}$	$\frac{206}{655}$	$\frac{234}{995}$	$\frac{29}{312}$	$\frac{13}{877}$	$-\frac{1}{4992}$

Table 4.6: Finite difference approximations for the sharp cutoff filter. Explicit and Padé-type finite difference approximation for the sharp cutoff filter with cutoff wavenumber $\kappa_c = \frac{2}{3}\kappa_{max}$.

approximation, which are obviously most important. The transfer function $\widehat{\mathscr{G}}(\kappa)$

$$\widehat{\mathscr{G}}(\kappa) = \frac{\sum_{j=-r}^{r} \beta_j e^{i\kappa j\Delta}}{\sum_{l=-q}^{q} \alpha_l e^{i\kappa l\Delta}} = \frac{\sum_{j=-r}^{r} \beta_j \left[\cos(j\kappa\Delta) + i\sin(j\kappa\Delta)\right]}{\sum_{l=-q}^{q} \alpha_l \left[\cos(l\kappa\Delta) + i\sin(l\kappa\Delta)\right]}, \tag{4.46}$$

of a filter, is obtained by substituting the discrete wave $\phi(x_{i+j}) = e^{i\kappa(x_i+j\Delta)}$ into the finite difference approximations (4.45). In accordance with the normalization condition (3.4), the transfer function (4.46) requires that

$$\widehat{\mathscr{G}}(0) = 1, \tag{4.47}$$

expressing the conservation of a constant. Moreover, it is desirable to have a filter characteristic that vanishes at κ_{max} in order to strictly satisfy the Nyquist criterion, such that

$$\widehat{\mathscr{G}}(\kappa_{max}) = 0. \tag{4.48}$$

Since the sharp cutoff filter is uniquely characterized by the cutoff wavenumber κ_c, it is necessary to impose an additional condition that determines the cutoff wavenumber of the smooth finite difference approximations of the filter. Typically, the cutoff wavenumber of a smooth filter is defined as[6]

$$\widehat{\mathscr{G}}(\kappa_c) = \frac{1}{2}. \tag{4.49}$$

Although conditions (4.47), (4.48) and also (4.49) form the minimum number of constraints that need to be imposed on the filter, it can be understood that additional

[6] Other definitions are possible.

conditions are required which allow to control the *sharpness* of the finite difference approximation to the ideal sharp cutoff filter. The sharpness is determined by the number of *vanishing moments* [50, 83] of the transfer function at $\kappa = 0$ and $\kappa = \kappa_{max} = \frac{\pi}{\Delta}$ [50], i.e.

$$\frac{\partial^n \widehat{\mathscr{G}}}{\partial \kappa^n}\left(a\frac{\pi}{\Delta}\right) = 0, \quad \forall n > 0,\ a = 0, 1 \tag{4.50}$$

Using *Leibniz' rule*, this set of constraints is worked out as

$$\sum_{k=0}^{n}\left\{\frac{n!}{k!\,(n-k)!}\left[\sum_{l=-q}^{q}\alpha_l\,(il\Delta)^{n-k}\,e^{ia\pi l}\right]\frac{\partial^k \widehat{\mathscr{G}}}{\partial \kappa^k}\left(a\frac{\pi}{\Delta}\right)\right\} = \sum_{j=-r}^{r}\beta_j\,(ij\Delta)^n\,e^{ia\pi j}, \quad \forall n > 0,\ a = 0, 1. \tag{4.51}$$

Assuming that for $a = 0$, the moments $1, 2 \ldots n$ vanish, i.e. derivatives $1, 2 \ldots n$ are zero, expression (4.51) reduces to

$$\widehat{\mathscr{G}}\,(0)\sum_{l=-q}^{q}\alpha_l\,(il\Delta)^n = \sum_{j=-r}^{r}\beta_j\,(ij\Delta)^n, \quad \forall n > 0. \tag{4.52}$$

Analogously, assuming that for $a = 1$, the moments $1, 2 \ldots m$ vanish, i.e. derivatives $1, 2 \ldots m$ are zero, expression (4.51) reduces to

$$\widehat{\mathscr{G}}\left(\frac{\pi}{\Delta}\right)\sum_{l=-q}^{q}\alpha_l\,(il\Delta)^m\,e^{i\pi l} = \sum_{j=-r}^{r}\beta_j\,(ij\Delta)^m\,e^{i\pi j}, \quad \forall m > 0. \tag{4.53}$$

Substitution of constraints (4.47) and (4.48) into equations (4.52) and (4.53) finally yields

$$\sum_{l=-q}^{q}\alpha_l l^n - \sum_{j=-r}^{r}\beta_j j^n = 0, \quad \forall n > 0 \tag{4.54}$$

$$\sum_{j=-r}^{r}\beta_j j^m \cos(j\pi) = 0, \quad \forall m > 0. \tag{4.55}$$

In order to determine the $2r + 2q + 2$ coefficients β_j and α_l, an equal amount of independent equations are required from the basic constraints (4.47), (4.48) and (4.49) and from the vanishing moments (4.54-4.55). With $\theta = \kappa_c/\kappa_{max}$, this set of

n	m	α_0	$\alpha_{\pm1}$	$\alpha_{\pm2}$	$\alpha_{\pm3}$	β_0	$\beta_{\pm1}$	$\beta_{\pm2}$	$\beta_{\pm3}$	$\beta_{\pm4}$
1	3	1				$\frac{25}{72}$	$\frac{35}{144}$	$\frac{11}{144}$	$\frac{1}{144}$	
1	1	2	$-\frac{1}{2}$			$\frac{1}{2}$	$\frac{1}{4}$			
1	3	$\frac{5}{4}$	$-\frac{1}{8}$			$\frac{3}{8}$	$\frac{1}{4}$	$\frac{1}{16}$		
3	5	$\frac{49}{16}$	$-\frac{13}{8}$	$\frac{19}{32}$		$\frac{5}{16}$	$\frac{15}{64}$	$\frac{3}{32}$	$\frac{1}{64}$	
5	7	$\frac{205}{32}$	$-\frac{559}{128}$	$\frac{123}{64}$	$-\frac{33}{128}$	$\frac{35}{128}$	$\frac{7}{32}$	$\frac{7}{64}$	$\frac{1}{32}$	$\frac{1}{256}$

Table 4.7: Finite difference approximations for the sharp cutoff filter. Explicit and Padé-type finite difference approximation for the sharp cutoff filter with cutoff wavenumbers $\kappa_c = \frac{1}{3}\kappa_{max}$.

equations can be written as the matrix equation

$$\begin{bmatrix} 1 & \cdots & 1 & -1 & \cdots & -1 \\ 0 & \cdots & 0 & \cos(-r\pi) & \cdots & \cos(r\pi) \\ \cos(-q\theta\pi) & \cdots & \cos(q\theta\pi) & -2\cos(-r\theta\pi) & \cdots & -2\cos(r\theta\pi) \\ \sin(-q\theta\pi) & \cdots & \sin(q\theta\pi) & -2\sin(-r\theta\pi) & \cdots & -2\sin(r\theta\pi) \\ (-q)^1 & \cdots & (q)^1 & (-r)^1 & \cdots & (r)^1 \\ \vdots & & \vdots & \vdots & & \vdots \\ (-q)^n & \cdots & (q)^n & (-r)^n & \cdots & (r)^n \\ 0 & \cdots & 0 & (-r)^1\cos(-r\pi) & \cdots & (r)^1\cos(r\pi) \\ \vdots & & \vdots & \vdots & & \vdots \\ 0 & \cdots & 0 & (-r)^m\cos(-r\pi) & \cdots & (r)^m\cos(r\pi) \end{bmatrix} \begin{bmatrix} \alpha_{-q} \\ \vdots \\ \alpha_q \\ \beta_{-r} \\ \vdots \\ \beta_r \end{bmatrix} = \begin{bmatrix} 0 \\ \vdots \\ 0 \\ 0 \\ \vdots \\ 1 \end{bmatrix} \tag{4.56}$$

where $m + n = 2r + 2q - 2$. Note that the last equation determines the leading order truncation term of the filter. Since the number of vanishing moments at the origin and at the cutoff influences the shape of the resulting transfer function, the parameters n and m need to be selected carefully in order to guarantee the monotonicity, with increasing wavenumber κ, of the transfer function. Overshoots or undershoots of the transfer function are not desirable since it leads to unphysical filtering behaviour. Due to the specific structure of the coefficient matrix in (4.56), all coefficients β_j and α_l are symmetric, i.e. $\beta_j = \beta_{-j}$ and $\alpha_j = \alpha_{-j}$. Hence, the imaginary part of the transfer function vanishes and the resulting symmetric filters only affect the amplitude of the signal ϕ. Asymmetric filters on the contrary, also induce a phase shift. Although symmetric filters are preferable, it may be necessary to use asymmetric filters at the boundaries. Table 4.6 gives an overview of various symmetric finite difference approximations for the sharp cutoff filter with $\kappa_c = \frac{2}{3}\kappa_{max}$, used for de-aliasing, whereas Table 4.7 gives some approximations for the sharp cutoff filter with $\kappa_c = \frac{1}{3}\kappa_{max}$, used in the dynamic procedure or for scale separation in multiscale modeling. The corresponding transfer functions are displayed in Figure 4.7. It can be seen that the finite difference approximations for

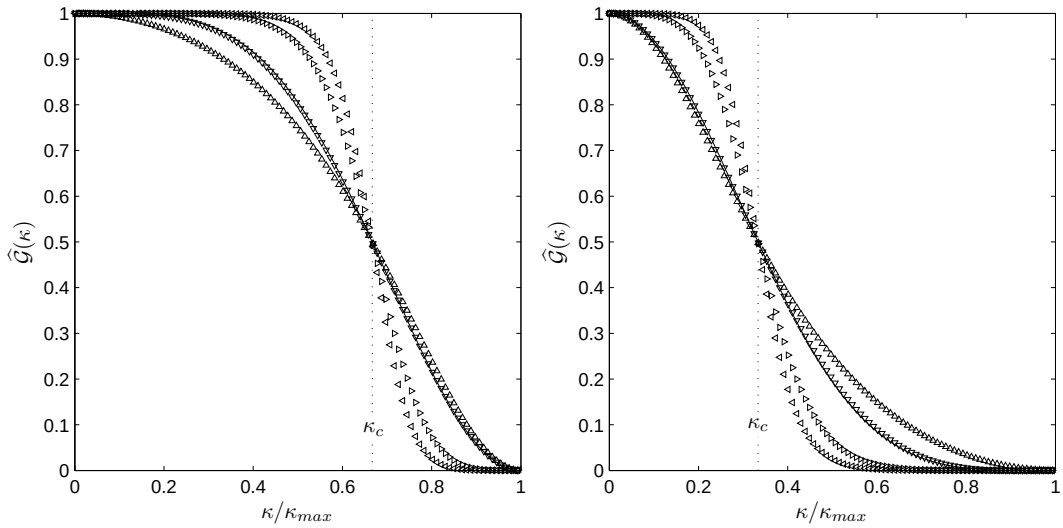

Figure 4.7: Transfer functions of sharp cutoff filter approximations. Transfer function $\widehat{\mathscr{G}}(\kappa)$ of explicit and implicit finite difference approximations for sharp cutoff filter with $\kappa_c = \frac{2}{3}\kappa_{max}$ (**left**) and $\kappa_c = \frac{1}{3}\kappa_{max}$ (**right**). $q = 0$, $r = 3$ (———), $q = 1$, $r = 1$ (△), $q = 1$, $r = 2$ (▽), $q = 2$, $r = 3$ (▷), $q = 3$, $r = 4$ (◁).

the sharp cutoff filter with $\kappa_c = \frac{2}{3}\kappa_{max}$ deviate significantly from the ideal filter. This implies that de-aliasing with these filters is only approximate since the orthogonality condition is not completely satisfied. For the same reason, the scales at $\kappa \leq \kappa_c$ are affected by the filter, especially close to the cutoff wavenumber. Nevertheless, the pentadiagonal and heptadiagonal filter approximations seems to be sufficiently accurate for real computations. Finally, Vasilyev *et al.* [83] showed that in order to perform a consistent derivation of the discrete LES-equations on a non-uniform grid using coordinate transformations, the filter requires at least $k-1$ vanishing moments at $\kappa = 0$ if the adopted finite difference approximation for the derivatives is of order k, such that the commutation error of the filter with the derivatives is also $\mathscr{O}\left(\Delta^k\right)$.

4.1.5 Boundary treatment

So far, only *symmetric* or *central* finite difference approximations were considered. Although these simple schemes display good performance, their application is restricted to the interior domain away from the boundaries. In the vicinity of boundaries alternative finite difference approximations for the derivatives must be defined. Here, three such boundary methods are briefly discussed.

i. One of the most pragmatic solutions to the problem of boundary discretization consists of reducing the order of accuracy, and thus the stencil width, of the central finite difference approximations when approaching the boundary.

n	β_{-4}	β_{-3}	β_{-2}	β_{-1}	β_0	β_1	β_2	β_3	β_4	k
1			$\frac{1}{12}$	$-\frac{2}{3}$	0	$\frac{2}{3}$	$-\frac{1}{12}$			4
				$-\frac{1}{4}$	$-\frac{5}{6}$	$\frac{3}{2}$	$-\frac{1}{2}$	$\frac{1}{12}$		4
		$-\frac{1}{12}$	$\frac{1}{2}$	$-\frac{3}{2}$	$\frac{5}{6}$	$\frac{1}{4}$				4
					$-\frac{25}{12}$	4	-3	$\frac{4}{3}$	$-\frac{1}{4}$	4
	$\frac{1}{4}$	$-\frac{4}{3}$	3	-4	$\frac{25}{12}$					4

Table 4.8: Asymmetric finite difference approximations for boundaries. Explicit asymmetric 4^{th} -order finite difference discretization for the 1^{st} derivative near a boundary.

Although this method allows one to maintain the non-dissipative symmetric finite difference approximations in the near vicinity of the boundary,[7] it does not provide an adequate solution for the evaluation of higher derivatives, filters with broad stencil support or derivatives at the boundary node. Moreover, since the order of accuracy is reduced in the boundary regions where typically large gradients appear, this method affects the overall accuracy of the computation.

ii. A more refined solution is to design asymmetric finite difference approximations in the vicinity of the boundaries. Since their construction is similar to that of the symmetric finite difference approximations, the derivation procedure is not repeated here. Table 4.8 gives an example of some asymmetric 4^{th} -order finite difference approximations for the 1^{st} derivative. Although this method is fully consistent and preserves the overall order of accuracy, an important drawback occurs. Aside from dispersive errors, dissipative errors occur due to the asymmetric definitions. Indeed, it can be verified that the modified wavenumber has now a real and imaginary part. Both dispersive and dissipative parts of the modified wavenumber are displayed in Figure 4.8. It can be seen that for the 2-point eccentric 4^{th} -order finite difference approximation, both the numerical dispersion and the numerical dissipation become very large in the range $\kappa \geq 0.5\kappa_{max}$. Nevertheless, numerical quality can be guaranteed if $\kappa \leq 0.2\kappa_{max}$. It should be emphasized that the accuracy further reduces for higher order asymmetric approximations. The more eccentricity, the more numerical dissipation and dispersion. Hence, very fine grids are needed in the boundary vicinity in order to control numerical quality.

iii. An alternative implementation of the previous method makes use of ghost-nodes outside the computational domain in order to evaluate the central finite

[7] The 1^{st} and 2^{nd} derivatives are then evaluated up to the first grid node near the boundary using symmetric finite difference approximations. In the first grid node near the wall, the finite difference approximation reduces to 3-point 2^{nd} -order central approximation.

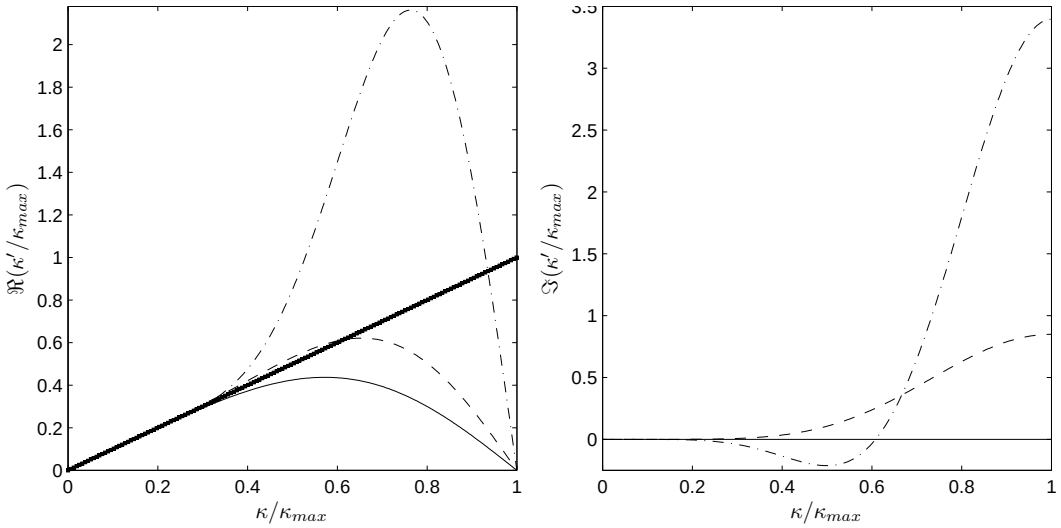

Figure 4.8: Modified wavenumber of asymmetric finite difference approximations. The real part (**left**) and imaginary part (**right**) of the modified wavenumber of a 4^{th} -order finite difference discretization for the 1^{st} derivative near a boundary. Symmetric (——), 1-point eccentric (− − −) and 2-point eccentric (−·−·) .

difference approximations in the boundary region. The required values at the ghost-nodes are then obtained by extrapolating the node values in the interior domain. Typically, locally fitted polynomial functions or spline functions are used in order to predict the value of the ghost-nodes. If the order of accuracy of the extrapolating polynomial is equal to that of the central scheme, a corresponding eccentric boundary scheme with the same order of accuracy is obtained. However, if the order of accuracy of the extrapolating polynomial is lower than that of the central scheme, the order of the eccentric scheme is not maintained and the method reduces to a combination of both previous boundary methods.

In this work, the asymmetric finite difference approximations are preferred, since this technique is believed to be consistent and most common.

4.2 Temporal Discretization: Runge-Kutta Method

Aside from the spatial discretization, the governing Navier-Stokes (2.2) equations also require temporal discretization, in order to integrate the solution in time. Consider the spatially discretized Navier-Stokes equations

$$\frac{\partial \overline{u}_i}{\partial t} = \mathscr{N}\left(\overline{u}_i, \overline{p}\right), \tag{4.57}$$

where the *Navier-Stokes operator* $\mathscr{N}(\overline{u}_i, \overline{p})$ is defined as

$$\mathscr{N}(\overline{u}_i, \overline{p}) = -\overline{u}_j \frac{\delta \overline{u}_i}{\delta x_j} - \frac{\delta \overline{p}}{\delta x_i} + \nu \frac{\delta^2 \overline{u}_i}{\delta x_j^2} + \frac{\delta \overline{\tau}_{ij}}{\delta x_j}. \tag{4.58}$$

The definition for the time derivative, called the *Euler method*, approximates the temporal derivative as

$$\frac{\partial \overline{u}_i}{\partial t}(t + \Delta t) = \lim_{\Delta t \to 0} \frac{\overline{u}_i^{t+1} - \overline{u}_i^t}{\Delta t}, \tag{4.59}$$

where the superscript indices denote the value of $\overline{u}_i$ at the old time t and the new time $t + 1$. This asymmetric definition provides an explicit expression for $\overline{u}_i^{t+1}$ at the new time level as function of $\overline{u}_i^t$ at the previous time level, i.e.

$$\overline{u}_i^{t+1} = \overline{u}_i^t + \Delta t \mathscr{N}(\overline{u}_i, \overline{p}) + \mathscr{O}(\Delta t). \tag{4.60}$$

It can be verified using Taylor series expansion that this approximation is only first order accurate in time. In analogy with the spatial discretization, it is possible to obtain higher order definitions involving earlier time levels. Although higher order accuracy is then obtained, these definitions lead to rapidly increasing memory requirements since a number of variables obtained at earlier time levels must be stored. Therefore these methods are not often used in practice.

Alternatively, higher order accuracy can be achieved by performing several Euler *stages* per time step without excessive memory requirements. Most familiar, are the low-storage explicit *Runge-Kutta* methods that require only two storage locations for one variable. The explicit *q-stage Runge-Kutta method* advances the solution from time level t to $t + 1$ by applying the recursive formula

$$\overline{u}_i^{t+\frac{j}{q}} = \overline{u}_i^t + \alpha_j \Delta t \mathscr{N}\left(\overline{u}_i^{t+\frac{j-1}{q}}, \overline{p}^{t+\frac{j-1}{q}}\right), \quad \forall j = 1, 2 \ldots q \tag{4.61}$$

where the index $t + \frac{j}{q}$ denotes the intermediate time level and α_j are the coefficients specific to the adopted method. These coefficients are obtained by assuming that $\mathscr{N}(\overline{u}_i, \overline{p})$ is a linear operator. Then substitution of (4.57) into (4.61) yields

$$\overline{u}_i^{t+1} = \overline{u}_i^t + \sum_{r=1}^{q} \prod_{j=q-r+1}^{q} \alpha_j \Delta t^r \frac{\partial^r \overline{u}_i^t}{\partial t^r}, \tag{4.62}$$

which corresponds to the classical truncated Taylor series expansion. Hence, matching the coefficients α_j gives

$$\prod_{j=q-r+1}^{q} \alpha_j = \frac{1}{r!}, \tag{4.63}$$

which results for a 4-stage standard Runge-Kutta method into the set

$$\alpha_1 = 1/4, \quad \alpha_2 = 1/3, \quad \alpha_3 = 1/2, \quad \alpha_4 = 1. \tag{4.64}$$

It can be verified that the 4-stage standard Runge-Kutta method is 4^{th} -order accurate if $\mathscr{N}(\overline{u}_i, \overline{p})$ is a linear operator. However, since $\mathscr{N}(\overline{u}_i, \overline{p})$ is obviously a strongly nonlinear operator, the method is only 2^{nd} -order accurate as is any low-storage Runge-Kutta method of this kind [6]. Following the work of *Hu et al.* [39] and *Bogey et al.* [6] and assuming $\mathscr{N}(\overline{u}_i, \overline{p})$ linear, the accuracy of a low-storage q-stage Runge-Kutta method can be obtained through Fourier analysis. Consider the temporal Fourier transform of expression (4.62)

$$\widehat{\overline{u}}_i^{t+1} = \widehat{\overline{u}}_i^{t} \left[1 + \sum_{r=1}^{q} \frac{1}{r!} \Delta t^r \left(i\omega \right)^r \right], \tag{4.65}$$

where ω denotes the time frequency of the velocity field and $\widehat{\overline{u}}$ denotes the temporal Fourier mode of the spatially sampled field $\overline{u}$. The *amplification factor* is now defined as

$$\widehat{\mathscr{G}}(\omega) = \frac{\widehat{\overline{u}}_i^{t+1}}{\widehat{\overline{u}}_i^{t}} = 1 + \sum_{r=1}^{q} i^r \frac{\pi^r}{r!} \left(\frac{\omega}{\omega_{max}} \right)^r, \tag{4.66}$$

where $\omega_{max} = \pi / \Delta t$ denotes the Nyquist frequency of the time discretization. The magnitude of the amplification factor, given by

$$\left| \widehat{\mathscr{G}}(\omega) \right| = \sqrt{\Re\left(\widehat{\mathscr{G}}(\omega) \right)^2 + \Im\left(\widehat{\mathscr{G}}(\omega) \right)^2}, \tag{4.67}$$

indicates the dissipation error, whereas the modified frequency of the amplification factor, given by

$$\omega^* = \arctan\left(\frac{\Im\left(\widehat{\mathscr{G}}(\omega) \right)}{\Re\left(\widehat{\mathscr{G}}(\omega) \right)} \right), \tag{4.68}$$

indicates the dispersion or phase error. Both the amplitude and the modified frequency are displayed in Figure 4.9 for the 2-, 3- and 4-stage Runge-Kutta methods. Obviously, the Runge-Kutta methods perform poor for large frequency ratio's ω/ω_{max}. In order to ensure numerical quality in linear problems, e.g. the 4-stage method requires approximately $\omega < 0.2\omega_{max}$. However, since the operator $\mathscr{N}(\overline{u}_i, \overline{p})$ is strongly nonlinear, the accuracy of the 4-stage Runge-Kutta method reduces to 2^{nd} -order. Hence, in order to ensure the numerical quality, it might be advantageous to decrease the frequency ratio, e.g. to a value of approximately $\omega < 0.1\omega_{max}$.

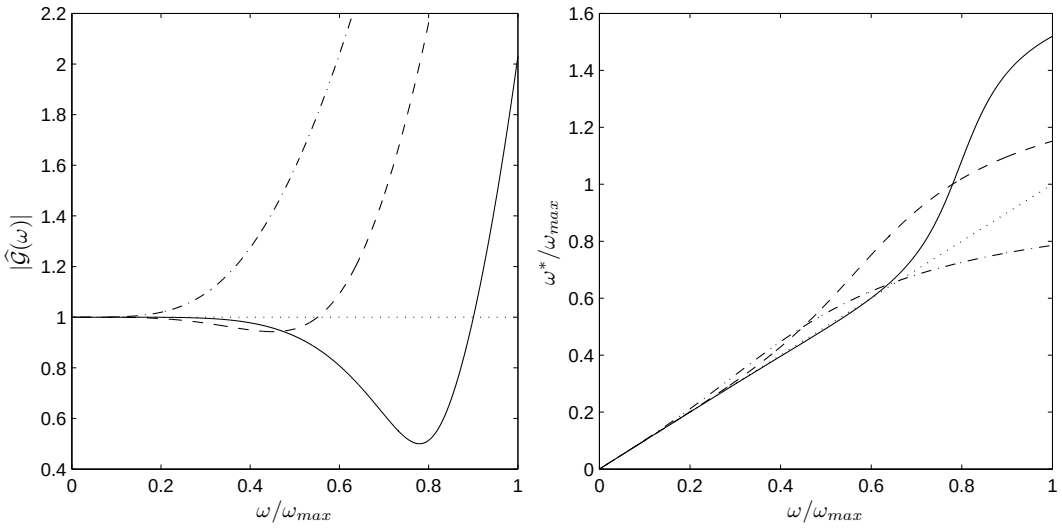

Figure 4.9: Dissipation and dispersion of a q-stage Runge-Kutta method. The dissipation errors of the q-stage Runge-Kutta method are visible from the magnitude $\left|\widehat{\mathscr{G}}(\omega)\right|$ (**left**), whereas the dispersion errors are visible from the modified frequency ω^* (**right**). 2-stage ($-\cdot-\cdot$), 3-stage ($---$), 4-stage (——).

Nevertheless, $\omega < 0.2\omega_{max}$ implies that the time increment Δt should be at least 10 times smaller than the smallest physical time scale in the turbulent flow, which is the Kolmogorov time scale $\tau_\eta = \eta^2/\nu$. The Kolmogorov time scale represents the unit of time needed for the energy in the Kolmogorov scales to be entirely dissipated. This is in accordance with the values suggested by *Pope* [70] as discussed in Section 2.4.4.

4.3 Numerical algorithms

The previous sections were devoted to the discussion of spatial and temporal discretization methods, which form the basic ingredients for the numerical procedure or *algorithm* for solving the Navier-Stokes equations and the continuity or Poisson equation. Two specific algorithms are applied in this work, i.e. the *Pseudo-Compressibility algorithm* or *Artificial Compressibility algorithm* and the *Pressure-Correction algorithm*. Before both methods are introduced, some particular implementation issues related to *energy conserving discretizations* and *odd-even decoupling* are discussed.

4.3.1 Conservative discretization

Although the conservation of mass, momentum and kinetic energy are a consequence of the analytical *inviscid* Navier-Stokes equations supplemented with the continuity equation, these conservation properties are not necessarily guaranteed

for the discrete set of equations. In Direct Numerical Simulations and Large-Eddy Simulations, the kinetic energy conservation of the nonlinear term is desirable in order to avoid harmful numerical dissipation on the small scales and preclude instability of the algorithms due to spurious energy pile-up, as argued by Morinishi *et al.* [65]. Typically, central finite difference approximations for the partial derivatives are preferred, since these schemes are non-dissipative. However, to ensure *a priori* the conservation of kinetic energy, the central discretization of the nonlinear convective term needs special attention. The vector field $u_i(x)$, $x \in \mathbb{R}$ is said to be *locally* conserved if it is *solenoidal* or *divergence-free*,[8] i.e.

$$\frac{\partial u_i}{\partial x_i} = 0, \tag{4.70}$$

whereas it is *globally* conserved if

$$\iiint_{\mathbf{\Omega}} \frac{\partial u_i}{\partial x_i} d\mathbf{x} = 0. \tag{4.71}$$

Note that in periodic domains, local conservation implies global conservation [65]. Obviously, mass is conserved *a priori* since the continuity equation appears in the divergence formulation. In analogy with continuous fields, the discrete vector field $\overline{u}_i$ is locally, respectively globally conserved if

$$\frac{\delta \overline{u}_i}{\delta x_i} = 0, \tag{4.72}$$

$$\sum_{\mathbf{\Omega}} \frac{\delta \overline{u}_i}{\delta x_i} = 0. \tag{4.73}$$

In order to examine the energy conservation of the nonlinear terms, three discretizations are considered:

$$\overline{u}_j \frac{\delta \overline{u}_i}{\delta x_j} \qquad (\textit{Advective form}), \tag{4.74}$$

$$\frac{\delta \overline{u}_j \overline{u}_i}{\delta x_j} \qquad (\textit{Divergence form}), \tag{4.75}$$

$$\frac{1}{2}\overline{u}_j \frac{\delta \overline{u}_i}{\delta x_j} + \frac{1}{2}\frac{\delta \overline{u}_j \overline{u}_i}{\delta x_j} \qquad (\textit{Skew-symmetric form}). \tag{4.76}$$

[8] Using Gauss's theorem, conservation is also expressed as

$$\iiint_{\Omega} \frac{\partial u_i}{\partial x_i} d\mathbf{x} = \iint_{\partial\Omega} u_i n_i dS = 0, \tag{4.69}$$

where n_i represents the outward pointing unit normal on the boundary $\partial\Omega$. This expression is used in e.g. finite volume methods which rely on the integral formulation of the governing equations, rather than the differential formulation.

The *analytical* equivalents of expressions (4.74), (4.75) and (4.76) are identical, since the vector field is solenoidal such that expression (4.70) is satisfied. In *discrete* space, however, epxressions (4.74), (4.75) and (4.76) are not identical. Morinishi *et al.* [65] demonstrated that multiplying the discrete Navier-Stokes equations, in which pressure and viscous terms are not considered, with $\overline{u}_i/2$ and summing over index i, only the skew-symmetric discretization leads a priori to the following transport equation for the kinetic energy

$$\frac{\delta \overline{k}}{\delta t} + \frac{\delta \overline{u}_j \overline{k}}{\delta x_j} = 0. \tag{4.77}$$

This expression is derived, regardless the (central) discretization of the partial derivatives in the skew-symmetric formulation. Hence, only the skew-symmetric formulation of the nonlinear term conserves the local kinetic energy a priori. On the other hand, Morinishi *et al.* [65] showed that the advective and divergence formulations (4.74) and (4.75) can only conserve the kinetic energy if an appropriate central discretization for the partial derivatives is used and if the discrete continuity equation (4.72) is exactly satisfied. Since both constraints are often not fulfilled, formulations (4.74) and (4.75) may be responsible for an increase or decrease of kinetic energy. Additionally, Blaisdell *et al.* [5] showed that the skew-symmetric form of the nonlinear term results in a reduced amplitude of the aliasing errors, due to imperfect filtering or modeling, compared to the other formulations.[9] This conclusion is confirmed by the work of Kravchenko *et al.* [49], although Chow *et al.* [19] found that the advective form lead to the smallest aliasing errors. In order to stabilize DNS and LES computations without numerical dissipation, the skew-symmetric formulation of the nonlinear term ought to be used.[10]

4.3.2 Odd-even decoupling

It is analytically possible to obtain the n^{th} derivative of the continuous variable $\phi(x)$, $x \in \mathbb{R}$ as two or more successive differentiations of that variable, such that

$$\frac{\partial^a}{\partial x^a}\left(\frac{\partial^b \phi}{\partial x^b}\right) = \frac{\partial^n \phi}{\partial x^n}, \quad a + b = n. \tag{4.78}$$

Although this property is conserved for finite difference approximations, some attention is required concerning the resulting discrete finite difference approximation. In order to avoid unnecessary complexity, the following discussion is restricted to

[9] It should be noted that Blaisdell *et al.* [5] used the skew-symmetric formulation (4.76) for their investigation on the one-dimensional Burgers' equation. However, for Burgers' equation the correct skew-symmetric formulation of the nonlinear term differs from (4.76). Hence, energy could not have been conserved a priori.

[10] Note that the skew-symmetric form does not conserve momentum *a priori*. Nevertheless, kinetic energy conservation is considered more important for DNS and LES.

the use of explicit symmetric finite difference derivatives. Assume the notation

$$\left.\frac{\delta^n\overline{\phi}}{\delta x^n}\right|_{-r}^{r}(x_i) = \frac{1}{\Delta^n}\sum_{j=-r}^{r}\beta_j\overline{\phi}(x_{i+j}) = \boldsymbol{\beta}|_{-r}^{r} * \overline{\phi} \tag{4.79}$$

which represents the k^{th}-order finite difference approximation with stencil width $2r+1$ of the n^{th} derivative. Recall that the order of accuracy k is related to the stencil width as

$$k = \begin{cases} 2r+1-n & \forall n \in 2\mathbb{N}+1 \\ 2r+2-n & \forall n \in 2\mathbb{N} \end{cases} . \tag{4.80}$$

Property (4.78) then reads

$$\underbrace{\left.\frac{\delta^a}{\delta x^a}\right|_{-r'}^{r'}\left(\left.\frac{\delta^b\overline{\phi}}{\delta x^b}\right|_{-r''}^{r''}\right)}_{\delta_1} \approx \underbrace{\left.\frac{\delta^n\overline{\phi}}{\delta x^n}\right|_{-r}^{r}}_{\delta_2}, \quad a+b=n. \tag{4.81}$$

Although both δ_1 and δ_2 represent approximations for the n^{th} derivative, they are not necessarily identical. Indeed, δ_1 has a stencil width $2r'+2r''+1$ and is of order $\min(k',k'')$ whereas δ_2 has a stencil support $2r+1$ and is of order k. It is verified for explicit finite difference approximations that δ_1 and δ_2 are only identical if $a \in 2\mathbb{N}$ or $b \in 2\mathbb{N}$ and if $k' = k'' = 2$. If these conditions are satisfied, then $k = \min(k',k'') = 2$, $r = 2r' + 2r'' + 1$ and

$$\boldsymbol{\beta}|_{-r'}^{r'} * \boldsymbol{\beta}|_{-r''}^{r''} \equiv \boldsymbol{\beta}|_{-r}^{r} . \tag{4.82}$$

However, if these conditions are not respected, the finite difference approximations δ_1 are typically of order $\min(k',k'') \leq k$ but have a wider stencil support than strictly required for this order of accuracy. In this dissertation, such finite difference approximations (that do not satisfy the conditions $a \in 2\mathbb{N}$ or $b \in 2\mathbb{N}$ and $k' = k'' = 2$) are named *incompact* finite difference approximations. Table 4.9 presents some examples of incompact finite difference schemes for the 2^{nd} derivative, constructed with expression (4.81) where $a = b = 1$. Not only are these incompact approximations computationally inefficient, they display very poor accuracy. This is understood by examining the modified wavenumber of δ_1, given by the expression

$$\kappa_a'^{\,a}(\kappa)\,\kappa_b'^{\,b}(\kappa) . \tag{4.83}$$

Figure 4.10 illustrates the modified wavenumber of the incompact schemes for the 2^{nd} derivative, presented in Table 4.9. The incompact finite difference approximations clearly display large dispersion errors over almost the entire wavenumber range. Moreover, in contrast to the normal finite difference approximations of the

n	β_{-4}	β_{-3}	β_{-2}	β_{-1}	β_0	β_1	β_2	β_3	β_4	k	k'	k''
2			$\frac{1}{4}$	0	$-\frac{1}{2}$	0	$\frac{1}{4}$			2	2	2
		$-\frac{1}{24}$	$\frac{8}{24}$	$\frac{1}{24}$	$-\frac{16}{24}$	$\frac{1}{24}$	$\frac{8}{24}$	$-\frac{1}{24}$		2	2	4
	$\frac{1}{144}$	$-\frac{16}{144}$	$\frac{64}{144}$	$\frac{16}{144}$	$-\frac{130}{144}$	$\frac{16}{144}$	$\frac{64}{144}$	$-\frac{16}{144}$	$\frac{1}{144}$	4	4	4

Table 4.9: Incompact finite difference approximations. Three incompact finite difference approximations for the 2^{nd} derivative constructed with expression (4.81) where $a = b = 1$.

2^{nd} derivative (Figure 4.3), the modified wavenumbers of these schemes fall to zero at the cutoff wavenumber κ_{max}. The latter property has severe repercussions for the discretization of the second order operators in the Navier-Stokes equations (2.87). In particular the discretization of the subgrid force in LES, given by

$$\frac{\delta\tau_{ij}}{\delta x_j} = -2\frac{\delta\nu_e\overline{S}_{ij}}{\delta x_j}, \quad \overline{S}_{ij} = \frac{1}{2}\left(\frac{\delta\overline{u}_i}{\delta x_j} + \frac{\delta\overline{u}_j}{\delta x_i}\right), \tag{4.84}$$

requires some attention. Although the subgrid force is supposed to dissipate sufficiently the small scales corresponding to high wavenumber Fourier modes, direct evaluation of $\frac{\delta\tau_{ij}}{\delta x_j}$ would result into weak dissipation due to the poor Fourier characteristics of the successive derivative operators (Figure 4.10). Moreover, spurious π-*modes* or *wiggles* at $\kappa = \kappa_{max}$, are not detected by the dissipative operator $\frac{\delta\tau_{ij}}{\delta x_j}$, since the Fourier characteristics vanish for these modes. Hence, they are not eliminated from the solution, unless explicit filtering is used. It is known that these π-*waves* severely pollute the solution and eventually destabilize the algorithm. Therefore, the dissipative operator is discretized as

$$\frac{\delta\tau_{ij}}{\delta x_j} = -2\frac{\delta\nu_e\overline{S}_{ij}}{\delta x_j} \tag{4.85}$$

$$= -2\frac{\delta\nu_e}{\delta x_j}\overline{S}_{ij} - 2\nu_e\frac{\delta\overline{S}_{ij}}{\delta x_j} \tag{4.86}$$

$$= -2\frac{\delta\nu_e}{\delta x_j}\overline{S}_{ij} - 2\nu_e\frac{\delta^2\overline{u}_i}{\delta x_j^2}. \tag{4.87}$$

The second term in (4.87) is now *compact* such that subgrid dissipation is guaranteed up to κ_{max}. Note that, although the first term in (4.87) contributes to the dissipation, the 1^{st} -order discrete derivatives do not detect the π-wave since $\kappa'(\kappa_{max}) = 0$. An analogous problem appears by enforcing the discrete continuity equation to the Navier-Stokes equations. In case of incompact discretizations, wiggles appear in the resulting pressure field. This problem, known as *odd-even decoupling* is explained further.

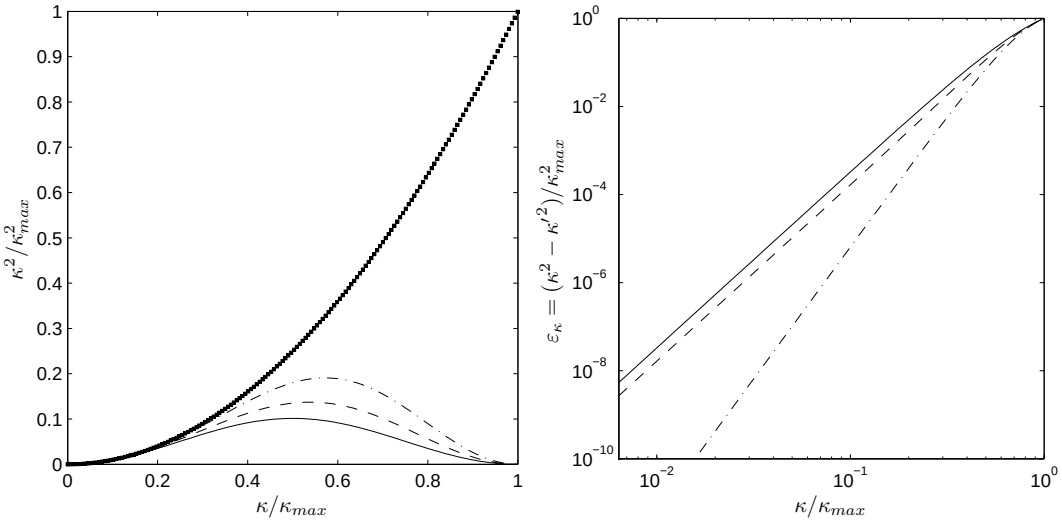

Figure 4.10: Modified wavenumbers for incompact finite difference approximations. The modified wavenumbers (**left**) and their errors (**right**) for the incompact finite difference approximations for the 2^{nd} derivative constructed with expression (4.81) where $a = b = 1$ and $k' = k'' = 2$ (——), $k' = 2$, $k'' = 4$ (− − −), $k' = k'' = 4$ (−·−·).

4.3.3 The Pseudo-Compressibility algorithm

As explained in Chapter 3, enforcing the continuity equation (2.1) leads to the Poisson equation for the pressure, the solution of which is far more time consuming than solving e.g. the Navier-Stokes equations 2.2. In 1967 *Chorin* [17, 18] presented a *Pseudo-Compressibility method* as an entirely new approach to satisfying solenoidality. In this method, the continuity equation (2.1) is replaced by the hyperbolic artificially compressible continuity equation

$$\frac{1}{c^2}\frac{\partial p}{\partial \tau} + \frac{\partial u_i}{\partial x_i} = 0, \tag{4.88}$$

where c denotes the artificial speed of sound and τ is called the *pseudo-time*. According to [71], formulation (4.88) corresponds with the definition of an artificial density $\rho = p/c^2$. Replacing the original continuity equation (2.1) with expression (4.88) eliminates the Poisson equation, leading to a method that is believed to be computationally less expensive [71]. The hyperbolic equation (4.88) can now be integrated numerically in pseudo-time. Therefore, the pseudo-time τ must be introduced into the Navier-Stokes equations, which yields

$$\frac{\partial u_i}{\partial \tau} + \frac{\partial u_i}{\partial t} + u_j\frac{\partial u_i}{\partial x_j} = -\frac{\partial p}{\partial x_i} + \nu\frac{\partial^2 u_i}{\partial x_j^2}, \tag{4.89}$$

It can be seen from this equation that a *dual-time stepping* algorithm is obtained. For every physical time step $t = t_k$, the algorithm converges to a steady state solution

of the Navier-Stokes problem in pseudo-time. Indeed, as soon as the velocity field becomes solenoidal at time level $t = t_k$, both the pressure and the velocity become independent of τ such that $\frac{\partial u_i}{\partial \tau} = 0$ and $\frac{\partial p}{\partial \tau} = 0$. Note that if the physical problem converges to a steady state, i.e. $\frac{\partial u_i}{\partial t} = 0$, the dual-time stepping algorithm reduces to a single-time stepping algorithm in τ. In this work, the Pseudo-Compressibility algorithm is only used for laminar steady-state flow calculations. Since the rate of convergence of the algorithm is extremely sensitive to the artificial speed of sound c in (4.88), its value must be chosen carefully for efficient computations. However, for the purposes in this work, the value of c is selected *ad hoc*, and no attempt is made to obtain optimal convergence. Adopting the low-storage q-stage Runge-Kutta method for time integration and assuming $\tau' = \tau + \frac{j}{q}$ and $\tau'' = \tau + \frac{j-1}{q}$, the resulting discrete algorithm at stage $j = 1, 2 \dots q$ yields,

$$\overline{p}_i^{\tau+\frac{j}{q}} = \overline{p}_i^{\tau} + \alpha_j c^2 \Delta\tau \left\{ -\frac{\delta \overline{u}_i^{\tau''}}{\delta x_i} + \mathscr{D}\left(\Delta^k\right) \right\} \tag{4.90}$$

$$\overline{u}_i^{\tau+\frac{j}{q}} = \overline{u}_i^{\tau} + \alpha_j \Delta\tau \left\{ \overline{u}_j^{\tau''} \frac{\delta \overline{u}_i^{\tau''}}{\delta x_j} + \frac{\delta \overline{p}^{\tau''}}{\delta x_i} - \nu \frac{\delta^2 \overline{u}_i^{\tau''}}{\delta x_j^2} \right\}, \tag{4.91}$$

As mentioned in the previous paragraph, the central difference approximation for the divergence in $\frac{\delta \overline{u}_i^{\tau''}}{\delta x_i}$ is insensitive to spurious π-waves. Therefore, an artificial dissipation $\mathscr{D}\left(\Delta^k\right)$ is needed in the discrete continuity equation in order to eliminate these wiggles. Typically $\mathscr{D}\left(\Delta^k\right)$ is constructed as

$$\mathscr{D}\left(\Delta^k\right) = \frac{\sigma}{u_{ref}} \Delta^k \frac{\delta^{k+1} \overline{p}^{\tau''}}{\delta x_i^{k+1}}. \tag{4.92}$$

where σ denotes the magnitude of the dissipation, u_{ref} is a reference velocity and k denotes the order of accuracy of the adopted finite difference approximation for $\frac{\delta \overline{u}_i^{\tau''}}{\delta x_i}$. This way, the artificial dissipation scales as the leading order truncation term Π^{Δ}, without destroying the order of accuracy of the adopted discretization. σ must be chosen such that the dissipation is just enough to eliminate the spurious wiggles.

4.3.4 The Pressure-Correction algorithm

In contrast to the Pseudo-Compressibility algorithm, the *Pressure-Correction* algorithm uses a Poisson equation in order to satisfy the continuity constraint in incompressible flows. The basic idea behind the Pressure-Correction method, is to integrate the Navier-Stokes equations in two steps. In the first step a the velocity field is *predicted* based on the velocity and pressure at the current time level. Since the predictor velocity field is not divergence free, a *correction* ϕ to the pressure p is obtained which enforces the solenoidality of the velocity field. Adopting the low-storage q-stage Runge-Kutta method for time integration and assuming $t' = t + \frac{j}{q}$ and $t'' = t + \frac{j-1}{q}$, the algorithm at stage $j = 1, 2 \dots q$ consists of 4 steps.

i. Given the velocity field $\overline{u}_i^{t''}$ and a pressure field $\overline{p}^{t''}$ at the current time level $t'' = t + \frac{j-1}{q}$, the Navier-Stokes equations are integrated leading to an intermediate *predictor velocity field* $\overline{u}_i^*$, that is

$$\overline{u}_i^* = \overline{u}_i^t - \alpha_j \Delta t \left\{ \frac{\overline{u}_j^{t''}}{2} \frac{\delta \overline{u}_i^{t''}}{\delta x_j} + \frac{1}{2} \frac{\delta \overline{u}_i^{t''} \overline{u}_j^{t''}}{\delta x_j} + \frac{\delta \overline{p}^{t''}}{\delta x_i} - \nu \frac{\delta^2 \overline{u}_i^{t''}}{\delta x_j^2} + \frac{\delta \tau_{ij}^{t''}}{\delta x_j} \right\}, \quad (4.93)$$

which is not divergence free.

ii. In the second step, it is assumed that the pressure at the new time level $t' = t + \frac{j}{q}$ can be formulated as a correction to the pressure at the current time level, i.e. $\overline{p}^{t'} = \overline{p}^{t''} + \overline{\phi}$. Then, the pressure correction $\overline{\phi}$ must be determined such that the solenoidality of the velocity field $\overline{u}_i^{t'}$ at the new time level is enforced and thus $\frac{\delta \overline{u}_i^{t'}}{\delta x_i} = 0$. Applying the discrete divergence operator to equation

$$\overline{\mathbf{u}}_\mathbf{i}^{\mathbf{t}'} = \overline{u}_i^t - \alpha_j \Delta t \left\{ \frac{\overline{u}_j^{t''}}{2} \frac{\delta \overline{u}_i^{t''}}{\delta x_j} + \frac{1}{2} \frac{\delta \overline{u}_i^{t''} \overline{u}_j^{t''}}{\delta x_j} + \frac{\delta \overline{\mathbf{p}}^{\mathbf{t}'}}{\delta x_i} - \nu \frac{\delta^2 \overline{u}_i^{t''}}{\delta x_j^2} + \frac{\delta \tau_{ij}^{t''}}{\delta x_j} \right\}, \quad (4.94)$$

results into a Poisson equation for the pressure-correction

$$\frac{\delta^2 \overline{\phi}}{\delta x_i^2} = \frac{\delta}{\delta x_i} \left(\overline{u}_i^* + \alpha_j \Delta t \frac{\delta \overline{p}^{t''}}{\delta x_i} \right) - \alpha_j \Delta t \frac{\delta^2 \overline{p}^{t''}}{\delta x_i^2}. \quad (4.95)$$

This formulation differs slightly from the traditional Poisson equation. Indeed, the *odd-even decoupling* due to the incompact discretization of the pressure on the right-hand side of (4.95) is precluded by explicitly compacting the pressure gradient at the new time level in expression (4.95). The pressure $\overline{p}^{t''}$ and the pressure correction $\overline{\phi}$ are then discretized consistently. Moreover, the spurious wiggles that might appear in the pressure $\overline{p}^{t''}$ are detected by the compact discretization and canceled by the pressure correction after solving (4.95). Note that this simple formulation is equivalent to *Rhie-Chow interpolation* [72], which uses an explicit operator to compact the Laplacian of the pressure. However, the current method bypasses the cumbersome construction of Rhie-Chow interpolants for higher order discretizations and allows straightforward and efficient implementation in the parallelized code used in this dissertation.

iii. Once the pressure-correction $\overline{\phi}$ is obtained, the predictor velocity field is updated as

$$\overline{u}_i^{t'} = \overline{u}_i^* - \alpha_j \Delta t \frac{\delta \overline{\phi}}{\delta x_i}, \quad (4.96)$$

iv. Finally, the pressure at the new time level is updated as

$$\overline{p}^{t'} = \overline{p}^{t''} + \overline{\phi} \tag{4.97}$$

The concept of a pressure-correction might be reduced to a formulation where the predictor velocity $\overline{u}_i^*$ is obtained without the pressure-gradient contribution. The entire pressure $\overline{p}^{t'}$ at the new time level is then obtained by solving the corresponding Poisson equation instead of a pressure correction. This method, known as the *fractional-step method*, immediately projects the predictor velocity field to a solenoidal field, similarly as would be done for spectral methods.
The Poisson-equation is typically solved using *multigrid* solvers. However, since in this work the Pressure-Correction method is solely used in periodic domains, the elliptic Poisson equation is solved by taking the Fourier transformation of (4.95), yielding

$$\left(\kappa_i'^2\right)\widehat{\overline{\phi}} = \mathscr{F}\left\{\frac{\delta}{\delta x_i}\left(\overline{u}_i^* + \alpha_j \Delta t \frac{\delta \overline{p}^{t''}}{\delta x_i}\right) - \alpha_j \Delta t \frac{\delta^2 \overline{p}^{t''}}{\delta x_i^2}\right\} \tag{4.98}$$

where $\kappa_i'^2$ denotes the modified wavenumber of the 2^{nd} derivative in the i^{th} spectral direction. The pressure-correction is now readily obtained from the linear system of equations (4.98).

4.4 Appraisal of the standard Finite Difference Methods for LES

4.4.1 Asymptotic order of accuracy

As discussed in Section 3.4, it is highly desirable in DNS and especially in LES to maximize the ratio between the physical resolution and the grid resolution in order to resolve as much scales as possible on a given computational grid. Due to the Nyquist criterion this ratio is limited to the value $\kappa_c/\kappa_{max} = 2/3$ [67]. In order to ensure that the magnitudes of the discretization errors (defined in Section 2.4.3) remain smaller than the magnitude of the modeled residual force of the unresolved scales of motion [32, 19, 4], the adopted numerical method requires sufficient accuracy for all scales in the range $0 \leq \kappa < \kappa_c$. As a consequence, the value of the filter-to-grid cutoff-ratio κ_c/κ_{max} depends on the adopted central finite difference approximation or vice versa. For 2^{nd} -order explicit finite difference schemes, Ghosal [32] and Chow *et al.* [19] recommend a filter-to-grid cutoff-ratio of at most $\kappa_c/\kappa_{max} \leq 1/4$, to ensure that the magnitudes of the discretization errors remain smaller than the magnitude of the modeled force of the subgrid scales. Hence, accurate resolution of the scales characterized by κ_c, increases the required number of nodes, and thus the computational cost, with a factor $(2\kappa_{max}/3\kappa_c)^3 \approx 20$ than theoretically necessary. This may be prohibitively expensive for most three-dimensional

LES computations. Higher order discretizations are often applied to allow for larger filter-to-grid cutoff-ratios and thus reduce the involved costs. However, in order to obtain acceptable dispersion errors up to $\kappa_c = \kappa_{max}/2$, which is still not the maximum resolution on the computational grid, Chow *et al.* [19] recommended to use at least a 10^{th} -order explicit finite difference scheme or a 6^{th} -order implicit Padé scheme. Although the grid requirements are only a factor $(2\kappa_{max}/3\kappa_c)^3 \approx 2.5$ higher than theoretically necessary, high-order schemes involve more floating point operations, which again inevitably leads to an increased computational cost. Despite the fact that the increase in accuracy makes high-order schemes worthwhile, optimized finite difference schemes can be constructed with an improved balance between accuracy and computational costs. Before the discussion is continued, it should be noted that in contrast to [32, 19, 4], Park *et al.* [69] found that the subgrid force was dominant for the *Eddy-Damped Quasi-Normal Markovian* (EDQNM) Large-Eddy Simulation of isotropic turbulence at low Reynolds number. Indeed, for low Reynolds numbers, the finite difference approximation of the subgrid force is relatively more important than for high Reynolds numbers [4], leading to somewhat different results and conclusions. Nevertheless, for high Reynolds numbers, the numerical error of the nonlinear term is dominant and can be larger than the subgrid force as shown by Berland *et al.* [4] using EDQNM theory.

It is common practice in Computational Fluid Dynamics to use (high-order) central schemes based on a truncated Taylor series, leading to a certain formal asymptotic order of accuracy for the largest scales. Although this may be sufficient for well-resolved Direct Numerical Simulations, it is not necessarily the optimal strategy for Large-Eddy Simulation. Indeed, for regular fields, which are sufficiently smooth on the computational grid, the Taylor series converge rapidly due to small contributions of the higher derivatives. Hence, the dispersion errors remain low. However, in case of highly fluctuating fields with marginal resolution on the grid, the contributions of the higher derivatives in the truncation terms of the Taylor series become much more important, slowing down the convergence of the Taylor series and thus leading to significant dispersion errors. Standard Taylor-based asymptotic finite difference approximations assume smooth fields and fast convergence of the Taylor series. However, in case of irregular LES-fields, where the Taylor series converge more slowly, it would be much more advantageous to minimize all contributions in the Taylor series in order to obtain good overall performance. In other words, preserving the global dispersion relation for the full range of scales up to $\kappa_c = \frac{2}{3}\kappa_{max}$ instead of focusing on asymptotic order of convergence, could be much more advantageous in Large-Eddy Simulations. Indeed, since in LES the smallest resolved scales are part of the inertial subrange and thus still contain a significant amount of energy compared to the largest resolved scales, the accuracy with which these scales are resolved could benefit from such a strategy.

This useful point of view was already introduced by Tam *et al.* [79] in the field of computational aero-acoustics, where accurate simulation of propagating waves re-

quire highly non-dispersive and non-dissipative finite difference schemes.[11] Whereas Tam *et al.* [79] restricted themselves to optimized explicit finite difference approximations, Kim *et al.* [45], Hixon [37], Ashcroft *et al.* [2] and Bogey *et al.* [6] extended the idea to implicit Padé schemes. Further, Hu *et al.* [39], Bogey *et al.* [6], and Berland *et al.* [3] applied this technology to Runge-Kutta schemes whereas Bogey *et al.* [6], and Berland *et al.* [3] also designed optimized finite difference filters. In general, these low-dispersive prefactored finite difference schemes are constructed by static least-square minimization of the dispersion errors of a particular finite difference approximation of the n^{th} derivative in a chosen wavenumber range $0 \leq \kappa \leq \kappa_\alpha$. In other words, the error between the modified wavenumber and the real wavenumber is minimized by solving

$$\frac{\partial}{\partial \alpha_l} \int_0^{\kappa_\alpha} \left(\kappa^n - {\kappa'_n}^n\right)^2 \mathscr{W}(\kappa)\, d\kappa = 0 \tag{4.99}$$

$$\frac{\partial}{\partial \beta_j} \int_0^{\kappa_\alpha} \left(\kappa^n - {\kappa'_n}^n\right)^2 \mathscr{W}(\kappa)\, \kappa = 0, \tag{4.100}$$

where α_l and β_j denote the scheme's coefficients, $\mathscr{W}(\kappa)$ is a weighting function and κ_α determines the range of optimization. Most commonly, some coefficients are determined a priori in order to ensure a minimal formal asymptotic order of accuracy. The remaining coefficients are then obtained from the least-square minimization (4.99) and (4.100). The choice of the weighting function is usually inspired by ad hoc motivations in order to accentuate the optimization range or to ensure the analytical integrability of expressions (4.99) and (4.100) [45]. Typically the range of optimization is determined by $0.5\kappa_{max} \leq \kappa_\alpha \leq 0.9\kappa_{max}$, although the exact value of κ_α differs from author to author. According to Kim *et al.* [45], it is preferable to omit the region between $0.9\kappa_{max} \leq \kappa \leq \kappa_{max}$ since minimizing the large dispersion or dissipation errors in this range is inefficient, and leads to poor Fourier characteristics of the optimized scheme. The past few years, an ample amount of optimized schemes was presented by various authors. Therefore, it is not opportune to discuss this plenitude of variants since they are mostly a matter of personal flavour. For further information, the reader is referred to [79, 45, 37, 2, 6]. As an example of such an optimized scheme, the original optimized 4^{th} -order explicit finite difference scheme of Tam *et al.* [79] for $\kappa_\alpha = 0.5\kappa_{max}$ is illustrated in Figure 4.11. Notice that this explicit finite difference approximation has the same 7-point stencil support of the standard 6^{th} -order explicit finite difference approximation. The formal 4^{th} -order of accuracy is obtained with 5 parameters whereas the two remaining parameters are obtained by the optimization procedure. In other words, the resulting scheme gives up its potential formal order of accuracy on the small wavenumbers in the interest of

[11] Earlier, Lele [50] constructed *spectral-like* schemes by imposing some ad-hoc constraints to the modified wavenumber. Nevertheless, Tam *et al.* [79] were the first to present a general optimization strategy.

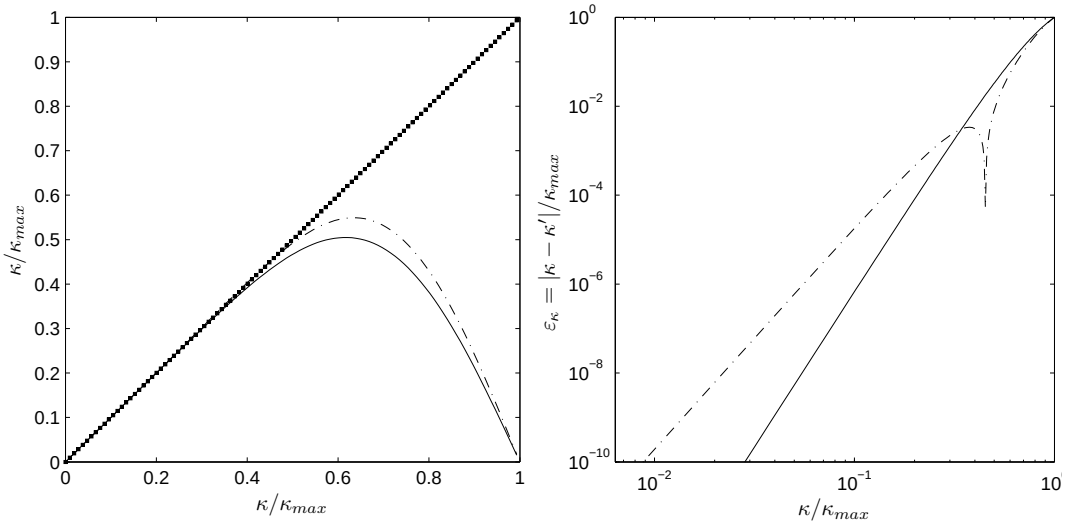

Figure 4.11: Modified wavenumber of Tam's optimized finite difference approximation. Modified wavenumbers (**left**) and their errors (**right**) for the explicit 6^{th} order finite difference approximation (———) and the 4^{th} -order optimized scheme of Tam (− · −·), for the 1^{st} derivative.

the large wavenumbers, which obtain higher accuracy than the asymptotic 6^{th} order approximation. It was demonstrated by [79, 45, 37, 2, 6, 4], that such optimized finite difference approximations lead to improved overall accuracy for non-smooth problems. This conclusion is confirmed by the results in Chapters 7 and 8. Moreover, optimized schemes are computationally efficient since the cost-to-accuracy ratio is significantly reduced. The main objective of the current dissertation is to further develop these Dispersion-Relation Preserving schemes.

4.4.2 Motivation of this work

As discussed previously, minimizing the contributions of all Taylor series truncation terms in the finite difference approximation of a derivative, and thus preserving the global dispersion relation for the range of scales up to κ_c instead of focusing on asymptotic order of convergence, might be an advantageous strategy for Large-Eddy Simulations. Obviously, the optimized finite difference schemes by [79, 45, 37, 2, 6] meet this strategy, leading to good results at acceptable costs. The advantage of using such optimized schemes over standard schemes in Large-Eddy Simulation was illustrated by Berland *et al.* [4], using EDQNM theory. These *prefactored* schemes are *statically* optimized by an a priori least-square procedure leading to predefined Fourier characteristics.

It might also be possible to minimize all truncation terms of the finite difference approximation in *real time* during the calculation. Such a strategy would allow one

to obtain an optimal finite difference approximation according to the flow characteristics at each time step. This implies that the Fourier characteristics of the adopted scheme vary during the simulation in such a way that the global dispersion error is always minimized. The proposed methodology could provide improved quality and more flexibility in numerical simulations. In the next chapter, a simple numerical experiment is conducted in which the coefficients of the discretized truncation terms in the Navier-Stokes equations and continuity equation are optimized by means of the *sampling-based dynamic procedure* proposed by [89, 88, 22, 46] in the context of LES subgrid modeling.

If at first the idea is not absurd,
then there is no hope for it.

Einstein, Albert

5

The Sampling-Based Dynamic Procedure

As extensively discussed in previous chapters, the accuracy of a simulation depends partially on the ability to control the discretization errors. Especially in Large-Eddy Simulation of turbulent flows, it is highly desirable to minimize the numerical errors such that their magnitude remains lower than the subgrid force [32, 49, 19, 4]. Traditionally, numerical accuracy is guaranteed by using fine grid resolutions with standard low-order numerical methods, or by using standard high-order methods. Nevertheless, both approaches are often prohibitively expensive for CFD simulations. However, it has been argued that the standard numerical methods, which focus on the formal order of accuracy, may be suboptimal for LES. Indeed, minimizing the contributions of all Taylor series truncation terms in the finite difference approximation of a derivative, and thus preserving the global dispersion relation for the range of scales up to the cutoff wavenumber, instead of focusing on asymptotic order of convergence, might be an advantageous strategy for Large-Eddy Simulations.

Recently, Winckelmans *et al.* [89, 88], Debliquy *et al.* [22] and Knaepen *et al.* [46] proposed to use the *sampling formalism* (Chapter 2), instead of the traditional filtering formalism (Chapter 3) as an alternative method to derive the LES-equations. By thinking in terms of such a sampling formalism, the nonlinearity in the momentum equations does not result in the generation of subgrid stresses, as the sampling operator commutes with the nonlinear terms. However, since the sampling operator is not commutative with spatial derivatives, a closure term appears which represents the loss of information due to the projection on the computational grid. In [89, 88, 22, 46] a Smagorinsky model was proposed that, by relying on a so-called *generalized dynamic procedure* or *sampling based dynamic procedure* which uses information from two different grid resolutions, succeeded in accounting for the sampling commuta-

tion errors.

In the present chapter, the sampling-based dynamic procedure is modified and applied in an new, alternative way in order to obtain improved numerical accuracy for various finite difference approximations. This new approach, which forms the core of the current dissertation, was already presented in Fauconnier *et al.* [27, 28] and is summarized hereafter. Using Taylor series expansion, an analytical formulation for the exact truncation error in the Navier-Stokes equations and the continuity equation is derived. By taking a *modified* leading order truncation term into account, a *model-formulation* for the truncation errors is developed, which allows one to minimize the global truncation error by means of a *dynamic coefficient*. Following [46, 27, 28], the generalized dynamic procedure is subsequently introduced with which the optimal coefficients of the model-formulation in the Navier-Stokes equations and continuity equation are obtained. Finally, the concept is evaluated for a two-dimensional steady laminar flow in a lid-driven cavity at a Reynolds number $\mathrm{Re} = 400$.

5.1 TRUNCATION ERRORS IN THE DISCRETE EQUATIONS

5.1.1 TRUNCATION ERRORS: ANALYTICAL FORMULATION

In Chapter 2 (Section 2.4.3), the discrete Navier-Stokes equations and the discrete continuity equation were derived by applying the sampling operator $\mathscr{S}^{\mathbf{\Delta}} = \mathscr{S}^{\Delta_{x_1}} \circ \mathscr{S}^{\Delta_{x_2}} \circ \mathscr{S}^{\Delta_{x_3}}$ to the equations (2.1) and (2.2). This operation results in a projection from the continuum spatial domain $\Omega \subset \mathbb{R}^3$ with Cartesian coordinates $\mathbf{x} \in \mathbb{R}^3$ to the discrete spatial domain $\Omega^{\Delta} \subset \mathbb{R}^3$ with discrete equispaced Cartesian coordinates $\mathbf{x_k} = [x_1(\mathbf{k}), x_2(\mathbf{k}), x_3(\mathbf{k})] \in \mathbb{R}^3$, and $\mathbf{k} = [k_1, k_2, k_3] \in \mathbb{N}^3$ the index vector. Let $\mathbf{N} = [N_1, N_2, N_3]$ represent the number of grid nodes in each direction such that $0 \leq k_j \leq N_j$, $j = 1, 2, 3$ and let $\mathbf{\Delta} = [\Delta_1, \Delta_2, \Delta_3]$ give the uniform grid spacing in each direction. Further, the sampling operator $\mathscr{S}^{\Delta_t}$ projects the Navier-Stokes equations (2.2) from continuum time $t \in \mathbb{R}$ to discrete time $t_n \in \mathbb{R}$, $n \in \mathbb{N}$ where Δt denotes the time interval. Using the short hand notation $\mathscr{C}(\overline{u}_i)$ for the continuity operator and $\mathscr{N}(\overline{u}_i, \overline{p})$ for the Navier-Stokes operator, the discrete continuity and the Navier-Stokes equations[1] are written as

$$0 = \frac{\delta \overline{u}_i}{\delta x_i} - \Pi^{\Delta} = \mathscr{C}(\overline{u}_i) - \Pi^{\Delta} \tag{5.1}$$

$$\frac{\delta \overline{u}_i}{\delta t} = -\overline{u}_j \frac{\delta \overline{u}_i}{\delta x_j} - \frac{\delta \overline{p}}{\delta x_i} + \nu \frac{\delta^2 \overline{u}_i}{\delta x_j^2} + \Sigma_i^{\Delta} = \mathscr{N}(\overline{u}_i, \overline{p}) + \Sigma_i^{\Delta}. \tag{5.2}$$

Due to the non-commutativity of the sampling operator $\mathscr{S}^{\mathbf{\Delta}}$ with the spatial partial derivatives, spatial *truncation errors*[2] arise in the continuity equation and the

[1] Note that the Poisson equation is not discussed here in order to simplify the current analysis.
[2] Truncation errors due to time discretization are not considered in this work.

Navier-Stokes equations, which are formally given by the relations

$$\Pi^{\Delta} = \frac{\delta \overline{u}_i}{\delta x_i} - \overline{\frac{\partial u_i}{\partial x_i}} \tag{5.3}$$

$$\Sigma_i^{\Delta} = \overline{u}_j \left(\frac{\delta \overline{u}_i}{\delta x_j} - \overline{\frac{\partial u_i}{\partial x_j}} \right) + \left(\frac{\delta \overline{p}}{\delta x_i} - \overline{\frac{\partial p}{\partial x_i}} \right) - \nu \left(\frac{\delta^2 \overline{u}_i}{\delta x_j^2} - \overline{\frac{\partial^2 u_i}{\partial x_j^2}} \right). \tag{5.4}$$

Assume that the spatial partial derivatives in the equations (5.1) and (5.2) are given by a k^{th}-order explicit finite difference approximation.[3] The n^{th} derivative is then approximated as

$$\frac{\delta^n \overline{u}_i}{\delta x_j^n}(\mathbf{x}, t) = \frac{1}{\Delta_j^n} \sum_{l=-r}^{r} \beta_{l,n} \overline{u}_i(\mathbf{x}, t), \tag{5.5}$$

where the $\beta_{l,n}$ denote the weighting coefficients which depend on the adopted discretization and the value of n. Using relation (4.7), the commutation error for the n^{th} derivative then reads,

$$\frac{\delta^n \overline{u}_i}{\delta x_j^n}(\mathbf{x}, t) - \overline{\frac{\partial^n u_i}{\partial x_j^n}}(\mathbf{x}, t) = \sum_{k'=k}^{\infty} \left(\sum_{l=-r}^{r} \frac{\beta_{l,n}\, l^{k'+n}}{(k'+n)!} \right) \Delta_j^{k'} \overline{\frac{\partial^{k'+n} u_i}{\partial x_j^{k'+n}}}(\mathbf{x}, t). \tag{5.6}$$

An analogous expansion is obtained for the pressure gradients in (5.2). Finally, substitution of expression (5.6) into equations (5.3) and (5.4) yields the exact analytical form for the truncation errors Π^{Δ} and Σ_i^{Δ}

$$\Pi^{\Delta} = \sum_{k'=k}^{\infty} c^*_{k',1} \Delta_i^{k'} \overline{\frac{\partial^{k'+1} u_i}{\partial x_i^{k'+1}}} \tag{5.7}$$

$$\Sigma_i^{\Delta} = \sum_{k'=k}^{\infty} \left\{ \overline{u}_j c^*_{k',1} \Delta_j^{k'} \overline{\frac{\partial^{k'+1} u_i}{\partial x_j^{k'+1}}} + c^*_{k',1} \Delta_i^{k'} \overline{\frac{\partial^{k'+1} p}{\partial x_i^{k'+1}}} - \nu c^*_{k',2} \Delta_j^{k'} \overline{\frac{\partial^{k'+2} u_i}{\partial x_j^{k'+2}}} \right\}, \tag{5.8}$$

in which the Taylor series coefficients $c^*_{k',n}$, $n = 1, 2$ are analytically determined as

$$c^*_{k',n} = \sum_{l=-r}^{r} \frac{\beta_{l,n}\, l^{k'+n}}{(k'+n)!}, \quad \forall k'. \tag{5.9}$$

In order to avoid an overload in the notation, a modified summation convention is assumed for the three repeated indices i in expression (5.7) as well as for the three repeated indices j in the nonlinear term of expression (5.8). This implicit summation is maintained further in this work. Expressions (5.7) and (5.8) are used further to construct a *model-formulation* for the truncation error which will allow to minimize the global truncation error.

[3] Note that the current discussion is restricted to explicit finite difference methods without any loss of generality. The application of implicit methods is straightforward, although more elaborate.

5.1.2 TRUNCATION ERRORS: MODEL-FORMULATION

As indicated in section 4.1.1, the central discretization of the leading order truncation term on the right-hand side of expression (5.6) results in an approximation of order $\mathscr{O}\left(\Delta^{k+2}\right)$. Taking more leading order truncation errors into account in the discretization, results into higher-order approximations. Although in principle the successive discretization of each new truncation term would eventually lead to an infinite order of accuracy, in practice all finite difference approximations require the truncation of the Taylor series to a certain order of accuracy.

In this work, a more accurate approximation is constructed by taking the leading order truncation term into account in the discretization. However, instead of using the theoretical Taylor value of the coefficient $c^*_{k,n}$, a *modified* coefficient $c_{k,n}$ is adopted, which is not necessarily equal to the Taylor-value and will be determined such that the global truncation error is minimized. This is explained further. Extracting first the *modified* leading order truncation terms from the truncation errors (5.7) and (5.8) and then *discretizing* this term yields

$$\Pi^{\Delta} = c_{k,1}\Delta_i^k \frac{\delta^{k+1}\overline{u}_i}{\delta x_i^{k+1}} + \left\{ \sum_{k'=k}^{\infty} c^*_{k',1}\Delta_i^{k'} \overline{\frac{\partial^{k'+1}u_i}{\partial x_i^{k'+1}}} - c_{k,1}\Delta_i^k \overline{\frac{\partial^{k+1}u_i}{\partial x_i^{k+1}}} \right\} \tag{5.10}$$

$$\begin{aligned} \Sigma_i^{\Delta} &= c_{k,1}\overline{u}_j\Delta_j^k \frac{\delta^{k+1}\overline{u}_i}{\delta x_j^{k+1}} + \overline{u}_j \left\{ \sum_{k'=k}^{\infty} c^*_{k',1}\Delta_j^{k'} \overline{\frac{\partial^{k'+1}u_i}{\partial x_j^{k'+1}}} - c_{k,1}\Delta_j^k \overline{\frac{\partial^{k+1}u_i}{\partial x_j^{k+1}}} \right\} \\ &+ c_{k,1}\Delta_i^k \frac{\delta^{k+1}\overline{p}}{\delta x_i^{k+1}} + \left\{ \sum_{k'=k}^{\infty} c^*_{k',1}\Delta_i^{k'} \overline{\frac{\partial^{k'+1}p}{\partial x_i^{k'+1}}} - c_{k,1}\Delta_i^k \overline{\frac{\partial^{k+1}p}{\partial x_i^{k+1}}} \right\} \\ &- \nu\frac{c_{k,1}}{\zeta}\Delta_j^k \frac{\delta^{k+2}\overline{u}_i}{\delta x_j^{k+2}} - \nu \left\{ \sum_{k'=k}^{\infty} c^*_{k',2}\Delta_j^{k'} \overline{\frac{\partial^{k'+2}u_i}{\partial x_j^{k'+2}}} - \frac{c_{k,1}}{\zeta}\Delta_j^k \overline{\frac{\partial^{k+2}u_i}{\partial x_j^{k+2}}} \right\}, \end{aligned} \tag{5.11}$$

with $c_{k,1}$ and $c_{k,2}$ the modified coefficients for the first and second derivatives respectively. Note that no summation is applied on the index k in the expressions above, since k denotes the order of accuracy. The scaling factor $\zeta = c_{k,1}/c_{k,2} = c^*_{k,1}/c^*_{k,2}$, is used in order to reformulate the modified leading order truncation term of the viscous terms as function of $c_{k,1}$. It is important to note that for expressions (5.10) and (5.11), the standard $(k+2)^{th}$-order finite difference approximation is obtained if $c_{k,n} = c^*_{k,n}$, whereas the accuracy remains of order k if $c_{k,n} \neq c^*_{k,n}$. Although in the latter case, the order of accuracy is not increased, it will be shown that an optimal value for the modified coefficient exists for which the magnitude of the remaining truncation error is minimal. The modified leading truncation term in each of the equations in (5.10) and (5.11) can now be converted into an expression with a single preceding coefficient $c_{k,1}$. In the following, the coefficient $c_{k,1}$ in the continuity equation (5.10) will be denoted as C^{π}, whereas the coefficients $c_{k,1}$ in each momentum equation (5.10) will be denoted as C_i^{σ}. Expressions (5.10) and (5.11) then finally

read

$$\Pi^{\Delta} = C^{\pi}\Delta_i^k \frac{\delta^{k+1}\overline{u}_i}{\delta x_i^{k+1}} + \mathscr{O}\left(\Delta^k\right) \tag{5.12}$$

$$\Sigma_i^{\Delta} = C_i^{\sigma}\left\{\Delta_j^k \overline{u}_j \frac{\delta^{k+1}\overline{u}_i}{\delta x_j^{k+1}} + \Delta_i^k \frac{\delta^{k+1}\overline{p}}{\delta x_i^{k+1}} - \frac{\nu}{\zeta}\Delta_j^k \frac{\delta^{k+2}\overline{u}_i}{\delta x_j^{k+2}}\right\} + \mathscr{O}\left(\Delta^k\right). \tag{5.13}$$

The optimal values for the coefficients C^{π} and C_i^{σ} must now be determined such that the global truncation error is minimal. Hereafter, it is explained that the sampling-based dynamic procedure is a useful tool for this purpose. It is emphasized that the current model-formulation has no other purpose than to demonstrate the capability of the generalized dynamic procedure to achieve improved accuracy, by minimizing the global magnitude of the truncation error. Other attempts to model the truncation error can be found in Fauconnier *et al.* [27], but are not discussed in this work.

5.2 The generalized dynamic procedure

In this section, the original dynamic procedure, based on the Germano identity [30] is extended to a more general approach so that it can be applied in the context of sampling. Note that Jeanmart *et al.* [43] already suggested the use of a sampling operator in the dynamic procedure. In analogy with the traditional filtering-based dynamic procedure, which relies on two filters with different cutoff wavenumber κ_c, the sampling-based dynamic procedure requires two sampling operators with different sampling frequency κ_s. This is explained further.

5.2.1 Concept

Consider sampling operators $\mathscr{S}^{\mathbf{\Delta}_1}$ and $\mathscr{S}^{\mathbf{\Delta}_2}$ which project the equations from the continuum spatial domain $\Omega \subset \mathbb{R}^3$ to two discrete spatial domains $\Omega^{\mathbf{\Delta}_1} \subset \mathbb{R}^3$ and $\Omega^{\mathbf{\Delta}_2} \subset \mathbb{R}^3$ with respectively $N_{1,j}$ and $N_{2,j}$ number of nodes in the j^{th} direction such that $N_{1,j} > N_{2,j}$, $\forall j = 1,2,3$. Let $\mathbf{\Delta}_1 = \Delta_{1,j}$ and $\mathbf{\Delta}_2 = \Delta_{2,j}$ denote the grid spacing in each direction j and assume that $\Delta_{2,j} = \alpha_j \Delta_{1,j}$, $\alpha_j \in \mathbb{N}$. Hence, only embedded computational grids are considered in this work, without any loss of generality.[4] Since the sampling operator is an orthogonal operator which satisfies the property

$$\mathscr{S}^{\mathbf{\Delta}_2} \circ \mathscr{S}^{\mathbf{\Delta}_1} \circ [u_i] = \mathscr{S}^{\mathbf{\Delta}_2} \circ [u_i], \tag{5.14}$$

$\mathscr{S}^{\mathbf{\Delta}_2}$ also projects Ω^{Δ_1} to Ω^{Δ_2}. Assume the notation $\mathscr{S}^{\mathbf{\Delta}_1} \circ u_i(\mathbf{x},t) = \overline{u}_i(\mathbf{x},t)$ and $\mathscr{S}^{\mathbf{\Delta}_2} \circ u_i(\mathbf{x},t) = \widetilde{u}_i(\mathbf{x},t) = \widetilde{\overline{u}}_i(\mathbf{x},t)$ for the sampled velocity field, and analogously

[4] Suppose $\alpha_j \in \mathbb{R}$, then appropriate interpolation functions must be used in order to evaluate these expressions on the same grid resolution.

for the sampled pressure field. Assume further the same notation as before for the discrete derivative operator $\mathscr{S}^{\mathbf{\Delta}_1} \circ \mathscr{S}^{\mathbf{\Delta}_2} \circ \partial = \delta$. Applying the operator $\mathscr{S}^{\mathbf{\Delta}_1}$ on the continuity equation (2.1) and Navier-Stokes equations (2.2) leads to

$$\begin{aligned} 0 &= \mathscr{C}(\overline{u}_i) - \Pi^{\Delta_1} && (5.15)\\ \frac{\partial \overline{u}_i}{\partial t} &= \mathscr{N}(\overline{u}_i, \overline{p}) + \Sigma_i^{\Delta_1}, && (5.16) \end{aligned}$$

where $\mathscr{C}(\overline{u}_i)$ and $\mathscr{N}(\overline{u}_i, \overline{p})$ respectively denote the continuity operator and the Navier-Stokes operator applied to the sampled velocity field $\overline{u}_i$ and pressure field $\overline{p}$. Similarly, applying $\mathscr{S}^{\mathbf{\Delta}_2}$ to the continuous set (2.1) and (2.2) yields

$$\begin{aligned} 0 &= \mathscr{C}(\widetilde{u}_i) - \Pi^{\Delta_2} && (5.17)\\ \frac{\partial \widetilde{u}_i}{\partial t} &= \mathscr{N}(\widetilde{u}_i, \widetilde{p}) + \Sigma_i^{\Delta_2}. && (5.18) \end{aligned}$$

Ideally, the latter set should also be obtained by applying the sampling operator $\mathscr{S}^{\mathbf{\Delta}_2}$ to the first set of equations (5.15)-(5.16) giving

$$\begin{aligned} 0 &= \mathscr{S}^{\mathbf{\Delta}_2} \circ \mathscr{C}(\overline{u}_i) - \mathscr{S}^{\mathbf{\Delta}_2} \circ \Pi^{\Delta_1} && (5.19)\\ \frac{\partial \widetilde{u}_i}{\partial t} &= \mathscr{S}^{\mathbf{\Delta}_2} \circ \mathscr{N}(\overline{u}_i, \overline{p}) + \mathscr{S}^{\mathbf{\Delta}_2} \circ \Sigma_i^{\Delta_1}. && (5.20) \end{aligned}$$

Consistency between formulations (5.17)-(5.18) and (5.19)-(5.20) imposes the following relations

$$\begin{aligned} -\mathscr{S}^{\mathbf{\Delta}_2} \circ \mathscr{C}(\overline{u}_i) + \mathscr{C}(\widetilde{u}_i) &= \Pi^{\Delta_2} - \mathscr{S}^{\mathbf{\Delta}_2} \circ \Pi^{\Delta_1} && (5.21)\\ \mathscr{S}^{\mathbf{\Delta}_2} \circ \mathscr{N}(\overline{u}_i, \overline{p}) - \mathscr{N}(\widetilde{u}_i, \widetilde{p}) &= \Sigma_i^{\Delta_2} - \mathscr{S}^{\mathbf{\Delta}_2} \circ \Sigma_i^{\Delta_1}, && (5.22) \end{aligned}$$

which explicitly express the commutation errors made by the projection $\Omega^{\Delta_1} \to \Omega^{\Delta_2}$. The left-hand sides of (5.21) and (5.22) are respectively called the scalar level and vector level equivalents of the Germano identity (3.60). They can be determined in terms of the resolved velocity $\overline{u}_i$, since $\mathscr{S}^{\mathbf{\Delta}_2} \circ u_i = \widetilde{u}_i = \widetilde{\overline{u}}_i$, and play the role of the Leonard scalar (5.21) or the Leonard vector (5.22). Assume that the truncation errors Π^{Δ_1} and $\Sigma_i^{\Delta_1}$ are approximated by a model-formulation as proposed in section (5.1.2)

$$\begin{aligned} \Pi^{\Delta_1} &= C^\pi m^\pi(\overline{u}_i) && (5.23)\\ \Sigma_i^{\Delta_1} &= C_i^\sigma m_i^\sigma(\overline{u}_i, \overline{p}), && (5.24) \end{aligned}$$

and analogously for Π^{Δ_2} and $\Sigma_i^{\Delta_2}$. Using a similar terminology as in the filtering-based dynamic procedure in section 3.3.3, expressions (5.21) and (5.22) can be redefined as

$$\begin{aligned} \mathscr{L}^\pi &= C^\pi \mathscr{M}^\pi && (5.25)\\ \mathscr{L}_i^\sigma &= C_i^\sigma \mathscr{M}_i^\sigma, && (5.26) \end{aligned}$$

in which the *Leonard terms* $\mathscr{L}$ and the *Model terms* $\mathscr{M}$ read

$$\mathscr{L}^\pi = -\mathscr{S}^{\mathbf{\Delta}_2} \circ \mathscr{C}(\overline{u}_i) + \mathscr{C}(\widetilde{u}_i) \tag{5.27}$$

$$\mathscr{L}_i^\sigma = \mathscr{S}^{\mathbf{\Delta}_2} \circ \mathscr{N}(\overline{u}_i, \overline{p}) - \mathscr{N}(\widetilde{u}_i, \widetilde{p}) \tag{5.28}$$

$$\mathscr{M}^\pi = m^\pi(\widetilde{u}_i) - \mathscr{S}^{\mathbf{\Delta}_2} \circ m^\pi(\overline{u}_i) \tag{5.29}$$

$$\mathscr{M}_i^\sigma = m_i^\sigma(\widetilde{u}_i, \widetilde{p}) - \mathscr{S}^{\mathbf{\Delta}_2} \circ m_i^\sigma(\overline{u}_i, \overline{p}). \tag{5.30}$$

The Leonard terms, which are resemblant to the expressions (5.3)-(5.4), are determined by

$$\mathscr{L}^\pi = -\widetilde{\frac{\delta\overline{u}_i}{\delta x_i}} + \frac{\delta\widetilde{\overline{u}}_i}{\delta x_i} \tag{5.31}$$

$$\mathscr{L}_i^\sigma = \widetilde{\overline{u}}_j \left(\widetilde{\frac{\delta\overline{u}_i}{\delta x_j}} - \frac{\delta\widetilde{\overline{u}}_i}{\delta x_j} \right) + \left(\widetilde{\frac{\delta\overline{p}}{\delta x_i}} - \frac{\delta\widetilde{\overline{p}}}{\delta x_i} \right) - \nu \left(\widetilde{\frac{\delta^2\overline{u}_i}{\delta x_j^2}} - \frac{\delta^2\widetilde{\overline{u}}_i}{\delta x_j^2} \right). \tag{5.32}$$

Using the expressions (5.12) and (5.13), and assuming that $\Delta_{1,j} = \Delta_j$ whereas $\Delta_{2,j} = \alpha_j \Delta_j$, similar expressions are obtained for the model terms, yielding

$$\mathscr{M}^\pi = -\Delta_i^k \left\{ \alpha_i^k \frac{\delta^{k+1}\widetilde{\overline{u}}_i}{\delta x_i^{k+1}} - \widetilde{\frac{\delta^{k+1}\overline{u}_i}{\delta x_i^{k+1}}} \right\} \tag{5.33}$$

$$\begin{aligned} \mathscr{M}_i^\sigma = {} & \widetilde{\overline{u}}_j \Delta_j^k \left\{ \alpha_j^k \frac{\delta^{k+1}\widetilde{\overline{u}}_i}{\delta x_j^{k+1}} - \widetilde{\frac{\delta^{k+1}\overline{u}_i}{\delta x_j^{k+1}}} \right\} + \Delta_i^k \left\{ \alpha_i^k \frac{\delta^{k+1}\widetilde{\overline{p}}}{\delta x_i^{k+1}} - \widetilde{\frac{\delta^{k+1}\overline{p}}{\delta x_i^{k+1}}} \right\} \\ & - \frac{\nu}{\zeta} \Delta_j^k \left\{ \alpha_j^k \frac{\delta^{k+2}\widetilde{\overline{u}}_i}{\delta x_j^{k+2}} - \widetilde{\frac{\delta^{k+2}\overline{u}_i}{\delta x_j^{k+2}}} \right\}. \end{aligned} \tag{5.34}$$

Notice that the ratio $\alpha_j = \Delta_{2,j}/\Delta_{1,j}$ determines the ratio of the sampling frequencies in each direction as $\alpha_j = \kappa_{s,1}/\kappa_{s,2}$.
Relations (5.25) and (5.26) determine a set of 4 independent linear equations for 4 independent unknown coefficients. However, in order to obtain expressions (5.25) and (5.26), the coefficients C^π and C_i^σ are necessarily assumed constant on both grid resolutions such that

$$C^\pi \mathscr{S}^{\Delta_2} \circ [m^\pi(\overline{u}_i)] = \mathscr{S}^{\Delta_2} \circ [C^\pi m^\pi(\overline{u}_i)] \tag{5.35}$$

$$C_i^\sigma \mathscr{S}^{\Delta_2} \circ [m_i^\sigma(\overline{u}_i, \overline{p})] = \mathscr{S}^{\Delta_2} \circ [C_i^\sigma m_i^\sigma(\overline{u}_i, \overline{p})]. \tag{5.36}$$

This is reminiscent to the assumptions of the filter-based dynamic procedure as discussed in section 3.3.3. Therefore, the constant coefficients C^π and C_i^σ are obtained by minimizing the mean-square error

$$\mathscr{E}^\pi = \left\langle (\mathscr{L}^\pi - C^\pi \mathscr{M}^\pi)^2 \right\rangle, \tag{5.37}$$

$$\mathscr{E}_i^\sigma = \left\langle (\mathscr{L}_i^\sigma - C_i^\sigma \mathscr{M}_i^\sigma)^2 \right\rangle, \tag{5.38}$$

where $\langle . \rangle$ denotes the spatial averaging over the entire computational domain. Note that $\mathscr{E}^{\pi}$ and $\mathscr{E}_i^{\sigma}$ are determined by the remaining truncation error $\mathscr{O}\left(\Delta^k\right)$ in expressions (5.12) and (5.13). Hence, minimization of the errors (5.37) and (5.38), implies minimization of the global truncation error. Finally, differentiation with respect to C^{π} and C_i^{σ} yields[5]

$$C^{\pi} = \frac{\langle \mathscr{L}^{\pi} \mathscr{M}^{\pi} \rangle}{\langle \mathscr{M}^{\pi} \mathscr{M}^{\pi} \rangle} \tag{5.39}$$

$$C_i^{\sigma} = \frac{\langle \mathscr{L}_i^{\sigma} \mathscr{M}_i^{\sigma} \rangle}{\langle \mathscr{M}_i^{\sigma} \mathscr{M}_i^{\sigma} \rangle}. \tag{5.40}$$

Since these coefficients are recalculated by the sampling-based dynamic procedure at each new iteration, their values will correspond according to the specific characteristics of the flow at that iteration. Moreover, it can already be understood that if the flow pattern is smooth, the truncation series converges very fast to zero, such that the resulting dynamic coefficients tend to their theoretical values, whereas for non-smooth flow patterns, the coefficients will differ significantly from their theoretical value due to the slowly converging truncation series. Once the value of the coefficients is determined, substitution into expressions (5.12) and (5.13) is expected to lead finally to an *optimized* finite difference scheme for the Navier-Stokes equations and the continuity equation.

5.2.2 Modification to the generalized dynamic procedure

Although the presented dynamic procedure is mathematically consistent, an oversensitivity to non-smooth fields has been observed, resulting into suboptimal values for the coefficients. In order to control the high-wavenumber sensitivity, the sampling-based dynamic procedure is slightly modified by introducing a *blending factor* f into the truncation errors Π^{Δ_2} and $\Sigma_i^{\Delta_2}$ such that

$$\Pi^{\Delta_2} = C^{\pi} \left[f m^{\pi}\left(\widetilde{u}_i\right) + (1-f)\, \alpha^k \mathscr{S}^{\Delta_2} \circ m^{\pi}\left(\overline{u}_i\right) \right] \tag{5.41}$$

$$\Sigma_i^{\Delta_2} = C_i^{\sigma} \left[f m_i^{\sigma}\left(\widetilde{u}_i, \widetilde{p}\right) + (1-f)\, \alpha^k \mathscr{S}^{\Delta_2} \circ m_i^{\sigma}\left(\overline{u}_i, \overline{p}\right) \right], \tag{5.42}$$

If $f = 1$, then the original dynamic procedure is recovered. If $f = 0$, the model terms $\mathscr{M}$ reduce to

$$\mathscr{M}^{\pi} = \left(\alpha^k - 1\right) \mathscr{S}^{\mathbf{\Delta}_2} \circ m^{\pi}\left(\overline{u}_i\right) \tag{5.43}$$

$$\mathscr{M}_i^{\sigma} = \left(\alpha^k - 1\right) \mathscr{S}^{\mathbf{\Delta}_2} \circ m_i^{\sigma}\left(\overline{u}_i, \overline{p}\right). \tag{5.44}$$

[5] No summation over index i in these expressions.

The dynamic coefficients are then readily obtained by (5.25) and (5.26) as

$$C^{\pi} = \frac{\mathscr{L}^{\pi}}{\mathscr{M}^{\pi}} = -\frac{\mathscr{S}^{\mathbf{\Delta}_2} \circ \mathscr{C}\left(\overline{u}_i\right) - \mathscr{C}\left(\widetilde{u}_i\right)}{\left(\alpha^k - 1\right) \mathscr{S}^{\mathbf{\Delta}_2} \circ m^{\pi}\left(\overline{u}_i\right)} \tag{5.45}$$

$$C_i^{\sigma} = \frac{\mathscr{L}_i^{\sigma}}{\mathscr{M}_i^{\sigma}} = \frac{\mathscr{S}^{\mathbf{\Delta}_2} \circ \mathscr{N}\left(\overline{u}_i, \overline{p}\right) - \mathscr{N}\left(\widetilde{u}_i, \widetilde{p}\right)}{\left(\alpha^k - 1\right) \mathscr{S}^{\mathbf{\Delta}_2} \circ m_i^{\sigma}\left(\overline{u}_i, \overline{p}\right)}. \tag{5.46}$$

Substitution of these expressions into (5.41) and (5.42) and further elaboration finally leads to the finite difference approximation for the continuity and Navier-Stokes equations on the coarse grid level

$$0 = \frac{\alpha^k \mathscr{S}^{\mathbf{\Delta}_2} \circ \mathscr{C}\left(\overline{u}_i\right) - \mathscr{C}\left(\widetilde{u}_i\right)}{\alpha^k - 1} + \mathscr{O}\left(\Delta^{k+1}\right) \tag{5.47}$$

$$\frac{\partial \widetilde{u}_i}{\partial t} = \frac{\alpha^k \mathscr{S}^{\mathbf{\Delta}_2} \circ \mathscr{N}\left(\overline{u}_i, \overline{p}\right) - \mathscr{N}\left(\widetilde{u}_i, \widetilde{p}\right)}{\alpha^k - 1} + \mathscr{O}\left(\Delta^{k+1}\right). \tag{5.48}$$

Both expressions are known as *Richardson extrapolation*, and are equivalent with a standard higher-order approximation with formal order of accuracy $\mathscr{O}\left(\Delta^{k+1}\right)$.[6] Moreover, it is verified that the dynamic coefficients reduce to their theoretical Taylor values such that $C^{\pi} = C^{\pi *}$ and $C_i^{\sigma} = C_i^{\sigma *}$ and thus $c_{k,n} = c_{k,n}^*$.

Summarizing, the introduced blending factor provides a blending between the dynamically optimized finite difference schemes ($f = 1$) and the standard high-order schemes $f = 0$. Therefore it allows to control the sensitivity of the procedure to high-wavenumber information, reflected by the magnitude of the truncation series. Although in the next chapter, a detailed analysis is given of Richardson extrapolation and the role of the blending factor, the current analysis suffices for the time being. The performance of the dynamically optimized scheme and the role of the blending factor f is examined in the following numerical experiment for the steady laminar flow in the lid-driven cavity.

5.3 A FIRST NUMERICAL EXPERIMENT

Hereafter, the capability of the generalized dynamic procedure to obtain higher accuracy by minimizing the global truncation error is evaluated for a two-dimensional steady laminar flow in the lid-driven cavity [27, 28]. Although the proposed method is designed for Large-Eddy Simulation where the velocity field is far from smooth, application to smooth laminar flows is expected to already demonstrate the performance of the method. Indeed, a laminar flow does not necessarily implicate that the resolved velocity field is well-resolved and smooth with respect to the grid resolution. Moreover, the laminar test case allows to avoid turbulence modeling ambiguities that interfere with the numerical accuracy as shown by the work of Meyers *et al.* [60, 59].

[6] For central finite difference approximations the formal order of accuracy becomes $\mathscr{O}\left(\Delta^{k+2}\right)$.

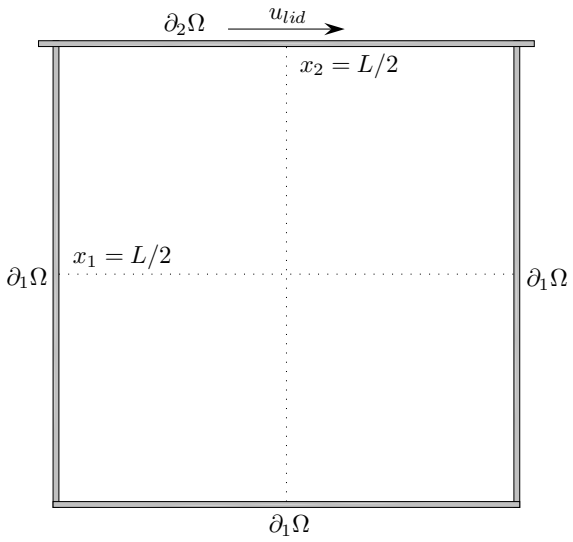

Figure 5.1: Lid-driven cavity. The two dimensional square lid driven cavity encloses the interior domain $\Omega = [0, \mathscr{L}] \times [0, \mathscr{L}] \subset \mathbb{R}^2$ and has uniform velocity u_{lid} at the boundary $\partial_2\Omega$.

5.3.1 THE LID-DRIVEN CAVITY: SETUP

In the driven cavity, an internal recirculating flow is generated by a uniform moving wall in a two-dimensional square closed domain as illustrated in Figure 5.1. The flow is representative for more complex situations with vortices and secondary flows, and is a challenging test case [77]. On each wall, impermeability conditions and no-slip conditions are imposed. This implies that the fluid is supposed to move with the lid at the lid, and that it is stationary at the two side walls and the bottom wall. This leads to so-called corner singularities at both top corners due to the discontinuity in the imposed boundary conditions. Shankar *et al.* [77] concluded that the effects of the corner singularities are confined to the neighborhood of the corners, and that the influence is negligible for the interior flow. However, since by definition a singularity is an infinite pole, the problem is ill-posed and the corner singularities are unphysical. In reality, slip must occur in the near vicinity of the corners in order to have a continuous regular flow. Some repercussions toward numerical simulation are observed if no-slip is enforced. The flow solution will not converge to a grid-independent solution when refining the computational grid. Indeed, it is observed that the variables, e.g. the pressure, at the singularities do not converge to a limit-value, but tend to infinity. As a consequence, the pressure gradients in the vicinity of the singularity also tend to infinity, which implies that the spectral content of the velocity field and the pressure field becomes infinite. In order to resolve such a flow, an LES-technique would be necessary that limits the spectral content according to the Nyquist criterion. In this work, a rough ad hoc

slip-model is assumed which imposes a sinusoidal velocity-profile of the fluid at the lid, instead of a uniform velocity-profile. It is emphasized that such a method has no other intention than ensuring the well-posedness of the problem and to avoid any ambiguity in the results. Hereafter, the consequences of this rough approximation will be demonstrated.

The pseudo-compressibility algorithm, described in section 4.3.3, is used in order to solve the analytical equations in the square two-dimensional domain $\Omega = [0, \mathscr{L}] \times [0, \mathscr{L}] \subset \mathbb{R}^2$, $\mathscr{L}$ being unity. The Reynolds number, based on the height and maximum lid-velocity, is chosen $Re = 400$ such that the flow is laminar and steady [77]. The governing equations then read

$$\frac{1}{c^2}\frac{\partial p}{\partial \tau} + \frac{\partial u_i}{\partial x_i} = 0 \tag{5.49}$$

$$\frac{\partial u_i}{\partial \tau} + u_j \frac{\partial u_i}{\partial x_j} = -\frac{\partial p}{\partial x_i} + \nu \frac{\partial^2 u_i}{\partial x_j^2}, \tag{5.50}$$

were c denotes the artificial speed of sound and τ is the pseudo time. These equations are supplemented with a set of Dirichlet boundary conditions

$$\partial_1\Omega \rightarrow u_i = 0, \quad i = 1, 2 \tag{5.51}$$

$$\partial_2\Omega \rightarrow u_1 = u_{lid} \sin(\pi x_1), \quad u_2 = 0. \tag{5.52}$$

The discrete equations are obtained by projecting the continuum equations from $\Omega \rightarrow \Omega^{\Delta}$ by means of the spatial sampling operator $\mathscr{S}^{\mathbf{\Delta}}$ and the temporal sampling operator $\mathscr{S}^{\Delta_t}$, yielding

$$\frac{1}{c^2}\frac{\delta \overline{p}}{\delta \tau} + \frac{\delta \overline{u}_i}{\delta x_i} = \Pi^{\Delta} + \mathscr{D}\left(\Delta^k\right) \tag{5.53}$$

$$\frac{\delta \overline{u}_i}{\delta \tau} + \overline{u}_j \frac{\delta \overline{u}_i}{\delta x_j} = -\frac{\delta \overline{p}}{\delta x_i} + \nu \frac{\delta^2 \overline{u}_i}{\delta x_j^2} + \Sigma_i^{\Delta}, \tag{5.54}$$

where $\mathscr{D}\left(\Delta^k\right)$ denotes the dissipator which precludes odd-even decoupling as described in 4.3.3. Time-stepping in pseudo-time τ is performed with a 3-stage Runge-Kutta method. The spatial derivatives are approximated using explicit central finite difference methods in the interior domain whereas at the boundaries eccentric finite difference approximations are used. Since no analytical solution exists, a highly accurate reference solution was generated on a 120×120 uniform computational grid with an 8^{th} -order finite difference method. The dissipator is determined as

$$\mathscr{D}\left(\Delta^7\right) = \frac{\sigma}{u_{lid}} \Delta_i^7 \frac{\delta^8 \overline{p}}{\delta x_i^8}, \quad \sigma = \frac{1}{512}, u_{lid} = 1 \tag{5.55}$$

such that the resulting reference solution is $\mathscr{O}\left(\Delta^7\right)$. All other finite difference simulations were performed on a 60×60 grid using the same dissipator as for the

reference solution. For the dynamically optimized finite difference method, using the model-formulation for the truncation errors in combination with the *modified* sampling-based dynamic procedure, a 2^{nd} -order finite difference method is used for approximating the partial derivatives in (5.53) and (5.54). Hence, the model-formulation of the leading order truncation terms is discretized as

$$\Pi^{\Delta} = C^{\pi}\Delta_i^2 \frac{\delta^3 \overline{u}_i}{\delta x_i^3} + \mathscr{O}\left(\Delta^2\right) \tag{5.56}$$

$$\Sigma_i^{\Delta} = C_i^{\sigma}\left\{\Delta_j^2 \overline{u}_j \frac{\delta^3 \overline{u}_i}{\delta x_j^3} + \Delta_i^2 \frac{\delta^3 \overline{p}}{\delta x_i^3} - \frac{\nu}{2}\Delta_j^2 \frac{\delta^4 \overline{u}_i}{\delta x_j^4}\right\} + \mathscr{O}\left(\Delta^2\right). \tag{5.57}$$

where the coefficients must have the values $C^{\pi} = 1/6$ and $C_i^{\sigma} = 1/6$, $\forall i$ in order to obtain formal 4^{th} -order accuracy. Nevertheless, both coefficients are determined each Runge-Kutta step in pseudo time using the *modified* sampling-based dynamic procedure, in which several values for the *blending factor* f are investigated. Note that the proposed dynamically optimized 2^{nd} -order finite difference approach requires at most a 5-point stencil, which is equivalent with the standard 4^{th} -order finite difference method requirements. Moreover, the evaluation of the dynamic coefficient requires also at most a 5-point stencil on both the fine-grid level and the coarse-grid level. Due to the current *multi-grid* implementation of the procedure, the computational cost of the dynamic procedure is acceptable. However, if the procedure's implementation would be done on a single grid, the required stencil width for the coarse formulation would be 9, which makes it computationally more expensive. Nevertheless, recall that the intention for this first test is to examine the potential of the current method rather than optimizing the technique. More efficient implementations will be presented in the following chapter and a general discussion about the computational cost will be given in Chapter 8, Section 8.6. In order to allow comparison of the quality of the dynamic finite difference scheme with that of standard explicit finite difference methods, 2^{nd} -, 4^{th} - and 6^{th} -order solutions were generated. The results are discussed in the following paragraph.

5.3.2 The Lid-Driven Cavity: results and discussion

Figure 5.2 demonstrates the 8^{th} -order reference solution (120×120) of the velocity field $\overline{\mathbf{u}}(\mathbf{x})$ and the pressure field $\overline{p}(\mathbf{x})$ in the steady state laminar cavity-flow at Reynolds number $\mathrm{Re} = 400$. In order to examine the consequences of replacing the no-slip boundary conditions at the lid with a sinusoidal fluid-velocity profile, the solution is compared with that obtained with a uniform fluid-velocity at the lid. Figure 5.3 shows the velocity components and the pressure field in two orthogonal cross-sections of the cavity (see Figure 5.1). Despite the different fluid-velocity profiles at the lid, both solutions compare reasonably well to each other and the general flow characteristics seem preserved. Nevertheless, slight differences are observed. Indeed, replacing the uniform profile with the sinusoidal profile, reduces

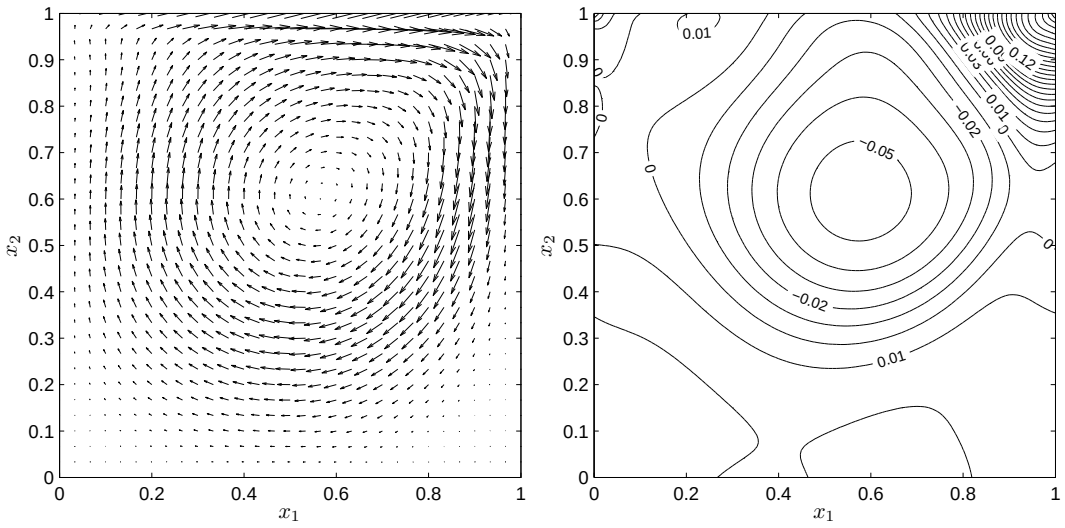

Figure 5.2: Lid-driven cavity at Re $= 400$**.** The velocity vectors $\mathbf{u}(\mathbf{x}) = u_i(x_j)$, $i,j = 1,2$ (**left**) and contours of the pressure field $p(\mathbf{x})$ (**right**) of the 8^{th} -order reference solution on a 120×120 grid. Note that the mean pressure is forced to be zero.

the mean vorticity magnitude of the cavity flow[7] with approximately 32.5% making the flow field smoother. As expected, the corner singularities vanish for the sinusoidal profile such that a grid independent solution is obtained in case of grid refinement. In summary, the current mathematical problem definition is well-posed and leads to a regular solution which is in reasonable agreement with that of the traditional problem definition. Hence, the proposed sinusoidal profile of the fluid-veloctiy at the lid is maintained for further calculations.

The accuracy of the dynamic finite difference scheme is investigated for different values of the blending factor $f = 1/i$, $i = 1, \ldots, 5$. The accuracy of the results is compared to that of the standard explicit 2^{nd} -, 4^{th} - and 6^{th} -order finite difference schemes. Figures 5.4 and 5.5 display the absolute errors between the solution of the various simulations on the 60×60 grid and that of the 8^{th} -order reference solution on the 120×120 grid, i.e. for a resolved variable $\overline{\phi}$

$$\varepsilon_{\overline{\phi}} = \left| \overline{\phi}_{reference} - \overline{\phi} \right|, \tag{5.59}$$

in the two orthogonal cross-sections ($x_1 = \mathscr{L}/2$ and $x_2 = \mathscr{L}/2$) indicated in Figure 5.1. Further, Table 5.1 gives an overview of the global accuracy per variable, for the

[7] The mean vorticity magnitude is defined as

$$\langle \omega \rangle = \iint |\nabla \times \mathbf{u}(\mathbf{x})| \, d\Omega. \tag{5.58}$$

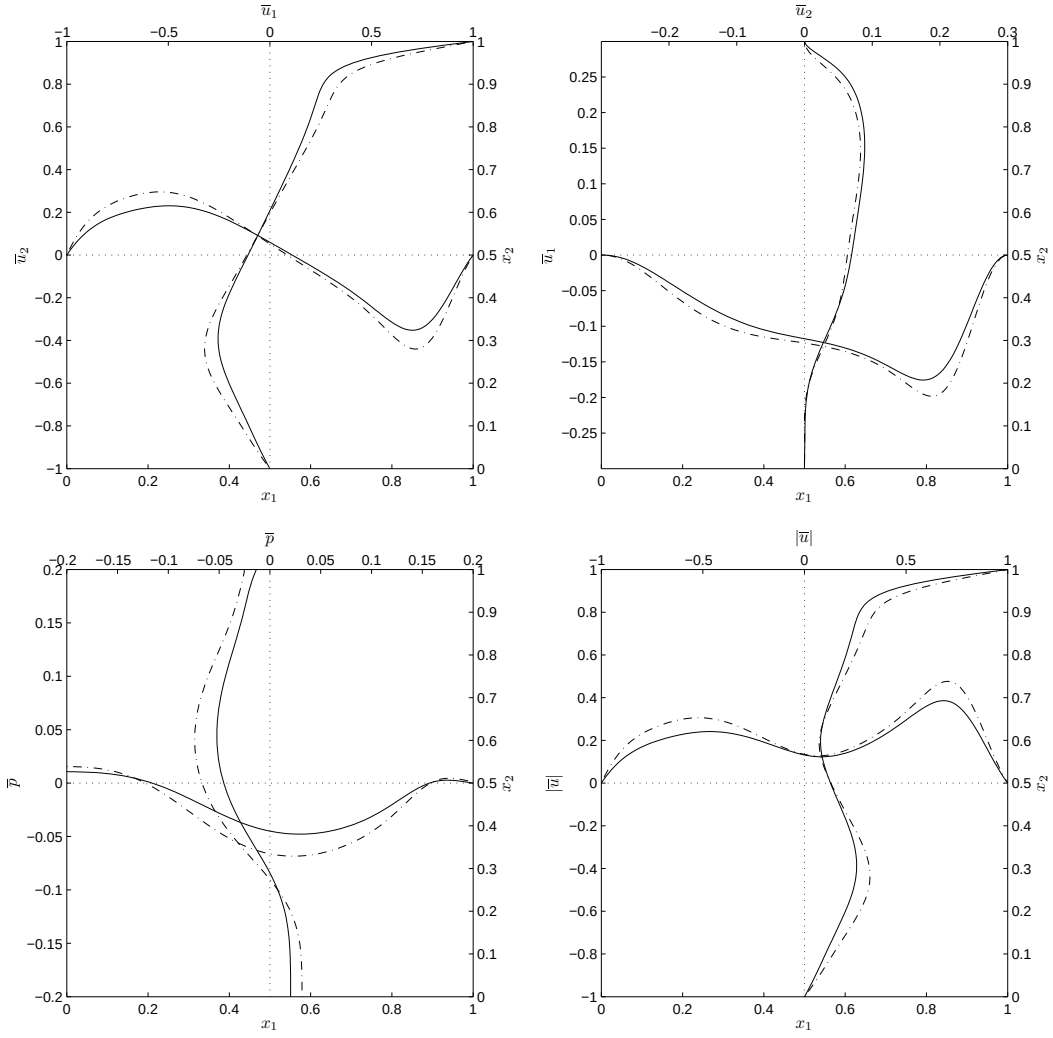

Figure 5.3: Lid-driven cavity at Re = 400**.** Various velocity and pressure profiles at the cross-sections $x_1 = \mathscr{L}/2$ and $x_2 = \mathscr{L}/2$ of the 8^{th} -order reference solution on a 120×120 grid, for a sinusoidal fluid-velocity (——) and a uniform fluid-velocity (–·–·) at the lid. Despite the differences, the general flow characteristics remain similar.

	2^{nd}	4^{th}	6^{th}	$f=\frac{1}{5}$	$f=\frac{1}{4}$	$f=\frac{1}{3}$	$f=\frac{1}{2}$	$f=1$
$L_{2,\overline{u}_1}$	0.3411	0.0230	0.0113	0.0120	0.0121	0.0126	0.0147	0.0333
$L_{2,\overline{u}_2}$	0.3932	0.0288	0.0142	0.0092	0.0091	0.0094	0.0115	0.0327
$L_{2,\overline{p}}$	0.1260	0.0340	0.0329	0.03013	0.0302	0.0302	0.0304	0.0321

Table 5.1: The L_2-norms for various finite difference schemes. Notice that for $f = 1$, poor accuracy is obtained, whereas for a nearly optimal value $f = 1/4$ the accuracy exceeds that of the 6^{th} -order solution.

different simulations. The global accuracy of a resolved variable $\overline{\phi}$ is defined by the L_2-norm

$$L_{2,\overline{\phi}} = \sqrt{\sum_{\Omega} \left(\overline{\phi}_{reference} - \overline{\phi}\right)^2}. \tag{5.60}$$

First, it is observed from Figures 5.4 and 5.5, that the original sampling-based dynamic procedure with blending factor $f = 1$ leads to rather poor results. Indeed, Table 5.1 confirms that for $f = 1$, the accuracy of the dynamic finite difference scheme lies between that of the 2^{nd} - and 4^{th} -order standard explicit schemes. As mentioned in the previous section, the sampling-based dynamic procedure with $f = 1$ appears to be extremely sensitive to high-wavenumber information leading to suboptimal predictions of the dynamic coefficients. This conclusion is supported by the results of the theoretical analysis in the next chapter. Nevertheless, decreasing the value of the blending factor results into a substantial accuracy improvement of the dynamic finite difference scheme. The various error profiles in Figures 5.4 and 5.5 reveal that the accuracy for $f \neq 1$ is at least as good as that of the 6^{th} -order standard finite difference scheme, and often better. Although comparable error levels are obtained for $f = 1/3$, $f = 1/4$ and $f = 1/5$, Table 5.1 indicates that $f = 1/4$ is closest to an optimal value. Note that the obtained solution for $f = 0$, is not explicitly shown in the graphs since it would collapse with that of the 4^{th} -order solution. It is verified from Table 5.2 that for $f = 0$, the dynamic coefficients tend to their theoretical Taylor series value, i.e. $C^{\pi} = 1/6$ $C_i^{\sigma} = 1/6$, $i = 1, 2$. Hence, the method reduces to pure Richardson extrapolation which is equivalent with the 4^{th} -order method as discussed section 5.2.2. Further Table 5.2 shows that the coefficients deviate from their Taylor series value for increasing values of the blending factor. Although the coefficients C^{π} and C_2^{σ} tend to increase with increasing f, the opposite behaviour is noticed for C_1^{σ}. For $f = 1$, the values are inconsistent with the observed tendency for lower blending factors. This supports the previous conclusion that $f = 1$ generates suboptimal coefficients due to the procedure's oversensitivity to high-wavenumber information. It should be emphasized that the dynamic coefficients in Table 5.2 are uniquely determined by the grid resolution, the specific implementation of the dynamic scheme, the value of f and the particular flow characteristics related to the Reynolds number. Hence, these values may not be considered universal and

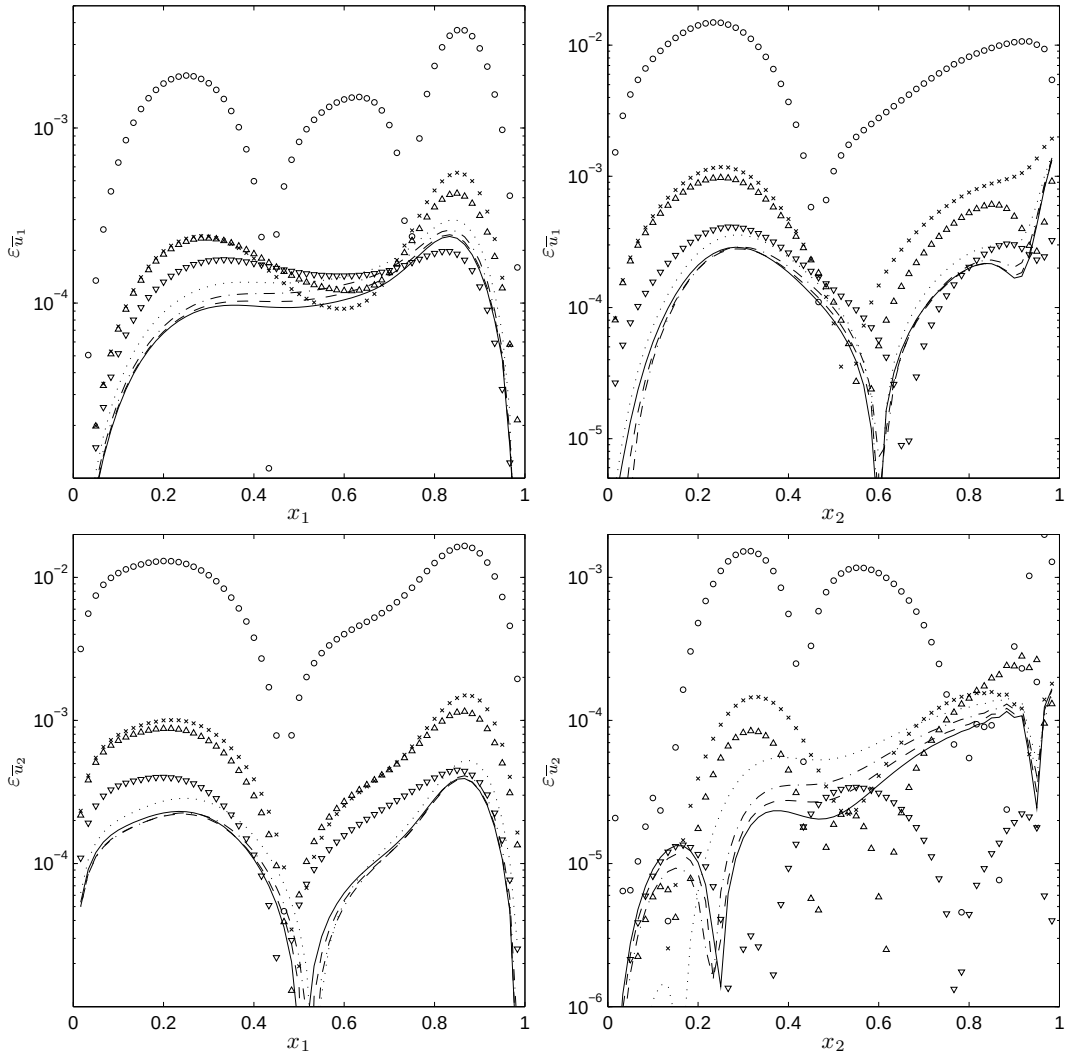

Figure 5.4: Lid-driven cavity at Re = 400**.** Error profiles for velocity components $\overline{u}_1$ (**upper**) and $\overline{u}_2$ (**lower**) at the cross-sections $x_1 = \mathscr{L}/2$ (**left**) and $x_2 = \mathscr{L}/2$ (**right**). Distinguish the dynamic schemes with $f = 1$ ($\times$), $f = \frac{1}{2}$ ($\cdots$), $f = \frac{1}{3}$ ($-\cdot-\cdot$), $f = \frac{1}{4}$ ($---$), $f = \frac{1}{5}$ (———) and the standard 2^{nd} -($\circ$), 4^{th} -($\triangle$), 6^{th} -order ($\triangledown$) explicit finite difference schemes.

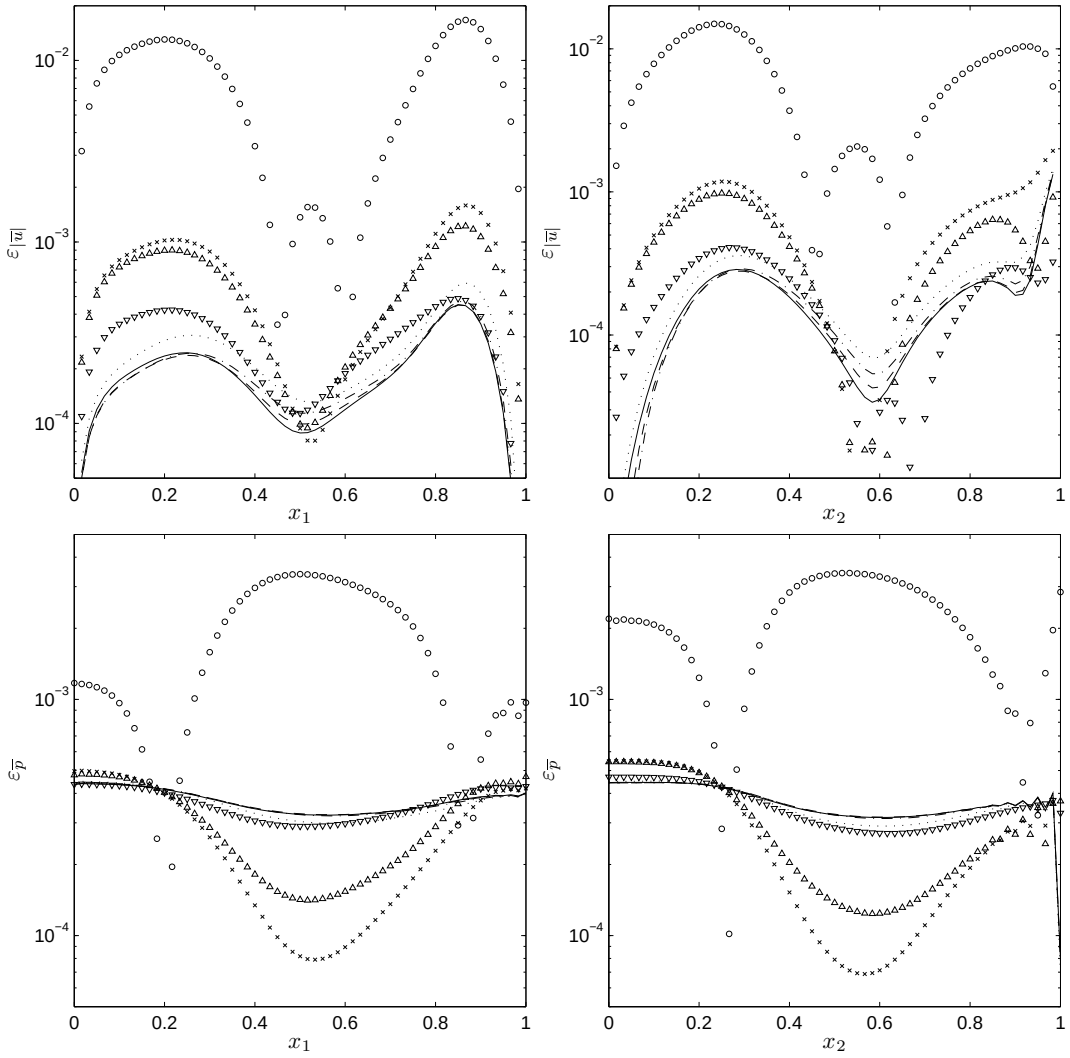

Figure 5.5: Lid-driven cavity at Re = 400**.** Error profiles for velocity magnitude $|\overline{\mathbf{u}}|$ (**upper**) and the pressure $\overline{p}$ (**lower**) at the cross-sections $x_1 = \mathscr{L}/2$ (**left**) and $x_2 = \mathscr{L}/2$ (**right**). Distinguish the dynamic schemes with $f = 1$ ($\times$), $f = \frac{1}{2}$ ($\cdots$), $f = \frac{1}{3}$ ($-\cdot-\cdot$), $f = \frac{1}{4}$ ($---$), $f = \frac{1}{5}$ (———) and the standard 2^{nd} -($\circ$), 4^{th} -($\triangle$), 6^{th} -order ($\triangledown$) explicit finite difference schemes.

	$f=0$	$f=\frac{1}{5}$	$f=\frac{1}{4}$	$f=\frac{1}{3}$	$f=\frac{1}{2}$	$f=1$
C^{π}	0.1667	0.1694	0.1699	0.1705	0.1708	0.1652
C_1^{σ}	0.1667	0.1633	0.1622	0.1603	0.1559	0.1400
C_2^{σ}	0.1667	0.1753	0.1770	0.1792	0.1834	0.1791

Table 5.2: The dynamic coefficients as function of the blending factor f. Notice that for $f = 0$, the theoretical Taylor series value 1/6 is recovered from the dynamic procedure. However, for increasing values of f, the dynamic coefficients deviate from this value.

are only *optimal* for this specific set of simulations. But it is exactly this self-adaptivity of the presented methodology that is very attractive since for every flow an optimal numerical method could be obtained.

5.4 Conclusions and Perspectives

In the present chapter, a dynamic finite difference method was constructed by using a specific model-formulation for the truncation error in which a coefficient must be optimized. This coefficient is determined by means of a modified sampling-based dynamic procedure whose sensitivity to high-wavenumber information is controlled by the appropriate choice of a blending factor. The presented results clearly demonstrate the ability of this dynamic procedure to obtain a nearly optimal coefficient in the adopted finite difference discretization. Hence, the dynamic finite difference method adapts itself in order to obtain optimal accuracy for a specific simulation. Application to the steady laminar flow in the lid-driven cavity (Re = 400), reveals that the optimized 2^{nd} -order scheme can achieve a higher accuracy than the standard 6^{th} -order finite difference scheme.

Although very promising and encouraging results were found, this numerical experiment was only intended as a first attempt to validate the concept and to demonstrate the potential of the proposed approach. Indeed, more efficient and more accurate finite difference approximations can, and will, be constructed with the current technology. First, the concept of the sampling-based dynamic procedure will be focussed to the finite difference approximations for a single derivative instead of for an entire partial differential equation. Since each derivative is then independently optimized, significant quality-improvement is expected. A thorough Fourier analysis of the resulting scheme will subsequently be performed, which allows one to better understand the role of the blending factor. A methodology is derived in order to determine the optimal blending factor corresponding to the energy spectrum of the flow. It will be shown that the resulting dynamic finite difference approximations are closely related to the Dispersion-Relation Preserving schemes of Tam *et al.* [79], but have the advantage to be self-adaptive according to the instantaneous flow characteristics.

Truth is ever to be found in the simplicity, and not in the multiplicity and confusion of things.

Newton, Isaac

6

Dynamic Finite Difference Approximations

In the previous chapter, a finite difference methodology was presented in which, for each partial differential equation, an optimal dynamic coefficient needed to be determined in order to minimize the global magnitude of the truncation error. A modified variant of the sampling-based dynamic procedure was proposed for calculating that coefficient. This approach succeeded in obtaining better accuracy for the simple numerical simulation of a two-dimensional laminar cavity flow. The results were found to be very promising and encouraging. Nevertheless, it was argued that refining this methodology by applying it to each derivative separately, instead of to an entire partial differential equation at once, might be beneficiary.

The current chapter is devoted to the mathematical construction of a family of dynamic low-dispersive finite difference approximations for the partial derivatives. Both explicit and implicit dynamic low-dispersive finite difference approximations are constructed by combining Taylor series expansions on two different grid resolutions. The accuracy of the constructed schemes is analyzed in Fourier space, using modified wavenumbers. Since one of these schemes is spatially nonlinear, a multiple-wave Fourier analysis of the transfer function is performed. This multiple-wave analysis provides a new approach for the analysis of spatially nonlinear finite difference schemes and was already presented in earlier work of Fauconnier *et al.* [27]. The relation of the dynamic schemes with the Dispersion-Relation-Preserving scheme of Tam *et al.* [79] and the Dispersion-Relation-Preserving compact Padé scheme of Kim *et al.* [45] is then demonstrated. Finally, a procedure to achieve the optimal blending factor in a dynamic finite difference scheme is proposed, in which a characteristic energy spectrum is assumed. The effect of the specific choice of the spectrum on this parameter is discussed.

6.1 CONSTRUCTION

In order to avoid an overload in notation the following discussion is restricted, without any loss of generality, to one spatial dimension, whereas the time-dimension is not explicitly written.

6.1.1 EXPLICIT DYNAMIC FINITE DIFFERENCE APPROXIMATIONS

Consider a k^{th}-order explicit *central* finite difference approximation for the n^{th} partial derivative of a variable $u(x) = u(x,t), x \in \mathbb{R}$ on a computational grid with grid spacing Δ, such that in a point $x = x_i$

$$\left.\frac{\delta^n \overline{u}}{\delta x^n}\right|^{\Delta}(x_i) = \frac{1}{\Delta^n}\sum_{j=-r}^{r}\beta_j \overline{u}(x_{i+j}). \tag{6.1}$$

The $2r+1$ weighting coefficients β_j depend on the adopted discretization and the value of n. Further, assume a similar k^{th}-order explicit finite difference approximation for the n^{th} partial derivative on the *same* computational grid with grid spacing Δ, but having a stencil width of $2\alpha r + 1$, $\alpha \in \mathbb{N}$, such that

$$\left.\frac{\delta^n \overline{u}}{\delta x^n}\right|^{\alpha\Delta}(x_i) = \frac{1}{(\alpha\Delta)^n}\sum_{j=-r}^{r}\beta_j \overline{u}(x_{i+\alpha j}). \tag{6.2}$$

The Taylor series expansions of both approximations (6.1) and (6.2) are then written as

$$\overline{\frac{\partial^n u}{\partial x^n}}(x) = \left.\frac{\delta^n \overline{u}}{\delta x^n}\right|^{\Delta} - \sum_{k'=k}^{\infty}\left(\sum_{j=-r}^{r}\frac{\beta_j\, j^{k'+n}}{(k'+n)!}\right)\Delta^{k'}\overline{\frac{\partial^{k'+n}u}{\partial x^{k'+n}}} \tag{6.3}$$

$$\overline{\frac{\partial^n u}{\partial x^n}}(x) = \left.\frac{\delta^n \overline{u}}{\delta x^n}\right|^{\alpha\Delta} - \sum_{k'=k}^{\infty}\left(\sum_{j=-r}^{r}\frac{\beta_j\, j^{k'+n}}{(k'+n)!}\right)(\alpha\Delta)^{k'}\overline{\frac{\partial^{k'+n}u}{\partial x^{k'+n}}}. \tag{6.4}$$

Two common techniques exist for achieving higher-order approximations from these series. One can either find a finite difference approximation for the leading order truncation term, or one can eliminate the coefficient of the leading order truncation term by combining the $\mathcal{O}\left(\Delta^{k+2}\right)$-truncated Taylor series in expressions (6.3) and (6.4). The latter technique, known as Richardson extrapolation, has no direct advantage over the first one, since both lead to a finite difference approximation of formal order of accuracy $k+2$. However, as will be shown below, the combination of both techniques can lead to a non-trivial self-adaptive dynamic scheme with basic order of accuracy k, but with better spectral characteristics.
Discretization of the leading order truncation term in both Taylor expansions (6.3)

and (6.4) with a 2^{nd} *-order* accurate finite difference approximation[1] results into the Taylor series expansions

$$\overline{\frac{\partial^n u}{\partial x^n}}(x) = \left.\frac{\delta^n \overline{u}}{\delta x^n}\right|^{\Delta} + c^*_{k,n}\Delta^k \left.\frac{\delta^{k+n}\overline{u}}{\delta x^{k+n}}\right|^{\Delta} + \sum_{k'=k+2}^{\infty} c^*_{k',n}\Delta^{k'}\overline{\frac{\partial^{k'+n}u}{\partial x^{k'+n}}} \tag{6.5}$$

$$\overline{\frac{\partial^n u}{\partial x^n}}(x) = \left.\frac{\delta^n \overline{u}}{\delta x^n}\right|^{\alpha\Delta} + c^*_{k,n}(\alpha\Delta)^k \left.\frac{\delta^{k+n}\overline{u}}{\delta x^{k+n}}\right|^{\alpha\Delta} + \sum_{k'=k+2}^{\infty} c^*_{k',n}(\alpha\Delta)^{k'}\overline{\frac{\partial^{k'+n}u}{\partial x^{k'+n}}}, \tag{6.6}$$

where the coefficients $c^*_{k,n}$ and $c^*_{k',n}$ are determined by the set of weighting coefficients β_j and n. Although the theoretical value of the coefficient of the leading order truncation term $c^*_{k,n}$ is known a priori, it is also possible to determine its value by combining the truncated expressions (6.5) and (6.6). The coefficient, obtained in that way, will not necessarily have the same value as the one obtained from the Taylor series, i.e. $c^*_{k,n}$, as it will be a function of $u(x)$ and its derivatives. Moreover, it will be shown that the obtained value of the coefficient can be optimal with respect to $\overline{u}(x)$, such that deficiencies of the resulting finite difference approximation, e.g. dispersion errors are minimized.
In order to retrieve the optimal value of the coefficient from equations (6.5) and (6.6) the *sampling-based dynamic procedure* is applied analogously as in the previous chapter. First the theoretical coefficient $c^*_{k,n}$ in equations (6.5) and (6.6) is replaced by the coefficient $c_{k,n}$. Further, a blending factor f is introduced into the coarse resolution equation (6.6), leading to a modified expression for the discretized leading order truncation term. The resulting equations then read

$$\overline{\frac{\partial^n u}{\partial x^n}}(x) = \left.\frac{\delta^n \overline{u}}{\delta x^n}\right|^{\Delta} + c_{k,n}\Delta^k \left.\frac{\delta^{k+n}\overline{u}}{\delta x^{k+n}}\right|^{\Delta} + \mathscr{O}\left(\Delta^k\right) \tag{6.7}$$

$$\overline{\frac{\partial^n u}{\partial x^n}}(x) = \left.\frac{\delta^n \overline{u}}{\delta x^n}\right|^{\alpha\Delta} + c_{k,n}(\alpha\Delta)^k \left\{ f \left.\frac{\delta^{k+n}\overline{u}}{\delta x^{k+n}}\right|^{\alpha\Delta} + (1-f) \left.\frac{\delta^{k+n}\overline{u}}{\delta x^{k+n}}\right|^{\Delta} \right\} + \mathscr{O}\left((\alpha\Delta)^k\right). \tag{6.8}$$

Unless $c_{k,n}$ has the exact Taylor value $c^*_{k,n}$, the order of accuracy in expressions (6.7) and (6.8) remains $\mathscr{O}\left(\Delta^k\right)$. This follows readily from the expression of the truncation series in (6.7), which is given by

$$\mathscr{O}\left(\Delta^k\right) = \sum_{k'=k}^{\infty} c^*_{k',n}\Delta^{k'}\overline{\frac{\partial^{k'+n}u}{\partial x^{k'+n}}} - c_{k,n}\Delta^k\overline{\frac{\partial^{k+n}u}{\partial x^{k+n}}}. \tag{6.9}$$

[1] Although other discretizations can be perfectly adopted, there would be no advantage in such an approach. Indeed, the higher-order accuracy is enitrely determined by the Taylor series in expressions (6.3) or (6.4) and not by the accuracy of the discretization of the leading order truncation term. Hence, in this work the 2^{nd} -order approximations are adopted for the discretization of the leading order truncation terms, which is the minimal order of accuracy.

The difference between the fine grid and coarse grid discretization is obtained by subtracting (6.8) from (6.7) giving,

$$\mathscr{E} \;=\; \mathscr{L} + c_{k,n}\mathscr{M} = \mathscr{O}\left((\alpha\Delta)^k\right) - \mathscr{O}\left(\Delta^k\right) \tag{6.10}$$

in which the *Leonard terms* $\mathscr{L}$ and the *Model terms* $\mathscr{M}$ read

$$\mathscr{L} \;=\; \left.\frac{\delta^n \overline{u}}{\delta x^n}\right|^{\Delta} - \left.\frac{\delta^n \overline{u}}{\delta x^n}\right|^{\alpha\Delta} \tag{6.11}$$

$$\mathscr{M} \;=\; \left(1-\alpha^k\right)\Delta^k \left.\frac{\delta^{k+n}\overline{u}}{\delta x^{k+n}}\right|^{\Delta} - \alpha^k\Delta^k f\left(\left.\frac{\delta^{k+n}\overline{u}}{\delta x^{k+n}}\right|^{\alpha\Delta} - \left.\frac{\delta^{k+n}\overline{u}}{\delta x^{k+n}}\right|^{\Delta}\right). \tag{6.12}$$

The magnitude of the difference (6.10), which is a function of parameter $c_{k,n}$, provides an indication about the accuracy with which the finite difference scheme on the fine grid resolution approximates the analytical derivative. If the difference is small, the resolution is sufficiently fine and ensures an accurate finite difference approximation on the fine grid. In contrast, a large difference $\mathscr{E}$ indicates that the resolution is not fine enough to guarantee an acceptable accuracy of the finite difference approximation on the fine grid. However, an optimal coefficient $c_{k,n}$ can be found such that the difference $\mathscr{E}$ is minimal. Then, the finite difference approximation on the fine grid must have an optimal accuracy (low dispersion error), since it differs only minimally with the accuracy of the coarse grid approximation. To examine the role of the blending factor $f \in [0,1]$, the cases $f = 0$ and $f \neq 0$ are discussed hereafter.

ASYMPTOTIC HIGH-ORDER SCHEMES FOR $f = 0$

Assume the blending factor $f = 0$, then the coefficient $c_{k,n}$ can be obtained from expression (6.10) by imposing the difference $\mathscr{E} = 0$, leading to

$$\left.\frac{\delta^n \overline{u}}{\delta x^n}\right|^{\Delta} - \left.\frac{\delta^n \overline{u}}{\delta x^n}\right|^{\alpha\Delta} = c_{k,n}\left(\alpha^k - 1\right)\Delta^k \left.\frac{\delta^{k+n}\overline{u}}{\delta x^{k+n}}\right|^{\Delta}. \tag{6.13}$$

It is observed that the left-hand-side discretization does not necessarily lead to a *compact* finite difference approximation with minimal stencil width for the right-hand side derivative. It is verified that the left-hand-side results into a discretization with a stencil width of $2\alpha r + 1$, whereas the right-hand-side only requires a discretization with stencil width $2r + 1 + 2$ for obtaining the same order of accuracy. Hence, both stencils are equal if $\alpha = 1/r + 1$, and since embedded grid resolutions are assumed such that $\alpha \in \mathbb{N}$, the former condition is only satisfied if $r = 1$. In the following, however, identity (6.13) is enforced such that a minimal stencil width for the right-hand-side is guaranteed[2] and thus, $c_{k,n} \equiv c^*_{k,n}$. Substitution of (6.13) into (6.7),

[2] In accordance with the discussion in Section 4.3.2, it is observed that ensuring the compactness of the stencils leads to superior quality.

eliminating $c_{k,n}$ leads to the finite difference approximation of order $\mathscr{O}\left(\Delta^{k+2}\right)$.

$$\overline{\frac{\partial^n u}{\partial x^n}}(x) = \frac{\alpha^k \left.\frac{\delta^n \overline{u}}{\delta x^n}\right|^{\Delta} - \left.\frac{\delta^n \overline{u}}{\delta x^n}\right|^{\alpha\Delta}}{\alpha^k - 1} + \mathcal{O}\left(\Delta^{k+2}\right) \tag{6.14}$$

which is Richardson's Extrapolation formula. Expression (6.14) is thus again an approximation with formal asymptotic order of accuracy $\mathscr{O}\left(\Delta^{k+2}\right)$, although it does not necessarily have a compact stencil support in the current formulation. The aim is to construct optimized finite difference schemes with good Fourier characteristics and abandoning the concept of formal asymptotic order of accuracy. Therefore, the case $f \neq 0$ is further investigated.

Optimized high order schemes for $f \neq 0$

For the case $f \neq 0$, the analysis is continued in a somewhat different manner than for $f = 0$. Imposing $\mathscr{E} = 0$ and eliminating $c_{k,n}$ straightforwardly from expression (6.10), would lead to a substitution of $c_{k,n}$ with a nonlinear expression. The resulting field for $c_{k,n}$ would be pointwise varying, in contrast to the constant value obtained from the Taylor series. Instead, a more general approach is followed by extracting $c_{k,n}$ from a least square optimization, in which the least square averaging domain is an additional degree of freedom. This allows to regulate the smoothness of the obtained coefficient.
First, expressions (6.11) and (6.12) can be further simplified by enforcing relation (6.13), yielding

$$\mathscr{L} = c^*_{k,n}\left(\alpha^k - 1\right)\Delta^k \left.\frac{\delta^{k+n}\overline{u}}{\delta x^{k+n}}\right|^{\Delta} \tag{6.15}$$

$$\mathscr{M} = \left(1-\alpha^k\right)\Delta^k \left.\frac{\delta^{k+n}\overline{u}}{\delta x^{k+n}}\right|^{\Delta} - \alpha^k \Delta^k f \left\{ c^{**}_{k,n}\left(1-\alpha^2\right)\Delta^2 \left.\frac{\delta^{k+n+2}\overline{u}}{\delta x^{k+n+2}}\right|^{\Delta} \right\} \tag{6.16}$$

with $c^*_{k,n}$ and $c^{**}_{k,n}$ constant coefficients known from Taylor series expansion. The optimized *dynamic coefficient* can be extracted by least square minimization of the difference (6.10), i.e. by solving

$$\frac{\partial}{\partial c_{k,n}}\left\langle \mathscr{E}^2 \right\rangle = 0 \tag{6.17}$$

where $\langle\cdot\rangle$ denotes an averaging operator (to be defined later), resulting finally in the *dynamic coefficient*

$$c^{dyn}_{k,n} = -\frac{\langle \mathscr{L}\mathscr{M} \rangle}{\langle \mathscr{M}\mathscr{M} \rangle}. \tag{6.18}$$

Once $c_{k,n}^{dyn}$ is calculated, its value can be used in the optimized finite difference approximation

$$\overline{\frac{\partial^n u}{\partial x^n}}(x) = \left.\frac{\delta^n \overline{u}}{\delta x^n}\right|^{\Delta} + c_{k,n}^{dyn}\Delta^k \left.\frac{\delta^{k+n}\overline{u}}{\delta x^{k+n}}\right|^{\Delta} + \mathscr{O}\left(\Delta^k\right). \tag{6.19}$$

The resulting dynamic scheme has a formal order of accuracy k unless $c_{k,n}^{dyn} = c_{k,n}^{*}$, which would lead to the formal order of accuracy $k+2$. Although the order of accuracy is not necessarily increased by this dynamic procedure, the scheme can have better Fourier characteristics. This is shown in the next section.

In this dissertation, only two averaging operations are considered, i.e. a global uniform averaging over the entire domain, and a local averaging over half the grid spacing $\Delta/2$.[3] Applying the global uniform averaging operator to expression (6.18) results into the following spatially constant coefficient

$$c_{k,n}^{dyn} = c_{k,n}^{*}\frac{\left\langle \left.\frac{\delta^{k+n}\overline{u}}{\delta x^{k+n}}\right|^{\Delta 2} - \frac{\alpha^k\left(1-\alpha^2\right)}{1-\alpha^k} f c_{k,n}^{**}\Delta^2 \left.\frac{\delta^{k+n+2}\overline{u}}{\delta x^{k+n+2}}\right|^{\Delta} \left.\frac{\delta^{k+n}\overline{u}}{\delta x^{k+n}}\right|^{\Delta} \right\rangle}{\left\langle \left(\left.\frac{\delta^{k+n}\overline{u}}{\delta x^{k+n}}\right|^{\Delta} - \frac{\alpha^k\left(1-\alpha^2\right)}{1-\alpha^k} f c_{k,n}^{**}\Delta^2 \left.\frac{\delta^{k+n+2}\overline{u}}{\delta x^{k+n+2}}\right|^{\Delta} \right)^2 \right\rangle}. \tag{6.20}$$

Substitution of $c_{k,n}^{dyn}$ into equation (6.19) leads to the so-called *linear dynamic finite difference approximation* since it remains invariant in the spatial domain. On the other hand, application of the local averaging operation to expression (6.18), results into a *pointwise varying* dynamic coefficient, determined as

$$c_{k,n}^{dyn} = -\frac{\mathscr{L}}{\mathscr{M}} = \frac{c_{k,n}^{*}}{1 - \frac{\alpha^k\left(1-\alpha^2\right)}{1-\alpha^k}\Delta^2 f c_{k,n}^{**} \frac{\left.\overline{\frac{\delta^{k+n+2}\overline{u}}{\delta x^{k+n+2}}}\right|^{\Delta}}{\left.\frac{\delta^{k+n}\overline{u}}{\delta x^{k+n}}\right|^{\Delta}}}. \tag{6.21}$$

Substitution of this coefficient into equation (6.19) leads to the *nonlinear dynamic finite difference approximation* since it may vary from node to node in the spatial domain.
Although both averaging approaches seem equally justified, three important remarks must be made concerning the nonlinear finite difference approximation.

i. It must be recognized that by definition, both Taylor series expansions (6.8) and (6.7) share the *constant coefficients* $c_{k,n}^{*}$. Comparison of both series expansions and extraction of the dynamic coefficient is thus only justified if $c_{k,n}^{dyn}$ is

[3] Clearly it is possible to perform local averaging over multiple grid spacings, but this case will not be considered in the present work.

identical on both grid resolutions, independent of α. Obviously, this condition is only satisfied exactly if the coefficient $c_{k,n}$ is independent of the grid. Since the locally averaged coefficient is not strictly grid-independent on both grid resolutions under consideration, the nonlinear finite difference approximation violates to some extent, the mathematical foundations of the multi-resolution concept.

ii. By definition, the nonlinear dynamic finite difference approximation does not preserve the linearity property of the analytical derivative, which it tries to approximate. It is verified that, in accordance with the analytical derivate, all linear (dynamic) finite difference approximations are conservative *a priori*, since they can be written in a discrete divergence formulation (see Section 4.3.1). However, the nonlinear dynamic finite difference approximation does not satisfy this property and is thus not conservative. Appendix B, proposes a remedy for this deficiency by constructing an a priori conservative equivalent of the nonlinear dynamic finite difference approximation. Although this alternative is used in practical simulations, it is not required for further theoretical analysis.

Appendix C gives a more detailed description of the implementation of a 2^{nd} -order linear and nonlinear explicit dynamic finite difference approximations and a 4^{th} -order linear explicit dynamic finite difference approximation. The quality of the both the linear and the nonlinear dynamic finite difference approximations is thoroughly investigated through an extensive Fourier analysis in Section (6.2). Moreover, their performance is demonstrated in the test cases in further chapters.
Although the basic *optimized* k^{th}-order finite difference approximation given by expression (6.19) requires only $2r+3$ nodes, the evaluation of the 2^{nd} -order accurate $(k+n+2)^{nd}$ derivative in expressions (6.20) and (6.21) requires $2r+5$ nodes. Note that the conservative formulation of the nonlinear scheme, described in appendix B, alleviates this problem. A similar conservative discretization might be constructed for the linear dynamic scheme. Further, the evaluation of the least-square averaged dynamic coefficient in the linear dynamic schemes at each time step, will lead inevitably to a computational overhead. However, it may be sufficient for the linear dynamic schemes to calculate the dynamic coefficient (6.20) only every few time steps, and only in the interior domain such that no boundary discretizations are required. Although this dissertation mainly focusses on the *proof of concept*, a strategy to increase the computational efficiency will be addressed briefly at the end of Chapter 8.

6.1.2 Implicit Dynamic Finite Difference Approximations

Although the development of implicit dynamic finite difference schemes is similar, but more complicated and elaborate then that of their explicit counterparts, an attempt is performed to deduce a general formulation for the implicit dynamic schemes. Consider the Taylor series of the k^{th}-order implicit *central* finite difference

approximation for the n^{th} derivative[4] of a variable $u(x)$, $x \in \mathbb{R}$, in a node $x = x_i$

$$\sum_{l=-q}^{q} \alpha_l \overline{\frac{\partial^n u}{\partial x^n}}(x_{i+l}) = \sum_{j=-r}^{r} \frac{\beta_j}{\Delta^n} \overline{u}(x_{i+j}) - \sum_{k'=k}^{\infty} c^*_{k',n} \Delta^{k'} \overline{\frac{\partial^{k'+n} u}{\partial x^{k'+n}}}(x_i). \tag{6.23}$$

Consider further a similar k^{th}-order implicit finite difference approximation for the n^{th} partial derivative on the *same* computational grid with grid spacing Δ, but expressed as if the grid resolution were $\alpha\Delta$, $\alpha \in \mathbb{N}$ such that the stencil width for the explicit part is $2\alpha r + 1$ whereas that for the implicit part is $2\alpha q + 1$. The Taylor series expansion then reads

$$\sum_{l=-q}^{q} \alpha_l \overline{\frac{\partial^n u}{\partial x^n}}(x_{i+\alpha l}) = \sum_{j=-r}^{r} \frac{\beta_j}{(\alpha\Delta)^n} \overline{u}(x_{i+\alpha j}) - \sum_{k'=k}^{\infty} c^*_{k',n} (\alpha\Delta)^{k'} \overline{\frac{\partial^{k'+n} u}{\partial x^{k'+n}}}(x_i). \tag{6.24}$$

For the construction of the optimized implicit finite difference approximation, the same methodology is adopted as for the explicit dynamic schemes. The leading order truncation terms in expressions (6.23) and (6.24) are discretized with a 2^{nd} *-order* finite difference approximation. Further, the theoretical Taylor coefficients $c^*_{k,n}$ are replaced by undetermined coefficients $c_{k,n}$. Finally, the blending factor f is introduced into the coarse-resolution equation (6.24). This procedure then yields

$$\sum_{l=-q}^{q} \alpha_l \overline{\frac{\partial^n u}{\partial x^n}}(x_{i+l}) = \sum_{j=-r}^{r} \frac{\beta_j}{\Delta^n} \overline{u}(x_{i+j}) + c_{k,n} \Delta^k \left. \frac{\delta^{k+n} \overline{u}}{\delta x^{k+n}} \right|^{\Delta} + \mathscr{O}\left(\Delta^k\right) \tag{6.25}$$

$$\begin{aligned} \sum_{l=-q}^{q} \alpha_l \overline{\frac{\partial^n u}{\partial x^n}}(x_{i+\alpha l}) &= \sum_{j=-r}^{r} \frac{\beta_j}{(\alpha\Delta)^n} \overline{u}(x_{i+\alpha j}) \\ &+ c_{k,n} (\alpha\Delta)^k \left\{ f \left. \frac{\delta^{k+n} \overline{u}}{\delta x^{k+n}} \right|^{\alpha\Delta} + (1-f) \left. \frac{\delta^{k+n} \overline{u}}{\delta x^{k+n}} \right|^{\Delta} \right\} + \mathscr{O}\left((\alpha\Delta)^k\right). \end{aligned} \tag{6.26}$$

Unless $c_{k,n}$ has the exact Taylor value $c^*_{k,n}$, the order of accuracy in both expressions remains $\mathscr{O}\left(\Delta^k\right)$. This is explained by the specific formulation of the truncation error analogously as for the explicit schemes. Subtracting (6.25) and (6.26) leads to an expression for the difference between both approximations, i.e.

$$\mathscr{E} = \mathscr{L} + c_{k,n} \mathscr{M} = \mathscr{O}\left((\alpha\Delta)^k\right) - \mathscr{O}\left(\Delta^k\right) \tag{6.27}$$

[4]The truncation series coefficients ${c_{k',n}}^*$ are determined as

$${c_{k',n}}^* = \sum_{l=-q}^{q} \frac{\alpha_l l^{k'}}{(k')!} - \sum_{j=-r}^{r} \frac{\beta_j j^{k'+n}}{(k'+n)!}. \tag{6.22}$$

in which

$$\begin{aligned}\mathscr{L} &= -\sum_{l=-q}^{q}\left\{\alpha_l\overline{\frac{\partial^n u}{\partial x^n}}\left(x_{i+l}\right)-\alpha_l\overline{\frac{\partial^n u}{\partial x^n}}\left(x_{i+\alpha l}\right)\right\} \qquad (6.28)\\ &+ \sum_{j=-r}^{r}\left\{\frac{\beta_j}{\Delta^n}\overline{u}\left(x_{i+j}\right)-\frac{\beta_j}{(\alpha\Delta)^n}\overline{u}\left(x_{i+\alpha j}\right)\right\}\\ \mathscr{M} &= \left(1-\alpha^k\right)\Delta^k\left.\frac{\delta^{k+n}\overline{u}}{\delta x^{k+n}}\right|^{\Delta}-\alpha^k\Delta^k f\left(\left.\frac{\delta^{k+n}\overline{u}}{\delta x^{k+n}}\right|^{\alpha\Delta}-\left.\frac{\delta^{k+n}\overline{u}}{\delta x^{k+n}}\right|^{\Delta}\right). \qquad (6.29)\end{aligned}$$

Again, the magnitude of the difference (6.27), which is a function of parameter $c_{k,n}$, provides an indication about the accuracy with which the finite difference scheme on the fine grid resolution approximates the analytical derivative. If the difference is small, the resolution is sufficiently fine and ensures an accurate finite difference approximation on the fine grid. In contrast, a large difference $\mathscr{E}$ indicates that the resolution is not fine enough to guarantee an acceptable accuracy of the finite difference approximation on the fine grid. However, an optimal coefficient $c_{k,n}$ can be found such that the difference $\mathscr{E}$ is minimal. Then, the finite difference approximation on the fine grid must have an optimal accuracy (low dispersion error), since it differs only minimally with the accuracy of the coarse grid approximation. Hereafter, both cases $f = 0$ and $f \neq 0$ are further investigated.

Asymptotic high-order schemes for $f = 0$

For a blending factor $f = 0$, the coefficient $c_{k,n}$ can be obtained from expression (6.27) by imposing the difference $\mathscr{E} = 0$, leading to

$$\begin{aligned}\sum_{l=-q}^{q}\left\{\alpha_l\overline{\frac{\partial^n u}{\partial x^n}}\left(x_{i+l}\right)-\alpha_l\overline{\frac{\partial^n u}{\partial x^n}}\left(x_{i+\alpha l}\right)\right\}-\sum_{j=-r}^{r}\left\{\frac{\beta_j}{\Delta^n}\overline{u}\left(x_{i+j}\right)-\frac{\beta_j}{(\alpha\Delta)^n}\overline{u}\left(x_{i+\alpha j}\right)\right\}\\ = c_{k,n}\left(1-\alpha^k\right)\Delta^k\left.\frac{\delta^{k+n}\overline{u}}{\delta x^{k+n}}\right|^{\Delta}. \qquad (6.30)\end{aligned}$$

Substitution of (6.30) into (6.25), eliminating $c_{k,n}$ leads to the finite difference approximation of order $\mathscr{O}\left(\Delta^{k+2}\right)$.

$$\begin{aligned}\sum_{l=-q}^{q}\left\{\alpha^k\left(\alpha_l\overline{\frac{\partial^n u}{\partial x^n}}\left(x_{i+l}\right)\right)-\alpha_l\overline{\frac{\partial^n u}{\partial x^n}}\left(x_{i+\alpha l}\right)\right\}\\ = \sum_{j=-r}^{r}\left\{\alpha^k\left(\frac{\beta_j}{\Delta^n}\overline{u}\left(x_{i+j}\right)\right)-\frac{\beta_j}{(\alpha\Delta)^n}\overline{u}\left(x_{i+\alpha j}\right)\right\}+\mathscr{O}\left(\Delta^{k+2}\right), \qquad (6.31)\end{aligned}$$

which is Richardson's Extrapolation formula for Padé schemes. Expression (6.31) is thus an approximation with formal asymptotic order of accuracy $\mathscr{O}\left(\Delta^{k+2}\right)$. Notice

that this approximation, which involves $2\alpha q + 2\alpha r + 2$ nodes, is *incompact*, since in principle only $2q + 2r + 4$ nodes are required in order to obtain this accuracy.[5] Nevertheless, in this work relation (6.30) is enforced such that $c_{k,n} = c^*_{k,n}$. Since the aim is to construct optimized finite difference schemes with good Fourier characteristics, abandoning the concept of formal asymptotic order of accuracy, the case where f is different from zero is further investigated.

Optimized high order schemes for $f \neq 0$

For the case $f \neq 0$, a more general approach is followed similarly to Paragraph 6.1.1. The coefficient $c_{k,n}$ is extracted from both equations by means of a least square optimization, in which the least square averaging domain is again an additional degree of freedom. Enforcing relation (6.30) and using relation (6.13), the former equations are reduced to

$$\mathscr{L} = c^*_{k,n}\left(\alpha^k - 1\right)\Delta^k \left.\frac{\delta^{k+n}\overline{u}}{\delta x^{k+n}}\right|^{\Delta} \tag{6.32}$$

$$\mathscr{M} = \left(1-\alpha^k\right)\Delta^k \left.\frac{\delta^{k+n}\overline{u}}{\delta x^{k+n}}\right|^{\Delta} - \alpha^k \Delta^k f \left\{ c^{**}_{k,n}\left(1-\alpha^2\right)\Delta^2 \left.\frac{\delta^{k+n+2}\overline{u}}{\delta x^{k+n+2}}\right|^{\Delta}\right\} \tag{6.33}$$

with $c^*_{k,n}$ and $c^{**}_{k,n}$ constant coefficients known from Taylor series expansion. The optimized *dynamic coefficient* can be extracted by least square minimization of the difference

$$\frac{\partial}{\partial c_{k,n}}\left\langle \mathscr{E}^2 \right\rangle = 0 \tag{6.34}$$

where $\langle\cdot\rangle$ denotes an averaging operator (to be defined later), resulting finally in the *dynamic coefficient*

$$c^{dyn}_{k,n} = -\frac{\langle \mathscr{L}\mathscr{M}\rangle}{\langle \mathscr{M}\mathscr{M}\rangle}. \tag{6.35}$$

In the current work, only global averaging operations for the implicit schemes are considered such that the *dynamic coefficient* is calculated as

$$c^{dyn}_{k,n} = c^*_{k,n}\frac{\left\langle \left.\frac{\delta^{k+n}\overline{u}}{\delta x^{k+n}}\right|^{\Delta 2} - \frac{\alpha^k\left(1-\alpha^2\right)}{1-\alpha^k} f c^{**}_{k,n}\Delta^2 \left.\frac{\delta^{k+n+2}\overline{u}}{\delta x^{k+n+2}}\right|^{\Delta} \left.\frac{\delta^{k+n}\overline{u}}{\delta x^{k+n}}\right|^{\Delta}\right\rangle}{\left\langle \left(\left.\frac{\delta^{k+n}\overline{u}}{\delta x^{k+n}}\right|^{\Delta} - \frac{\alpha^k\left(1-\alpha^2\right)}{1-\alpha^k} f c^{**}_{k,n}\Delta^2 \left.\frac{\delta^{k+n+2}\overline{u}}{\delta x^{k+n+2}}\right|^{\Delta}\right)^2\right\rangle}. \tag{6.36}$$

[5] Note that the approximation is compact if $\alpha = 1 + 1/(q+r)$, such that for integer values of α, q must be zero whereas $r = 1$.

Remark that expressions (6.20) and (6.36) are equivalent for the explicit and implicit finite difference approximations.
Once $c_{k,n}^{dyn}$ is calculated, its value can be used in the optimized implicit finite difference approximation

$$\sum_{l=-q}^{q} \alpha_l \overline{\frac{\partial^n u}{\partial x^n}}\left(x_{i+l}\right) = \sum_{j=-r}^{r} \frac{\beta_j}{\Delta^n} \overline{u}\left(x_{i+j}\right) + c_{k,n}^{dyn} \Delta^k \left.\frac{\delta^{k+n}\overline{u}}{\delta x^{k+n}}\right|^{\Delta} + \mathscr{O}\left(\Delta^k\right). \tag{6.37}$$

However, formulation (6.37) undermines the advantageous philosophy of compact schemes. Indeed, using an explicit finite difference approximation for the $(k+n)^{th}$ derivative results into an implicit scheme with a larger explicit stencil width than strictly required for this order of accuracy. This is remedied by substituting the explicit $(k+n)^{th}$ derivative by an implicit formulation, which is equivalent of writing (6.37) immediately in its most compact formulation. Consider therefore the compact and incompact $(k+2)^{nd}$-order implicit schemes

$$\sum_{l=-q}^{q} \alpha_l \overline{\frac{\partial^n u}{\partial x^n}}\left(x_{i+l}\right) = \sum_{j=-r}^{r} \frac{\beta_j}{\Delta^n} \overline{u}\left(x_{i+j}\right) + c_{k,n}^{*} \Delta^k \left.\frac{\delta^{k+n}\overline{u}}{\delta x^{k+n}}\right|^{\Delta} + \mathscr{O}\left(\Delta^{k+2}\right) \tag{6.38}$$

$$\sum_{l=-q}^{q} \alpha_l' \overline{\frac{\partial^n u}{\partial x^n}}\left(x_{i+l}\right) = \sum_{j=-r-1}^{r+1} \frac{\beta_j'}{\Delta^n} \overline{u}\left(x_{i+j}\right) + \mathscr{O}\left(\Delta^{k+2}\right). \tag{6.39}$$

Assuming that both expressions (6.38) and (6.39) are equal, and combination with equation (6.37) finally yields,

$$\sum_{l=-q}^{q} \left[\alpha_l - \frac{c_{k,n}^{dyn}}{c_{k,n}^{*}}\left(\alpha_l - \alpha_l'\right)\right] \overline{\frac{\partial^n u}{\partial x^n}}\left(x_{i+l}\right) = \sum_{j=-r}^{r} \frac{\beta_j}{\Delta^n} \left[1 - \frac{c_{k,n}^{dyn}}{c_{k,n}^{*}}\right] \overline{u}\left(x_{i+j}\right) + \frac{c_{k,n}^{dyn}}{c_{k,n}^{*}} \sum_{j=-r-1}^{r+1} \frac{\beta_j'}{\Delta^n} \overline{u}\left(x_{i+j}\right) + \mathscr{O}\left(\Delta^k\right). \tag{6.40}$$

Although for the higher derivatives in (6.36) again compact Padé schemes may be used, in this work they are obtained using explicit approximations for reasons of simplicity. The resulting dynamic scheme (6.40) has a formal order of accuracy k unless $c_{k,n}^{dyn} = c_{k,n}^{*}$, which would lead to the formal order of accuracy $k+2$. Appendix C describes in more detail a 4^{th} -order linear implicit dynamic finite difference approximation. The high quality of the Fourier characteristics of these schemes will be demonstrated in next section.

6.2 FOURIER ANALYSIS

In this section, a thorough Fourier analysis is performed of both the explicit and implicit dynamically optimized finite difference approximations for an n^{th} derivative. The following Fourier analysis focusses in particular on the dynamic coefficient since this coefficient is considered crucial for obtaining good quality of the optimized finite difference approximation. Remark that for the dynamic coefficient (6.21) in the *nonlinear dynamic finite difference approximation*, the Fourier analysis is only valid for a *single wave component* and cannot be extrapolated straightforwardly to a composed wave, since superposition is not applicable to nonlinear expressions. Nevertheless, a Fourier analysis of a *composed wave* is presented that demonstrates the impact of the nonlinearity.

As discussed in Section 4.1.3, the n^{th} finite difference derivative is represented in Fourier space as

$$\mathscr{F}\left\{\frac{\delta^n \overline{u}}{\delta x^n}\right\} = \left(i\kappa'_n\right)^n \mathscr{F}\left\{\overline{u}\right\} \tag{6.41}$$

where κ'_n denotes the modified wavenumber. Recall that the real part of the modified wavenumber κ'_n represents dispersion errors, whereas the imaginary part represents dissipation errors which are absent in the current symmetric or central finite difference approximations. Generally, the modified wavenumber of a k^{th}-order explicit or implicit dynamic finite difference approximation of the n^{th} derivative can be formulated as function of the dynamic coefficient $c_{k,n}^{dyn}$. Since the method for obtaining the modified wavenumber was already explained in Section 4.1.3, it is not repeated in this section for the optimized finite difference approximations. Obviously $\mathscr{O}\left(\Delta^{k+2}\right)$ is recovered if $c_{k,n}^{dyn}$ equals the theoretical value $c_{k,n}^{*}$ obtained from Taylor expansion. Nevertheless, it is clear by now that the actual value of the coefficient $c_{k,n}^{dyn}$ will depend on the nature of the resolved field $\overline{u}\left(x\right)$, its derivatives and the value of the blending factor f. Hence, the spectral behaviour of $c_{k,n}^{dyn}$ will heavily influence the behaviour of the modified wavenumber, and further analysis is inevitable. Paragraph 6.2.1 will discuss the constant dynamic coefficient used in the linear dynamic finite difference approximations, whereas Paragraph 6.2.2 will discuss the pointwise varying dynamic coefficient used in the nonlinear dynamic finite difference approximations.

6.2.1 LINEAR FOURIER ANALYSIS

Since the spectral content of the flow field is mostly reflected by the energy spectrum, an attempt is made to analyze the behaviour of the dynamic coefficient by transforming the error definition into Fourier space. Using $\widehat{\cdot}$ to denote the Fourier transform, the error definitions (6.10) and (6.27) in respectively the explicit and

implicit *linear* dynamic schemes are transformed to Fourier space as

$$\widehat{\mathscr{E}}(\kappa) = \widehat{\mathscr{L}} + c_{k,n}\widehat{\mathscr{M}}, \tag{6.42}$$

with $c_{k,n}$ the *constant dynamic coefficient* and

$$\widehat{\mathscr{L}}(\kappa) = c^*_{k,n}\left(\alpha^k - 1\right)\Delta^k\left(i\kappa'_{k+n}\right)^{k+n}\widehat{u} \tag{6.43}$$

$$\begin{aligned}\widehat{\mathscr{M}}(\kappa) &= \left(1-\alpha^k\right)\Delta^k\left(i\kappa'_{k+n}\right)^{k+n}\widehat{u} \\ &- \alpha^k\left(1-\alpha^2\right)\Delta^{k+2} f c^{**}_{k,n}\left(i\kappa'_{k+n+2}\right)^{k+n+2}\widehat{u},\end{aligned} \tag{6.44}$$

corresponding to equations (6.15) and (6.16), or (6.32) and (6.33). Using expression (6.42), the following energy spectrum is defined (* denotes the complex conjugate)

$$E_{\widehat{\mathscr{E}}}(\kappa) = \widehat{\mathscr{E}}\widehat{\mathscr{E}}^* = \widehat{\mathscr{L}}\widehat{\mathscr{L}}^* + c_{k,n}\widehat{\mathscr{M}}\widehat{\mathscr{L}}^* + c_{k,n}\widehat{\mathscr{M}}^*\widehat{\mathscr{L}} + c^2_{k,n}\widehat{\mathscr{M}}\widehat{\mathscr{M}}^*. \tag{6.45}$$

Since the basic order of accuracy k is even for central schemes, it can be verified that in that case $\widehat{\mathscr{M}}\widehat{\mathscr{L}}^* = \widehat{\mathscr{M}}^*\widehat{\mathscr{L}}$ and thus

$$E_{\widehat{\mathscr{E}}}(\kappa) = \widehat{\mathscr{E}}\widehat{\mathscr{E}}^* = \widehat{\mathscr{L}}\widehat{\mathscr{L}}^* + 2c_{k,n}\widehat{\mathscr{M}}\widehat{\mathscr{L}}^* + c^2_{k,n}\widehat{\mathscr{M}}\widehat{\mathscr{M}}^* \tag{6.46}$$

The optimal value for the coefficient $c_{k,n}$ can now be found by a least square approximation in Fourier space, defined as[6]

$$\frac{\partial}{\partial c_{k,n}}\int_0^{\frac{\pi}{\Delta}} E_{\widehat{\mathscr{E}}}(\kappa)\,d\kappa = 0. \tag{6.47}$$

Working out this integral expression leads to following expression for the ratio $c^{dyn}_{k,n}/c^*_{k,n}$

$$\frac{c^{dyn}_{k,n}}{c^*_{k,n}} = \frac{\displaystyle\int_0^{\frac{\pi}{\Delta}}\left(\kappa'_{k+n}\right)^{k+n}\left[\left(\kappa'_{k+n}\right)^{k+n} + \frac{\alpha^k\left(1-\alpha^2\right)}{1-\alpha^k}\Delta^2 f c^{**}_{k,n}\left(\kappa'_{k+n+2}\right)^{k+n+2}\right]\widehat{u}\widehat{u}^* d\kappa}{\displaystyle\int_0^{\frac{\pi}{\Delta}}\left[\left(\kappa'_{k+n}\right)^{k+n} + \frac{\alpha^k\left(1-\alpha^2\right)}{1-\alpha^k}\Delta^2 f c^{**}_{k,n}\left(\kappa'_{k+n+2}\right)^{k+n+2}\right]^2\widehat{u}\widehat{u}^* d\kappa} \tag{6.48}$$

in which the product $\widehat{u}\widehat{u}^*$ represents the energy spectrum $E_u(\kappa)$ of the flow field $u(x)$. Once the shape of the energy spectrum of the flow field is known or a *model spectrum* is assumed, and a value of the blending factor f is chosen, it is possible

[6]Note that this definition is equivalent with equation (6.17) due to Parseval's theorem.

to calculate the dynamic coefficient for that spectrum from the integral expression (6.48). For the theoretical analysis in the current section, a uniform Heaviside-like spectrum shape is assumed, defined as

$$E_u(\kappa) = 1 - H(\kappa - \kappa_c) = \begin{cases} 1 & \kappa < \kappa_c \\ 0 & \kappa > \kappa_c \end{cases}, \tag{6.49}$$

where the cutoff wavenumber κ_c indicates the highest appearing wavenumber in the (resolved) field $\overline{u}(x)$. Although this theoretical spectrum has no direct relation to real turbulence, it is selected in this work to examine analytically the potential of the constructed dynamic schemes. Moreover, the uniform spectrum will be used in this work for the optimization of the Dispersion-Relation Preserving schemes, in accordance with the work of e.g. Tam *et al.* [79]. The influence of the energy spectrum will be demonstrated in Section 6.3. The simple uniform spectrum makes the expression analytically integrable, and the resulting equation describes a surface of the coefficient as function of κ_c and f. This surface is represented as a parametric plot in Figure 6.1. For $f = 0$, it is observed that the Taylor value $c^*_{k,n}$ is recovered regardless of the spectral content of the signal, represented by the filter-to-grid cutoff-ratio κ_c/κ_{max}. In case of $f \neq 0$, different profiles for $c^{dyn}_{k,n}$ as function of the filter-to-grid cutoff-ratio κ_c/κ_{max} appear. Moreover, if $\kappa_c/\kappa_{max} \to 0$, i.e. for very smooth fields $\overline{u}(x)$ that contain only few Fourier modes, the dynamic coefficients always converge to the theoretical Taylor value $c^*_{k,n}$ regardless of the value of the blending factor. This means that each dynamic finite difference approximation recovers the asymptotic order of accuracy $\mathscr{O}\left(\Delta^{k+2}\right)$ for very smooth fields.[7] In order to understand better the consequences of the blending factor f, the impact of the resulting dynamic coefficient on the linear dynamic finite difference approximation is examined. Figures 6.2, 6.3 and 6.4 display the modified wavenumbers $(n = 1, 2)$ for the 2^{nd} - and 4^{th} -order explicit linear dynamic schemes and the 4^{th} -order implicit dynamic scheme, described in Appendix C. For the determination of the constant dynamic coefficient, the filter-to-grid cutoff-ratio $\frac{\kappa_c}{\kappa_{max}} = \frac{2}{3}$ is assumed, corresponding to the de-aliasing filter cutoff in a Large-Eddy Simulation. Clearly, the linear dynamic finite difference approximation acts as an optimized k^{th} order finite difference scheme, in which the optimized parameter $c^{dyn}_{k,n}$ is obtained dynamically, according to the spectral content of the flow indicated by the ratio κ_c/κ_{max} and the choice of a blending factor f. First, it is observed that the accuracy of the dynamic schemes at a certain filter-to-grid cutoff-ratio is entirely determined by the value of f and the corresponding ratio $c^{dyn}_{k,n}/c^*_{k,n}$. As mentioned earlier, the formal order of accuracy $k + 2$ is obtained if $f = 0$ since $c^{dyn}_{k,n} = c^*_{k,n}$. Increasing the blending factor f affects the value of the ratio $c^{dyn}_{k,n}/c^*_{k,n}$ and may lead to an increase of the overall accuracy, despite the fact that the formal order of accuracy remains

[7] Remark that in case of a constant field $\overline{u}(x)$ for which $\kappa_c/\kappa_{max} = 0$, expression (6.48) reduces to 0/0, and the dynamic coefficient $c^{dyn}_{k,n}$ becomes *indefinite*. This makes sense since any finite difference approximation is exact for a constant. Hence, this particularity can be safely avoided by setting $c^{dyn}_{k,n} = 0$ or $c^{dyn}_{k,n} = c^*_{k,n}$ as soon as $\mathscr{L} = 0$ and $\mathscr{M} = 0$.

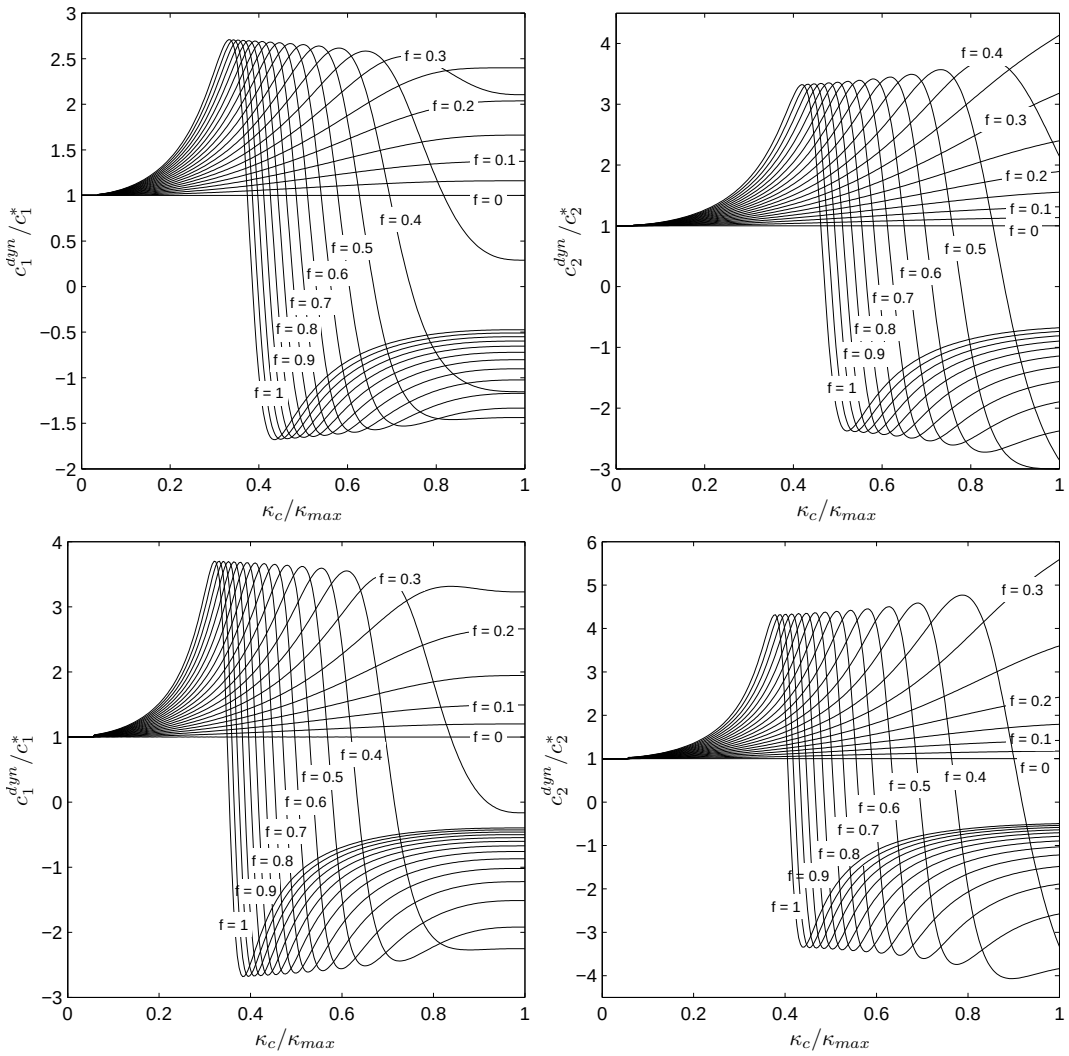

Figure 6.1: Parametric plot of the dynamic coefficient $c_{k,n}^{dyn}$ for the linear dynamic finite difference approximations. Parametric plot of $c_{k,n}^{dyn}/c_{k,n}^* = c_n^{dyn}/c_n^*$ as function of the cutoff wavenumber κ_c and the blending factor f for the explicit and implicit dynamic schemes with $k = 2, \alpha = 2$ (**upper**), $k = 4, \alpha = 2$ (**lower**) and $n = 1$ (**left**), $n = 2$ (**right**).

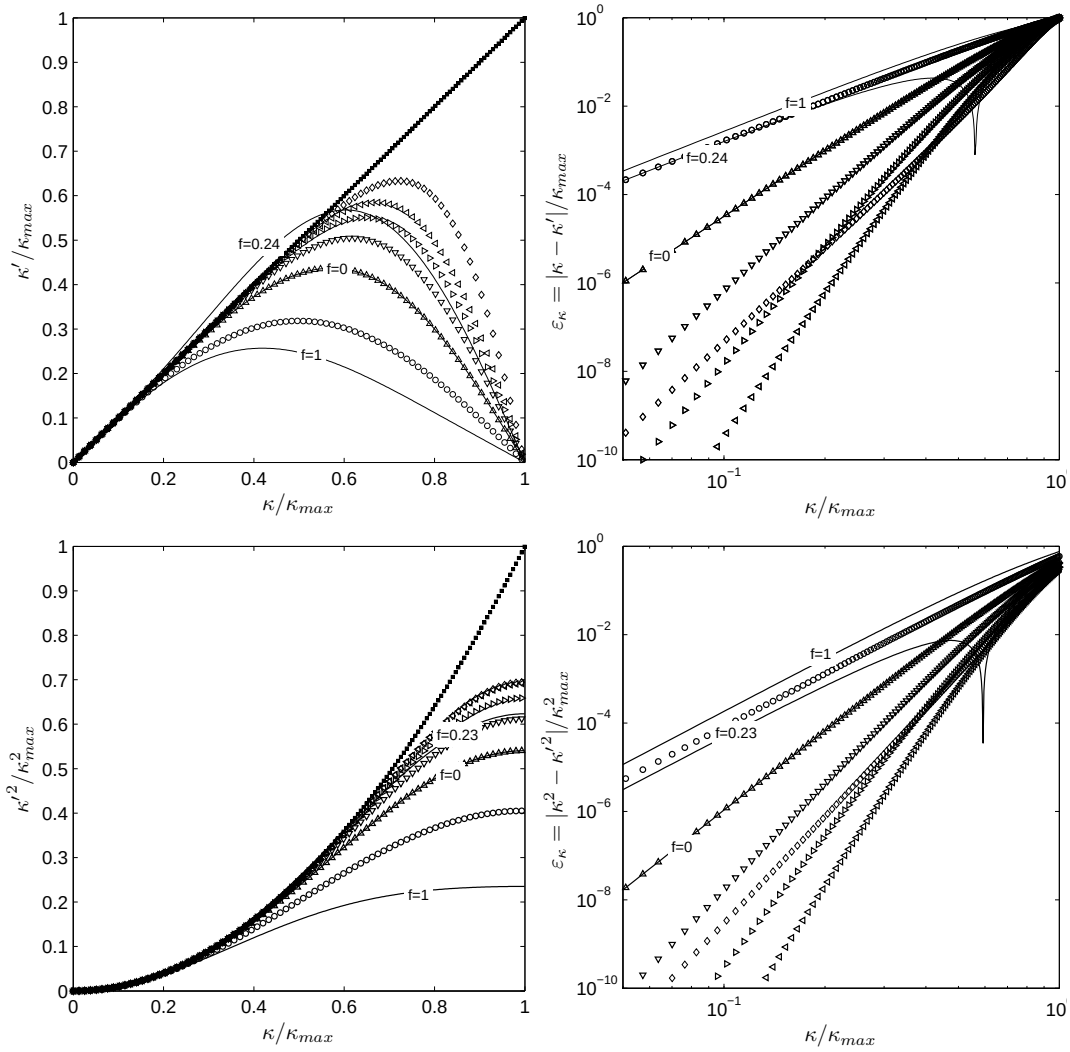

Figure 6.2: Linear explicit dynamic finite difference approximation with $k = 2$. Modified wavenumbers ${\kappa'_n}^n$ (**left**) and the absolute errors ε_κ (**right**), for the n^{th} derivatives with $n = 1$ (**upper**) and $n = 2$ (**lower**). (■) spectral; (○) 2^{nd} -order central; (△) 4^{th} -order central; (▽) 6^{th} -order central; (▷) 8^{th} -order central; (◁) 10^{th} -order central; (◇) 6^{th} -order tridiagonal Padé; (——) Linear dynamic scheme with various f.

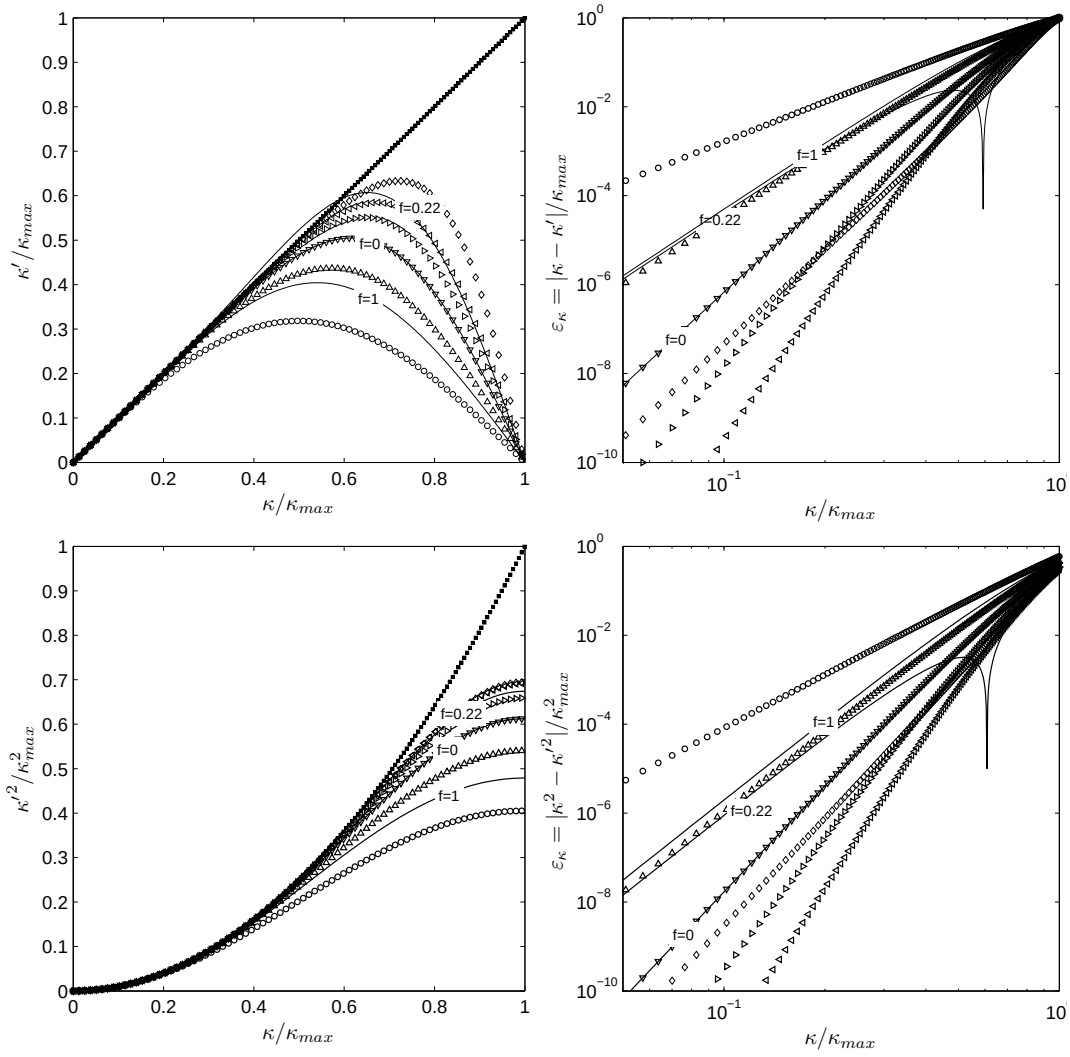

Figure 6.3: Linear explicit dynamic finite difference approximation with $k = 4$. Modified wavenumbers ${\kappa'_n}^n$ (**left**) and the absolute errors ε_κ (**right**), for the n^{th} derivatives with $n = 1$ (**upper**) and $n = 2$ (**lower**). (■) spectral; (○) 2^{nd} -order central; (△) 4^{th} -order central; (▽) 6^{th} -order central; (▷) 8^{th} -order central; (◁) 10^{th} -order central; (◇) 6^{th} -order tridiagonal Padé; (——) Linear dynamic scheme with various f.

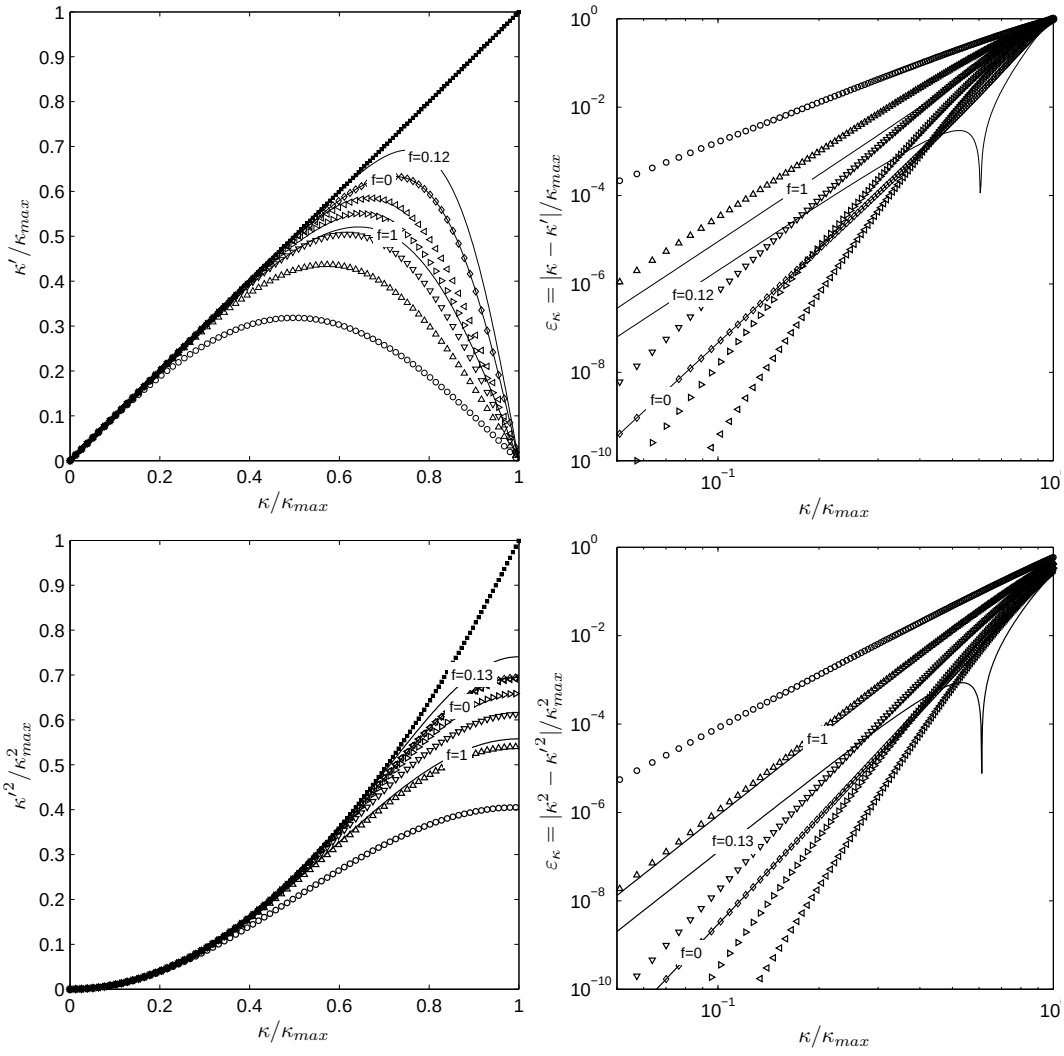

Figure 6.4: Linear implicit dynamic finite difference approximation with $k = 4$. Modified wavenumbers ${\kappa'_n}^n$ (**left**) and the absolute errors ε_κ (**right**), for the n^{th} derivatives with $n = 1$ (**upper**) and $n = 2$ (**lower**). (■) spectral; (○) 2^{nd} -order central; (△) 4^{th} -order central; (▽) 6^{th} -order central; (▷) 8^{th} -order central; (◁) 10^{th} -order central; (◇) 6^{th} -order tridiagonal Padé; (——) Linear dynamic scheme with various f.

k. However, it is observed that the quality of the dynamic schemes is significantly reduced as soon as f tends to unity. This indicates that the ratio $c_{k,n}^{dyn}/c_{k,n}^{*}$, and thus the blending factor f, have to meet certain conditions in order to obtain the desired Fourier characteristics. It is clear that if the ratio $0 \leq c_{k,n}^{dyn}/c_{k,n}^{*} < 1$, the scheme's Fourier characteristic will lie between that of the k^{th}-order and $(k+2)^{nd}$-order standard scheme, and does not result into the desired spectral behaviour. Moreover, if $c_{k,n}^{dyn}/c_{k,n}^{*} < 0$, i.e. $c_{k,n}^{dyn}$ has an opposite sign in comparison with its Taylor value $c_{k,n}^{*}$, poor Fourier characteristics are observed that lie below that of the k^{th}-order scheme. Hence, the f-values should be chosen such that $c_{k,n}^{dyn}/c_{k,n}^{*} \geq 1$ for all values of the wavenumber ratio κ_c/κ_{max}. Further, $c_{k,n}^{dyn}$ acts like a sensor for the wave number content in the field $\overline{u}$. It should therefore be a monotonic function of the filter-to-grid cutoff-ratio κ_c/κ_{max} such that each value of $c_{k,n}^{dyn}$ corresponds to a unique value of $\frac{\kappa_c}{\kappa_{max}}$. Both conditions are mathematically expressed by

$$\frac{c_{k,n}^{dyn}}{c_{k,n}^{*}} \geq 1 \tag{6.50}$$

$$\frac{1}{c_{k,n}^{*}}\frac{\partial c_{k,n}^{dyn}}{\partial \kappa} \geq 0, \quad \forall \kappa \tag{6.51}$$

and bound the value of f to a certain interval in which an optimal value can be found. Although the optimal value of f is determined in Section 6.3, Figures 6.2, 6.3 and 6.4 already demonstrate the nearly optimal behaviour of the dynamic schemes.

6.2.2 Non-linear Fourier analysis

The following discussion is restricted to nonlinear *explicit* finite difference approximations. In contrast to the linear dynamic finite difference approximations, the coefficient $c_{k,n}^{dyn}$ of the nonlinear dynamic finite difference scheme is not least-square averaged such that it reduces *de facto* to a pointwise varying coefficient. Although the modified wavenumber for the nonlinear explicit dynamic finite difference scheme can be obtained, it will only be representative for a field $u(x)$ containing a single wave Fourier mode, and is not necessarily representative for more general fields that contain an entire spectrum of Fourier modes. Hence, a multiple wave Fourier analysis will be performed in order to study such general fields. First, the discussion is started with a single-wave quasi-linear Fourier analysis.
After some mathematical manipulations, the single-wave Fourier expression of the resulting nonlinear dynamic coefficient (6.21) is found to be

$$c_{k,n}^{dyn} = \frac{c_{k,n}^{*}}{1 - \frac{\alpha^k(1-\alpha^2)}{1-\alpha^k} f c_{k,n}^{**} 2\left(\cos\left(\kappa\Delta\right) - 1\right)}. \tag{6.52}$$

It is verified that in Fourier space, the ratio of the higher derivatives $\frac{\delta^{k+n+2}\overline{u}}{\delta x^{k+n+2}}/\frac{\delta^{k+n}\overline{u}}{\delta x^{k+n}}$ in expression (6.21) is always represented by $2\left(\cos\left(\kappa\Delta\right) - 1\right)$, independently of n and k.

Moreover, the resulting expression for $c_{k,n}^{dyn}$ depends only on the wavenumber κ, and is not influenced by the shape of the energy spectrum nor by the cutoff wavenumber κ_c. Since this function is bounded in the interval $[-3, 0]$ for $\kappa \in \left[0, \frac{2\pi}{3\Delta}\right]$, the same bounds on $\frac{\delta^{k+n+2}\overline{u}}{\delta x^{k+n+2}} / \frac{\delta^{k+n}\overline{u}}{\delta x^{k+n}}$ in physical space are imposed for the numerical computations in further chapters. Hence, possible singularities or erroneous values are precluded. Using expression (6.52) for $c_{k,n}^{dyn}$, a rational expression for the resulting modified wavenumber of the nonlinear *explicit* finite difference approximation is obtained, in which the denominator is that of expression (6.52). Such a rational expression is reminiscent to that obtained for compact Padé approximations. Without going into the mathematical details, it is now possible to reformulate the modified wavenumber of the nonlinear dynamic scheme into the characteristic form of a tridiagonal compact Padé scheme. Remark that the Padé coefficients thus depend on $c_{k,n}^{*}$, $c_{k,n}^{**}$ and f. This hints to the fact that the nonlinear dynamic finite difference approximation attempts to be an explicit formulation of the tridiagonal compact scheme. When applying conditions (6.50) and (6.51) to $c_{k,n}^{dyn}$, it is easy to verify that the coefficient $c_{k,n}^{dyn}$ remains strictly negative and monotonic in the Fourier domain $0 \rightarrow \kappa_{max}$, if

$$0 \leq f < \frac{1-\alpha^k}{\alpha^{k-2}\left(1-\alpha^2\right)c_{k,n}^{**}}. \tag{6.53}$$

The behaviour of the dynamic coefficient, taking this limitation into account, is illustrated in Figure 6.5. Indeed, the ratio $c_{k,n}^{dyn}/c_{k,n}^{*}$ increases monotonically with the wavenumber κ_c for all values of f, and displays similar behaviour to that of the linear dynamic scheme. The modified wavenumber is shown in Figure 6.6. As expected, the k^{th}-order nonlinear explicit dynamic finite difference approximation reduces to the explicit $(k+2)^{nd}$-order explicit scheme for $f = 0$. If $f = 1$ the denominator changes sign and a singularity is observed in the modified wavenumber. However, as long as condition (6.53) is satisfied, singularities are avoided. It is observed from the single-wave analysis that for well chosen intermediate values of f, the nonlinear dynamic finite difference approximation of the derivatives can lead to highly accurate schemes which outperform the asymptotic explicit schemes, the linear dynamic scheme and even the standard 6^{th} -order tridiagonal Padé scheme. This is not surprising since it was argued that the modified wave number of the nonlinear scheme is equivalent to that of the tridiagonal compact Padé scheme with coefficients dependent on f. It can be proven that, by imposing the standard constraints to obtain formal order of accuracy [50], for a value $f = \frac{1}{5}$, the modified wavenumber reduces to that of the Padé approximant, shown Figure 6.6.
Although these results are encouraging, it must be reminded that the former analysis is only valid for fields which contain a single Fourier mode. A Fourier analysis for fields which contain an entire spectrum of Fourier modes, would involve complicated convolution integrals that result from the transformation of the nonlinear dynamic scheme from physical space to Fourier space. In order to avoid such an elaborate and probably impossible analysis, the scheme's response to a multiple-wave field is

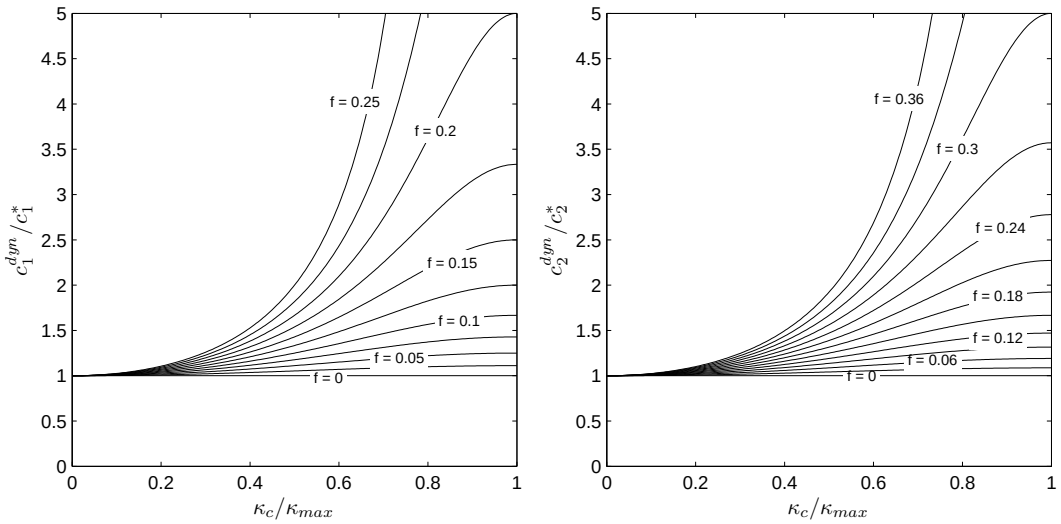

Figure 6.5: Parametric plot of the dynamic coefficient $c_{k,n}^{dyn}$ for the nonlinear explicit dynamic finite difference approximation. Parametric plot of $c_{k,n}^{dyn}/c_{k,n}^* = c_n^{dyn}/c_n^*$ as function of the cutoff wavenumber κ_c and the blending factor f for the explicit nonlinear dynamic scheme with $k = 2, \alpha = 2$ for $n = 1$ (**left**), $n = 2$ (**right**).

investigated in a semi-analytical way by looking at the transfer function. Assume the arbitrary field

$$u(\kappa, x) = \sum_{j=1}^{m} e^{(i\kappa_j x)}, \tag{6.54}$$

containing m wave components with *uniformly* distributed magnitude. The analytic expression of the n^{th} -derivative is then defined as

$$\frac{\partial^n u}{\partial x^n}(\kappa, x) = \sum_{j=1}^{m} (i\kappa_j)^n e^{(i\kappa_j x)}. \tag{6.55}$$

Obviously, the different wave components of the field will interact with each other in the evaluation of the nonlinear scheme. Since the modified wave number can no longer be used to assess the performance, the transfer function is calculated in physical space for various wave-combinations κ_j. This transfer function is defined at a random position $x = x_i$ as

$$\widehat{\mathscr{G}}(\kappa) = \frac{\left|\frac{\delta^n \overline{u}}{\delta x^n}(\kappa, x_i)\right|}{\left|\frac{\partial^n u}{\partial x^n}(\kappa, x_i)\right|}. \tag{6.56}$$

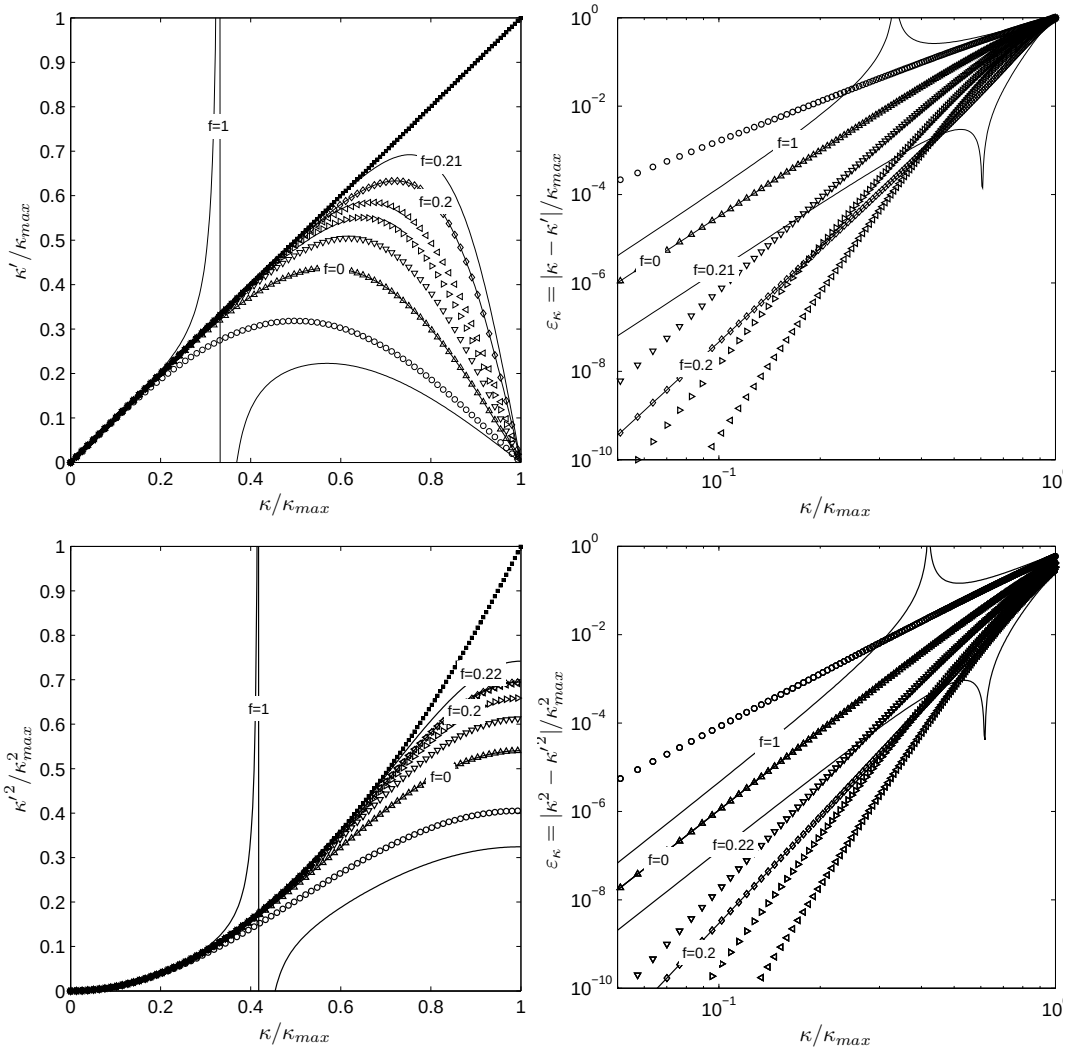

Figure 6.6: Non-linear explicit dynamic finite difference approximation with $k = 2$. Modified wavenumbers ${\kappa'_n}^n$ (**left**) and the absolute errors ε_κ (**right**), for the n^{th} derivatives with $n = 1$ (**upper**) and $n = 2$ (**lower**). (■) spectral; (○) 2^{nd} -order central; (△) 4^{th} -order central; (▽) 6^{th} -order central; (▷) 8^{th} -order central; (◁) 10^{th} -order central; (◇) 6^{th} -order tridiagonal Padé; (———) Non-linear dynamic scheme with various f.

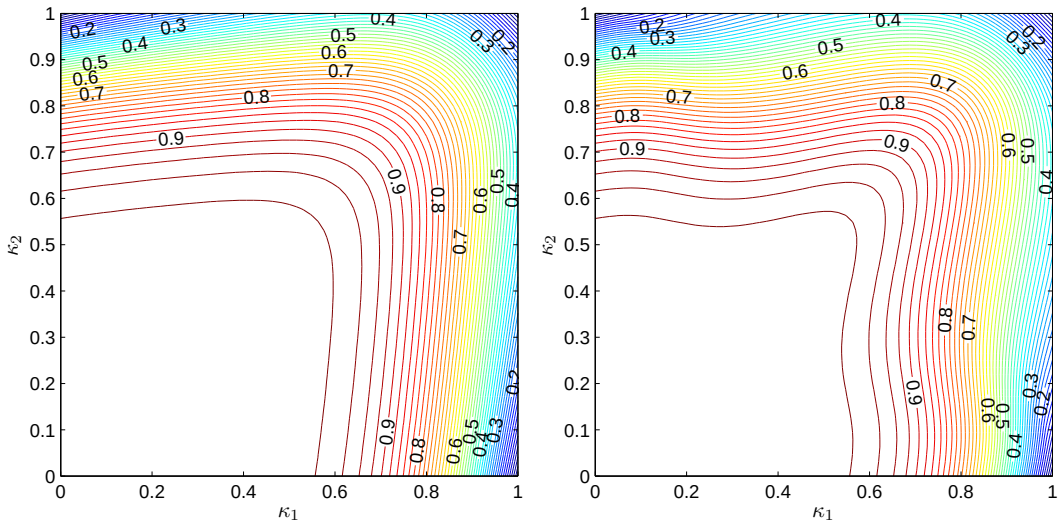

Figure 6.7: Transfer functions for a dual-wave field.. Transfer functions $\widehat{\mathscr{G}}(\kappa)$ for the 6^{th} -order tridiagonal Padé scheme (**left**) and the nonlinear explicit dynamic scheme ($k = 2$) with $f = \frac{1}{5}$ (**right**).

The transfer function $\widehat{\mathscr{G}}(\kappa)$, which goes from unity to zero for finite difference approximations, is examined for the case $n = 1$ and $k = 2$. It has been shown earlier that the modified wavenumber of the nonlinear dynamic scheme collapses with that of the Padé scheme if $f = \frac{1}{5}$. Hence, comparison between the standard 6^{th} -order tridiagonal Padé scheme and the nonlinear scheme with $f = \frac{1}{5}$ should give information on the influence of the nonlinear interactions. Results are shown in Figures 6.7 and 6.8 for a dual-wave field with $m = 2$ and for a triple-wave field with $m = 3$. Looking at the transfer functions, there seems to be a *relatively weak* influence of the nonlinear interactions. The general performance still seems to be in good agreement with that of the Padé scheme, although a slight decrease in accuracy is observed for certain wavenumber combinations $(\kappa_1, \kappa_2, \kappa_3)$. To visualize and quantify the errors introduced by nonlinear interactions only, the error between the transfer functions of the Padé scheme and the nonlinear dynamic scheme with $f = \frac{1}{5}$ are shown in Figure 6.9 for the dual-wave signal with $m = 2$ and the triple-wave signal with $m = 3$. Apparently, the largest errors due to nonlinear interactions appear in the high-wavenumber region were $\kappa_j > \frac{2}{3}$. However, this region is of little interest and ideally these modes should be eliminated through a de-aliasing filter in real computations. Summarizing, the impact of the nonlinear interactions seems to remain rather limited. However, further evaluation for a spectrum of waves is necessary and will be performed in the numerical study in further chapters.

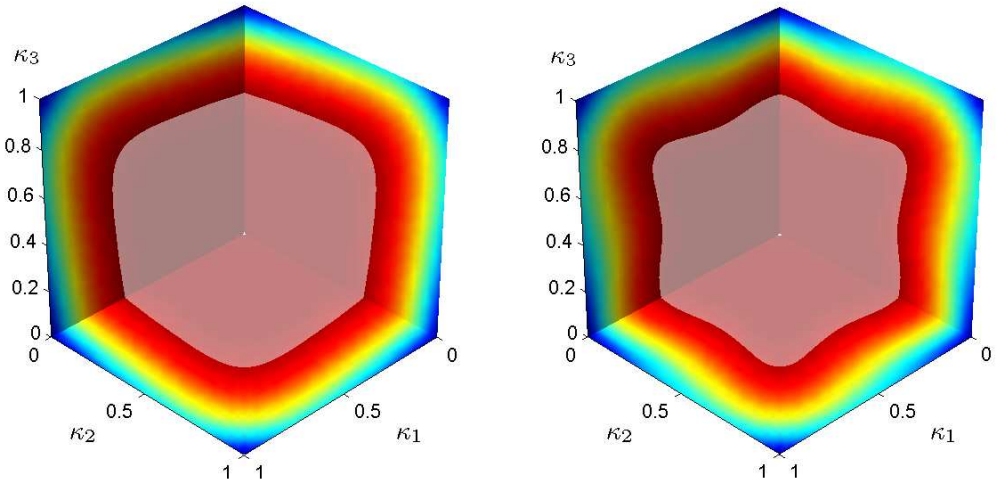

Figure 6.8: Transfer functions for a triple-wave field.. Transfer functions $\widehat{\mathscr{G}}(\kappa)$ and isosurfaces $\widehat{\mathscr{G}}(\kappa) = 0.95$ for the 6^{th} -order tridiagonal Padé scheme (**left**) and the nonlinear explicit dynamic scheme ($k = 2$) with $f = \frac{1}{5}$ (**right**).

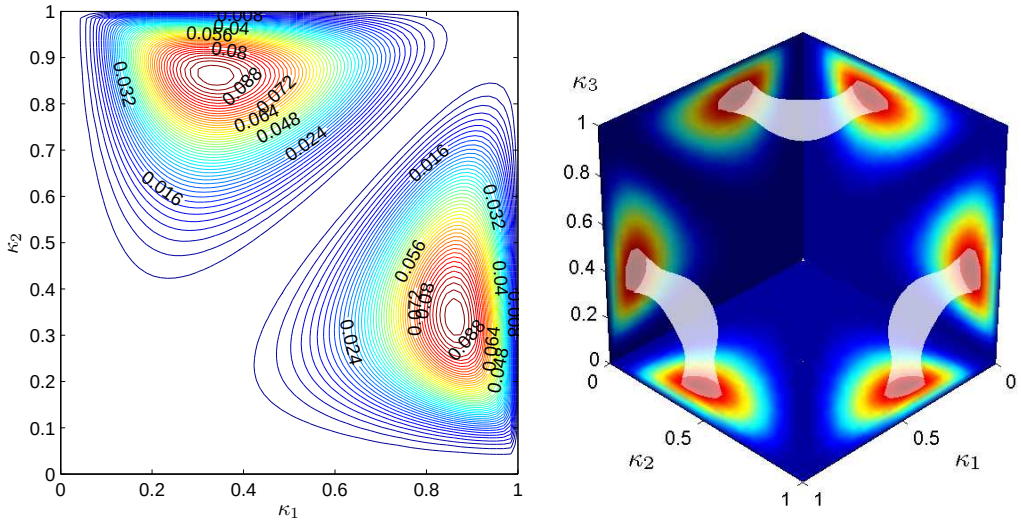

Figure 6.9: Absolute error due to the nonlinearity for the dual- and triple-wave field. Error between the transfer function of the 6^{th} -order tridiagonal Padé scheme and the nonlinear explicit dynamic scheme ($k = 2$) with $f = \frac{1}{5}$ for $M = 2$ (**left**) and $M = 3$ with isosurface at 90% of maximum error (**right**).

6.3 Calibration of the blending factor

It may be clear by now, that the linear explicit or implicit dynamic finite difference approximations are comparable to the Dispersion-Relation Preserving finite difference schemes of e.g. Tam *et al.* [79] or Kim *et al.* [45], discussed in Section 4.4.1. In contrast to these *prefactored* schemes, which have predefined fixed Fourier characteristics, the *linear dynamic schemes* optimize their *dynamic coefficient* according to the flow characteristics, such that the Fourier characteristics are variable. This way the scheme varies between the asymptotic $(k+2)^{nd}$-order finite difference approximation and an optimized k^{th}-order finite difference approximation, depending on the spectral content on the grid and the choice of the blending factor f. The latter merely accentuates the sensitivity of the dynamic scheme to the spectral content of the field. Similarly, the *nonlinear dynamic finite difference scheme* can be seen as an explicit formulation of a Dispersion-Relation Preserving Padé scheme. Here, the choice of f (which is the only degree of freedom in the dynamic schemes) determines the relative importance of each wave component in the procedure.

In the current section, a natural approach is proposed for determining the optimal value of the blending factor f. The idea is to minimize the kinetic energy associated to the resulting finite difference error. This way, the energy spectrum of the flow is taken into account as a natural weighting function. Although the method is similar to the traditional methods used by e.g. Tam *et al.* [79] or Kim *et al.* [45], the weighting function in the current method has a clear meaning rather than being an ad-hoc function.

The spectral error between the exact n^{th} derivative and an arbitrary finite difference approximation with modified wavenumber κ'_n, is defined as

$$\widehat{\mathscr{E}}(\kappa) \;=\; i^n \left(\kappa^n - \kappa'^{\,n}_n(\kappa, f)\right) \Delta^n \widehat{u}. \tag{6.57}$$

The related error spectrum is then determined as

$$E_{\widehat{\mathscr{E}}}(\kappa) \;=\; \widehat{\mathscr{E}}\widehat{\mathscr{E}}^* = \left(\kappa^n - \kappa'^{\,n}_n(\kappa, f)\right)^2 \Delta^{2n} E_u(\kappa), \tag{6.58}$$

where $E_u(\kappa)$ represents the energy spectrum of the flow field $u(x)$ given by the product $\widehat{u}\widehat{u}^*$. The optimal value for the blending factor f can be calculated by finding the minimum of the integral over all wave components, i.e. by solving

$$\frac{\partial}{\partial f} \int_0^{\frac{\pi}{\Delta}} \left(\kappa^n - \kappa'^{\,n}_n(\kappa, f)\right)^2 E_u(\kappa)\, \mathscr{W}(\kappa)\, d\kappa = 0, \tag{6.59}$$

where the additional weighting function $\mathscr{W}(\kappa)$ is set to unity unless the integrand is not analytically integrable [45] (e.g. for compact schemes). In the following paragraphs, the integral in (6.59) is solved numerically with $\mathscr{W}(\kappa) = 1$ by assuming three

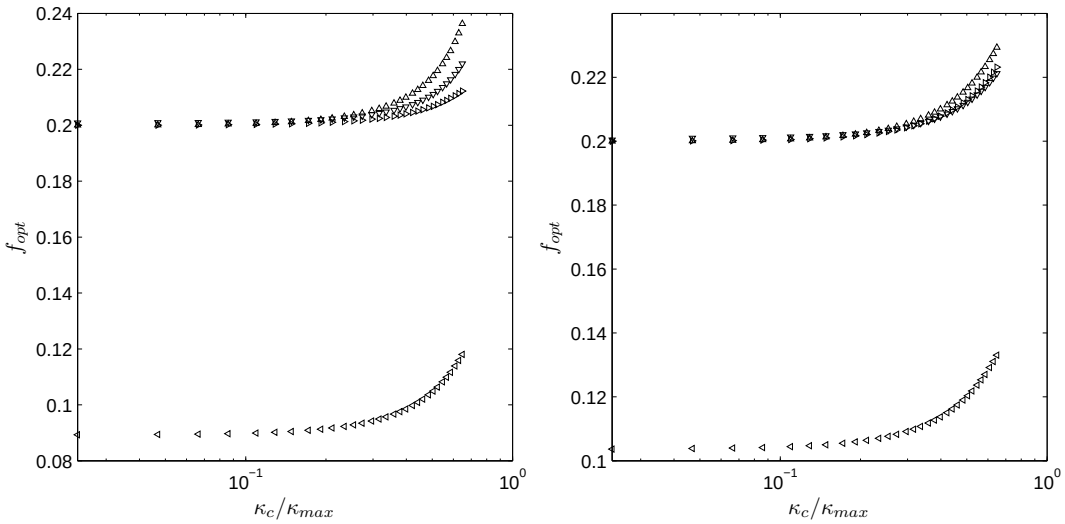

Figure 6.10: Optimal blending factor for uniform spectrum. The optimal blending factor $f_{opt} = f\left(\kappa_c \leq \frac{2\pi}{3\Delta}\right)$ for 1^{st} derivative (**left**) and 2^{nd} derivative (**right**). Distinguish the linear explicit dynamic scheme ($k = 2$) ($\triangle$), the linear explicit dynamic scheme ($k = 4$) ($\triangledown$), the nonlinear explicit dynamic scheme ($k = 2$) ($\triangleright$) and the linear implicit dynamic scheme ($k = 4$) ($\triangleleft$).

spectrum shapes. In Paragraph 6.3.1, a *uniform* spectrum shape is adopted. Since most often, the uniform spectrum is implicitly assumed for the construction of the Dispersion-Relation Preserving schemes, e.g. [79], it will also be used for the derivation of such schemes in this work. Moreover, the influence of the assumption of the standard uniform spectrum in comparison with other spectra will be demonstrated. Since the dynamic finite difference schemes will be applied to *Burgers' equation* in Chapters 7 and to the *Navier-Stokes equations* in Chapter 8, the energy spectra that correspond with these flows are adopted in Paragraphs 6.3.3 and 6.3.4, in order to retrieve the optimal blending factor in the dynamic finite difference approximations. Both spectra are hereafter termed *generic* since they may be considered representative for a wide range of *Burgers' flows*, characterized by a κ^{-2} spectrum, and a wide range of *turbulent flows*, characterized by the $\kappa^{-5/3}$ spectrum.

6.3.1 Uniform spectrum

When adopting the uniform spectrum (6.49) for $E_u(\kappa)$, the integrals can be calculated very easily in an analytical way, leading to an expression for the optimal blending factor as function of the highest appearing wavenumber κ_c, $f_{opt} = f(\kappa_c)$. The values of f_{opt} obtained for the 1^{st} and 2^{nd} derivative for the different schemes are given in Figure 6.10. Remark that the optimal value of f depends on the wavenumber range one wants to optimize for, indicated by κ_c. Since most dispersive errors exist in the range $\frac{2}{3}\kappa_{max} < \kappa_c < \kappa_{max}$, it is preferable that this wave number

range is omitted in the optimization. Minimizing the errors in this range would be inefficient, leading to poor accuracy. Moreover, in the current LES-framework with the double decomposition and sharp cutoff filtering, all modes in this region are filtered out in order to prevent aliasing errors. Therefore, f_{opt} was not obtained in this high-wavenumber range. Notice that for $\kappa_c/\kappa_{max} \to 0$, the optimal blending factor tends to an asymptotic value, denoted hereafter as f^*_{opt}. Further a cusp is observed in the profiles if $\kappa_c/\kappa_{max} \to 2/3$.

6.3.2 Model spectrum

Although the adopted uniform spectrum shape makes analytical integration easy, the presented optimal values for $f_{opt} = f\left(\kappa_c < \frac{2\pi}{3\Delta}\right)$ are most likely suboptimal for e.g. turbulent flows that are characterized by the Kolmogorov spectrum. Therefore, a more general model spectrum could be assumed, e.g. similarly to the one proposed by Pope [70]

$$E_u(\kappa) = \Gamma \kappa^{\alpha} F_L(\kappa) F_\eta(\kappa) \tag{6.60}$$

in which α determines the slope of the spectrum and Γ is a constant which can remain unspecified for our purposes. This spectrum was already introduced in Chapter 2, Section 2.3.3 for the description of homogeneous isotropic turbulence. Recall that functions $F_L(\kappa)$ and $F_\eta(\kappa)$ determine the shape of the energy containing range respectively the dissipation range. Several prescriptions are known for both functions which must generally be tuned to fit the experimental data. Especially $F_L(\kappa)$ cannot be captured easily in a universal expression as it is dominated by the large-scale flow characteristics of the specific geometry. The shape of the dissipation range displays a more universal behaviour and $F_\eta(\kappa)$ is usually defined as function of the Kolmogorov wavenumber κ_η. In order to obtain a useful model spectrum for determining the optimal value of f as function of a characteristic *cutoff* wavenumber, the model spectrum should be expressed as function of that particular wavenumber which is related to the Kolmogorov wavenumber κ_η.
Although such a model spectrum may theoretically be constructed, the analytical evaluation of the integral in equation (6.59) is quite difficult. Therefore, it is considered more feasible in this work to use directly a *developing energy spectrum* from Direct Numerical Simulation of a generic flow that develops into turbulence. Such a benchmark simulation would then provide a *generic spectrum* which initially contains only a few Fourier modes but evolves to a fully developed turbulent spectrum with a clear inertial range. Although the generic DNS-spectrum may be directly used in the optimization procedure, it can be understood that the use of optimized schemes may not be that interesting in the case of DNS, where the flow is assumed to be well resolved on the computational grid. Indeed, for a very well resolved DNS, the optimal scheme would tend to a higher formal order of accuracy as motivated earlier. In order to obtain a spectrum that is more suitable and challenging for the dynamic schemes, it is proposed to filter the DNS solution with a sharp Fourier filter to a certain cutoff wavenumber κ_c that lies within the inertial range of the fully

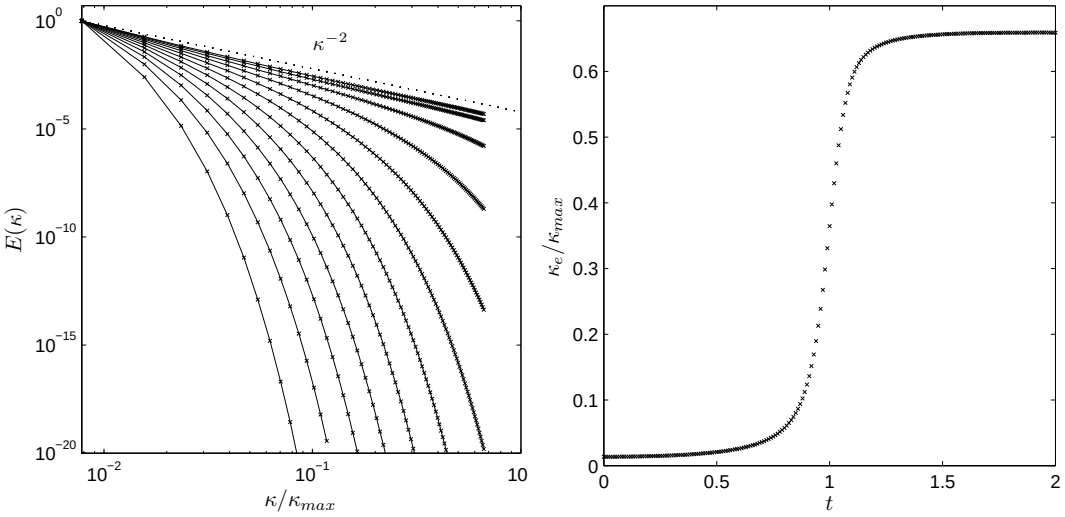

Figure 6.11: Generic Burgers' spectrum. The evolution of the L_2-normalized generic Burger's LES spectrum in time (**left**) and the effective wavenumber cutoff-ratio $\frac{\kappa_e}{\kappa_{max}}$ as function of time (**right**).

developed DNS-spectrum. After sampling the filtered DNS solution to a discrete grid with resolution κ_{max} such that $\kappa_c = \frac{2}{3}\kappa_{max}$, the corresponding LES-spectrum can be calculated, for which the optimized schemes are indeed relevant.[8] Using the developing LES energy spectrum into the optimization procedure, is expected to lead to an optimal blending factor that corresponds to each intermediate shape of the energy spectrum.
In this work, two flows are selected for extracting a generic energy spectrum, i.e. the one-dimensional developing *Burgers' equation* and the three-dimensional *Taylor-Green Vortex flow*. Both cases start with an initial velocity field that contains only a single Fourier mode. Due to the nonlinear interactions, more Fourier modes are generated as the flow evolves, and after some time, a fully developed spectrum is obtained which displays a clear inertial range.

6.3.3 Generic Burger's spectrum

The generic Burgers' LES-spectrum is obtained by filtering and sampling the DNS solution before calculating the normalized energy spectrum. The time-evolution of the truncated and normalized energy spectrum is displayed in the left parametric plot in Figure 6.11. At each time step, an optimal blending factor can be determined for the corresponding spectrum shape. However, it can be understood from

[8] It is emphasized that the proposed approach is not unique. Indeed, alternative procedures could be designed to retrieve the optimal blending factors. For instance, one could think of a procedure in which a fully developed turbulent spectrum with a clear inertial range is successively filtered with a decreasing cutoff wavenumber κ_c and sampled to successively coarser meshes. Nevertheless, such an approach might be more complex and difficult to automate since multiple grids are involved.

Figure 6.11 that in contrast to the uniform spectrum, it is not possible to define a unique cutoff wavenumber κ_c that indicates unambiguously the spectral content of the solution on the computational grid and its specific distribution in spectral space. In order to allow comparison with the uniform spectrum, an effective wavenumber $\kappa_e(t)$ is proposed that gives an indication of the spectral content of the solution and its distribution in Fourier space.
Assuming the analytical function $E_u(\kappa, t) \propto \kappa^{-\alpha}$, which describes a general inertial range spectrum with slope $-\alpha$, the dimensionless effective wavenumber ratio is defined in this work as,

$$\frac{\kappa_e(t)}{\kappa_{max}} = \left[\frac{1}{\kappa_{max}^3} \int_0^{\kappa_{max}} 3\kappa^{2+\alpha} \frac{E_u(\kappa, t)}{\|E_u(\kappa, t)\|} d\kappa \right]^{1/2}, \tag{6.61}$$

where the norm of the energy spectrum is defined as

$$\|E_u(\kappa, t)\| = \frac{1}{\kappa_{max}} \int_0^{\kappa_{max}} \kappa^{\alpha} E_u(\kappa, t) d\kappa. \tag{6.62}$$

This *ad hoc* definition, which can easily be obtained from a numerical simulation, is expected to provide a good indication about the shape of the instantaneous energy spectrum. Indeed, in case of the uniform spectrum, i.e. $\alpha = 0$, the effective wavenumber ratio reduces to

$$\frac{\kappa_e(t)}{\kappa_{max}} = \left[\frac{1}{\kappa_{max}^3} \int_0^{\kappa_c} 3\kappa^2 \frac{\kappa_{max}}{\kappa_c} d\kappa \right]^{1/2} = \frac{\kappa_c}{\kappa_{max}}, \tag{6.63}$$

It is emphasized that, unless the spectrum is uniform, the effective wavenumber κ_e does not represent exactly the highest wavenumber κ_c in the solution. Nevertheless, it provides an indication of the instantaneous spectral content of the solution on the computational grid. This is illustrated for the Burgers' equation in Figure 6.11. Numerical evaluation of the integral expression (6.59), for each individual spectrum shape, results into an optimal value f_{opt} for the blending factor f. Calculating the effective wavenumber κ_e, that corresponds to each intermediate spectrum, allows to represent the optimal blending factors as a function of κ_e. $f_{opt} = f(\kappa_e)$ is displayed in Figure 6.12. For the limit $\kappa_e \to 0$, the optimal blending factor f_{opt} tends to the same asymptotic value f_{opt}^* as for the uniform spectrum. Due to the creation of new wavenumber modes on the computational grid, the energy spectrum expands, and a corresponding increase of the blending factor is observed. As soon as the highest Fourier modes on the computational grid are energized, i.e. at $t \approx 0.7$ or $\frac{\kappa_e}{\kappa_{max}} \approx 0.05$, the filtered spectrum switches from DNS-resolution to LES-resolution and f_{opt} increases significantly. Moreover, a maximum is observed for the linear dynamic schemes in the region $0.1 \geq \kappa_e/\kappa_{max} \geq 0.3$. Once the filtered inertial range

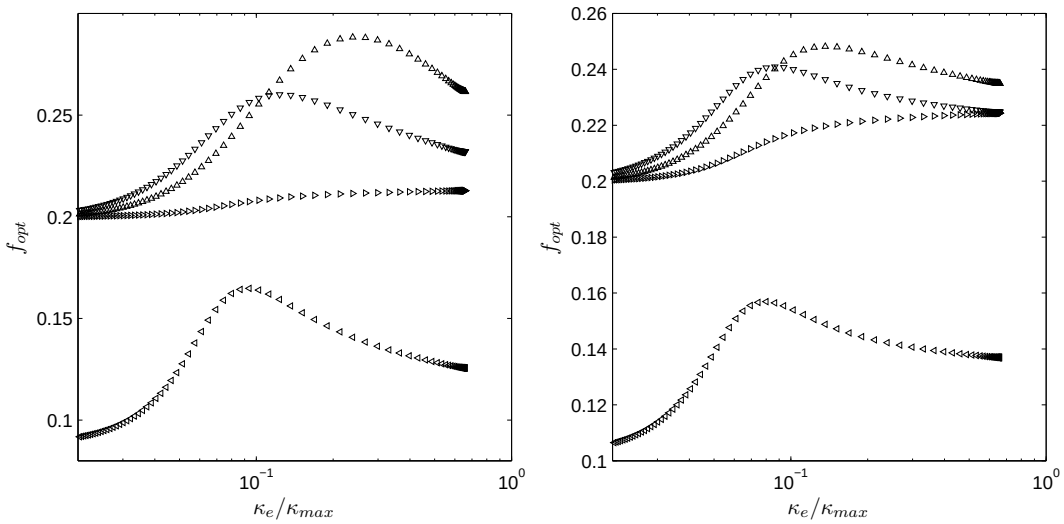

Figure 6.12: Optimal blending factor for Burger's spectrum. The optimal blending factor $f_{opt} = f(\kappa_e)$ for 1^{st} derivative (**left**) and 2^{nd} derivative (**right**). Distinguish the linear explcit dynamic scheme ($k = 2$) ($\triangle$), the linear explicit dynamic scheme ($k = 4$) ($\triangledown$), the nonlinear explicit dynamic scheme ($k = 2$) ($\triangleright$) and the linear implicit dynamic scheme ($k = 4$) ($\triangleleft$).

spectrum becomes fully established, i.e. at $\frac{\kappa_e}{\kappa_{max}} \geq 0.6$, the optimal blending factor of the linear dynamic schemes reaches a final value $f_{opt}(\max(\kappa_e))$, which will be used for the practical computations in this dissertation. Indeed, since the fully developed inertial range spectrum is characteristic for a wide range of Burgers' flows, the corresponding $f_{opt}(\max(\kappa_e))$ is also considered characteristic and independent of the specific flow features. As a consequence, the dynamic finite difference schemes with $f_{opt}(\max(\kappa_e))$ are expected to be optimal for a wide range of fully developed Burgers' flow.

Although κ_e is an indication for the spectral content that is resolved on the computational grid, it remains difficult to compare unambiguously the results obtained with the uniform spectrum and the Burgers' spectrum (Figures 6.10 and 6.12). An alternative way to demonstrate the influence of the energy spectrum in the optimization procedure (6.59) is to represent the optimal blending factor f_{opt} as function of the corresponding constant dynamic coefficient $c_{k,n}^{dyn}$. Indeed, for a given spectrum shape (indicated by κ_e or κ_c) an optimal value for the blending factor f can be found with equation (6.59), such that the corresponding constant dynamic coefficient $c_{k,n}^{dyn}$ leads to an optimal dynamic finite difference approximation for that particular spectrum shape. Hence, each optimal blending factor corresponds to an optimal constant dynamic coefficient. For the *linear dynamic schemes* the optimal dynamic coefficient $c_{k,n}^{dyn}$, which corresponds to f_{opt}, is a constant value. However, for the *nonlinear dynamic schemes* $c_{k,n}^{dyn}$, which corresponds to f_{opt}, is a pointwise

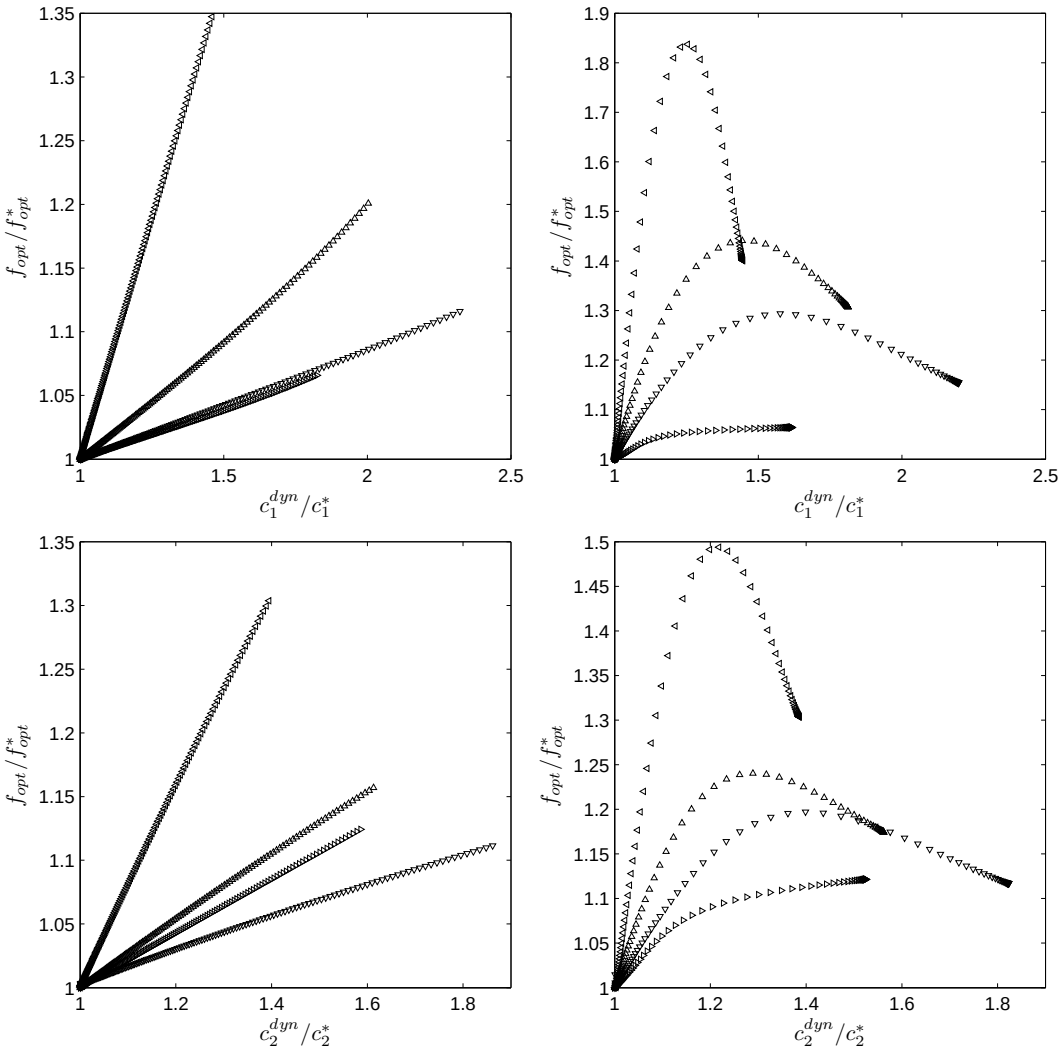

Figure 6.13: The optimal blending factor as function of the constant dynamic coefficient. The normalized optimal blending factor f_{opt}/f^*_{opt} ($f^*_{opt} = \lim_{\kappa_e \to 0 f_{opt}}$) as function of the normalized constant dynamic coefficient $c^{dyn}_{k,n} = c^{dyn}_n$ for 1^{st} derivative (**upper**) and 2^{nd} derivative (**lower**) and for the uniform (**left**) and Burgers' spectrum (**right**). Distinguish the linear explicit dynamic scheme ($k = 2$) ($\triangle$), the linear explicit dynamic scheme ($k = 4$) ($\triangledown$), the nonlinear explicit dynamic scheme ($k = 2$) ($\triangleright$) and the linear implicit dynamic scheme ($k = 4$) ($\triangleleft$).

varying field and cannot be represented as a single value. Therefore, it is replaced here by the constant coefficient $c_{k,n}^{dyn}$ of the linear dynamic scheme for corresponding order of accuracy. Figure 6.13 compares the normalized optimal blending factors f_{opt}/f_{opt}^{*} ($f_{opt}^{*} = \lim_{\kappa_e \to 0} f_{opt}$) as function of $c_{k,n}^{dyn}/c_{k,n}^{*}$ for the uniform spectrum and the Burger's spectrum. Obviously, the spectrum-related weighting functions in the integral expressions for f_{opt} and $c_{k,n}$, have a significant influence on the resulting behaviour. More specific, the optimal value f_{opt} as function of increasing κ_e depends strongly to the instantaneous shape of the energy spectrum that is related to $u\,(x)$. For the developing uniform spectrum, f_{opt}/f_{opt}^{*} seems to vary linearly with the coefficient ratio $c_{k,n}^{dyn}/c_{k,n}^{*}$, whereas for the developing Burgers' spectrum, f_{opt}/f_{opt}^{*} varies obviously not monotonously with $c_{k,n}^{dyn}/c_{k,n}^{*}$.

6.3.4 Generic Taylor-Green spectrum

Similarly to the previous paragraph, the generic Taylor-Green LES-spectrum is obtained by filtering and sampling the DNS solution before calculating the normalized energy spectrum. However, some attention is required concerning the optimization of the finite difference approximations for the partial derivatives in the Navier-Stokes equations. In contrast to the Burgers' equation, the Navier-Stokes equations contain, besides the various discrete derivatives of the velocity field, the finite difference approximation of the pressure gradient which must be optimized. Although the energy spectrum of the velocity components is characterized by a finite inertial range that scales with $\kappa^{-5/3}$, the energy spectrum of the pressure in homogeneous isotropic turbulence is found to have a finite inertial range that scales with $\kappa^{-7/3}$ and is followed by a bump of nearly $\kappa^{-5/3}$ at higher wave numbers [34]. In principle, the optimization of the finite difference approximations for the pressure derivatives must be calibrated using a $\kappa^{-7/3}$ generic spectrum, whereas the optimization of the finite difference approximations of the velocity derivatives must be calibrated with the traditional Kolmogorov scaling. Moreover, optimization of the finite difference approximations for the derivatives of the turbulent viscosity, which is needed for the evaluation of the Smagorinsky subgrid force, requires the spectrum of the strain-rate magnitude.[9] Secondly, since a derivative of a variable is defined as the convolution of a one-dimensional finite difference kernel with that variable along a single Cartesian direction, it is considered more relevant to optimize these finite difference approximations using a characteristic one-dimensional spectrum instead of the typical isotropic energy spectrum. In this work, a rather pragmatic approach is adopted in order to obtain such a characteristic one-dimensional spectrum of the velocity field $\mathbf{u}\,(\mathbf{x}) = u_i,\ i = 1, 2, 3$ respectively the pressure field $\overline{p}\,(\mathbf{x})$. The one-dimensional spectrum of the velocity-field and the pressure field are defined

[9] Note that the energy spectrum of the strain-rate magnitude cannot be deduced a priori from the Kolmogorov scaling. Indeed, the Fourier transform of the absolute value in $|S| = \sqrt{2}\sqrt{S_{ij}S_{ij}}$ is not consistently defined since it is a nonlinear operator.

as

$$E_{u,1}(\kappa_1,t) = \iint_{-\infty}^{\infty} E(\boldsymbol{\kappa},t)\,d\kappa_2 d\kappa_3 = \iint_{-\infty}^{\infty} \frac{1}{2}\widehat{u}_i(\boldsymbol{\kappa},t)\,\widehat{u}_i^*(\boldsymbol{\kappa},t)\,d\kappa_2 d\kappa_3 \tag{6.64}$$

$$E_{p,1}(\kappa_1,t) = \iint_{-\infty}^{\infty} \frac{1}{2}\widehat{p}(\boldsymbol{\kappa},t)\,\widehat{p}^*(\boldsymbol{\kappa},t)\,d\kappa_2 d\kappa_3, \tag{6.65}$$

and analogously for $E_{u,2}(\kappa_2,t)$, $E_{u,3}(\kappa_3,t)$, $E_{p,2}(\kappa_2,t)$ and $E_{p,3}(\kappa_3,t)$. Since in a periodic cubical box $\kappa_1 = \kappa_2 = \kappa_3 = \kappa$, the characteristic one-dimensional energy spectra, used in the optimization procedure for obtaining the optimal value of the blending factor f, are defined as

$$E_u(\kappa,t) = E_{u,1}(\kappa,t) + E_{u,2}(\kappa,t) + E_{u,3}(\kappa,t) \tag{6.66}$$

$$E_p(\kappa,t) = E_{p,1}(\kappa,t) + E_{p,2}(\kappa,t) + E_{p,3}(\kappa,t). \tag{6.67}$$

The characteristic one-dimensional spectrum of the strain-rate magnitude is obtained in analogy with (6.67). The time-evolution of the *normalized* one-dimensional energy spectra is displayed in the parametric graphs in Figure 6.14. In order to allow comparison with the uniform spectrum, an effective wavenumber κ_e is defined for the Taylor-Green flow by using expression (6.61) with $\alpha = 5/3$. The effective wavenumber is illustrated for the Taylor-Green velocity spectrum in Figure 6.14. Numerical evaluation of the integral expression (6.59) using the characteristic one-dimensional Taylor-green spectra, leads to an optimal value for the blending factor f_{opt} for the dynamic finite difference approximations of the derivatives of the velocity, the pressure and the strain-rate magnitude. The blending factors $f_{opt} = f(\kappa_e)$ for the derivatives of the velocity field and the pressure field are displayed in Figure 6.15. Note that those of the strain-rate magnitude, which are not shown here, are very similar. Similarly to the uniform spectrum and the Burgers' spectrum, the blending factor converges for the Kolmogorov spectrum to the same asymptotic value f_{opt}^* for $\kappa_e \to 0$. If the energy spectrum starts to expand, a corresponding increase of the blending factor is observed. As soon as the highest Fourier modes on the computational grid are energized, i.e. already at $t \approx 2$ or $\frac{\kappa_e}{\kappa_{max}} \approx 0.6$, the filtered spectrum switches from DNS-resolution to LES-resolution and f_{opt} increases quite sharply. In case of the linear dynamic schemes, a maximum value for f_{opt} is observed again in the region $0.1 \geq \kappa_e/\kappa_{max} \geq 0.3$. Once the filtered inertial range spectrum becomes fully established, i.e. at $\frac{\kappa_e}{\kappa_{max}} \geq 0.6$, the optimal blending factors of the linear dynamic schemes reach again a final value $f_{opt} = f_{opt}(\max(\kappa_e))$, which will be used for the practical computations in this dissertation. Analogously as for the Burgers' spectrum, the fully developed inertial range spectrum is characteristic for a wide range of turbulent flows such that $f_{opt}(\max(\kappa_e))$ is also considered characteristic and thus independent of the specific flow features. As a consequence, the dynamic finite difference schemes with $f_{opt}(\max(\kappa_e))$ are expected to be optimal for

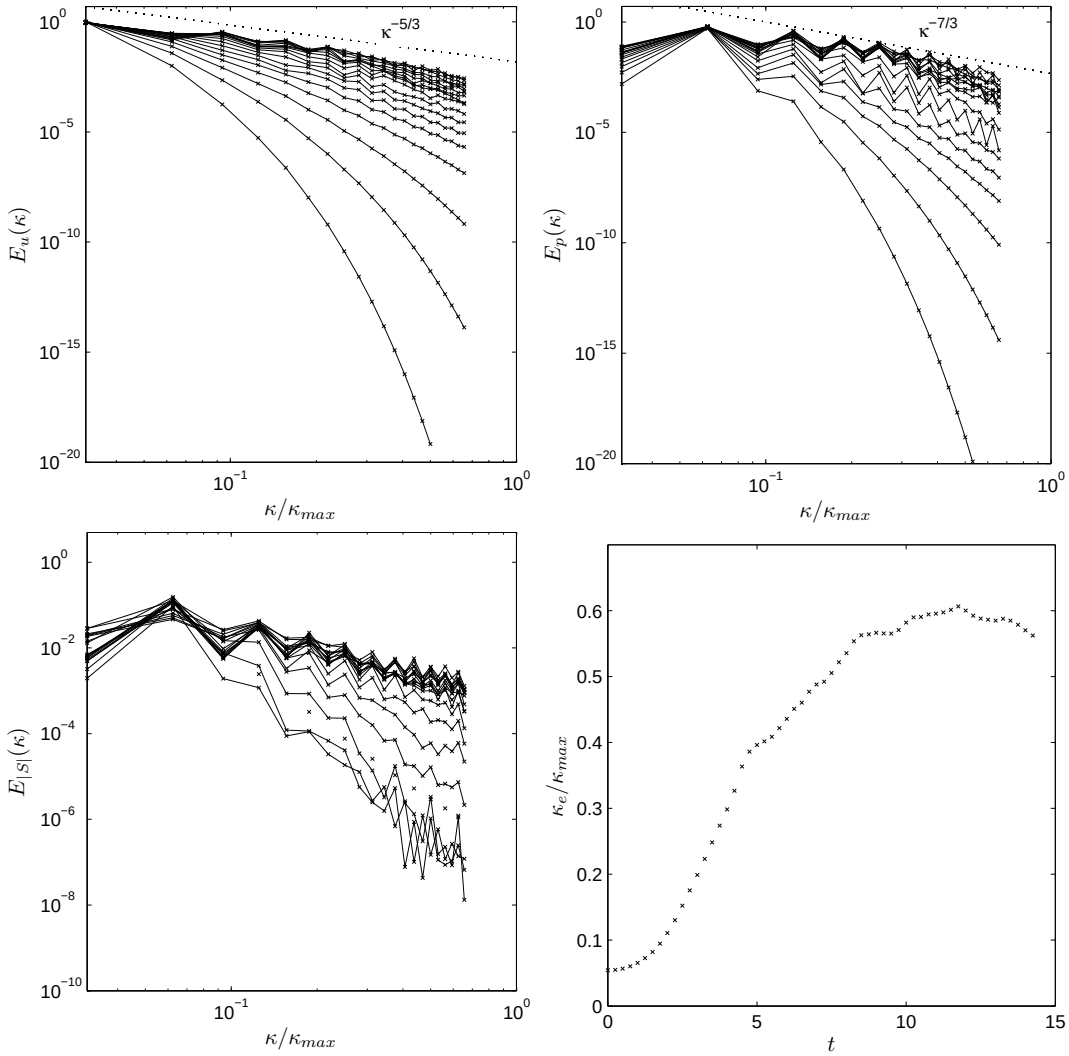

Figure 6.14: Generic Taylor-Green one-dimensional spectrum. The time-evolution of the normalized generic Taylor-Green LES spectrum for the velocity field $\mathbf{u}(\mathbf{x})$ (**upper left**), the pressure field $\overline{p}(\mathbf{x})$ (**upper right**) and the strain-rate magnitude $\left|\overline{S}\right|(\mathbf{x})$ (**lower left**). Finally, the effective wavenumber cutoff-ratio $\frac{\kappa_e}{\kappa_{max}}$ as function of time is displayed (**lower right**).

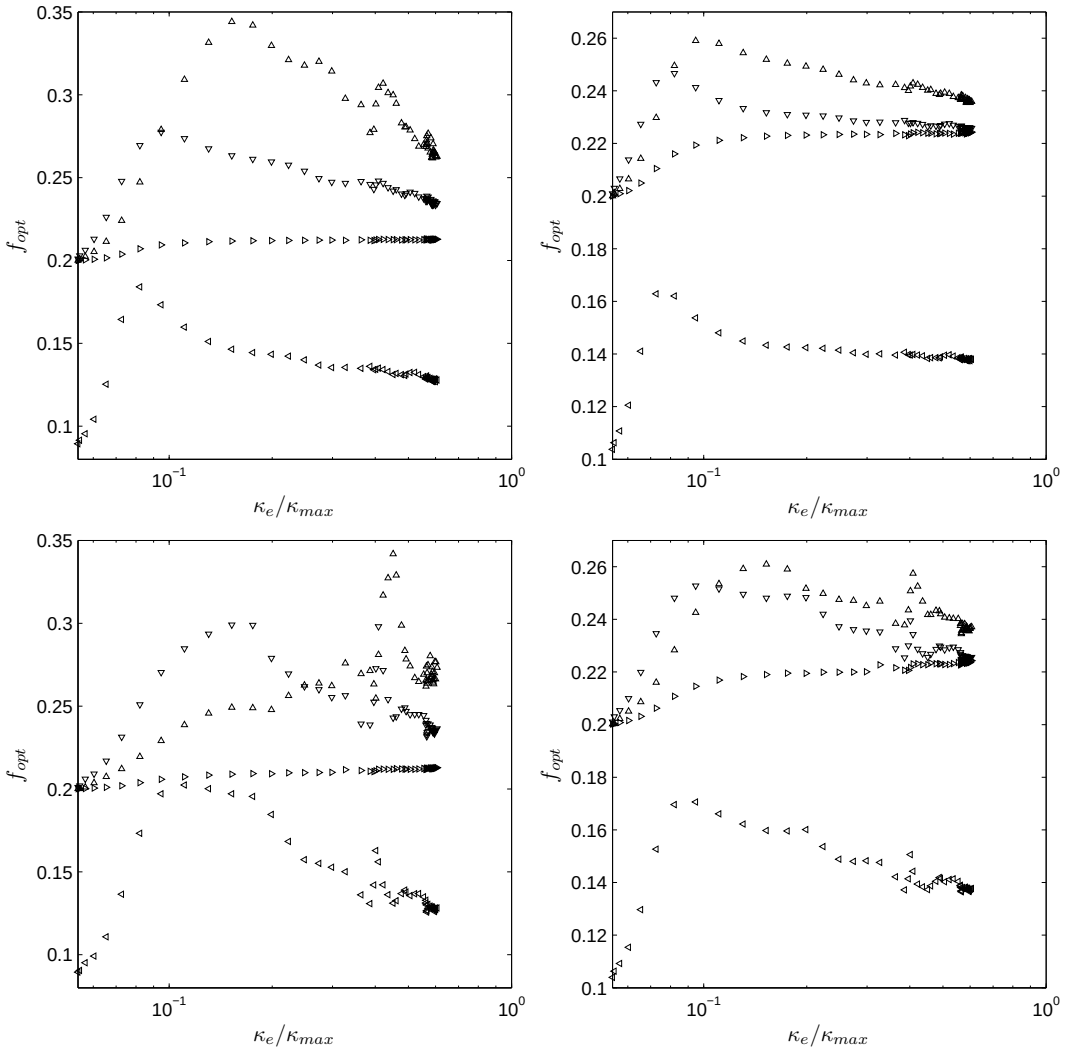

Figure 6.15: Optimal blending factor for Talyor-green spectrum. The optimal blending factor $f_{opt} = f(\kappa_e)$ for 1^{st} derivative (**left**) and 2^{nd} derivative (**right**) of the velocity field (**upper**) and the pressure field (**lower**). Distinguish the linear explcit dynamic scheme ($k = 2$) ($\triangle$), the linear explicit dynamic scheme ($k = 4$) ($\triangledown$), the nonlinear explicit dynamic scheme ($k = 2$) ($\triangleright$) and the linear implicit dynamic scheme ($k = 4$) ($\triangleleft$).

a wide range of fully developed turbulent flow.
In order to compare better the results of the Taylor-Green spectrum with those of the uniform spectrum and the Burgers' spectrum, the normalized optimal blending factors f_{opt}/f^*_{opt}, with $f^*_{opt} = \lim_{\kappa_e \to 0}$ are shown as function of $c^{dyn}_{k,n}/c^*_{k,n}$ in Figure 6.16. The spectrum-related weighting functions in the integral expressions for f_{opt} and $c_{k,n}$ display a similar influence as for the Burgers' spectrum.

6.3.5 Dispersion-Relation Preserving vs. Dynamic Finite Difference Approximations

In both the *Dispersion-Relation Preserving* finite difference schemes of e.g. Tam *et al.* [79] and Kim *et al.* [45], and the *dynamic* finite difference schemes presented in this dissertation, a predefined parameter must be determined by using a least-square minimization over a certain wavenumber range characterized by a cutoff wavenumber κ_c.
In case of the *dynamic finite difference schemes* the optimal blending factor f_{opt}, solely determines a certain quasi-optimal *trajectory* of the dynamic coefficient $c^{dyn}_{k,n}$ as function of an a priori assumed generic shape of the fully developed inertial range spectrum as illustrated in Figure 6.1. Hence, the role of f_{opt} is restricted to the calibration of the dynamic finite difference approximation such that a minimal dispersion error is obtained for that particular predefined fully developed inertial range spectrum. Since this predefined energy spectrum is assumed characteristic for a wide range of high-Reynolds number turbulent flows, the corresponding optimal blending factors f_{opt} are expected to be generally applicable to various numerical simulations. Once f_{opt} is defined, the dynamic finite difference scheme will optimize itself in real-time through the dynamic coefficient $c^{dyn}_{k,n}$ such that a minimal dispersion error is obtained according to the instantaneous energy spectrum of the flow. It is emphasized that this instantaneous energy spectrum may differ from the generic spectrum, used for retrieving f_{opt}. This implies that the dynamic scheme has *variable* Fourier characteristics which depend on the real-time value of $c^{dyn}_{k,n}$. As a consequence, if the flow is well resolved, the dynamic schemes will return to the standard Taylor-based finite difference schemes, regardless the value f_{opt}.
In the *Dispersion-Relation Preserving* (DRP) finite difference schemes, the optimal parameter is the constant coefficient $c_{k,n}$ itself and has to be determined by a similar least-square minimization as that used in the dynamic schemes. As a consequence, these schemes are *prefactored* and have *predefined* Fourier characteristics which are optimized for an a priori assumed shape of the energy spectrum. Typically, a uniform spectrum shape with $\kappa_c = \frac{2}{3}\kappa_{max}$ is adopted for the determination of $c_{k,n}$ in the DRP schemes.
It may be obvious that the value of $c_{k,n}$ used in the DRP schemes must be identical to that of the dynamic coefficient $c^{dyn}_{k,n}$ in case of a uniform spectrum, such that $c_{k,n}\left(\kappa_c = \frac{2}{3}\kappa_{max}\right) = c^{dyn}_{k,n}\left(f_{opt}, \kappa_c = \frac{2}{3}\kappa_{max}\right)$.
In the tables hereafter, the values of the optimal blending factors, that are applied

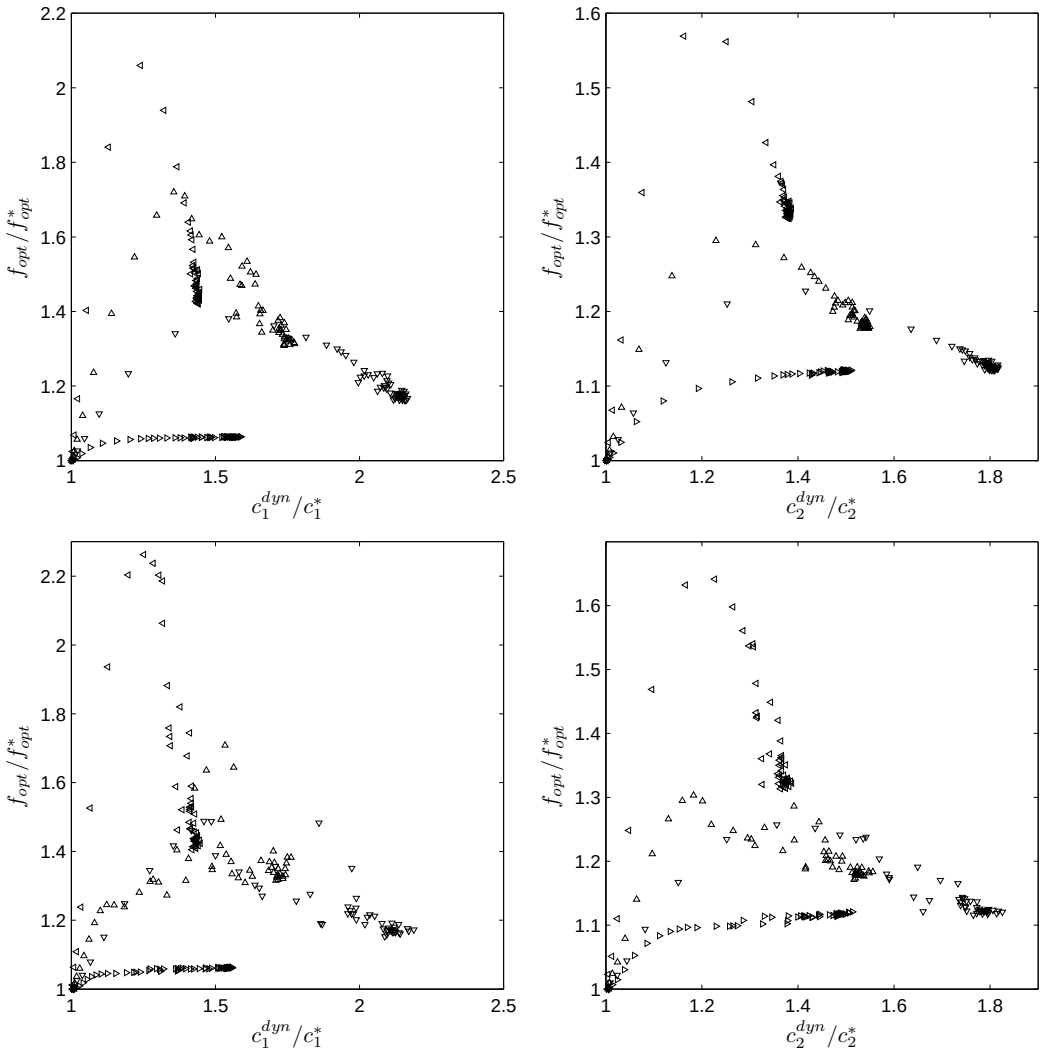

Figure 6.16: The optimal blending factor as function of the constant dynamic coefficient. The normalized optimal blending factor f_{opt}/f^*_{opt} ($f^*_{opt} = \lim_{\kappa_e \to 0} f_{opt}$) as function of the normalized constant dynamic coefficient $c^{dyn}_{k,n} = c^{dyn}_n$ for 1^{st} derivative (**left**) and 2^{nd} derivative (**right**) of the velocity field (**upper**) and the pressure field (**lower**). Distinguish the linear explicit dynamic scheme ($k = 2$) ($\triangle$), the linear explicit dynamic scheme ($k = 4$) ($\triangledown$), the nonlinear explicit dynamic scheme ($k = 2$) ($\triangleright$) and the linear implicit dynamic scheme ($k = 4$) ($\triangleleft$).

	$n=1$		$n=2$	
	f_{opt}	c_1^{dyn}	f_{opt}	c_2^{dyn}
Linear explicit $k=2$	0.2403148409	−0.334363121	0.2314394545	−0.134556615
Linear explicit $k=4$	0.2242833402	0.0775493930	0.2215576290	0.0206187300
Non-linear explicit $k=2$	0.2125572156		0.2244367639	
Linear implicit $k=4$	0.1159028279	0.0119669674	0.1308208736	0.00689073167

Table 6.1: Optimal blending factors and coefficients for the uniform spectrum. The analytically obtained optimal blending factors f_{opt} and the corresponding $c_{k,n}^{dyn} = c_n^{dyn}$ at $\kappa_c = \frac{2}{3}\kappa_{max}$ for a selection of dynamic finite difference approximations of the n^{th} derivative.

	$n=1$		$n=2$	
	f_{opt}	c_1^{dyn}	f_{opt}	c_2^{dyn}
Linear explicit $k=2$	0.2615500000	−0.301919628	0.2349700000	−0.130154404
Linear explicit $k=4$	0.232000000	0.0732383440	0.224720000	0.0202549970
Non-linear explicit $k=2$	0.212800000		0.224300000	
Linear implicit $k=4$	0.125630000	0.0120483470	0.136960000	0.0069263710

Table 6.2: Optimal blending factors and coefficients for the Burgers' spectrum. The numerically obtained optimal blending factors f_{opt} and the corresponding $c_{k,n}^{dyn} = c_n^{dyn}$ at $\kappa_e = \max(\kappa_e)$ for a selection of dynamic finite difference approximations of the n^{th} derivative.

in further numerical simulations, are given. Moreover, the (linear) dynamic coefficient that corresponds with this f_{opt} is shown, for a certain value of the effective wavenumber or cutoff wavenumber. Notice that for the nonlinear scheme it is meaningless to define a certain value of $c_{k,n}^{dyn}$, as it is a fluctuating field which determines a different $c_{k,n}^{dyn}$ for each wave component. Values of f_{opt} and the corresponding $c_{k,n}^{dyn}$ for the uniform spectrum with $\kappa_c = \frac{2}{3}\kappa_{max}$ are given in Table 6.1, whereas Table 6.2 gives f_{opt} and the corresponding $c_{k,n}^{dyn}$ for the Burgers spectrum at $\kappa_e = \max(\kappa_e)$. For the Taylor-Green spectrum, the optimal blending factor is obtained by averaging the quasi constant value of f_{opt} in the range $9 \leq t$ or $0.55 \leq \kappa_e$. Tables 6.3, 6.4 and 6.5 give the mean optimal blending factor, and the corresponding dynamic coefficient $c_{k,n}^{dyn}$ at $\max(\kappa_e)$, for the velocity field, the pressure field and the strain-rate magnitude. It is generally observed that the optimal value of the linear dynamic coefficient (corresponding to f_{opt}) decreases with decreasing slope of inertial range in the energy spectrum. This agrees with the expectations, since for steeper spectrum slopes, the smallest resolved scales contain less energy, and are thus less important than the largest resolved scales. As mentioned before, the above optimal values for the blending factor are used for the dynamic finite difference approximations in the numerical simulations hereafter. For the Dispersion-Relation Preserving schemes the coefficients $c_{k,n}$ obtained with the uniform spectrum (Table 6.1) are used in further simulations, since they correspond to the original schemes of e.g. Tam *et al.* [79].

	$n=1$		$n=2$	
	f_{opt}	c_1^{dyn}	f_{opt}	c_2^{dyn}
Linear explicit $k=2$	0.266805909	−0.29205720	0.236493636	−0.12841917
Linear explicit $k=4$	0.235410000	0.071582971	0.225802273	0.020083301
Non-linear explicit $k=2$	0.212648182		0.224079091	
Linear implicit $k=4$	0.128254091	0.012007761	0.137990000	0.006910196

Table 6.3: Optimal blending factors and coefficients for the Taylor-Green spectrum. The numerically obtained mean optimal blending factors f_{opt} and the corresponding $c_{k,n}^{dyn} = c_n^{dyn}$ at $\kappa_e = \max(\kappa_e)$ for a selection of dynamic finite difference approximations of the n^{th} derivative of the velocity field $\mathbf{u}(\mathbf{x})$.

	$n=1$		$n=2$	
	f_{opt}	c_1^{dyn}	f_{opt}	c_2^{dyn}
Linear explicit $k=2$	0.269222727	−0.29201951	0.236451363	−0.12823489
Linear explicit $k=4$	0.235444091	0.071686922	0.225475909	0.019991095
Non-linear explicit $k=2$	0.212401818		0.223640000	
Linear implicit $k=4$	0.127971364	0.011993550	0.137504545	0.006887905

Table 6.4: Optimal blending factors and coefficients for the Taylor-Green spectrum. The numerically obtained mean optimal blending factors f_{opt} and the corresponding $c_{k,n}^{dyn} = c_n^{dyn}$ at $\kappa_e = \max(\kappa_e)$ for a selection of dynamic finite difference approximations of the n^{th} derivative of the pressure field $p(\mathbf{x})$.

	$n=1$		$n=2$	
	f_{opt}	c_1^{dyn}	f_{opt}	c_2^{dyn}
Linear explicit $k=2$	0.249608636	−0.32235447	0.232970455	−0.132510930
Linear explicit $k=4$	0.227886364	0.075681831	0.223670909	0.020453642
Non-linear explicit $k=2$	0.212920000		0.224469545	
Linear implicit $k=4$	0.122888182	0.012118708	0.135990455	0.006946174

Table 6.5: Optimal blending factors and coefficients for the Taylor-Green spectrum. The numerically obtained mean optimal blending factors f_{opt} and the corresponding $c_{k,n}^{dyn} = c_n^{dyn}$ at $\kappa_e = \max(\kappa_e)$ for a selection of dynamic finite difference approximations of the n^{th} derivative of the strain-rate magnitude $|S|(\mathbf{x})$.

A scientist is happy, not in resting on his attainments but in the steady acquisition of fresh knowledge.

Planck, Max

7

The one-dimensional Burgers' equation

For the quality assessment of the dynamic finite difference approximations, developed in the previous chapter, it may be more useful to consider first a simpler problem than the Large-Eddy Simulation of three-dimensional Navier-Stokes turbulence for which these schemes were designed. Following the work of Love [54] and Das *et al.* [20], the one-dimensional viscous Burgers' equation with periodic boundary conditions is selected as a less complicated but eligible alternative to the Navier-Stokes equations. Similar to the Navier-Stokes equations, the Burgers' equation contains a quadratic nonlinear term and it exhibits an inertial range in the energy spectrum, as in real turbulence.

After a short introduction on the one-dimensional Burgers' flow as a simple model for turbulence, the numerical setup for Direct Numerical Simulation and Large-Eddy Simulation of Burgers' turbulence is discussed. The Direct Numerical Simulation provides a reference solution that allows for comparison among the different LES-solutions which are obtained with different numerical finite difference methods. In order to perform an honest, consistent and reliable quality assessment for the various finite difference approximations, the *error decomposition* of Vreman *et al.* [87] and Meyers *et al.* [60, 59] is adopted, which allows to separate the errors due to subgrid modeling and those due to the numerical method. In addition to this error decomposition, two error definitions are introduced, i.e. the *mathematics-based* error definition and the *physics-based* error definition. Using these definitions, the numerical quality of the dynamic finite difference approximations is examined for the LES of Burgers' equation, adopting either a *perfect* subgrid-scale model or a *dynamic Smagorinsky* model. In the latter case, the interactions of the numerical errors with the modeling errors are closely investigated.

7.1 BURGERS' TURBULENCE

Consider the one-dimensional *homogeneous flow* governed by the viscous Burgers' equation for the velocity field $u(x,t)$ in non-dimensional form[1]

$$\frac{\partial u}{\partial t} + \frac{1}{2}\frac{\partial u^2}{\partial x} = \nu \frac{\partial^2 u}{\partial x^2}, \quad \forall x \in \mathbb{R},\ t \in \mathbb{R}^+. \tag{7.1}$$

Obviously, equation (7.1) can be interpreted as the one-dimensional equivalent of the Navier-Stokes equations, but without the pressure gradient. Indeed, similar to the Navier-Stokes equations, Burgers' equation (7.1) contains a quadratic nonlinear term which is responsible for the generation of small-scale structures. These small scales are eventually dissipated by the viscous force. Moreover, the energy spectrum of the viscous Burgers' equation is characterized by an *inertial range*, through which energy is transferred from the large scales to the small scales until it is dissipated by the viscosity in the *dissipation range*. Since this process is similar to that of the Navier-Stokes equations, Johannes Martinus Burgers [11, 12] proposed equation (7.1) as a simplified model for turbulence. Despite the agreements, the small-scale dynamics of Burgers' turbulence and real turbulence are substantially different. In Burgers' turbulence, the small scales represent shock waves, with thickness in the order of the viscous scale. Instead of a successive breakdown of the large structures into smaller ones as in real turbulence, the small structures tend to merge into large ones. The corresponding inertial range scaling for a shock-wave spectrum is found to be κ^{-2}. Nevertheless, since in Burgers' model turbulence the large and small scales are separated in Fourier space by a characteristic inertial range κ^{-2} and are thus statistically independent due to the energy cascade, it is considered as a useful tool, not only for investigating the influence of the subgrid modeling, but also for assessing the quality of the proposed dynamic finite difference approximations in a Large-Eddy Simulation environment. Hence, Burgers' equation is considered here merely as a vehicle for producing a flow field characterized by an inertial range spectrum.
In the current dissertation, Burgers' equation is subjected to the periodic boundary conditions[2] in a one-dimensional domain $0 \leq x \leq 2\pi$

$$u(x,t) = u(x + 2\pi, t). \tag{7.2}$$

Furthermore, the initial sinusoidal velocity profile

$$u(x,0) = \sin(x), \tag{7.3}$$

[1] This implies that the quantities $u(x,t)$, x, t and ν are expressed relatively to a reference value such that they become dimensionless.

[2] The periodic boundary conditions are selected in this work in order to avoid ambiguities with eccentric boundary discretizations, which may affect the quality of the various finite difference approximations.

is imposed at $t = 0$, which corresponds to a single Fourier mode. Assuming a unit length and velocity as reference, the Reynolds number is set to $\mathrm{Re} = \frac{1}{\nu} = 500$. The initial kinetic energy and dissipation rate are then calculated as

$$k(t=0) = \int_0^{\kappa_\eta} E(\kappa, t=0)\, d\kappa = \frac{1}{2\pi} \int_0^{2\pi} \frac{1}{2} \left[u(x, t=0)\right]^2 dx = \frac{1}{4}, \tag{7.4}$$

$$\varepsilon(t=0) = \int_0^{\kappa_\eta} 2\nu\kappa^2 E(\kappa, t=0)\, d\kappa = \frac{2\nu}{2\pi} \int_0^{2\pi} \left[\frac{\partial u}{\partial x}(x, t=0)\right]^2 dx = \frac{1}{\mathrm{Re}}. \tag{7.5}$$

For $t > 0$, the initial sinusoidal velocity profile evolves into a stationary shock at $x = \pi$. Due to the viscous forces, this shock decays and eventually dies out. Therefore, this test case can be seen from a numerical point of view as the one-dimensional equivalent of the Taylor-Green transitional flow, discussed in the next chapter. As mentioned before, the corresponding shock-wave energy spectrum exhibits an inertial range κ^{-2}, through which energy is transferred from the large scales to the small scales, and finally dissipated by the viscosity.
Although analytical solutions can be found for the periodic viscous Burgers' equation by means of the Cole-Hopf transformation, the reference solution used in the present work is generated by means of *pseudo-spectral* Direct Numerical Simulation of equation (7.1). This is discussed further.

7.2 Numerical simulation of Burgers' turbulence

In the following, the numerical setup for Direct Numerical Simulation and Large-Eddy Simulation is discussed in detail.

7.2.1 Direct Numerical Simulation

A reference solution for the Burgers system is generated from a Direct Numerical Simulation. In order to resolve all scales up to the viscous scale, a uniform grid is adopted with $N = 8192$ nodes such that the grid cutoff-wavenumber is given by $\kappa_{max} = \frac{\pi}{\Delta} = 4096$.[3] Hence, de-aliasing is not required since the viscous scale is fully resolved, i.e. $\kappa_\eta = 2\pi/\eta \ll \kappa_{max}$, and thus aliasing is assumed negligible. The non-linear term is discretized in the energy conserving skew-symmetric form.[4] Applying

[3] Note that Das *et al.* [20] used only $N = 2048$ nodes corresponding to 1024 Fourier modes for the Direct Numerical Simulation of the viscous Burgers' equation at Reynolds number $\mathrm{Re} = 1000$, whereas de Stefano *et al.* used $N = 32768$ grid nodes or 16384 Fourier modes for the DNS at Reynolds number $\mathrm{Re} = 20000$. In the current work, the number of Fourier modes and the Reynolds number are selected such that the dissipation range is resolved almost to machine precision.

[4] Remark that for Burgers' equation the skew-symmetry formulation differs from that in the Navier-Stokes equations, due to the absence of a continuity equation. Indeed, the skew-symmetric form is constructed by combination of the advective form and the divergence form in the respective proportions 1/3 and 2/3, whereas for the Navier-Stokes equations these proportions are 1/2 and 1/2.

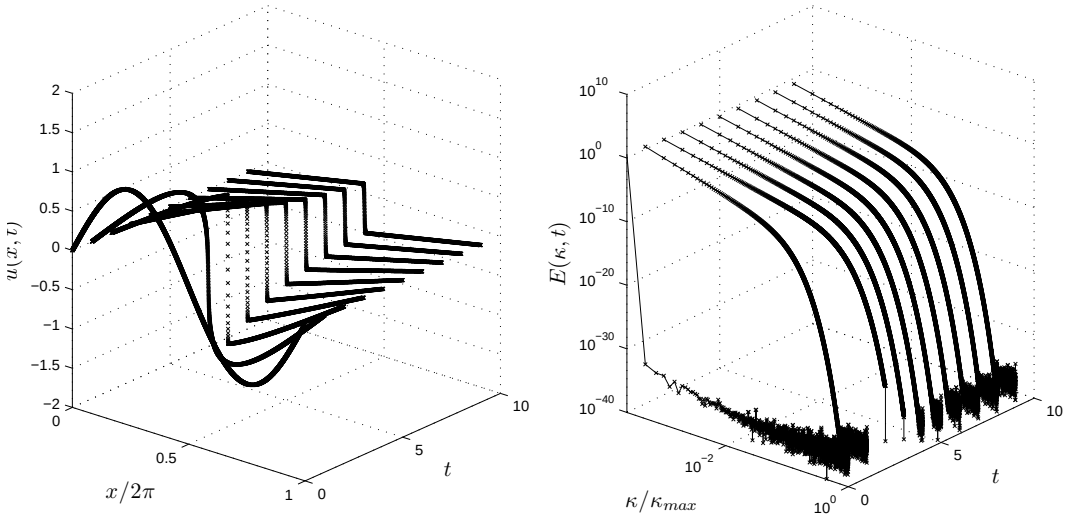

Figure 7.1: Direct Numerical Simulation of Burgers' equation. An impression of the resolved velocity field $u(x,t)$ (**left**) and its corresponding energy spectrum $E(\kappa,t)$ (**right**).

the one-dimensional sampling operator $\mathscr{S}^{\Delta}$, defined in Chapter 2, to equation (7.1) leads to the discrete Burgers' equation

$$\frac{\delta u}{\delta t} + \frac{1}{3}\frac{\delta u^2}{\delta x} + \frac{1}{3}u\frac{\delta u}{\delta x} = \nu\frac{\delta^2 u}{\delta x^2}. \tag{7.6}$$

In order to avoid later confusion with the filtering operation, the resolved velocity field is represented by u instead of $\overline{u}$. A *pseudo-spectral* numerical method is adopted in which the *exact* partial derivatives are calculated in Fourier space. Hence, numerical discretization errors or finite difference errors are excluded. For the time-stepping, a standard 4-stage Runge-Kutta method with standard coefficients $\left[\frac{1}{4}, \frac{1}{3}, \frac{1}{2}, 1\right]$ (see Section 4.2) is selected. The time step is set to $\Delta t = 1.10^{-5}$ such that numerical dissipation is minimal and both the *Courant-Friederichs-Lewy* condition and the *Neumann* conditions are satisfied at all times, i.e.

$$\text{CFL} \leq \frac{\Delta t \max|u(x,0)|}{\Delta} \approx 1.10^{-2} \ll 1 \tag{7.7}$$

$$\text{Neu} = \frac{2\nu\Delta t}{\Delta^2} \approx 7.10^{-2} \ll \mathscr{O}(1). \tag{7.8}$$

The decaying shock wave is followed until $t = 10s$. Simulation results of $u(x, t = t_j)$ and the corresponding energy spectrum are illustrated in Figure 7.1. The decay of kinetic energy and the rate of dissipation are shown in Figure 7.2 as function of time.

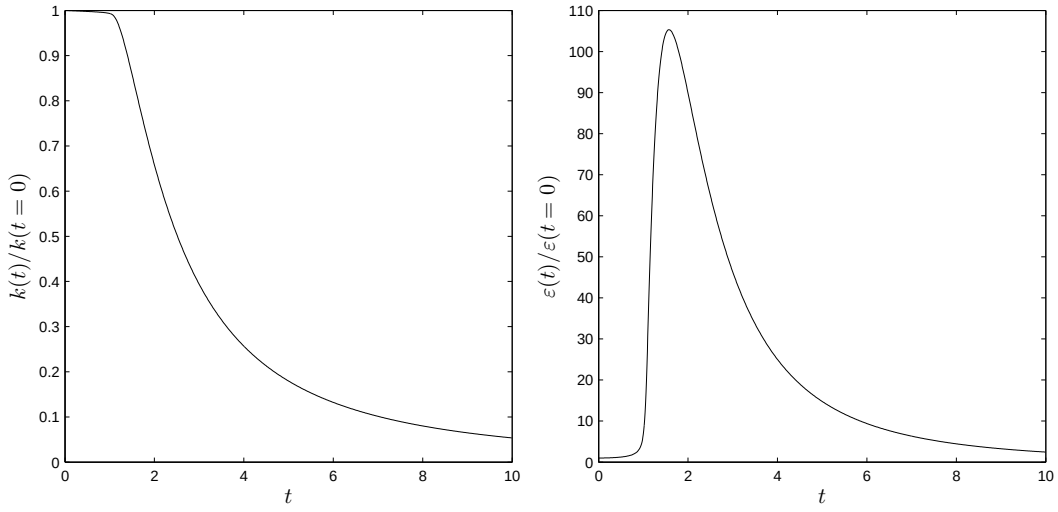

Figure 7.2: Direct Numerical Simulation of Burgers' equation. Temporal evolution of the decaying kinetic energy k (**left**) and the rate of dissipation ε (**right**).

7.2.2 Large-Eddy Simulation

The goal of Large-Eddy Simulation is to reproduce the dynamics of the filtered DNS solution by resolving only the high energetic large scale features (low wavenumbers) in the flow, corresponding to ideally 80% of the total kinetic energy, while neglecting the low energetic small scales (high wavenumbers). It was already argued in Chapter 3 that in this work, the sharp spectral Fourier filter is preferred as the ideal LES filter since it leads to a clear scale separation in wavenumber space, eliminating modes above the cutoff and leaving modes below the cutoff unharmed. It was also discussed that when using sharp Fourier filters, the Gibbs-phenomenon arises, due to the trunctation of an infinite Fourier series. Although elimination of the Gibbs oscillations is subject to shock capturing schemes, they are part of the filtered solution in the current context of LES [20, 21].
The continuous Burgers' LES equation with the *double decomposition* are derived by applying the sharp Fourier filter with cutoff wavenumber $\kappa_c = \frac{\pi}{\Delta_c}$ to expression (7.1), yielding

$$\frac{\partial \overline{u}}{\partial t} + \frac{1}{2}\frac{\partial \overline{\overline{u}\,\overline{u}}}{\partial x} = \nu \frac{\partial^2 \overline{u}}{\partial x^2} - \frac{1}{2}\frac{\partial \tau}{\partial x}. \tag{7.9}$$

Here, $\bar{\cdot}$ denotes the filtered variable and the subgrid stress is defined as

$$\tau = \overline{uu} - \overline{\overline{u}\,\overline{u}}. \tag{7.10}$$

Remind from Chapters 2 and 3 that the explicitly filtered nonlinear term in the double decomposition framework allows to preclude aliasing errors [67, 55]. Since

equation (7.1) is unclosed, an appropriate subgrid-scale model is needed to close it. Two models are considered in this dissertation, i.e. *the perfect subgrid-scale model* and a *dynamic Smagorinsky model*. In case of the *the perfect subgrid-scale model*, the exact subgrid-stresses are extracted at each Runge-Kutta step from a simultaneous running DNS-simulation. This results in a perfect LES that is expected to recover exactly the filtered DNS results in case of exact numerics. Note that this approach was already proposed by de Stefano *et al.* [21] for the study of the filter shape in LES.
Besides the perfect subgrid model, also an eddy-viscosity subgrid model is used in the current work, following the work of Love [54]. Although Love examined various constant coefficient Smagorinsky-like subgrid closures for the Burgers' equation, in the current dissertation a *dynamic Smagorinsky model* is proposed to obtain the model coefficient. The *de-aliased* eddy-viscosity subgrid closure is given by

$$\tau = -2\nu_t \overline{\frac{\partial \overline{u}}{\partial x}}, \tag{7.11}$$

where the turbulent viscosity is defined as

$$\nu_t = C^2 \Delta_c^2 \left\langle \left| \frac{\partial \overline{u}}{\partial x} \right| \right\rangle_w, \tag{7.12}$$

and $\langle . \rangle_w$ denotes the average over a length w [54]. For the limit $w \to \Delta$, (7.12) tends to the one-dimensional equivalent of the Smagorinsky model, whereas $w \to \mathscr{L}, \mathscr{L} = 2\pi$ tends to the subgrid model advocated by Leslie *et al.* [51]. In the current work, $w = \mathscr{L}, \mathscr{L} = 2\pi$ is preferred since better results are obtained. This conclusion is supported by the findings of Love [54]. Since the subgrid model should only be engaged if the nonlinear term starts to produce small-scale structures that are not visible on the LES grid, the dynamic Germano procedure [30] is used to calculate the appropriate value of C^2. With $\widetilde{\cdot}$ denoting the coarse filter, the resolved stress and the closure term are now defined on two different filter resolutions κ_c and κ_c/α leading to

$$\overline{uu} = \overline{\overline{u}\,\overline{u}} - 2C^2 \Delta_c^2 \overline{\left\langle \left| \frac{\partial \overline{u}}{\partial x} \right| \right\rangle_w \frac{\delta \overline{u}}{\delta x}} \tag{7.13}$$

$$\widetilde{uu} = \widetilde{\widetilde{u}\widetilde{u}} - 2C^2 \left(\alpha \Delta_c\right)^2 \widetilde{\left\langle \left| \frac{\partial \widetilde{u}}{\partial x} \right| \right\rangle_w \frac{\partial \widetilde{u}}{\partial x}} \tag{7.14}$$

Remark that the projective property of the sharp cutoff filter implies that $\widetilde{\overline{\cdot}} = \widetilde{\cdot}$. The model coefficient C^2 is now extracted by comparing both equations on the same coarse resolution level. Hence, the least square minimization of the error between both expressions finally yields,

$$C^2 = \frac{\langle \mathscr{L}\mathscr{M} \rangle}{\langle \mathscr{M}\mathscr{M} \rangle}, \tag{7.15}$$

where

$$\mathscr{L} = \widetilde{\overline{u}\,\overline{u}} - \widetilde{\overline{u}}\widetilde{\overline{u}} \tag{7.16}$$

$$\mathscr{M} = 2\Delta_c^2 \left[\left\langle \left| \widetilde{\frac{\delta \overline{u}}{\delta x}} \right| \right\rangle_w \frac{\delta \overline{u}}{\delta x} - \alpha^2 \left\langle \left| \widetilde{\frac{\delta \widetilde{u}}{\delta x}} \right| \right\rangle_w \frac{\delta \widetilde{u}}{\delta x} \right] \tag{7.17}$$

Applying the one-dimensional sampling operator, defined in Chapter 2, the Burgers' LES-equation is now projected from the continuum unbounded domain to the discrete unbounded domain with maximum grid resolution $\kappa_{max} = \frac{\pi}{\Delta}$ such that $\Delta = \frac{2}{3}\Delta_c$ as suggested by the work of Orszag [67]. Adopting again the skew-symmetric formulation of the nonlinear term and thus ensuring the discrete conservation of kinetic energy, the discrete Burgers' LES equation then reads

$$\frac{\delta \overline{u}}{\delta t} + \frac{1}{3}\overline{\overline{u}\frac{\delta \overline{u}}{\delta x}} + \frac{1}{3}\frac{\delta \overline{\overline{u}\,\overline{u}}}{\delta x} = \nu \frac{\delta^2 \overline{u}}{\delta x^2} - \frac{1}{2}\frac{\delta \tau}{\delta x}, \tag{7.18}$$

Equation (7.18) is solved with various finite difference methods on a uniform mesh with $N = 256$ nodes corresponding with a maximum grid resolution $\kappa_{max} = \frac{\pi}{\Delta} = 128$. The physical resolution is defined by the filter cutoff wavenumber $\kappa_c = \frac{2}{3}\kappa_{max} = 85$. For time integration, again the 4-stage Runke-Kutta method is used. Further, the same time step of $t = 1.10^{-5}$ as in the DNS simulation is adopted.

As mentioned before, the main purpose of the current Large-Eddy Simulation study is to investigate the quality of the dynamic finite difference approximations, designed in the previous chapter, and compare it to that of various other techniques among which the Dispersion-Relation Preserving schemes [79, 45]. However, first some particularities concerning the dynamic finite difference approximation of the skew-symmetric formulation of the nonlinear term must be addressed. Since $\overline{u}$ and $\overline{u}\overline{u}$ are characterized by strongly different energy spectra, the *constant* dynamic coefficients $c_{k,n}^{dyn}$, obtained by expression (6.20), will be different in the *linear* dynamic finite difference approximations of the advective operator and divergence operator, used into the construction of the skew-symmetric formulation. As a consequence, the skew-symmetry property and thus the conservation of kinetic energy is lost. In order to preserve skew-symmetry, the same dynamic coefficient $c_{k,n}^{dyn}$ is required in both contributions. A first solution that can be thought off, is to construct a single dynamic finite difference approximation for the entire skew-symmetric operator. Such an approach is reminiscent to the one used in Chapter 5. Hence a single coefficient $c_{k,n}^{dyn}$ is then obtained for the skew-symmetric operator which should be an optimal compromise between the spectra of $\overline{u}$ and $\overline{u}\overline{u}$. The Leonard term and the

model term for the calculation of this coefficient are determined as

$$\mathscr{L} = c^{*}_{k,n}\left(\alpha^{k}-1\right)\Delta^{k}\left\{\overline{\left.\overline{u}\frac{\delta^{k+n}\overline{u}}{\delta x^{k+n}}\right|^{\Delta}} + \left.\frac{\delta^{k+n}\overline{\overline{u}\,\overline{u}}}{\delta x^{k+n}}\right|^{\Delta}\right\} \tag{7.19}$$

$$\begin{aligned}\mathscr{M} = {} & \left(1-\alpha^{k}\right)\Delta^{k}\left\{\overline{\left.\overline{u}\frac{\delta^{k+n}\overline{u}}{\delta x^{k+n}}\right|^{\Delta}} + \left.\frac{\delta^{k+n}\overline{\overline{u}\,\overline{u}}}{\delta x^{k+n}}\right|^{\Delta}\right\} \\ & -\alpha^{k}\Delta^{k} f c^{**}_{k,n}\left(1-\alpha^{2}\right)\Delta^{2}\left\{\overline{\left.\overline{u}\frac{\delta^{k+n+2}\overline{u}}{\delta x^{k+n+2}}\right|^{\Delta}} + \left.\frac{\delta^{k+n+2}\overline{\overline{u}\,\overline{u}}}{\delta x^{k+n+2}}\right|^{\Delta}\right\}\end{aligned} \tag{7.20}$$

where α denotes the double grid resolution. Although such an approach is perfectly viable and might be interesting for further investigation, the use of an alternative method is preferred instead. In this method, the dynamic coefficient $c^{dyn}_{k,n}$ that is obtained for the finite difference approximation of the advective operator, is also used in the finite difference approximation of the divergence operator. This approach is motivated by the fact that it is equivalent with the traditional discretization approach of the skew-symmetric operator using traditional standard schemes or prefactored optimized schemes.

Secondly, some attention is required for the discretization of the subgrid force of the *perfect subgrid-scale model*. Indeed, in order to obtain the exact filtered DNS solution from the perfect LES, the discretization of the subgrid force must be identical to that of the nonlinear term. Hence, the same dynamic coefficient $c^{dyn}_{k,n}$ is used for the linear dynamic finite difference approximation of the subgrid force as for the skew-symmetric operator. Notice that this problem does not occur for the discretization of the *eddy-viscosity* subgrid force, since it is discretized analogously to the molecular viscous term. Hence, the dynamic coefficient $c^{dyn}_{k,n}$ of the 2^{nd} derivative is applied here without ambiguity. Although in case of the *nonlinear* dynamic scheme, $c^{dyn}_{k,n}$ depends theoretically neither on $\overline{u}$ or $\overline{uu}$, the same procedure is applied for the discretization of the skew-symmetric term using the conservative formulation of the nonlinear dynamic scheme (see Appendix B). Nevertheless, the skew-symmetry property is not maintained since the scheme itself produces spurious scales due to its nonlinearity. Hence for this scheme, the updated velocity field $u\,(x)$ must be filtered every Runge-Kutta step with the de-aliasing filter instead of only to the nonlinear term in equation (7.9).

7.3 Quantification of numerical errors

Before assessing the quality of the dynamic finite difference approximations in the LES of the Burgers' equation, an appropriate and consistent evaluation method must be defined that allows to quantify the different sources of error due to modeling and numerical approximation, and their interactions. In order to separate modeling and numerical errors the *error decomposition method* of Vreman *et al.* [87] and Meyers *et al.* [60, 59, 61] is adopted. Once the error sources are identified by this separation method, a certain *error norm* can be defined which quantifies the magnitude of the respective error sources. The described approach is further discussed in more detail.

Consider the reference solution, obtained by e.g. Direct Numerical Simulation, which is characterized by the viscous scale κ_η. Further consider a specific flow variable of interest ϕ. The *total error* on the variable ϕ obtained by the Large-Eddy Simulation with physical resolution $\kappa_c = \frac{\pi}{\Delta_c}$ and grid resolution $\kappa_{max} = \frac{\pi}{\Delta}$, is then defined as

$$\varepsilon_{\phi,total}\left(\kappa_c, \kappa_{max}\right) = \overline{\phi_s\left(\kappa_\eta, \frac{3}{2}\kappa_\eta\right)} - \overline{\phi}_{fd}\left(\kappa_c, \kappa_{max}\right), \tag{7.21}$$

where, $\overline{\phi_s\left(\kappa_\eta, \frac{3}{2}\kappa_\eta\right)}$ represents the filtered *spectral* DNS solution, and $\overline{\phi}_{fd}\left(\kappa_c, \kappa_{max}\right)$ represents the *finite difference* LES solution with cutoff κ_c on an LES grid with maximum wavenumber κ_{max}. In order to separate the modeling error contributions and the numerical error contributions within the total error, the latter is decomposed as

$$\varepsilon_{\phi,model}\left(\kappa_c, \kappa_{max}\right) = \overline{\phi_s\left(\kappa_\eta, \frac{3}{2}\kappa_\eta\right)} - \overline{\phi}_s\left(\kappa_c, \kappa_{max}\right) \tag{7.22}$$

$$\varepsilon_{\phi,num}\left(\kappa_c, \kappa_{max}\right) = \overline{\phi}_s\left(\kappa_c, \kappa_{max}\right) - \overline{\phi}_{fd}\left(\kappa_c, \kappa_{max}\right), \tag{7.23}$$

where $\overline{\phi}_s\left(\kappa_c, \kappa_{max}\right)$ represents the *spectral* LES solution with cutoff wavenumber κ_c and numerical resolution κ_{max} determined by the LES grid. Note that this solution would be equivalent with the finite difference LES-solution on an infinitely fine grid $\overline{\phi}_{fd}\left(\kappa_c, \kappa_\infty\right)$. The modeling error $\varepsilon_{\phi,model}$ is related to the adopted subgrid closure, whereas the numerical error $\varepsilon_{\phi,num}$ contains contributions of the aliasing errors as well as discretization errors or finite difference errors. If proper de-aliasing is applied through explicit filtering of the nonlinear term, the numerical $\varepsilon_{\phi,num}$ reduces exactly to the finite difference discretization errors.
Although $\varepsilon_{\phi,num}$ is well defined for a perfect subgrid model or a static Smagorinsky model in which the value of the model constant C^2 is chosen a priori, the errors are not clearly separated in case of a dynamic model where the value of model coefficient C^2 is affected by the numerics. In the latter case numerical errors and

modeling errors continuously interfere through the feedback of the numerically obtained dynamic model constant C^2. Hence, in this work the discretization errors of the LES-equations and those of the dynamic procedure will be considered separately, and the the influence of the numerics on the calculation of the dynamic model coefficient will be demonstrated.
The value of the model coefficient C^2 is considered to be a *theoretical* model parameter that corresponds to the instantaneous energy spectrum of the resolved velocity field. Therefore, the dynamic procedure by which C^2 is determined, might be considered as a theoretical post-processing procedure at each time step. In this work, an attempt is done to separate the discretization of the LES-equations and that of the dynamic procedure. Then, three coefficients can be distinguished. First the coefficient $C_{s,s}$ denotes the theoretical optimal value that is obtained by applying the dynamic procedure, in which the derivatives are evaluated spectrally, to the solution of the pseudo-spectral Large-Eddy Simulation of Burgers' equation. Further the coefficient $C_{s,fd}$ is defined, which represents the optimal value that is obtained by applying the dynamic procedure, in which the derivatives are also evaluated spectrally, to the of the finite difference LES solution of Burgers' equation. Although $C_{s,fd}$ is affected by the finite difference errors in the LES-solution due to the discretization of the basic LES equation, its calculation is not liable to finite difference errors. Hence, this allows to isolate more or less the influence of the numerical errors in the Burgers' solution on the model coefficient. Finally, $C_{fd,fd}$ denotes the finite difference approximation to the expected value $C_{s,fd}$. This coefficient is obtained in a finite difference Large-Eddy Simulation of Burgers' equation in which the derivatives within the dynamic procedure are also evaluated with the same finite difference method. In summary, both coefficients $C_{s,fd}$ and $C_{fd,fd}$ contain influences of the discretization of the LES-equations, however $C_{s,fd}$ does not suffer from discretizations in its calculation, in contrast to $C_{fd,fd}$. The finite difference discretization errors (7.23) are now decomposed as

$$\varepsilon_{\phi,num}\left(\kappa_c,\kappa_{max}\right) = \varepsilon_{\phi,numI}\left(\kappa_c,\kappa_{max}\right)+\varepsilon_{\phi,numII}\left(\kappa_c,\kappa_{max}\right), \tag{7.24}$$

in which

$$\varepsilon_{\phi,numI}\left(\kappa_c,\kappa_{max}\right) = \overline{\phi}_s\left(\kappa_c,\kappa_\eta,C_{s,s}\right)-\overline{\phi}_{fd}\left(\kappa_c,\kappa_{max},C_{s,fd}\right) \tag{7.25}$$

$$\varepsilon_{\phi,numII}\left(\kappa_c,\kappa_{max}\right) = \overline{\phi}_{fd}\left(\kappa_c,\kappa_{max},C_{s,fd}\right)-\overline{\phi}_{fd}\left(\kappa_c,\kappa_{max},C_{fd,fd}\right). \tag{7.26}$$

In the expressions above, $\varepsilon_{u,numI}$ represents the numerical errors due to discretization of the LES-equation, since spectral derivatives of the finite difference solution are used for the evaluation of the Germano procedure. On the other hand, $\epsilon_{u,numII}$ represents only errors due to the discretization in the evaluation of the Germano procedure itself.

Once the different error contributions are separated and identified, their respective magnitude may be represented by various error definitions. Two definition

types are adopted in the present dissertation, i.e. the *mathematics-based* and the *physics-based* error definitions. Note that similar definitions were already introduced by Meyers *et al.* [62], and the same terminology will be adopted here. First the mathematics-based error definitions are considered, which are comparable to those used in the work of Chow *et al.* [19]. The error spectrum of the pointwise error ε_ϕ of the variable ϕ is defined as

$$E_{\varepsilon_\phi}(\kappa) = \widehat{\varepsilon_\phi}(\kappa)\,\widehat{\varepsilon_\phi}^{\,*}(-\kappa)\,. \tag{7.27}$$

The error spectrum of ε_ϕ is a function of the wavenumber κ and reflects the energy content of the total error on each Fourier mode. Further, various global mathematics-based error norms are obtained by integrating the wavenumber-weighted energy spectrum

$$\left\|E_{\varepsilon_\phi}\right\|_q = \int_0^{\kappa_{max}} \kappa^q E_{\varepsilon_\phi}(\kappa)\,d\kappa, \quad \forall q \in \mathbb{Z}. \tag{7.28}$$

It is obvious that for $q > 0$, the small scales are accentuated in the calculation of the global error norm, whereas for $q < 0$ the large scales are more accentuated. In the particular case $q = 0$, the error norm corresponds with the global magnitude k_{ε_ϕ} related to the error and is expressed as

$$k_{\varepsilon_\phi} = \int_0^{\kappa_{max}} E_{\varepsilon_\phi}(\kappa)\,d\kappa. \tag{7.29}$$

Remark that the *magnitude* k_{ε_ϕ} corresponds to the L_2-norm,[5] often used in error evaluation, as $L_2(t) = 2\pi\sqrt{k_{\varepsilon_\phi}(t)}$ and that this error always has a positive sign.
In contrast to the mathematics-based error definitions, the physics-based error definitions consider the error between energy spectra rather than the spectrum of the errors [60]. Hence, the error on the energy spectrum $E_\phi(\kappa) = \frac{1}{2}\widehat{\phi}\widehat{\phi}^*$ of the variable of interest ϕ is defined as

$$\varepsilon_E(\kappa) = \Delta E_\phi(\kappa)\,, \tag{7.31}$$

where Δ denotes the difference between the spectra of the two compared solutions of ϕ. In analogy with the mathematics-based error definitions, a global physics-based

[5] The L_2-norm is defined as

$$L_2(t) = \sqrt{\frac{1}{2\pi}\int_0^{\pi} \left[\varepsilon_\phi(\mathbf{x},t)\right]^2 dx}. \tag{7.30}$$

error norm is defined by integrating the weighted error spectrum, yielding

$$\|\varepsilon_E\|_q = \int_0^{\kappa_{max}} \kappa^q \Delta E_\phi(\kappa)\, d\kappa, \quad \forall q \in \mathbb{Z}. \tag{7.32}$$

As mentioned before, $q < 0$ accentuates the large scale errors, whereas the small scale errors are accentuated for $q > 0$. The general definition (7.32) can now be related to physics-based error measures for the velocity field as variable of interest for some specific choices of the weighting q. Indeed, for Burgers' turbulence, one can obtain the total error on the kinetic energy ε_k, and the total error on the dissipation rate ε_ε by choosing respectively $q = 0$ and $q = 2$, yielding

$$\varepsilon_k = \Delta k = \int_0^{\kappa_{max}} \Delta E_u(\kappa)\, d\kappa \tag{7.33}$$

$$\varepsilon_\varepsilon = \Delta\varepsilon = \int_0^{\kappa_{max}} \kappa^2 \Delta E_u(\kappa)\, d\kappa \tag{7.34}$$

Remark that the sign of ε_k and ε_ε could be either positive or negative, enabling to see interactions between different error sources.

It may be clear that the physics-based error definitions represent only errors on the amplitude of the solution, assumed that the influence of phase is not accumulated in time, whereas the mathematics-based errors contain contributions of both amplitude and phase errors in the solution at a certain time. Meyers *et al.* [62] found that some physics-based error definitions may lead to an overly optimistic accuracy, which is confirmed by our numerical results. Hence, mathematics-based error definitions are more strict as they contain information about phase and amplitude. Both error definitions are used further for analyzing the performance of finite difference schemes, and interactions with the subgrid model.

7.4 A priori Burgers' study

In the current section, an *a priori* quality assessment is performed for a selection of four dynamic finite difference approximations described in Appendix C, i.e. the 2^{nd} -order explicit linear and nonlinear linear dynamic finite difference approximations, the 4^{th} -order explicit linear dynamic finite difference approximation and the 4^{th} -order implicit linear dynamic finite difference approximation. In this a priori study, the dynamic finite difference approximations of the 1^{st} derivative of the resolved velocity field are calculated from the *filtered DNS-solution* at every time step, and their performance is compared to that of the standard central finite difference approximations as well as the Dispersion-Relation-Preserving (DRP) schemes of e.g.

Symbols - Simulations			
$+$	filtered DNS	$\bullet$	2^{nd} -order DRP scheme
$\times$	pseudo-spectral LES	$\blacktriangle$	4^{th} -order DRP scheme
$\circ$	2^{nd} -order central	$\blacksquare$	4^{th} -order tridiagonal DRP Padé scheme
$\triangle$	4^{th} -order central	———	2^{nd} -order explicit linear dynamic scheme
$\triangledown$	6^{th} -order central	– – –	4^{th} -order explicit linear dynamic scheme
$\triangleright$	8^{th} -order central	–·–·	4^{th} -order implicit linear dynamic scheme
$\triangleleft$	10^{th} -order central	· · ·	2^{nd} -order explicit nonlinear dynamic scheme
$\square$	6^{th} -order tridiagonal Padé		

Table 7.1: Simulation overview. Overview of the various a priori or a posteriori simulations of Burgers' equation, and their corresponding symbol notation.

Tam *et al.* [79]. The variable of interest is thus $\phi = \frac{\delta u}{\delta x}$, such that the error is defined as $\varepsilon_{dudx} = \frac{\partial u}{\partial x} - \frac{\delta u}{\delta x}$, in which the exact derivative $\frac{\partial u}{\partial x}$ is obtained spectrally.
Since physics-based error definitions are meaningless in the current a priori study, only mathematics-based error definitions are considered, more specifically, the energy spectrum of the error $E_\varphi(\kappa)$ and the magnitude of the error k_φ where $\varphi = \varepsilon_{dudx}$. As mentioned before, the latter is related to the L_2-norm by $L_2 = 2\pi\sqrt{k_\varphi}$. Table 7.1 gives an overview of the performed simulations, and the corresponding symbol notation used in the plots to follow.

Figure 7.3 presents the global magnitude as function of time. First, the linear dynamic schemes are discussed. At the early stages of the simulation, when the spectrum is still developing and the small scales contain little or no energy, the 2^{nd} - and 4^{th} -order linear explicit and 4^{th} -order implicit dynamic schemes almost collapse with their asymptotic counterparts, i.e. the 4^{th} - and 6^{th} -order explicit standard central schemes and the 6^{th} -order tridiagonal Padé scheme. This is in contrast to the equivalent 2^{nd} - and 4^{th} -order Dispersion-Relation Preserving schemes and the 4^{th} -order Dispersion-Relation Preserving Padé scheme, which achieve 2^{nd} - respectively 4^{th} -order accuracy. When the flow evolves and the simulation shifts from DNS-resolution to LES-resolution, the linear dynamic schemes seamlessly adapt according to the developing energy spectrum. Once the shock is formed and the energy spectrum contains a fully developed inertial range, the linear dynamic schemes have adapted accordingly, such that they act like the Dispersion-Relation Preserving schemes and achieve much higher accuracy in comparison with the standard schemes. More specifically, it is observed that the 2^{nd} -order explicit linear dynamic scheme outperforms the standard 6^{th} -order schemes, whereas the accuracy of the 4^{th} -order explicit linear dynamic scheme reaches that of the 10^{th} -order central scheme. Further, the 4^{th} -order implicit linear dynamic scheme obtains very high accuracy since the errors are several orders of magnitude smaller than that of the 6^{th} -order tridiagonal Padé scheme. At the final stages of the simulation, the accuracy of the linear dynamic schemes seems to decrease more slowly than that of the standard schemes with formal order of accuracy. Indeed, since the energy spectrum of the

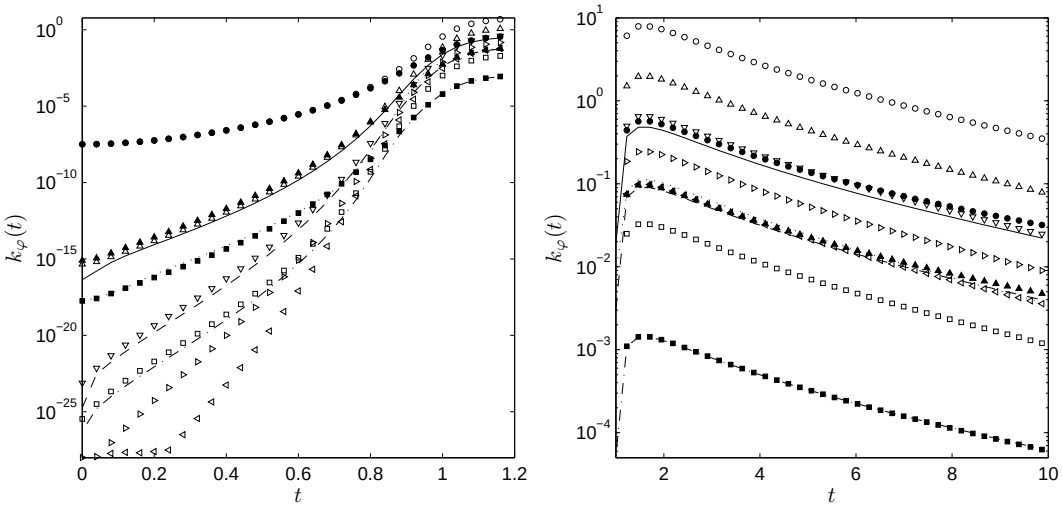

Figure 7.3: A priori Burgers' study. The magnitude k_φ of the error $\varphi = \varepsilon_{dudx}$ on the 1^{st} derivative before shock-formation, i.e. $0 \leq t \leq 1.2$ (**left**) and after shock-formation and during the decay, i.e. $1 \leq t \leq 10$ (**right**). (Symbols: see Table 7.1).

decaying shock wave shrinks, the linear dynamic schemes tend toward their initial behaviour with formal order of accuracy. For $t \to \infty$ the dynamic schemes should eventually reduce to the corresponding asymptotic standard schemes.
The results in Figure 7.3 are confirmed by looking at snapshots of the error spectrum. Figure 7.4 displays the snapshot of the spectrum $E_\varphi(\kappa)$, $\varphi = \varepsilon_{dudx}$ before the shock-formation at $t = 0.5s$ (DNS-resolution), and after the shock-formation near maximum dissipation at $t = 1.8s$ (LES-resolution). Both spectra differ significantly at these time steps. At $t = 0.5s$ the linear dynamic schemes reduce almost to their asymptotic counterparts, i.e. the 4^{th} - and 6^{th} -order explicit standard central schemes and the 6^{th} -order tridiagonal Padé scheme. Clearly, the linear dynamic schemes are now optimized for the largest resolved scales which contain most of the energy. This is in contrast to the equivalent Dispersion-Relation Preserving schemes which are optimized for a specific developed energy spectrum and therefore reach 2^{nd} - respectively 4^{th} -order accuracy at the time considered. At $t = 1.8s$ the spectrum is fully developed and the linear dynamic schemes have adapted accordingly. The same accuracy as the 2^{nd} - respectively 4^{th} -order standard asymptotic schemes is obtained for the largest resolved scales, whereas the error on the smallest resolved scales is significantly reduced compared to the traditional central schemes. As expected, similar performance for the DRP schemes is observed here. To illustrate the adaptivity of the linear dynamic schemes, Figure 7.5 shows the ratio of the dynamic coefficient to its Taylor value $c_{k,n}^{dyn}/c_{k,n}^{*}$ as function of time. Clearly there is a sharp increase of this ratio around $t \approx 1$ where the shock is being formed and the simulation shifts from DNS-resolution to LES-resolution.

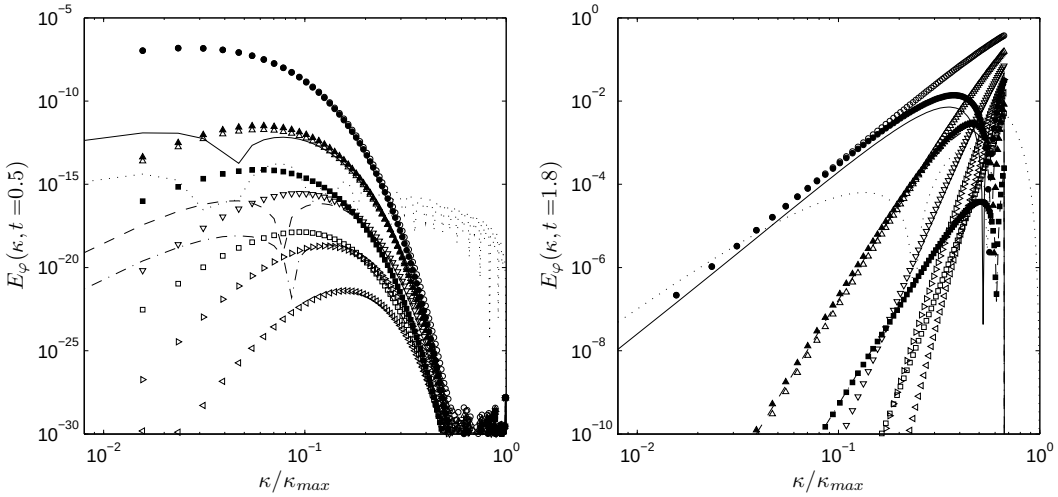

Figure 7.4: A priori Burgers' study. Snapshots of the spectrum $E_\varphi(\kappa, t)$ of the error $\varphi = \varepsilon_{dudx}$ on the 1^{st} derivative at times $t = 0.5s$ (developing spectrum) (**left**) and $t = 1.8s$ (fully developed spectrum) (**right**). (Symbols: see Table 7.1)

The results obtained with the 2^{nd} -order nonlinear explicit scheme display a more inconsistent and irregular behaviour. Although the nonlinear scheme is expected to obtain similar performance as the 4^{th} -order tridiagonal Dispersion-Relation Preserving Padé scheme, its accuracy is only comparable at early times in the simulation. Once the spectrum is fully developed, the quality of the nonlinear scheme seems partially lost since it cannot achieve the accuracy of the 4^{th} -order tridiagonal DRP Padé scheme. This suggests that the theoretically expected performance is neutralized due to nonlinear pollution of the scheme. Indeed, looking at the snapshots of the energy spectrum in Figure 7.4, it can be observed that although at $t = 0.5s$ the accuracy of the lower wavenumber modes lies between that of the 4^{th} - and 6^{th} -order central scheme, the error does not fade out in the high-wavenumber region, in contrast to the linear schemes. This clearly indicates that the nonlinear dynamic scheme produces spurious scales, due to the nonlinear interactions in the scheme. These scales are distributed over the entire wavenumber range and affect the quality of every Fourier mode. At $t = 1.8s$, again spurious energy is created in the entire wavenumber range and even beyond the filter-cutoff, such that the accuracy decreases to that of the 2^{nd} -order scheme for the largest resolved scales. Although the nonlinear scheme seems to have better performance than its linear variant, it never reaches the accuracy of the 4^{th} -order DRP Padé scheme. These findings support those of the nonlinear Fourier analysis that was performed in the previous chapter. Hence, the nonlinearity may impose an obstruction in order to safely apply this scheme in LES. This is further discussed in the a posteriori studies.

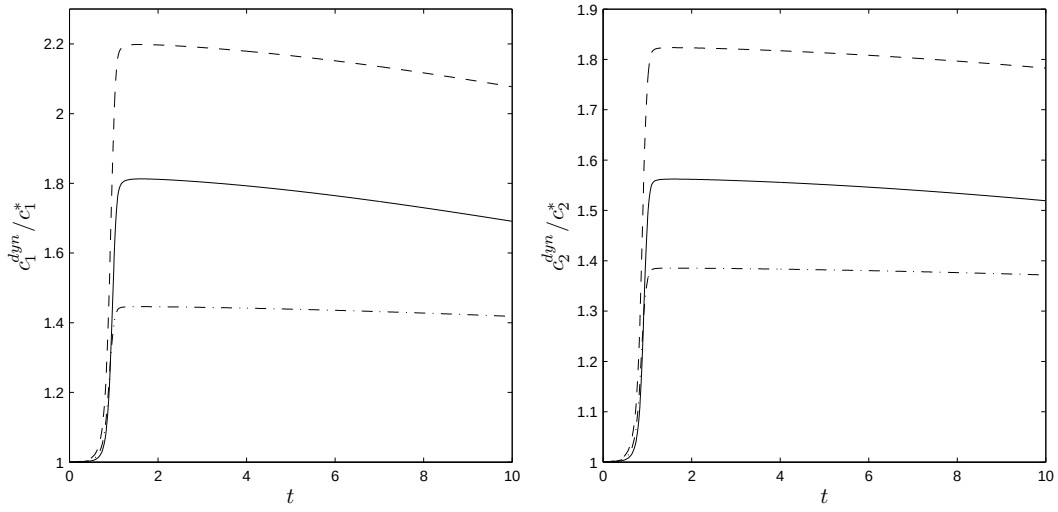

Figure 7.5: A priori Burgers' study. Ratio of the dynamic coefficient to its Taylor value $c_{k,n}^{dyn}/c_{k,n}^* = c_n^{dyn}/c_n^*$ for the 2^{nd} -order (——) and 4^{th} -order (– – –) explicit linear dynamic schemes and for the 4^{th} -order (–·–·) linear implcit dynamic scheme for the 1^{st} derivative (**left**) and the 2^{nd} derivative (**right**).

7.5 A POSTERIORI BURGERS' STUDY

7.5.1 THE PERFECT SUBGRID-SCALE MODEL

For the Large-Eddy Simulation of the Burgers' equation, using the perfect subgrid scale model, modeling errors are absent and the LES-solution should approximately return the filtered DNS-solution. Indeed, it is verified from Figure 7.6 which demonstrates the very small modeling errors on the kinetic energy and the dissipation rate. Numerical errors are thus dominant for these simulations, such that the results are expected to be similar to those of the a priori study. However, in contrast to the a priori study, the solution is affected by the systematic accumulation of the finite difference errors at each time step of the LES simulation. This is illustrated in Figure 7.7, where snapshots of the error spectra at $t = 0.5s$, i.e. before shock-formation and at $t = 1.8s$, i.e. after shock-formation are shown for the various finite difference schemes. It can be seen that for $t = 0.5s$, less accurate finite difference methods such as the 2^{nd} -order central scheme are slightly too dissipative in comparison with more accurate methods. Most likely, this is due to the substantial dispersion errors at higher wavenumbers related to the finite difference approximations of the 1^{st} derivative. Remind that it was already argued in Section 4.1.3 that (low-order) finite difference approximations induce implicit filtering of the corresponding velocity field. However, at $t = 1.8s$ when the energy spectrum is fully developed, the opposite behaviour is observed. The lower order schemes lead systematically to an energy pile-up at the filter-cutoff. This observation suggests

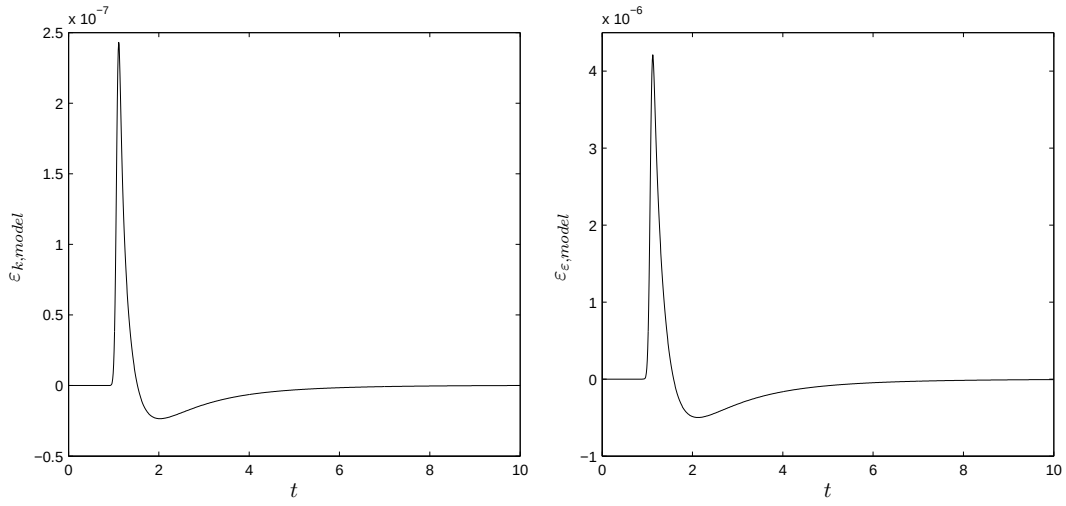

Figure 7.6: A posteriori Burgers' study: Perfect model. The modeling errors on the total kinetic energy (**left**) and the total dissipation rate (**right**) as function of time.

a reduced effectiveness of the subgrid dissipation on the smallest resolved scales, probably caused by the dispersion errors related to the finite difference approximation of the subgrid force. Hence, the implicit filtering that is generally attributed to low accurate finite difference methods, appears to have a reversed impact in the fully developed regime. Notice again the production of spurious small scales by the nonlinear dynamic scheme at $t = 0.5s$.

Figure 7.8 shows the magnitude of the numerical error as function of time. This error corresponds to the well-known L_2-norm which is a mathematics-based error quantity, reflecting the error contributions on both amplitude and phase of the solution. The results look very similar to those of the a priori study. Note that an anomaly is observed in the performance of the 10^{th} -order finite difference scheme in the early stages of the simulation where the spectrum is still developing, i.e. $t \leq 0.8$. There, the 10^{th} -order method appears to perform worse than the 4^{th} -order method. It was verified that this numerical artifact is related to the stencil coefficients in the 10^{th} -order finite difference approximation of the 2^{nd} derivative (see Table 4.2) which are only rational approximations to the real numerical values. As a consequence, the sum of the weighting coefficients is not exactly zero, but has a residual of approximately 10^{-6}. Nevertheless, once the smallest scales in the solution are energized, i.e. $t \geq 1$, this artifact becomes negligible and the 10^{th} -order scheme behaves again as expected. It is emphasized that this anomaly does not undermine the further conclusions in this work. Except for the nonlinear dynamic scheme, all linear dynamic schemes perform very well, as expected from the a priori results. In the initial stages of the simulation (DNS-resolution), the accuracy of the 2^{nd} - and 4^{th} -order explicit linear dynamic schemes closely approaches

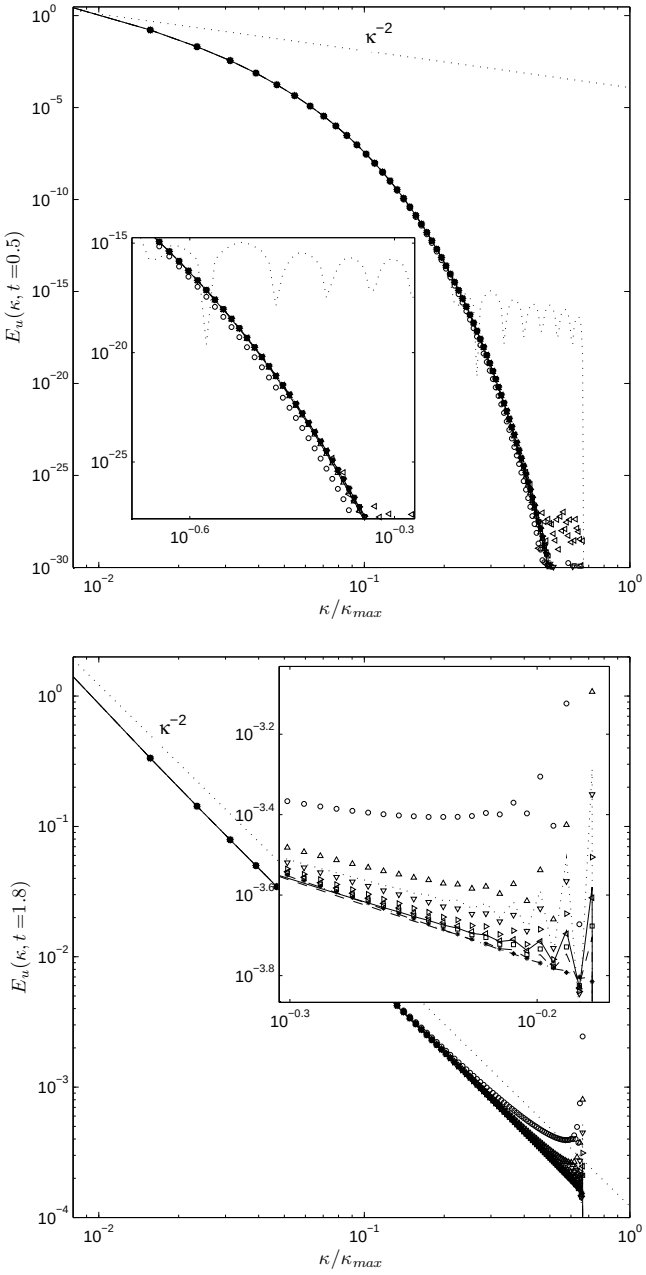

Figure 7.7: A posteriori Burgers' study: Perfect model. Snapshots of the energy spectrum of the velocity field $E_u(\kappa, t)$ at times $t = 0.5s$ (developing spectrum) (**upper**) and $t = 1.8s$ (fully developed spectrum) (**lower**). Notice that the lower order schemes tend to be too dissipative at $t = 0.5s$ when the model is not active, whereas the opposite is observed at $t = 1.8s$ where the model is active. Remark the creation of spurious modes for the nonlinear dynamic finite difference scheme. (Symbols: see Table 7.1)

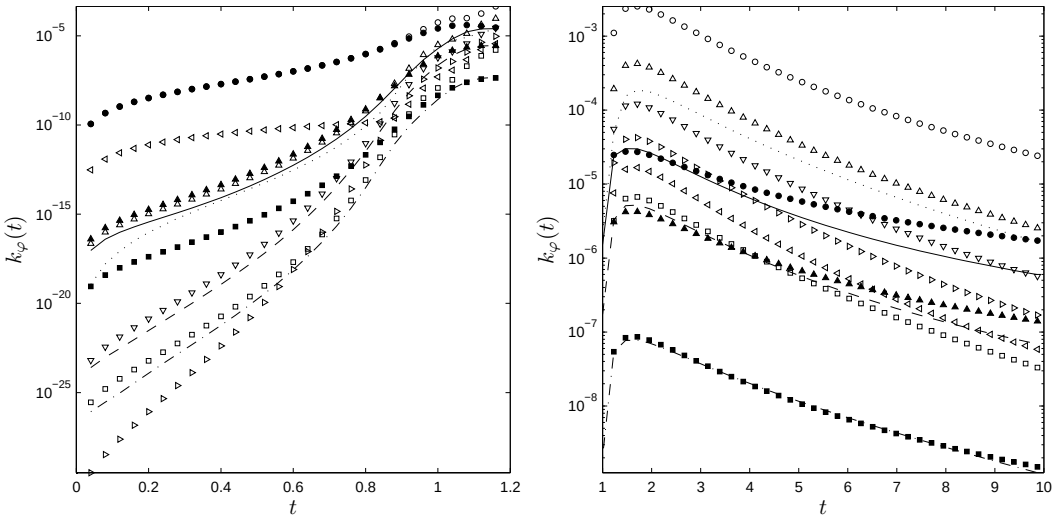

Figure 7.8: A posteriori Burgers' study: Perfect model. The magnitude k_φ of the error $\varphi = \varepsilon_u$ on the resolved velocity field before shock-formation, i.e. $0 \leq t \leq 1.2$ (**left**) and after shock-formation and during the decay, i.e. $1 \leq t \leq 10$ (**right**). (Symbols: see Table 7.1)

that of their 4^{th} - respectively 6^{th} -order standard asymptotic counterparts, whereas the corresponding Dispersion-Relation Preserving schemes obtain respectively 2^{nd} - and 4^{th} -order accuracy. Similarly, the 4^{th} -order implicit linear dynamic finite difference approximation tend to the 6^{th} -order tridiagonal Padé scheme. Once the stationary shock-wave is at full strength, i.e. at $1 \leq t \leq 3$ such that the simulation is shifted from DNS-resolution to LES-resolution, the linear dynamic schemes have adapted accordingly and achieve comparable accuracy as the corresponding Dispersion-Relation Preserving schemes. More specific, both the 2^{nd} -order dynamic explicit schemes and 2^{nd} -order DRP schemes obtain higher accuracy than the 6^{th} -order standard asymptotic scheme, whereas both the 4^{th} -order dynamic explicit schemes and the 4^{th} -order explicit schemes outperform the 6^{th} -order tridiagonal Padé scheme. The 4^{th} -order implicit linear dynamic finite difference approximation almost collapses with its Dispersion-Relation Preserving variant, displaying an error-level which is a few orders of magnitude below that of the standard 6^{th} -order tridiagonal Padé scheme.

As the shock-wave decays further, e.g. at times $t \geq 3$, it can be seen that the accuracy of the explicit or implicit DRP schemes decreases much faster than the linear explicit or implicit dynamic schemes. This clearly demonstrates that the dynamic schemes adapt themselves according to the instantaneous flow solution such that a minimal dispersion error is achieved. For $t \to \infty$ the dynamic schemes should reduce again to their asymptotic equivalents. Figure 7.9 displays two snapshots of the spectrum of the numerical error $E_\varphi(\kappa)$, $\varphi = \varepsilon_u$ at times $t = 0.5$ and $t = 1.8$, which reflect the adaptable Fourier characteristics of the linear dynamic schemes.

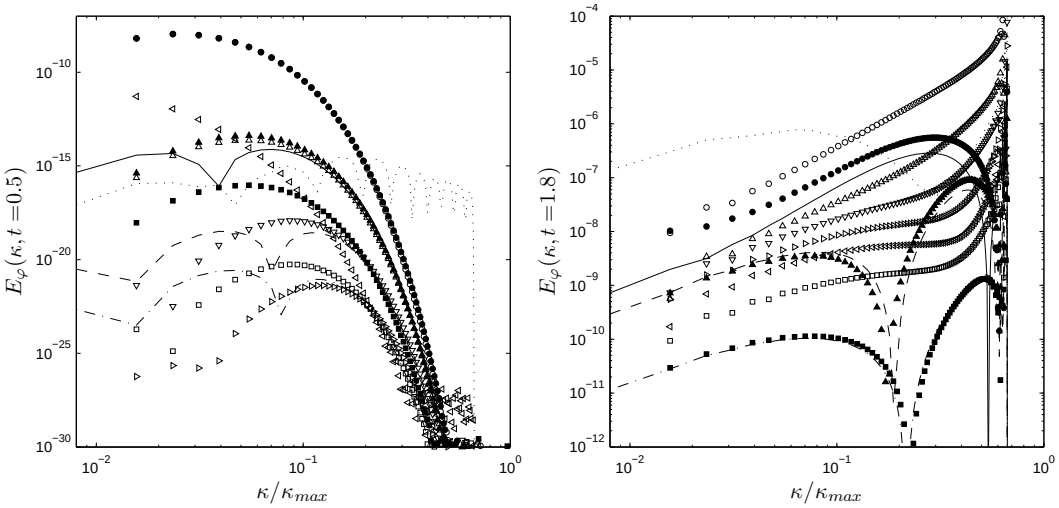

Figure 7.9: A posteriori Burgers' study: Perfect model. Snapshots of the spectrum $E_\varphi(\kappa, t)$ of the error $\varphi = \varepsilon_u$ of the resolved velocity field at times $t = 0.5s$ (developing spectrum) (**left**) and $t = 1.8s$ (fully developed spectrum) (**right**). Remark again the spurious modes generated by the nonlinear dynamic finite difference scheme. (Symbols: see Table 7.1)

The error on the energy spectrum ε_φ, $\varphi = E_u(\kappa)$ gives qualitatively similar results and is therefore not shown.

Figures 7.8 and 7.9 also show the performance of the 2^{nd} -order explicit nonlinear dynamic finite difference approximation. The results are obviously much worse than for the a priori study, due to the accumulation of finite difference errors and nonlinear pollution at each time step. Generally, the accuracy remains around that of the 4^{th} -order standard asymptotic scheme although for the initial stages of the simulation, i.e. at $t \leq 0.04$, where the spectrum contains only few Fourier modes, the error level decreases to that of the 4^{th} -order DRP Padé scheme. It may be clear from Figure 7.9 that the nonlinear interactions of the scheme severely pollute the solution. Indeed, the nonlinear finite difference operator creates spurious modes which are distributed over the entire wavenumber range. For instance, at $t = 0.5s$ spurious Fourier modes are observed in the high-wavenumber region of the spectrum, whereas at $t = 1.8$, the largest scales are significantly affected by the nonlinearity leading to a severely reduced accuracy compared to the linear Fourier analysis.
Although the mathematics-based errors give a reliable and undisguised picture about the quality of the various finite difference approximations, one is often interested in obtaining physics-related quantities from the LES simulation such as kinetic energy or dissipation rate. Therefore, the quality of the difference schemes on the physics-based errors is examined further. Figure 7.10 display the numerical errors on the kinetic energy and dissipation rate. The observations and conclusions from the mathematics-based errors, shown in Figure 7.8, also mainly apply to the

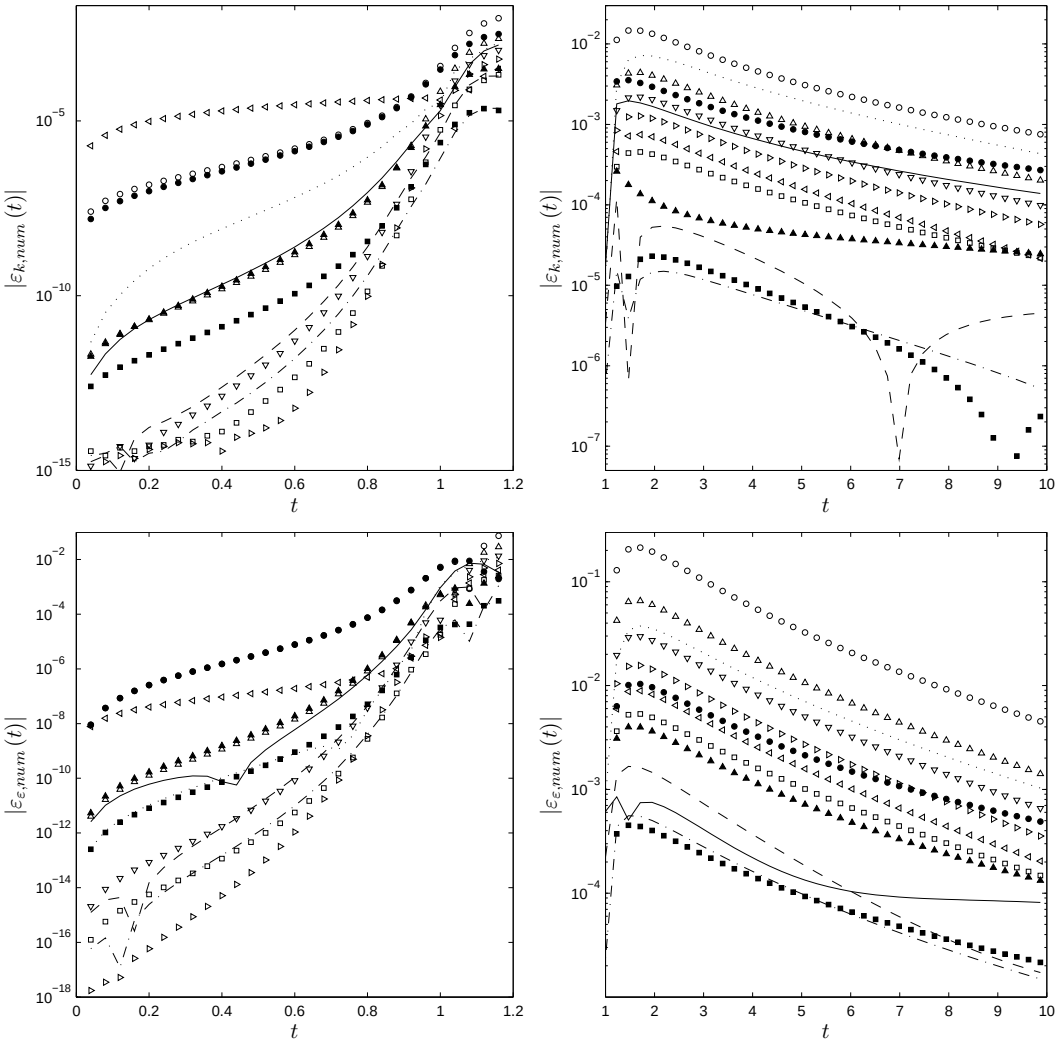

Figure 7.10: A posteriori Burgers' study: Perfect model. Error on the kinetic energy $\varepsilon_k = \Delta k_u$ (**upper**) and error on the dissipation rate $\varepsilon_\varepsilon = \Delta\varepsilon$ (**lower**) before shock-formation, i.e. $0 \leq t \leq 1.2$ (**left**) after shock-formation and during the decay, i.e. $1 \leq t \leq 10$ (**right**). (Symbols: see Table 7.1)

physics-based errors of Figure 7.10. The linear explicit and implicit dynamic schemes perform very well as they converge to the asymptotic standard schemes for smooth velocity fields with low spectral content at the beginning of the simulation (DNS-resolution), whereas they adapt toward the Dispersion-Relation Preserving schemes as soon as the energy spectrum is entirely developed and the inertial range is established (LES-resolution). Similarly, the 4^{th} -order implicit linear dynamic finite difference scheme varies during the simulation between the 6^{th} -order tridiagonal Padé scheme and the implicit Dispersion-Relation Preserving scheme. Remarkably, the 2^{nd} - and 4^{th} -order explicit linear dynamic schemes predict the kinetic energy and the dissipation rate significantly better than the equivalent 2^{nd} - and 4^{th} -order DRP schemes. This is explained by the fact that, instead of the uniform spectrum, the Burgers' spectrum is used in the optimization procedure in Section 6.3.3 in order to obtain the optimal value f_{opt} of the blending factor f. Although a similar improvement would be expected for the 4^{th} -order implicit linear dynamic finite difference scheme, the accuracy of the corresponding DRP schemes appears equally good. This may be understood since for very high-order schemes, the gain of a possible optimization is smaller in comparison with that for low-order schemes. Hence, the spectrum shape in the optimization procedure for f_{opt} will also be less important than for low-order schemes. Again, it is seen that the 2^{nd} -order nonlinear scheme leads to very poor accuracy improvement, as consequence of the nonlinear pollution.

7.5.2 The dynamic Smagorinsky model

In this paragraph, the performance of the dynamic finite difference methods in the Large-Eddy Simulation of the Burgers' equation is further examined for the dynamic Smagorinsky model. In contrast to the perfect subgrid scale model, now significant modeling errors arise, which will interact with the numerical errors and vice versa, as shown by Meyers *et al.* [60, 59]. Note that the dynamic procedure of Germano *et al.* [30] is believed to give a nearly minimal total error since it is sensitive to the energy spectrum of the solution as well as the numerics [61]. Therefore, an attempt is made to visualize these interactions by separating modeling errors and numerical errors as discussed in Section 7.3. Figure 7.11 displays the energy spectra obtained with the various finite difference schemes together with those of the spectral method and the filtered DNS at times $t = 0.5s$ and $t = 1.8s$. Again, a clear influence of the discretization method is seen from these figures. For instance, the difference between the spectrum of the pseudo-spectral LES and that of the filtered DNS spectrum, reveals the modeling error due to the dynamic Smagorinsky model. Obviously, the Smagorinsky model appears to be slightly too dissipative for the largest resolved scales and medium resolved scales, whereas for the smallest resolved scales, an energy pile-up is observed near the filter cutoff. This pile-up originates from the inability of the eddy viscosity model to describe well the cusped behaviour of the spectral viscosity at the cutoff wavenumber (see Figure 3.3). Nevertheless, the general performance of the dynamic Smagorinsky model is considered satisfactory since the κ^{-2} inertial range is approached fairly good. The modeling error on the

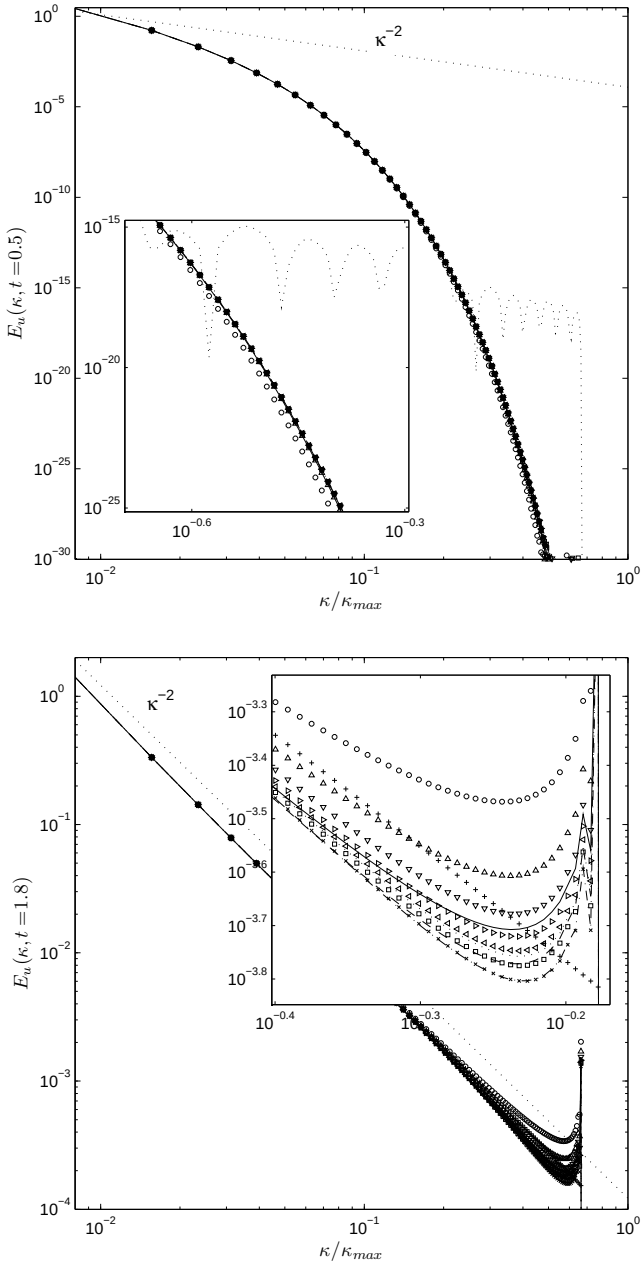

Figure 7.11: A posteriori Burgers' study: Dynamic Smagorinsky. Snapshots of the energy spectrum of the velocity field $E_u(\kappa, t)$ at times $t = 0.5s$ (developing spectrum) (**upper**) and $t = 1.8s$ (fully developed spectrum) (**lower**). Notice that the lower order schemes tend to be too dissipative at $t = 0.5s$ when the model is not active, whereas the opposite is observed at $t = 1.8s$ where the model is active. Remark the creation of spurious modes for the nonlinear dynamic finite difference scheme. (Symbols: see Table 7.1)

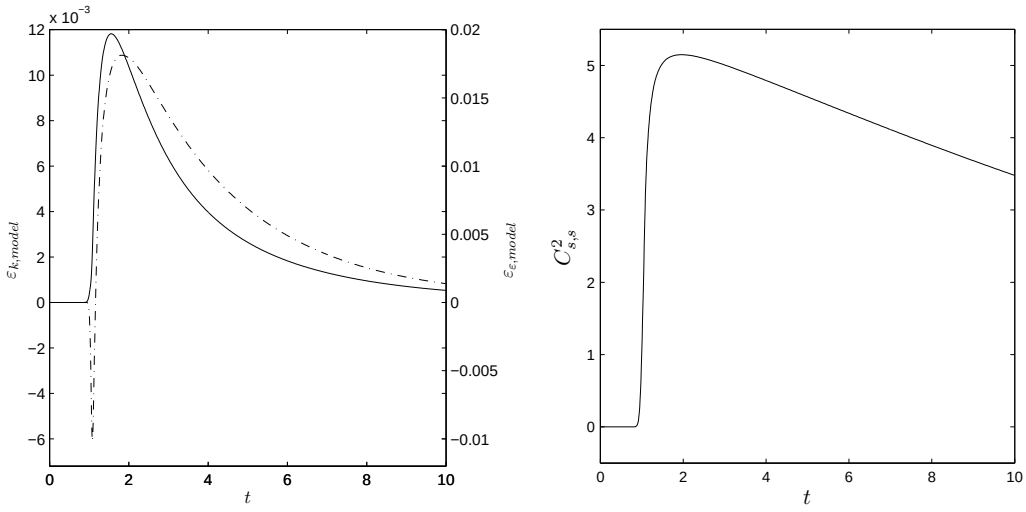

Figure 7.12: A posteriori Burgers' study: Dynamic Smagorinsky. The modeling errors on the total kinetic energy (———) and the total dissipation rate (—·—·) as function of time (**left**). The profile of the dynamic model coefficient $C^2_{s,s}$ of the pseudo-spectral LES during the simulation (**right**).

kinetic energy and the dissipation rate are shown in Figure 7.12. The mainly positive error profiles confirm that the dynamic Smagorinsky model is slightly too dissipative, meaning that the kinetic energy of the spectral LES solution is smaller than that of the filtered DNS solution. Further, the dynamic model coefficient $C^2_{s,s}$ of the pseudo-spectral LES is shown in Figure 7.12. As expected, the dynamic procedure engages the model at $t \approx 1$ and automatically determines a quasi-optimal value as the shock decays.

The discussion is continued by investigating the numerical errors induced by the finite difference approximations. As explained in Section 7.3, an attempt is made to decouple the influence of the discretization of the basic Burgers' LES-equation and that of the discretization errors in the calculation procedure of the dynamic model coefficient itself, leading to the numerical errors of type I and II. Figure 7.13 represents the magnitude of the numerical errors (related to L_2-norm) on the velocity field, whereas Figure 7.14 shows the more detailed spectrum of the numerical errors before the shock formation, i.e. at $t = 0.5s$ and after the shock is fully established, i.e. at $t = 1.8s$. Both errors are mathematics-based errors that involve amplitude- and phase-information of the solution. Remark again the numerical anomaly for the 10^{th} -order solution at the beginning of the simulation. This phenomenon was already explained in the previous paragraph. Both graphs display the contributions of the errors $\varepsilon_{u,numI}$ and $\varepsilon_{u,numII}$ which were previously defined. $\varepsilon_{u,numI}$ represents the errors due to discretization of the LES-equation only. More specific, only

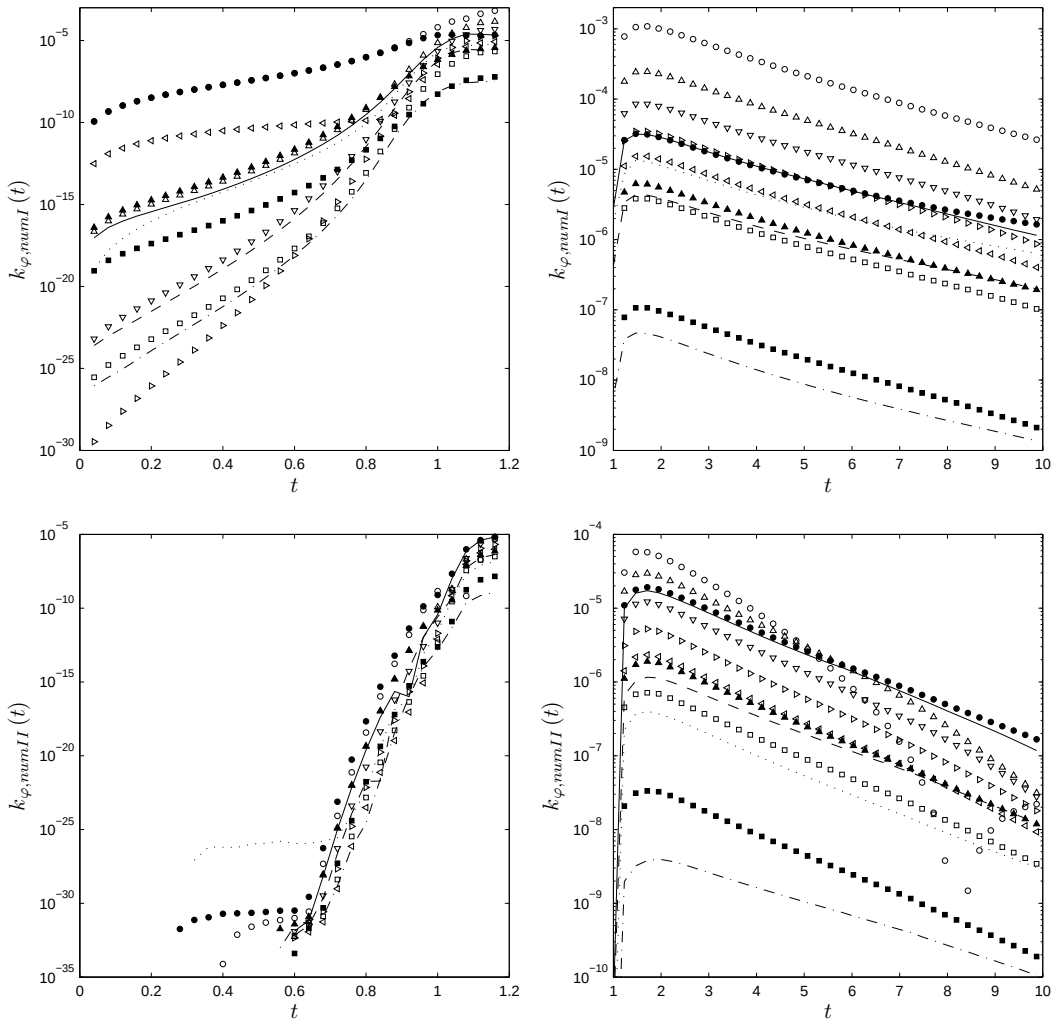

Figure 7.13: A posteriori Burgers' study: Dynamic Smagorinsky. The global magnitude k_φ of the numerical errors $\varphi = \varepsilon_u$ on the resolved velocity field before shock-formation, i.e. $0 \leq t \leq 1.2$ (**left**) and after shock-formation and during the decay, i.e. $1 \leq t \leq 10$ (**right**). (Symbols: see Table 7.1)

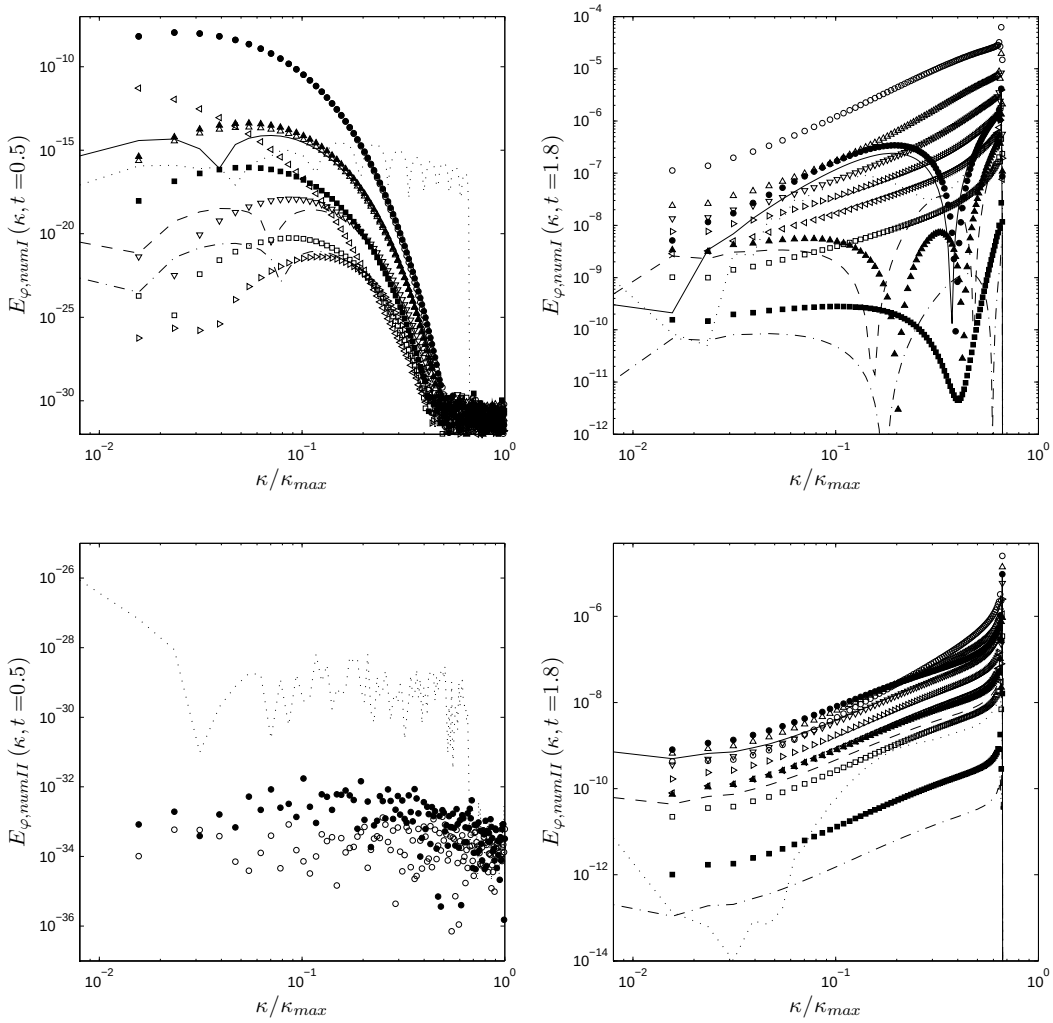

Figure 7.14: A posteriori Burgers' study: Dynamic Smagorinsky. Snapshots of the spectrum $E_\varphi(\kappa, t)$ of the error $\varphi = \varepsilon_u$ of the resolved velocity field at times $t = 0.5s$ (developing spectrum) (**left**) and $t = 1.8s$ (fully developed spectrum) (**right**). Remark again the spurious modes generated by the nonlinear dynamic finite difference scheme. (Symbols: see Table 7.1)

spectral derivatives of the finite difference solution are used for the evaluation of the Germano procedure. Hence, the obtained dynamic model coefficient $C^2_{s,fd}$ is considered as the optimal-model parameter for the current finite difference solution of the Burgers' LES-equation, and is thus not liable to finite difference errors in its calculation. On the other hand, $\varepsilon_{u,numII}$ represents the errors only due to the discretization errors in the evaluation of the Germano procedure itself. Therefore, the obtained model coefficient $C^2_{fd,fd}$ is considered an approximation for $C^2_{s,fd}$. Figures 7.13 and 7.14 show that the errors of the first type $\varepsilon_{u,numI}$ are clearly dominant as they differ almost an order of magnitude with the errors of the second type $\varepsilon_{u,numII}$. Of course the latter are absent at the beginning of the simulation since the model constant is still zero.
Apparently, the same conclusion applies for the linear explicit and implicit dynamic schemes as for the Burgers' study with the perfect subgrid model. It is observed that the linear dynamic schemes recover the asymptotic order of accuracy in the early stages of the simulation where the flow is still smooth and the spectrum does not contain an inertial range yet. This is in contrast to the Dispersion-Relation Preserving schemes, which are suboptimal for smooth flows. As the flow evolves into a shock-wave, and thus the simulation shifts from DNS-resolution to LES-resolution, the linear dynamic schemes adapt to the flow, leading to a slightly better accuracy compared to the Dispersion-Relation Preserving schemes. Due to the calibration procedure, the optimized schemes are *de facto* optimal for fully developed flows. Both the dynamic and DRP schemes perform much better in comparison with the standard central schemes. The 2^{nd} -order explicit linear dynamic scheme achieves an accuracy which is better than that of the 8^{th} -order central scheme, whereas the 4^{th} -order explicit linear dynamic scheme obtains almost the quality of the 6^{th} -order standard Padé scheme. The 4^{th} -order dynamic implicit finite difference approximation outperforms all other schemes and displays even better quality than its Dispersion-Relation Preserving counterpart. Moreover, a general tendency is observed toward slightly better performance of the linear dynamic schemes in comparison with the DRP schemes. Obviously, this is explained by the calibration of the blending factor f in the dynamic schemes using the Burgers' spectrum, instead of a uniform spectrum.

Despite the fact that the 2^{nd} -order nonlinear dynamic scheme still produces spurious small scales that inevitably interact with all scales of motion in the solution, it performs surprisingly better in combination with the dynamic Smagorinsky model instead of with the perfect subgrid scale model. Although the exact reason for this behaviour remains unclear, it is assumed that the creation of spurious scales compensates the over-dissipative nature of the Smagorinsky model, resulting in a better overall behaviour. Despite this unforeseen advantage, application of the nonlinear scheme remains questionable for Large-Eddy Simulation.

Figures 7.15 and 7.16 show the error on the kinetic energy and on the dissipation

rate. Notice again that the numerical error contributions $\varepsilon_{u,numI}$ are dominant over the contributions $\varepsilon_{u,numII}$. Results are analogous to the ones previously discussed. Nevertheless, some remarkable behaviours occurs which requires further discussion. The error on the kinetic energy $\varepsilon_{k,numI}$ in Figure 7.15 shows that especially the 2^{nd} -order explicit linear dynamic scheme performs very well, as it reaches almost the quality of the 6^{th} -order standard Padé scheme. However, this is not observed for the error on the dissipation rate $\varepsilon_{\varepsilon,numI}$ in Figure 7.16 where the 2^{nd} -order explicit linear dynamic scheme reaches approximately 10^{th} -order accuracy. This is explained by the fact that the error on the dissipation rate ε focusses more on the accuracy of the small scales than does the error on the kinetic energy k. This emphasizes the importance of looking at different error measures, since they indicate different phenomena, and supports the findings of Meyers *et al.* [62]. Both numerical errors on the kinetic energy as well as on the dissipation rate are represented in a semi-logarithmic graph in order to make the differences clearly visible. However, it is not possible to determine from such a graph whether $\varepsilon_{k,numI}$ and $\varepsilon_{k,numII}$, or $\varepsilon_{\varepsilon,numI}$ and $\varepsilon_{\varepsilon,numII}$ reinforce each other, or on the contrary, counteract with each other. Nevertheless, it was verified that $\varepsilon_{k,numI}$ or $\varepsilon_{k,numII}$ were negative for all schemes, except for the 2^{nd} -order linear dynamic scheme and the 2^{nd} -order DRP scheme. Similarly, $\varepsilon_{\varepsilon,numI}$ and $\varepsilon_{\varepsilon,numII}$ remain negative for all schemes, without exception. Since all numerical errors appear to have the same negative sign, it is concluded that in general, the numerical errors I and II reinforce each other. The total numerical error is given in Figure 7.17. Although the interaction of the different numerical errors are represented by Figure 7.17, it might be more instructive to examine the model coefficients $C_{s,fd}$ and $C_{s,s}$. Figure 7.18 shows the relative error-percentages between the model coefficients $C_{s,fd}$ and $C_{s,s}$, and the deviation between $C_{s,fd}$ and $C_{fd,fd}$. These relative errors are defined by

$$\Delta C_s^2 = \frac{C_{s,s}^2 - C_{s,fd}^2}{C_{s,s}^2} \tag{7.35}$$

$$\Delta C_{fd}^2 = \frac{C_{s,fd}^2 - C_{fd,fd}^2}{C_{s,fd}^2} \tag{7.36}$$

Obviously, the value of the model coefficient $C_{s,fd}$ is systematically overestimated for the lower order schemes. Indeed, the dynamic procedure tries to compensate for the reduced effectiveness of the subgrid dissipation which results from using these low-order schemes. In other words, it responds to numerical shortcomings of the finite difference approximations used in the LES-equation. This connects closely to the results of Meyers et al. [61]. Moreover, the influence of discretization errors on the derivatives used in the Germano procedure, systematically results in a underestimation of the dynamic model coefficient $C_{fd,fd}$ compared to $C_{s,fd}$. However, it is observed that the 2^{nd} -order central scheme in particular, tends to overestimate $C_{fd,fd}$ compared to $C_{s,fd}$ at the end of the simulation. This effect seems to disappear for higher order schemes. Nevertheless, it may be concluded that the overestimation of theoretically optimal parameter $C_{s,fd}$ is compensated by the underestimation

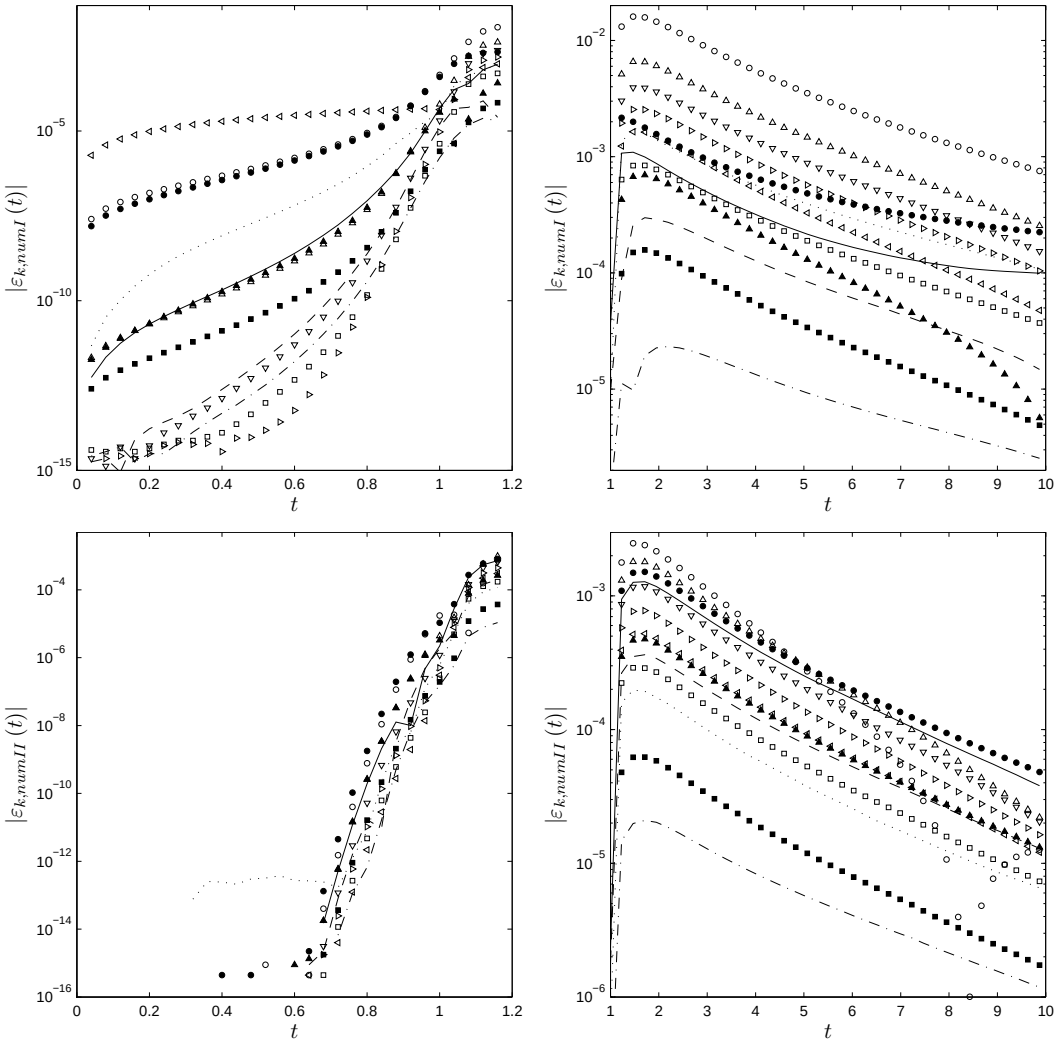

Figure 7.15: A posteriori Burgers' study: Dynamic Smagorinsky. Numerical errors on the kinetic energy ε_k before shock-formation, i.e. $0 \leq t \leq 1.2$ (**left**) after shock-formation and during the decay, i.e. $1 \leq t \leq 10$ (**right**). (Symbols: see Table 7.1)

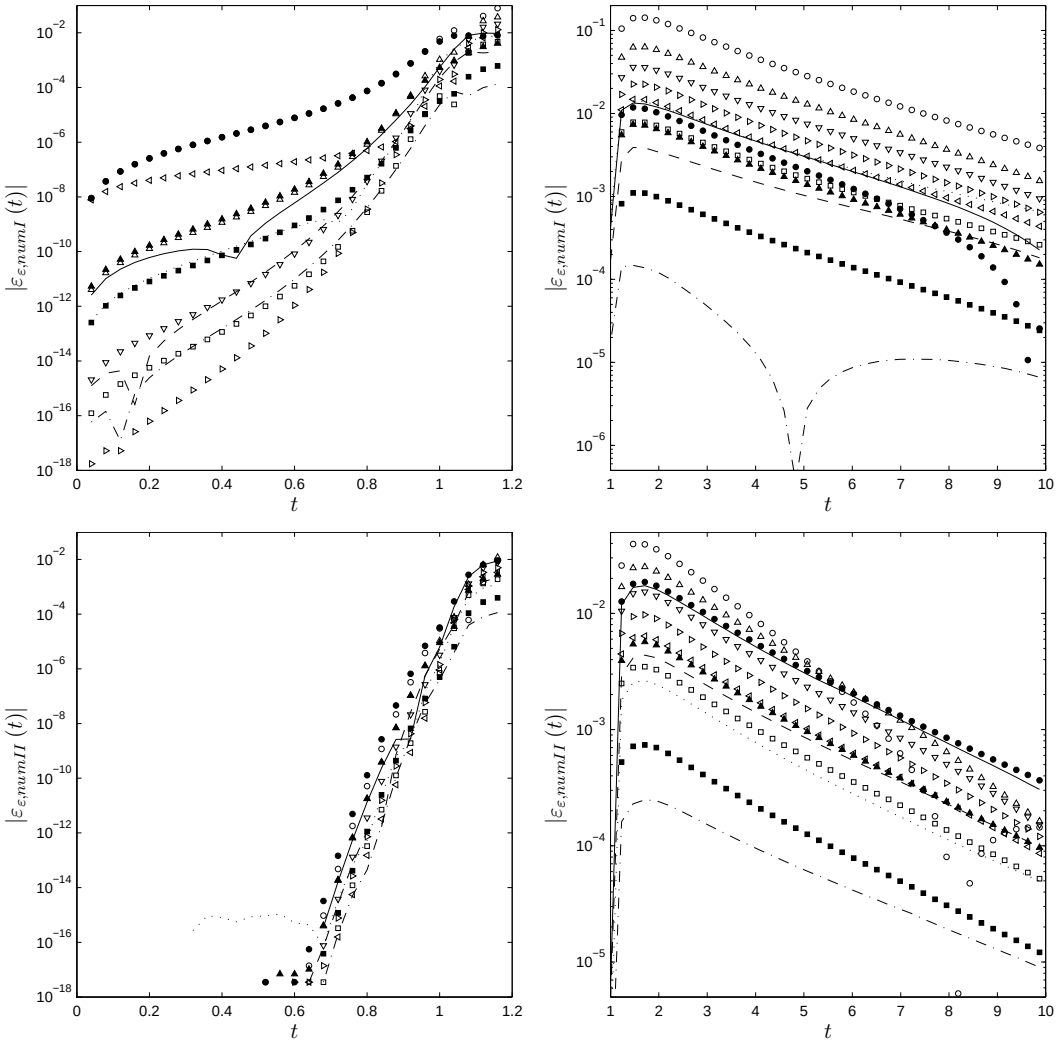

Figure 7.16: A posteriori Burgers' study: Dynamic Smagorinsky. Numerical errors on the dissipation rate ε_ε before shock-formation, i.e. $0 \leq t \leq 1.2$ (**left**) after shock-formation and during the decay, i.e. $1 \leq t \leq 10$ (**right**). (Symbols: see Table 7.1)

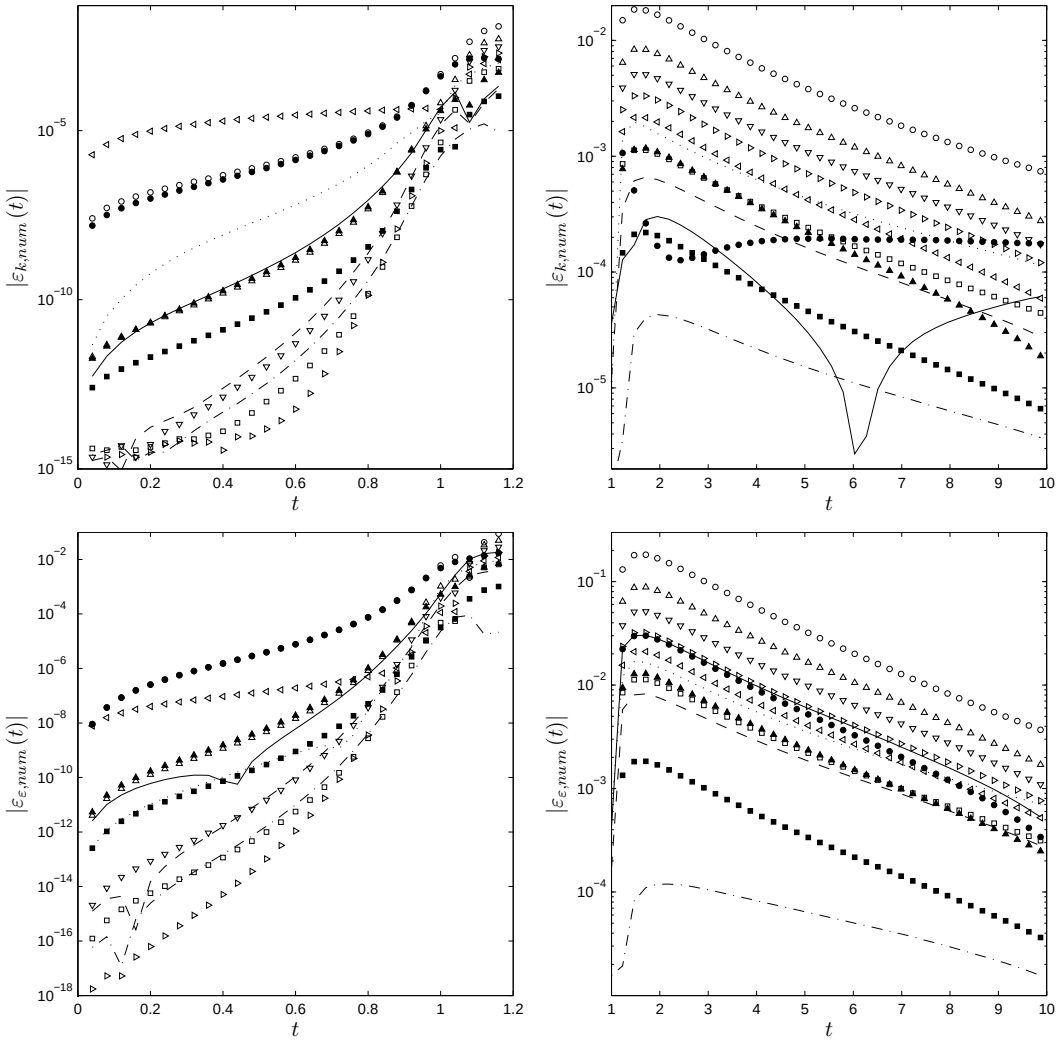

Figure 7.17: A posteriori Burgers' study: Dynamic Smagorinsky. Total numerical error on the kinetic energy $\varepsilon_k = \Delta k_u$ (**upper**) and on the dissipation rate $\varepsilon_\varepsilon = \Delta\varepsilon$ (**lower**) before shock-formation, i.e. $0 \leq t \leq 1.2$ (**left**) after shock-formation and during the decay, i.e. $1 \leq t \leq 10$ (**right**). (Symbols: see Table 7.1)

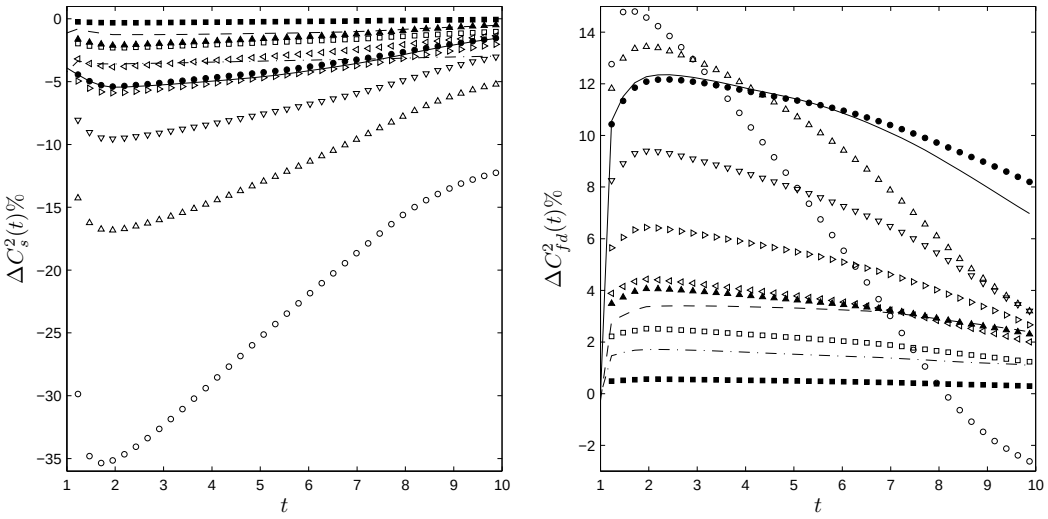

Figure 7.18: A posteriori Burgers' study: Dynamic Smagorinsky. Relative error of $C_{s,fd}$ compared to $C_{fd,fd}$ (**left**), indicating the influence of the finite difference errors on the value of the dynamic model coefficient, and the relative error of $C_{fd,fd}$ compared to $C_{s,fd}$ (**right**), which indicates the influence of finite difference errors on the calculation of the dynamic constant in the Germano procedure. (Symbols: see Table 7.1)

of the approximation $C_{fd,fd}$, resulting in a reduced subgrid dissipation and higher levels of kinetic energy in the LES-simulation. This is advantageous for the overall performance of the Smagorinsky model which is observed to be too dissipative.

It may be clear by now that numerics and modeling are completely entwined in Large-Eddy Simulations, especially when using more advanced subgrid models such as the dynamic model. In the previous discussion the influence of the interactions between numerics and modeling on the level of the model constant was shown. Although this gave more insight in how the dynamic Smagorinsky model is influenced by the adopted numerics, it does not indicate whether a better numerical approximation of the model will lead to a better overall performance. Therefore, further investigation is required by comparing the finite difference LES solutions with those of the filtered DNS instead of with the pseudo-spectral LES. In the first approach, the total error $\varepsilon_{u,tot}$, which includes numerical errors and modeling errors, is taken into account, whereas in the latter approach only the total numerical error $\varepsilon_{u,num}$ is taken into account. Figure 7.19 shows the error between the fully developed energy spectra at $t = 1.8s$ of the finite difference LES-solutions on the one hand, and the filtered DNS-solution or the pseudo-spectral LES-solution on the other hand. In accordance with the results of the perfect subgrid scale model, the total numerical error decreases with increasing accuracy of the numerical schemes. However, almost

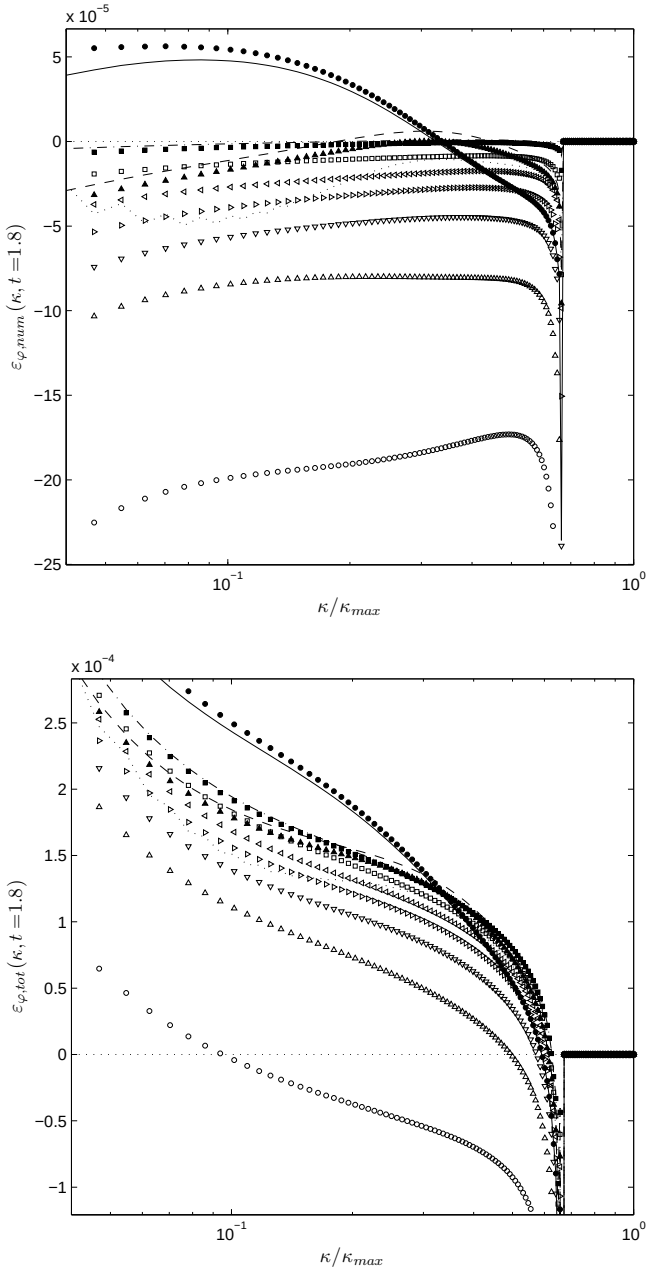

Figure 7.19: A posteriori Burgers' study: Dynamic Smagorinsky. Numerical error $\varepsilon_{\varphi,num}(\kappa,t)$ (**upper**) and total error $\varepsilon_{\varphi,tot}(\kappa,t)$ (**lower**) on the energy spectrum of the velocity field $\varphi = E_u(\kappa,t)$ at fully developed inertial range ($t = 1.8s$). (Symbols: see Table 7.1)

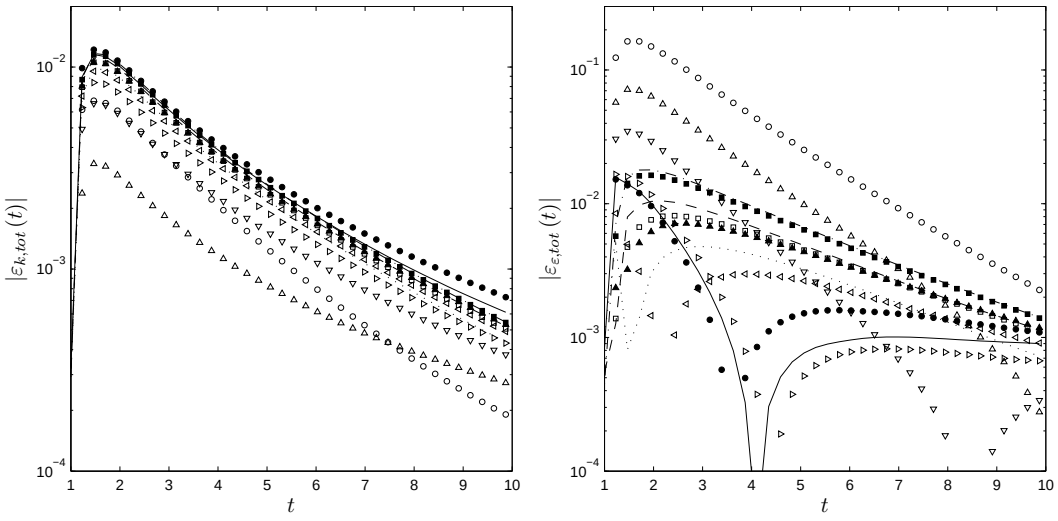

Figure 7.20: A posteriori Burgers' study: Dynamic Smagorinsky. The total error, i.e modeling error and numerical error, on the kinetic energy (**left**) and the dissipation rate (**right**). Note that the error on the dissipation rate gives relatively more information about the quality of the small scales in comparison with the error on the kinetic energy. (Symbols: see Table 7.1)

the opposite is observed when looking at the total error which involves interactions of numerical and modeling errors. Surprisingly, the lower-order schemes appear to achieve a better total accuracy for almost the entire range of resolved scales in comparison with higher order methods, despite the fact that their numerical accuracy is worse. This proves that partial cancellation between the numerical errors and modeling errors can occur as shown by Meyers *et al.* [60, 59]. This conclusion is supported by the results of the total error on the kinetic energy, depicted in Figure 7.20. However, the results of the total error on the dissipation rate in Figure 7.20 show a different behaviour. There, the more accurate schemes lead to smaller total errors on the dissipation rate. As mentioned before, the dissipation rate reveals more information about the small scales, whereas the kinetic energy gives relatively more information about the large scales. Hence, the observed error behaviour of both quantities seem to confirm that the more accurate schemes tend to predict better the small scales despite the fact that the modeling error severely interferes with the total accuracy. Moreover, this supports the initial hypothesis of this dissertation, that it is important to guarantee numerical quality on the small scales since the dynamic Germano procedure or the multi-scale technique uses just that information.

7.6 Conclusions and Discussion

In the current chapter, the ability of the dynamic finite difference approximations was demonstrated for the Large-Eddy Simulation of Burgers' turbulence. It was clearly shown that the linear dynamic finite difference approximations seamlessly adapt according to the spectral content of the flow, leading to a quasi-optimal finite difference technique that achieves a significant accuracy improvement compared to standard schemes. The observed properties are enumerated below.

i. All results clearly indicate that for smooth solutions, which are very well resolved on the computational grid with DNS-resolution, the linear dynamic schemes adapt to obtain maximum accuracy on the large scales and thus recover the corresponding asymptotic behaviour of the high-order standard central schemes. This is clearly an advantage over the Dispersion-Relation Preserving schemes, which remain suboptimal for those flows, since they are designed a priori under the assumption of a uniform spectrum distribution in the entire wavenumber range.

ii. Further it was observed that during transitional stages, where the Fourier modes of the small scales are energized, the linear dynamic schemes seamlessly optimize themselves according to the developing energy spectrum.

iii. Once the flow is fully developed, exhibiting a full inertial range, the linear dynamic schemes act like the Dispersion-Relation Preserving schemes, minimizing the dispersion errors for all scales in the wavenumber range $\kappa \in \left[0, \frac{2\pi}{3\Delta}\right]$.

It may be concluded from the present study that the very good performance of the presented linear dynamic schemes might make them a useful tool for numerically accurate Large-Eddy Simulations of turbulent flows. This will be further investigated in the next chapter.

Despite the promising results, it was observed that the linear dynamic schemes lead to an additional computational cost of about 20% in the current framwork of Burgers' turbulence.[6] The computational overhead mainly arises due to the evaluation of the scheme's dynamic coefficients at each Runge-Kutta step. However, several strategies are available for decreasing significantly the computational cost, making the method competitive for pratical computations. Such strategies are presented in Section 8.6 for the Large-Eddy Simulation of the Taylor-Green Vortex flow, since reducing the computational overhead is more relevant and challenging for three-dimensional Navier-Stokes turbulence than for one-dimensional Burgers' turbulence.

In contrast to the linear dynamic schemes, the nonlinear dynamic schemes did not succeed in obtaining the theoretically expected quality due to the generation

[6] Remark that the computational overhead depends heavily on the efficiency of the implementation.

of spurious Fourier modes by nonlinear interactions of the scheme. These spurious scales were seen to be distributed along the entire wavenumber range, and strongly affect the accuracy of the solution. Consequently, these findings suggest that the use of nonlinear schemes may not be appropriate for the purpose of accurate flow simulations. This important conclusion is not restricted to the presented nonlinear dynamic schemes, but applies most likely to all nonlinear schemes in general.

Finally, it was observed from the Large-Eddy Simulations with the dynamic Smagorinsky model, that modeling issues and numerical issues are entirely entwined. Indeed, numerical accuracy improvement did not lead systematically to a smaller total error, since numerical errors and modeling errors might cancel each other. These results support the conclusions of Meyers *et al.* [60, 59]. Although it is tempting to resign to application of lower order discretizations in combination with dissipative models, trusting upon contingent cancellation of different errors, the current author strongly defends a more systematic approach where better models are developed, in combination with highly-accurate discretizations, such that both modeling and numerical errors are well under control.

It doesn't matter how beautiful your theory is, it doesn't matter how smart you are. If it doesn't agree with the experiment, it's wrong.

Feynman, Richard

8

The Taylor-Green Vortex Flow

In the previous chapter, an elaborate quality assessment was performed on the application of the dynamic finite difference schemes for the Large-Eddy Simulation of Burgers' turbulence. Although the one-dimensional Burgers' turbulence is only a simplified model for the Large-Eddy Simulation of three-dimensional Navier-Stokes turbulence [11, 12], the results clearly showed the excellent performance of the linear dynamic finite difference schemes in an LES-like environment. It was concluded that the developed linear dynamic schemes might provide an advantageous and viable tool for application in the Large-Eddy Simulation of real turbulent flows.

In the current chapter, the previous quality assessment is continued by examining the performance of the linear dynamic finite difference schemes for the Large-Eddy Simulation of the three-dimensional *Taylor-Green Vortex flow*. The Taylor-Green Vortex flow develops from the initial steady state motion of a single vortex structure which becomes unstable and eventually grinds down into successively smaller eddies, leading to turbulence [80]. Hence, it is perhaps one of the simplest prototype systems in which to study the breakdown process of large-scale vortices into successively smaller ones and may be interpreted as transition into turbulence. The selected flow is therefore very well suited for the current quality assessment of the dynamic finite difference approximations. As mentioned in the previous chapter, only the linear dynamic finite difference schemes are investigated further. Indeed, the nonlinear dynamic schemes are considered inappropriate for LES, since they inevitably produce spurious numerical turbulence.

8.1 TAYLOR-GREEN VORTEX: TRANSITION INTO TURBULENCE

The viscous Taylor-Green Vortex flow, first introduced in 1937 by Taylor *et al.* [80], is considered as a prototype system that describes the fundamental production of small-scale eddies due to the mechanism of vortex-line stretching in homogeneous isotropic turbulence [68, 8]. It is perhaps one of the simplest environments in which to study the breakdown process of large-scale vortices into successively smaller ones and the resulting homogeneous isotropic turbulence.
According to Brachet *et al.* [8], the generalized Taylor-Green Vortex is defined as the periodic three-dimensional incompressible flow, governed by the Navier-Stokes equations (2.2) and the continuity equation (2.1) in non-dimensional form, which develops from the initial solenoidal velocity field $\mathbf{u}(\mathbf{x}, t=0)$

$$\begin{aligned} u_1(\mathbf{x},0) &= \frac{2}{\sqrt{3}}\sin\left(\gamma+\frac{2\pi}{3}\right)\sin(x_1)\cos(x_2)\cos(x_3) \\ u_2(\mathbf{x},0) &= \frac{2}{\sqrt{3}}\sin\left(\gamma-\frac{2\pi}{3}\right)\cos(x_1)\sin(x_2)\cos(x_3) \\ u_3(\mathbf{x},0) &= \frac{2}{\sqrt{3}}\sin(\gamma)\cos(x_1)\cos(x_2)\sin(x_3)\,. \end{aligned} \tag{8.1}$$

The parameter γ, here referred to as the *shape factor*, determines the shape and orientation of the initial anisotropic vortex structure.[1] The initial pressure field $p(\mathbf{x}, t=0)$, that follows from the initial solenoidal velocity field, is obtained by solving the Poisson equation (2.3), yielding

$$\begin{aligned} p(\mathbf{x},0) &= p_0 + \frac{1-\cos(2\gamma)}{24}\left[\cos(2x_1)\cos(2x_2)+2\cos(2x_3)\right] \\ &+ \frac{2+\cos(2\gamma)+\sqrt{3}\sin(2\gamma)}{48}\left[\cos(2x_1)\cos(2x_3)+2\cos(2x_2)\right] \\ &+ \frac{2+\cos(2\gamma)-\sqrt{3}\sin(2\gamma)}{48}\left[\cos(2x_2)\cos(2x_3)+2\cos(2x_1)\right], \end{aligned} \tag{8.3}$$

where the arbitrary mean pressure component p_0 is chosen zero in this work.
It was pointed out by Orszag [68] and Brachet *et al.* [8] that the Taylor-Green Vortex

[1] Note, that the initial vorticity is obtained by $\boldsymbol{\omega}(\mathbf{x},0) = \nabla\times\mathbf{u}(\mathbf{x},0)$, yielding

$$\begin{aligned} \omega_1(\mathbf{x},0) &= -\frac{2\sqrt{3}}{3}\left(\sin(\gamma)-\sin\left(\gamma-\frac{2\pi}{3}\right)\right)\cos(x_1)\sin(x_2)\sin(x_3) \\ \omega_2(\mathbf{x},0) &= -\frac{2\sqrt{3}}{3}\left(\sin\left(\gamma+\frac{2\pi}{3}\right)-\sin(\gamma)\right)\sin(x_1)\cos(x_2)\sin(x_3) \\ \omega_3(\mathbf{x},0) &= \frac{2\sqrt{3}}{3}\left(\sin\left(\gamma+\frac{2\pi}{3}\right)-\sin\left(\gamma-\frac{2\pi}{3}\right)\right)\sin(x_1)\sin(x_2)\cos(x_3)\,, \end{aligned} \tag{8.2}$$

whereas the total helicity $\mathscr{H}$ is exactly zero since $\mathscr{H}(t=0) = \mathbf{u}\cdot\boldsymbol{\omega} \equiv 0$.

flow is characterized by various symmetries. For instance, all cross-section planes $x_j = n\pi$, $\forall n \in \mathbb{N}$ are stress-free and mirror-symmetric at all times, regardless the value of the shape factor γ in the initial conditions. This implies that the flow is actually confined in an *impermeable* box $0 \leq x_j \leq \pi$ such that no fluid crosses the boundary planes $x_j = n\pi$, $\forall n \in \mathbb{N}$. Hence, the Taylor-Green Vortex flow in the *periodic* box $0 \leq x_j \leq \mathscr{L}$, $\mathscr{L} = 2\pi$ is determined by reflecting the velocity and pressure profiles, obtained in the impermeable box, around these planes. Moreover, the flow within the impermeable box appears to be invariant under rotations of π about any axis defined by $x_1 = x_2 = \left(n + \frac{1}{2}\right)\pi$, $x_2 = x_3 = \left(n + \frac{1}{2}\right)\pi$ or $x_1 = x_3 = \left(n + \frac{1}{2}\right)\pi$.
Taking the Fourier transform of the initial velocity field (8.1), one obtains the Fourier coefficients

$$\begin{aligned}
\widehat{u}_1(\boldsymbol{\kappa}, 0) &= i\frac{2}{\sqrt{3}}\sin\left(\gamma + \frac{2\pi}{3}\right)\prod_{k=1}^{3}\frac{\upsilon_{k,1}\delta(\kappa_k - 1) - \delta(\kappa_k + 1)}{2} \\
\widehat{u}_2(\boldsymbol{\kappa}, 0) &= i\frac{2}{\sqrt{3}}\sin\left(\gamma - \frac{2\pi}{3}\right)\prod_{k=1}^{3}\frac{\upsilon_{k,2}\delta(\kappa_k - 1) - \delta(\kappa_k + 1)}{2} \\
\widehat{u}_3(\boldsymbol{\kappa}, 0) &= i\frac{2}{\sqrt{3}}\sin(\gamma)\prod_{k=1}^{3}\frac{\upsilon_{k,3}\delta(\kappa_k - 1) - \delta(\kappa_k + 1)}{2},
\end{aligned} \tag{8.4}$$

where $\delta(\kappa)$ denotes the *Dirac delta-function* and the coefficient $\upsilon_{k,j}$, $j = 1, 2, 3$ takes the value -1 if $k = j$ or 1 if $k \neq j$. Expression (8.4) clearly indicates that the initial condition (8.1) corresponds to eight Fourier modes, located at the positions $\boldsymbol{\kappa} = (\pm 1, \pm 1, \pm 1)$. Obviously, condition (8.1) represents a single vortex scale which is located at the spherical wavenumber-shell with radius $|\kappa| = \sqrt{3}$. It was further verified that the Fourier modes related to the pressure field are located on two spherical wavenumber-shells with respective radius $|\kappa| = \sqrt{6}$ and $|\kappa| = 3$. The total amount of kinetic energy in the initial flow is obtained from equation (2.20) as

$$k(t = 0) = \frac{1}{8\pi^3}\iiint_{\mathbf{0}}^{\mathbf{2\pi}}\frac{1}{2}u_i(\mathbf{x}, 0)\, u_i(\mathbf{x}, 0)d\mathbf{x} = \frac{1}{8}, \tag{8.5}$$

whereas the total amount of initial dissipation is obtained by expression (2.22) as

$$\varepsilon(t = 0) = \frac{1}{8\pi^3}\iiint_{\mathbf{0}}^{\mathbf{2\pi}}\nu\frac{\partial u_i}{\partial x_j}(\mathbf{x}, 0)\frac{\partial u_i}{\partial x_j}(\mathbf{x}, 0)d\mathbf{x} = \frac{3}{4}\frac{1}{\mathrm{Re}}. \tag{8.6}$$

Brachet *et al.* [8] defined the Reynolds number as $\mathrm{Re} = 1/\nu$, noting that the length and velocity scales of the initial flow (8.1) are of order 1. In the early times of the simulation, the large-scale vortex flow is highly organized and thus characterized as

laminar. However, the non-linear term in the Navier-Stokes equations (2.2) starts to generate successively smaller structures which interact with the large scales. If the Reynolds number is large enough, this results into process of vortex-stretching and eventually into a breakdown of the large scales into smaller ones which is interpreted as *turbulence.* Therefore, the Taylor-Green flow is believed to describe the fundamental process of transition into isotropic turbulence. Obviously, this transitional behaviour is determined entirely by the choice of the Reynolds number. Brachet *et al.* [8] observed that for $\mathrm{Re} \geq 500$ the small-scale structures in the Taylor-Green flow undergo profound changes. Indeed, for high Reynolds numbers, the *turbulent* flow becomes nearly isotropic at $t = 7s$ with no memory to the initial conditions, whereas the dissipation rate reaches a maximum at $t = 9s$. However, for low Reynolds numbers, the maximum dissipation occurs earlier, whereas the flow retains some of its initial anisotropy at all times. A clear inertial range behaviour was observed once $\mathrm{Re} \geq 1000$. For $t \to \infty$, the isotropic turbulence, which is not maintained by an external forcing, dies out due to viscosity.
In the current dissertation, the Reynolds number is set to $\mathrm{Re} = 1500$, whereas the shape factor is chosen $\gamma = 0$ according to Brachet *et al.* [8]. The resulting turbulent flow field is expected to exhibit a clear inertial range that corresponds with the Kolmogorov scaling $\kappa^{-5/3}$. Similarly to the Burgers' equation, a reference solution is obtained from a pseudo-spectral Direct Numerical Simulation of the selected Taylor-Green Vortex flow at $\mathrm{Re} = 1500$. The computational requirements, which determine the numerical setup, and the obtained results are discussed further.

8.2 Numerical Simulation of the Taylor-Green Vortex

8.2.1 Direct Numerical Simulation

Computational Requirements

As discussed in Chapter 2, the smallest turbulent scales, characterized by the Kolmogorov scale η, entirely determine the numerical requirements for the accurate and consistent Direct Numerical Simulation of a turbulent flow. In particular, several relations were derived in Paragraph 2.4.4 that allow to deduce the minimal computational requirements in case of homogeneous isotropic turbulence in a periodic box $2\pi \times 2\pi \times 2\pi$. Since the fundamental physics of the turbulent Taylor-Green flow at $\mathrm{Re} = 1500$ are not different from those of the isotropic turbulence, these relations are used to determine the computational setup for the Direct Numerical Simulation. According to relation (2.35) the Reynolds number Re is related to that based on the

taylor micro-scale Re_λ such that[2]

$$\mathrm{Re}_\lambda = \sqrt{2\mathrm{Re}} \approx 55. \tag{8.7}$$

Based on Re_λ, the minimal required number of uniformly distributed nodes N in each Cartesian direction is then readily obtained from expression (2.96) by

$$N \approx \frac{8}{\pi}\left(\frac{3}{20}\right)^{\frac{3}{4}} \frac{\pi}{\zeta}\left(\frac{12}{\mathrm{Re}_\lambda} + 0.43\right)\mathrm{Re}_\lambda^{\frac{3}{2}}, \tag{8.8}$$

where $\zeta = \kappa_\eta / 2\kappa_{max}$ denotes the ratio of the grid spacing to the Kolmogorov length scale. Although aliasing is only rigorously precluded if $\zeta \leq 1/3$ [67], Pope [70] argued that $\zeta \approx 2.1$ suffices in order to ensure that the aliasing errors are negligible. Substituting $\zeta = 2.1$ and $\mathrm{Re}_\lambda \approx 55$ into (8.8), it is found that the required number of nodes in one Cartesian direction must be at least $N \approx 242$. Since the Fast-Fourier Transformations, used in the pseudo-spectral method, are most efficient if the number of nodes N is a power of 2, N is converted to the next *power-of-two* number, which is $N = 2^8 = 256$. The grid cutoff wavenumber is then $\kappa_{max} = \frac{\pi}{\Delta} = 128$.

Hence, the Direct Numerical Simulation of the periodic Taylor-Green Vortex flow at $\mathrm{Re} = 1500$ ($\mathrm{Re}_\lambda \approx 55$) is performed on the uniform computational grid with 256^3 nodes. This implies that only the first 128^3 Fourier modes in the flow field are resolved.[3] Since the DNS simulation is expected to be well-resolved and thus aliasing may be assumed negligible [70], no explicit de-aliasing is performed. As mentioned before, the partial derivatives are calculated in Fourier space by a *pseudo-spectral* numerical method in order to exclude finite difference errors from the solution. Further, the skew-symmetric formulation is adopted for the discretization of the nonlinear term, as discussed in Section 4.3.1. The Navier-Stokes equations are solved by means of the Pressure-Correction algorithm (4.3.4), whereas the Poisson equation for the pressure-correction is solved in Fourier-space according to the methods discussed in that same section. The time stepping is performed with the explicit 4-stage Runge-Kutta method with standard coefficients $\left[\frac{1}{4}, \frac{1}{3}, \frac{1}{2}, 1\right]$, which was discussed in Section 4.2. The time step is determined by relation (2.103), i.e.

$$\Delta t = \frac{\theta}{2}\frac{\pi^2}{16}\left(\frac{20}{3}\right)^{\frac{3}{2}}\left\{\frac{\mathrm{Re}_\lambda}{(12 + 0.43\mathrm{Re}_\lambda)^2}\right\}, \tag{8.9}$$

[2]Note that this relation seems to underestimates Re_λ. For instance, Brachet *et al.* [8] reported for the Taylor-Green flow at $\mathrm{Re} \approx 3000$ a Taylor Reynolds number $\mathrm{Re}_\lambda \approx 110$, whereas relation (2.35) predicts $\mathrm{Re}_\lambda \approx 77$. Both values differ approximately with a factor $\sqrt{2}$. Most likely, Brachet *et al.* [8] defined Re_λ on the *longitudinal Taylor scale* λ_f instead of the *transversal Taylor scale* λ_g, since both length scales compare as $\lambda_f = \lambda_g\sqrt{2}$.

[3]Note that the current settings compare well to those of Brachet *et al.* [8], who used a uniform grid with $N^3 = 256^3$ for the Direct Numerical Simulation of the Taylor-Green Vortex flow with Reynolds numbers $\mathrm{Re} = 100, 200, 400, 1600, 3000$.

in which the timescale ratio is denoted by $\theta = \Delta t/\tau_\eta$. In order to guarantee the numerical accuracy of the adopted 4-stage Runge-Kutta time-stepping method, the timescale ratio must be chosen very small. In this study, the value $\theta = 0.02$ is chosen such that the dispersion and dissipation errors related to the adopted Runge-Kutta method remain sufficiently low. The time-step is then readily obtained from (8.9) and rounded off to $\Delta t = 0.005s$. The corresponding *Courant-Friederichs-Lewy* and *Neumann* conditions do not exceed their initial values, i.e.

$$\text{CFL} \leq \frac{\Delta t \max |\mathbf{u}(\mathbf{x}, 0)|}{\Delta} \approx 0.2037 \ll 1 \tag{8.10}$$

$$\text{Neu} = \frac{2\nu\Delta t}{\Delta^2} \approx 0.011 \ll \mathscr{O}(1). \tag{8.11}$$

during the simulation.[4]

RESULTS OF THE DIRECT NUMERICAL SIMULATION.

The decay of the homogeneous isotropic turbulence, that results from the Taylor-Green flow, is followed until $t = 14.25s$. Figure 8.1 illustrates the spectrum development of the resolved velocity field $u(x, t = t_j)$ in Taylor-Green Vortex flow. It is seen that the energy spectrum develops from a single characteristic Fourier mode toward an entire range of modes.[5] As suggested by Pope [70], the Taylor-Green flow is expected to be well-resolved for $\zeta = \kappa_\eta/2\kappa_{max} = 2.1$. Despite the fact that the DNS is slightly under-resolved since it does not satisfy the Nyquist criterion, the solution is believed to be sufficiently accurate as a reference. Indeed, Brachet *et al.* [8] estimated the error of the DNS at $\text{Re} = 1600$ on the same computational grid, in the order of only a few percents.
The temporal evolution of the decaying kinetic energy and the dissipation rate are shown in Figure 8.2. It is verified that the evolution of the dissipation rate $\varepsilon(t)$ is in very good agreement with that obtained by Brachet *et al.* [8] for $\text{Re} = 1600$. One observes that the dissipation rate $\varepsilon(t)$ rises relatively sharply around $t \geq 4s$ and reaches a maximum at $t = 9s$. Brachet *et al.* [8] reported that the Taylor-Green flow pattern becomes heavily distorted around $t = 7s$, which may be interpreted as *turbulence*. The coherent structure itself, finally breaks down around $t = 8s$. Therefore, it is expected that for $t \geq 9s$, the flow is fully turbulent and nearly-isotropic. The energy spectrum at maximum dissipation rate is shown in Figure 8.3. It is clearly

[4] The Direct Numerical Simulation was performed on a cluster of 2 Dell PowerEdge 1950 servers, each with 2 Quad-core Intel Xeon $X5355$ processors (16 CPU's), at 2.66GHz and required approximately 16GB of RAM-memory. The velocity data and pressure data were stored each $0.25s$ in the simulation and required a storage capacity of approximately 810MB per file. The total simulation required approximately 451.58 CPU-hours of computational time.

[5] Note that the tail of the energy-spectrum at $\kappa > \kappa_{max}$ consists of insignificant Fourier modes [70] that lay outside the sphere $|\boldsymbol{\kappa}| = \kappa_{max}$.

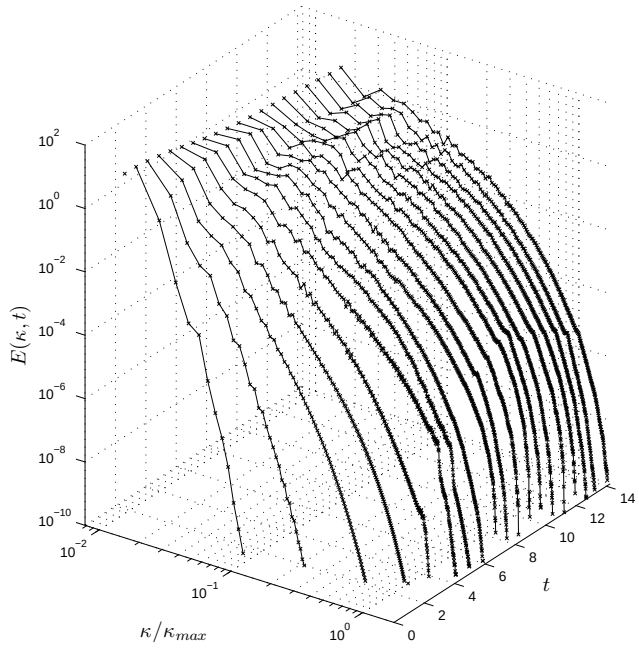

Figure 8.1: Direct Numerical Simulation of Taylor-Green Vortex. An impression of the temporal evolution of the energy spectrum $E(\kappa, t)$ in the Taylor-Green Vortex flow.

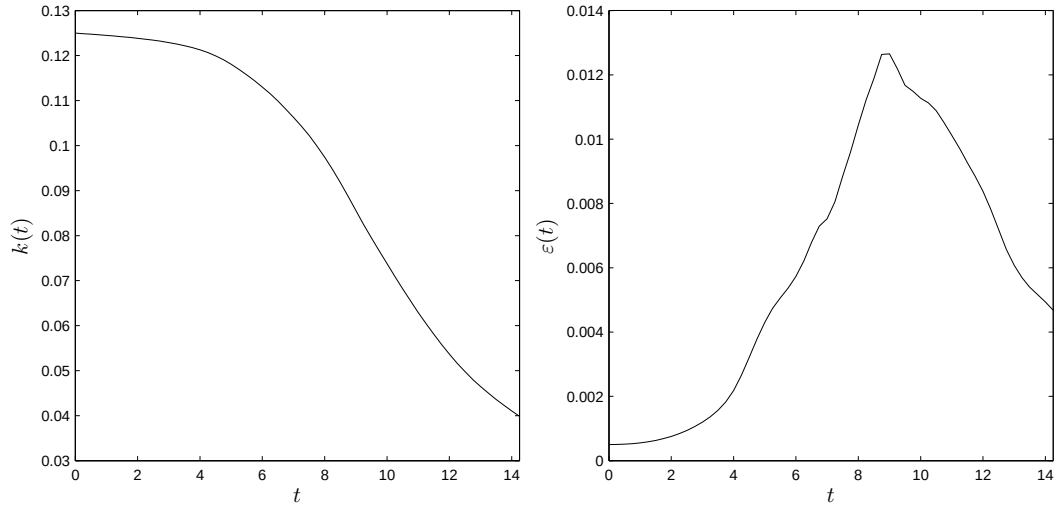

Figure 8.2: Direct Numerical Simulation of Taylor-Green Vortex. Temporal evolution of the decaying kinetic energy $k(t)$ (**left**) and the rate of dissipation $\varepsilon(t)$ (**right**). Notice the maximum dissipation at $t = 9s$.

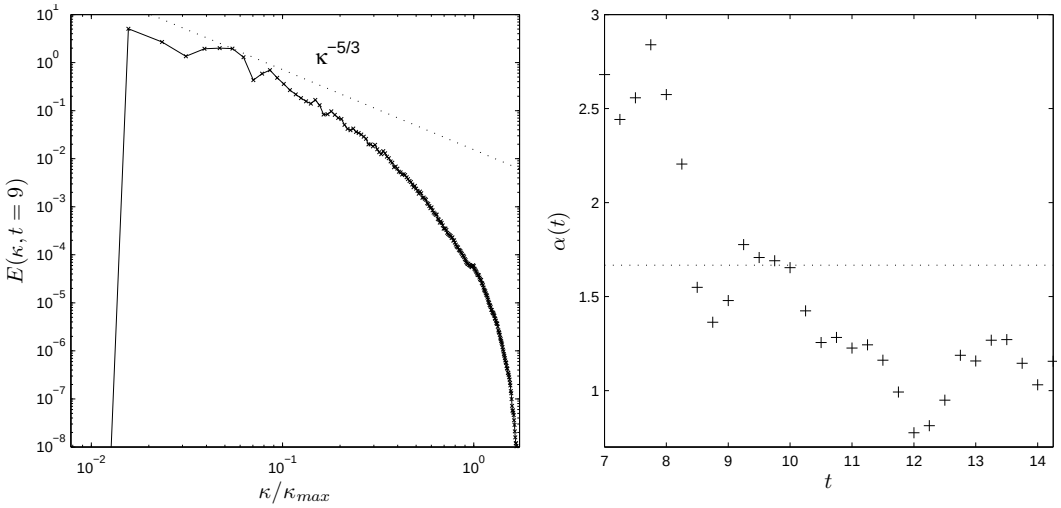

Figure 8.3: Direct Numerical Simulation of Taylor-Green Vortex. The energy spectrum at maximum dissipation $E(\kappa, t = 9s)$ (**left**) and the scaling exponent $\alpha(t)$ (**right**). Notice that only for $9 \leq t \leq 10$ $\alpha(t)$ approximates the value $5/3$ $(\cdots)$ quite accurately.

observed that the inertial range and the dissipation range overlap due to the moderate Reynolds number $\mathrm{Re} = 1500$. As a consequence, the classic Kolmogorov $-5/3$ scaling is hardly distinguished. In order to verify if the turbulent energy spectrum is indeed characterized by an inertial range behaviour, Brachet *et al.* [8] proposed to fit a functional energy spectrum of the form,[6]

$$E(\kappa, t) = \Gamma(t)\, \kappa^{-\alpha(t)} e^{-\beta(t)\kappa}, \tag{8.12}$$

where $\Gamma(t)$ correspond to $C_k \varepsilon^{2/3}$. Fitting this model spectrum to the numerical energy spectra in the wavenumber range $\frac{1}{10}\kappa_{max} \leq \kappa \leq \frac{2}{3}\kappa_{max}$ should allow to distinguish the separate contributions of the inertial range and the dissipation range by examining the exponents α and β. The calculated exponent α, which is expected to return approximately the Kolmogorov exponent $5/3$, is shown in Figure 8.3 for the time interval $7 \leq t \leq 14.25$. Obviously, for $7 \leq t \leq 8$ the exponent $\alpha(t) \geq 5/3$. At $t = 8s$, a sudden decrease is observed due to the breakdown of the coherent structure. For $9 \leq t \leq 10$ the exponent $\alpha(t)$ appears to approximate quite accurately the Kolmogorov value. However, once $t \geq 10$, the slope of the spectrum remains significantly lower than expected, and reaches a local minimum at $t = 12s$. Although the inertial range is only established for the relatively small time-window $9 \leq t \leq 10$, the Large-Eddy Simulation of the Taylor-Green Vortex flow at $\mathrm{Re} = 1500$ may suffice for the intended quality assessment of the dynamic finite difference schemes. Moreover, the significant variations of the scaling exponent may form an extra challenge for

[6] Note that this prescription is known as the *Pao* spectrum.

demonstrating the adaptivity of the dynamic schemes.
Finally, the development of the vortex structures in the Taylor-Green Vortex flow at time levels $t = 5$ and $t = 9$ is illustrated in Figures 8.4 and 8.5, by an iso-surface that satisfies the λ_2-criterion[7] of Jeong *et al.* [44]. The vortex-structures are coloured by the value of the helicity $\mathscr{H} = \mathbf{u} \cdot \boldsymbol{\omega} = \mathbf{u} \cdot (\nabla \times \mathbf{u})$. Note that a positive helicity $\mathscr{H}$ corresponds to a clockwise screw motion, whereas a negative helicity corresponds to a counter-clockwise screw motion. It is observed that at $t = 5$, the Taylor-Green Vortex flow is still well organized and thus laminar, whereas at $t = 9$, the large-scale coherent structures have been broken down into smaller vortices and the flow is turbulent.

8.2.2 Large-Eddy Simulation

The Large-Eddy Simulation of the periodic Taylor-Green Vortex flow at Re = 1500 ($\mathrm{Re}_\lambda \approx 55$) is performed on the uniform computational grid with 64^3 nodes and with grid cutoff wavenumber $\kappa_{max} = \pi/\Delta = 32$. As discussed in Chapter 3, the LES-equations with the double decomposition is preferred in this dissertation, in order to rigorously preclude aliasing and eliminate numerical errors in the high-wavenumber region [32, 49, 19, 56, 55, 35, 36, 9, 10]. This choice was extensively motivated in Chapters 3 and 4. Hence, the nonlinear terms are explicitly filtered with the sharp cutoff filter with cutoff wavenumber $\kappa_c = \frac{2}{3}\kappa_{max} \approx 21$, as suggested by Orszag [67]. In order to close the LES-equations, the dynamic Smagorinsky model by Germano *et al.* [30] was adopted, in which the magnitude of the subgrid dissipation is automatically adapted according to the resolved scales in the flow. Hence, the subgrid model is only engaged when the resolution is not sufficient any longer in order to resolve all scales of motion. Moreover, the dynamic procedure is expected to return to the theoretical value $C_s = 0.17$ found by Lilly [52] as soon as the flow is fully turbulent. A more detailed analysis of this model was already given in Paragraphs 3.3.2 and 3.3.3. Further, the skew-symmetric formulation is adopted for the discretization of the nonlinear term, as motivated in Section 4.3.1. The Navier-Stokes equations are solved by means of the Pressure-Correction algorithm of Section 4.3.4, in which the Poisson equation for the pressure-correction is solved in Fourier-space. The time stepping is performed again with the explicit 4-stage Runge-Kutta method with standard coefficients $\left[\frac{1}{4}, \frac{1}{3}, \frac{1}{2}, 1\right]$, as derived in Section 4.2. The time step is set to $\Delta t = 0.005s$, corresponding to that of the Direct Numerical Simulation. The numerical errors due to the time-stepping are thus expected to be

[7] The λ_2-criterion of Jeong *et al.* [44], identifies a vortex as a region where

$$\lambda_2\left(S^2 + \Omega^2\right) < 0, \tag{8.13}$$

where the $\lambda_2(\cdot)$-operator denotes the intermediate eigenvalue of the symmetric tensor $S^2 + \Omega^2$. This criterion is believed to be more reliable and accurate than the Q-criterion which defines a vortex as

$$Q = \frac{1}{2}\left(\Omega^2 - S^2\right) > 0. \tag{8.14}$$

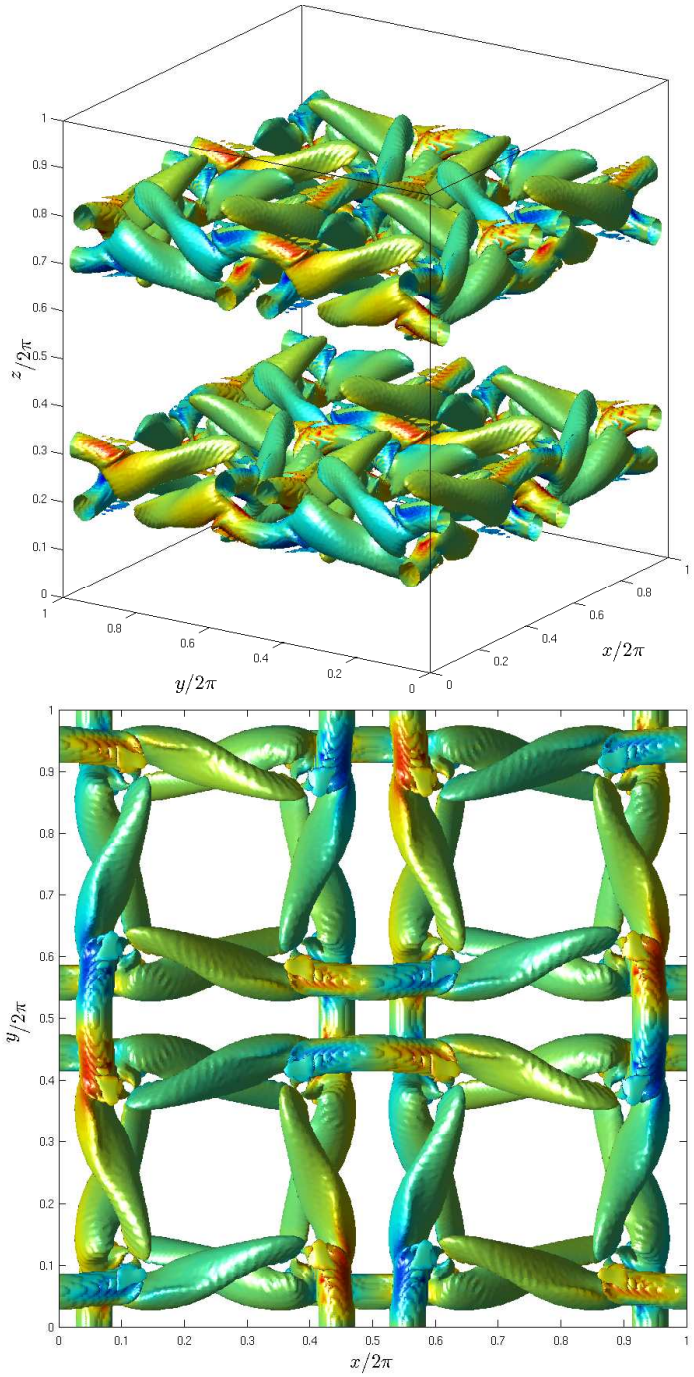

Figure 8.4: Direct Numerical Simulation of Taylor-Green Vortex. Well-orgainezed coherent vortex structures in the Taylor-Green Vortex flow at $t = 5s$, obtained with the λ_2-criterion and coloured by the Helicity $\mathscr{H}$.

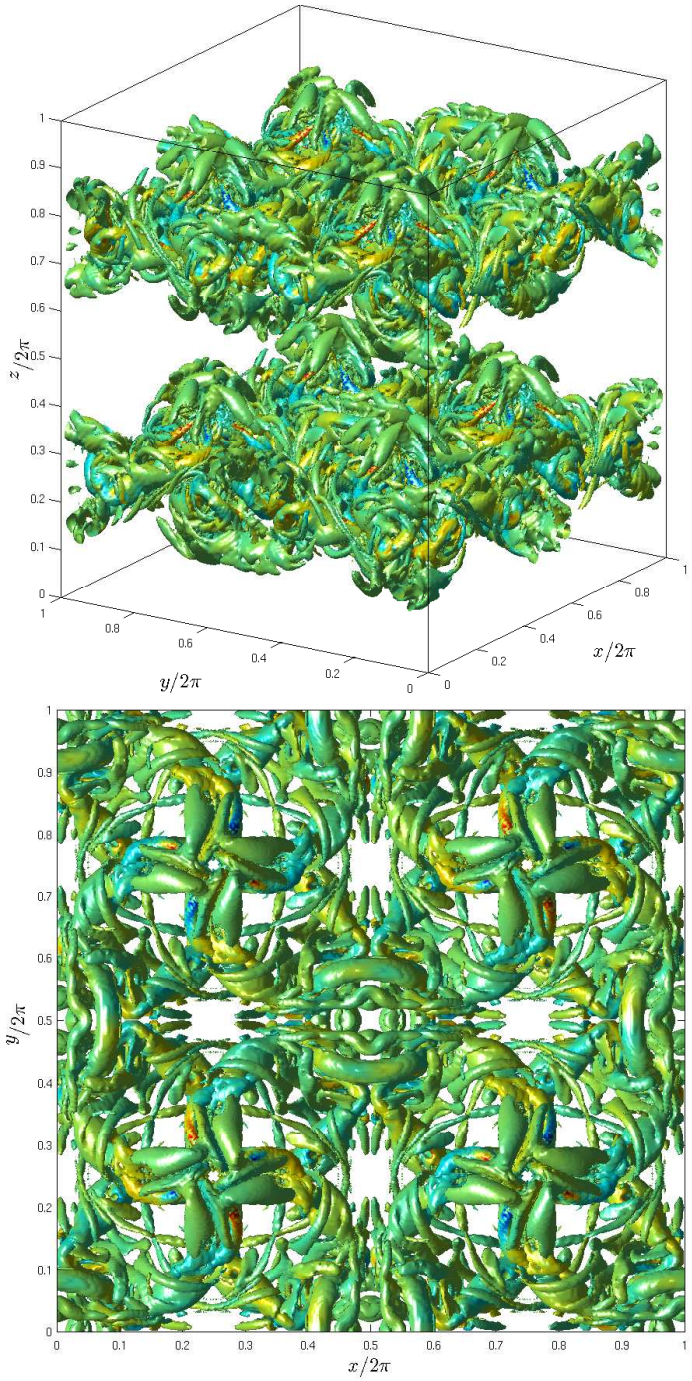

Figure 8.5: Direct Numerical Simulation of Taylor-Green Vortex. The turbulent small-scale vortex structures in the Taylor-Green Vortex flow at $t = 9s$, obtained with the λ_2-criterion and coloured by the Helicity $\mathscr{H}$.

very small. It was verified that the *Courant-Friederichs-Lewy* condition does not exceed its initial value, i.e.

$$\text{CFL} \leq \frac{\Delta t \max |\mathbf{u}(\mathbf{x}, 0)|}{\Delta} \approx 0.05162 \ll 1, \tag{8.15}$$

during the simulation.[8]

Similarly to the Large-Eddy Simulation of Burgers' equation, some particularities must be addressed concerning the implementation of the linear dynamic finite difference approximations for the Large-Eddy Simulation of the Taylor-Green Vortex flow. Indeed, since the spectra related to fields $\overline{u_i}$ and $\overline{u_j u_i}$ are substantially different, the constant value of the dynamic coefficients $c_{k,n}^{dyn}$ (expression (6.20)) in the *linear* dynamic finite difference approximations of the advective operator is not the same as the one obtained for the divergence operator. As a consequence, the skew-symmetric formulation of the nonlinear term, constructed by a fixed weighting between the advective and divergence formulation, looses the a priori conservation of kinetic energy. Hence, in order to preserve the skew-symmetry property, and thus the conservation of kinetic energy, the same dynamic coefficient $c_{k,n}^{dyn}$ obtained for the the advective operator is used for the divergence operator. As motivated before, such an approach is equivalent with the traditional discretization approach of the skew-symmetric operator using standard schemes or prefactored optimized schemes. In the current study, each partial derivative in the Navier-Stokes equations or the Poisson equation is discretized straightforwardly by using the appropriate dynamic finite difference approximation. However, this implementation involves the calculation of multiple dynamic coefficients at each Runge-Kutta step. An overview of all required dynamic coefficients in the system of equation is given below.

i. The finite difference approximation of the nonlinear term in the Navier-Stokes equations requires the calculation of 9 dynamic coefficients, i.e. one per component of the skew-symmetric operator.

ii. Similarly, 3 dynamic coefficients are needed for the finite difference approximation of the pressure gradient in the Navier-Stokes equations.

iii. Since the molecular viscosity term uses the Laplacian of the velocity field, again 9 coefficients must be determined.

iv. As discussed in Section 4.3.2, the subgrid force is implemented *compactly* according to expression (4.87). Therefore, this discretization requires 9 dynamic

[8] The Large-Eddy Simulations with the dynamic Smagorinsky model were performed on a single Dell PowerEdge 1950 server which consists of 2 Quad-core Intel Xeon $X5355$ processors (8 CPU's) at 2.66GHz. The velocity data and pressure data were stored each $0.25s$ in the simulation and required a storage capacity of approximately 10.6MB per file. The total simulation required approximately 5.26 CPU-hours of computational time for the spectral LES simulation.

coefficients for the partial derivatives of the turbulent viscosity. Nevertheless, for the discretization of the Laplacian part in expression (4.87), the same coefficients are used as those obtained in for the molecular term.

v. As mentioned earlier, the Pressure-Correction algorithm is used in order to impose the continuity constraint. This algorithm involves the solution of the Poisson equation for the pressure correction. For the construction of the Poisson matrix, the stencils of the Poisson operator must be specified a priori and thus 9 values of the dynamic coefficients must be determined in advance. However, since the pressure correction field is not known a priori, these coefficients can only be obtained from the pressure at the previous subiteration level.

vi. Finally, for the approximation of the divergence operator of predictor velocity u_i^* in the Poisson equation, 3 dynamic coefficients must be calculated.

The above considerations bring the total amount of required dynamic coefficients per Runge-Kutta step to 42. Note that the optimal blending factors f, used in the enlisted dynamic approximations, can be found in Tables 6.3, 6.4 and 6.5. Obviously, the proposed straightforward application of the dynamic finite difference method will most likely lead to a significant computational overhead. However, in order to make a fair analysis of the costs involved (see Section 8.6), the accuracy of the scheme must be evaluated first. In order to appraise unambiguously the quality of the linear dynamic finite difference method for Large-Eddy Simulation, a reliable framework for evaluation of the numerical errors must be defined first.

8.3 Quantification of numerical errors

Before assessing the quality of the dynamic finite difference approximations for the Large-Eddy Simulation of the Taylor-Green Vortex, the main definitions for evaluating and quantifying the errors are repeated here briefly for the three-dimensional case.

Using the same terminology as in Section (7.3), the total error on a variable of interest ϕ is decomposed into a modeling error contribution and a numerical error contribution, leading to the expressions ($\kappa_c = \frac{\pi}{\Delta_c}$, $\kappa_{max} = \frac{\pi}{\Delta}$)

$$\varepsilon_{\phi,total}\left(\kappa_c,\kappa_{max}\right) = \overline{\phi_s\left(\kappa_\eta,\frac{3}{2}\kappa_\eta\right)} - \overline{\phi}_{fd}\left(\kappa_c,\kappa_{max}\right) \tag{8.16}$$

$$\varepsilon_{\phi,model}\left(\kappa_c,\kappa_{max}\right) = \overline{\phi_s\left(\kappa_\eta,\frac{3}{2}\kappa_\eta\right)} - \overline{\phi}_{s}\left(\kappa_c,\kappa_{max}\right) \tag{8.17}$$

$$\varepsilon_{\phi,num}\left(\kappa_c,\kappa_{max}\right) = \overline{\phi}_{s}\left(\kappa_c,\kappa_{max}\right) - \overline{\phi}_{fd}\left(\kappa_c,\kappa_{max}\right), \tag{8.18}$$

Recall that in case of proper de-aliasing, the numerical error reduces exactly to the errors due to the finite difference discretization.

In analogy with the work of Meyers *et al.* [62], the different errors are then quantified using the *mathematics-based* and *physics-based* error definitions. Two *mathematics-based* error definitions are used in the present chapter, i.e. the spectrum of the pointwise error ε_ϕ of a variable ϕ

$$E_{\varepsilon_\phi}(\boldsymbol{\kappa}, t) = \widehat{\varepsilon_\phi}(\boldsymbol{\kappa}, t)\, \widehat{\varepsilon_\phi}^*(-\boldsymbol{\kappa}, t), \tag{8.19}$$

and its magnitude k_{ε_ϕ}

$$k_{\varepsilon_\phi}(t) = \iiint_{\mathbf{0}}^{\boldsymbol{\kappa_{max}}} E_{\varepsilon_\phi}(\boldsymbol{\kappa}, t)\, d\boldsymbol{\kappa}. \tag{8.20}$$

Recall that the magnitude k_{ε_ϕ} corresponds to the L_2-norm,[9] as $L_2(t) = \sqrt{k_\varphi(t)}$ and that this error has always a positive sign.
Further, three global *physics-based* error norms are introduced, i.e. the total error on the longitudinal integral length scale L_{11}, the total error on the kinetic energy ε_k, and the total error on the dissipation rate ε_ε, given by respectively

$$\varepsilon_L = \Delta L_{11} = \iiint_{\mathbf{0}}^{\boldsymbol{\kappa_{max}}} \boldsymbol{\kappa}^{-1} \Delta E_u(\boldsymbol{\kappa})\, d\boldsymbol{\kappa} \tag{8.22}$$

$$\varepsilon_k = \Delta k = \iiint_{\mathbf{0}}^{\boldsymbol{\kappa_{max}}} \Delta E_u(\boldsymbol{\kappa})\, d\boldsymbol{\kappa} \tag{8.23}$$

$$\varepsilon_\varepsilon = \Delta \varepsilon = \iiint_{\mathbf{0}}^{\boldsymbol{\kappa_{max}}} \boldsymbol{\kappa}^2 \Delta E_u(\boldsymbol{\kappa})\, d\boldsymbol{\kappa}, \tag{8.24}$$

in which the error on the energy spectrum of the velocity field is given by

$$\varepsilon_E(\boldsymbol{\kappa}, t) = \Delta E_u(\boldsymbol{\kappa}, t), \tag{8.25}$$

Remark that the sign of ε_k and ε_ε could be either positive or negative, enabling to see interactions between different error sources.
It is emphasized that the mathematics-based error definitions reflect both amplitude and phase errors in the solution whereas the physics-based definitions represent only errors on the amplitude. Both error definitions are used further for analyzing the performance of finite difference schemes, and interactions with the subgrid model.

[9] The L_2-norm is defined as

$$L_2(t) = \sqrt{\frac{1}{8\pi^3} \iiint_{\mathbf{0}}^{\mathbf{2\pi}} [\varepsilon_\phi(\mathbf{x}, t)]^2\, d\mathbf{x}}. \tag{8.21}$$

Symbols - Simulations			
$+$	filtered DNS	$\square$	6^{th} -order tridiagonal Padé
$\times$	pseudo-spectral LES	$\bullet$	2^{nd} -order static DRP scheme
$\circ$	2^{nd} -order central	$\blacktriangle$	4^{th} -order static DRP scheme
$\triangle$	4^{th} -order central	$\blacksquare$	4^{th} -order static tridiagonal DRP Padé scheme
$\triangledown$	6^{th} -order central	———	2^{nd} -order explicit linear dynamic scheme
$\triangleright$	8^{th} -order central	– – –	4^{th} -order explicit linear dynamic scheme
$\triangleleft$	10^{th} -order central	–·–·	4^{th} -order implicit linear dynamic scheme

Table 8.1: Simulation overview. Overview of the various a priori or a posteriori simulations of Tayor-Green vortex, and their corresponding symbol notation.

8.4 A PRIORI STUDY OF THE TAYLOR-GREEN VORTEX

Before assessing the quality of the linear dynamic schemes, described in Appendix C, in a real Large-Eddy Simulation of the Taylor-Green flow, first an *a priori* quality assessment is performed for these schemes. In the following, the 2^{nd} -order explicit linear dynamic finite difference approximation, the 4^{th} -order explicit linear dynamic finite difference approximation and the 4^{th} -order implicit linear dynamic finite difference approximation are considered. Following the work of Chow *et al.* [19], the error spectra of the various finite difference errors on the skew-symmetric formulation of the nonlinear force are compared. These finite difference errors are obtained by subtracting the nonlinear force, calculated with the finite difference approximations, from the nonlinear force calculated with the spectral derivatives in Fourier space. Note that the described method corresponds to the mathematics-based error definition. Besides the error spectrum $E_\varphi(\boldsymbol{\kappa}, t)$, where φ denotes the nonlinear force, its magnitude k_φ is also evaluated. As mentioned before, the latter is related to the L_2-norm by $L_2(t) = \sqrt{k_\varphi(t)}$. Table 8.1 gives an overview of the performed simulations, and the corresponding symbol notation used in the plots to follow.

Figure 8.6 presents the global magnitude as function of time. At the early stages of the simulation ($t \leq 2$) where the Taylor-Green flow is still laminar and the small scales contain little or no energy, the 2^{nd} - and 4^{th} -order linear explicit and 4^{th} -order implicit dynamic schemes almost collapse with their asymptotic counterparts, i.e. the 4^{th} - and 6^{th} -order explicit standard central schemes and the 6^{th} -order tridiagonal Padé scheme. The corresponding 2^{nd} - and 4^{th} -order Dispersion-Relation Preserving schemes and the 4^{th} -order Dispersion-Relation Preserving Padé scheme, achieve 2^{nd} - respectively 4^{th} -order accuracy for the subgrid force in the laminar flow region. Despite the fact that the flow remains laminar until approximately $t \approx 6-7$, the simulation shifts rapidly from DNS-resolution to LES-resolution around $t \approx 2$, due to production of low-energy small scales by the nonlinear term that fall beyond the grid cutoff wavenumber. It is observed that the linear dynamic schemes seamlessly adapt according to the developing energy spectrum and approach the DRP schemes. The accuracy of both the dynamic and the DRP schemes appears to be better than that of the standard asymptotic schemes. The same conclusions apply

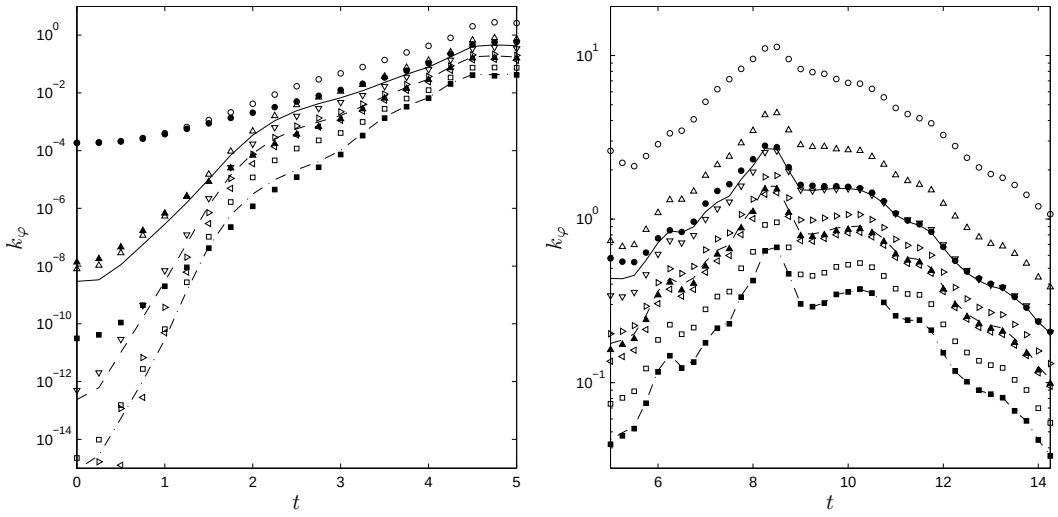

Figure 8.6: A priori results on Taylor-Green Vortex. The global magnitude k_φ of the finite difference error on the subgrid force φ of the laminar Taylor-Green Vortex flow, i.e. $0 \leq t \leq 5$ (**left**) and the transitional and turbulent Taylor-Green flow, i.e. $5 \leq t \leq 14.25$ (**right**). (Symbols: see Table 8.1)

during the flows' transition into turbulence ($5 \leq t \leq 8.5$). Once the flow has become fully turbulent, i.e. for $t \geq 9$ such that the energy spectrum tends to display a weak inertial range behaviour, the linear dynamic schemes adapt according to the turbulent flow characteristics and achieve higher accuracy in comparison with the standard asymptotic schemes. Notice that the error levels of both the Dispersion-Relation Preserving schemes and dynamic finite difference schemes collapse. More specific, the 2^{nd} -order explicit linear dynamic scheme and the standard 6^{th} -order schemes perform equally good, whereas the accuracy of the 4^{th} -order explicit linear dynamic scheme reaches that of the 10^{th} -order central scheme. Further, the 4^{th} -order implicit linear dynamic scheme obtains very high accuracy and is clearly better than the standard 6^{th} -order tridiagonal Padé scheme. It may be obvious that for $t \to \infty$ the dynamic schemes should eventually reduce to the corresponding asymptotic standard schemes. However, in order to illustrate this, the simulation should be continued much longer.

The results in Figure 8.6 are confirmed by looking at snapshots of the error spectrum $E_\varphi(\kappa, t)$, displayed in Figure 8.7, for the laminar flow at $t = 1s$ (DNS-resolution), and after the Taylor-Green Vortex has gone into turbulence at maximum dissipation i.e. $t = 9s$ (LES-resolution). Both energy spectra differ significantly. At $t = 1s$ the linear dynamic schemes recover almost the behaviour of their asymptotic counterparts, i.e. the 4^{th} - and 6^{th} -order explicit standard central schemes and the 6^{th} -order tridiagonal Padé scheme. Clearly, the linear dynamic schemes are now optimized for the largest resolved scales which contain most of the energy. This is in contrast

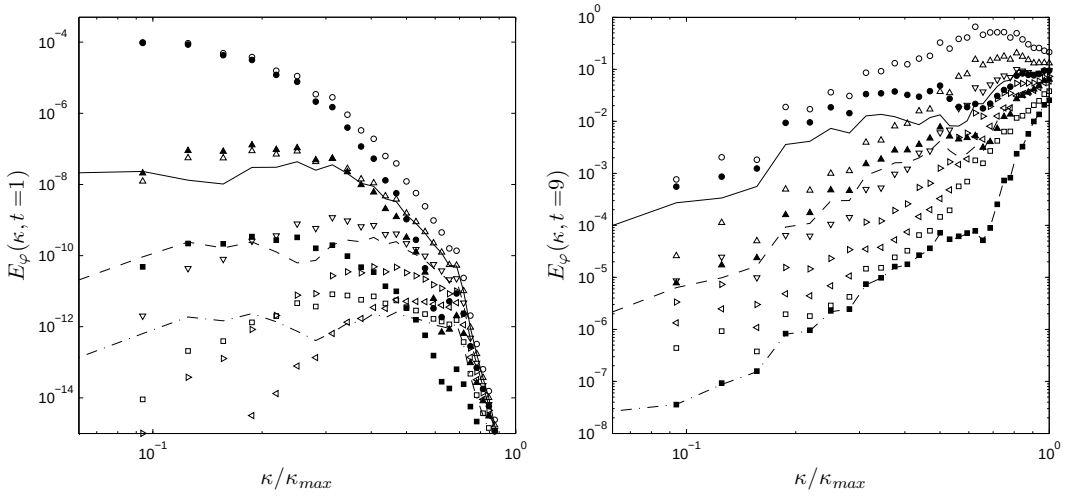

Figure 8.7: A priori results on Taylor-Green Vortex. Snapshots of the spectrum $E_\varphi(\kappa, t)$ of the finite difference error on the subgrid force φ of the laminar Taylor-Green Vortex flow at $t = 1s$ (**left**) and the fully turbulent Taylor-Green flow at $t = 9s$ (**right**). (Symbols: see Table 8.1)

to the equivalent Dispersion-Relation Preserving schemes which are optimized for a predefined fully developed spectrum and therefore reach 2^{nd} - respectively 4^{th} -order accuracy. At $t = 9s$ the flow is fully turbulent and the linear dynamic schemes have adapted accordingly. The dynamic schemes achieve the same accuracy as the 2^{nd} - respectively 4^{th} -order standard asymptotic schemes for the largest resolved scales, whereas the error on the smallest resolved scales is significantly reduced compared to the traditional central schemes. As expected, similar performance for the DRP schemes is observed here. Although only the results for the nonlinear force were shown, the same conclusions apply for the a priori results on the pressure gradient and the viscous force.

To illustrate the adaptivity of the linear dynamic schemes, Figure 8.8 shows the various ratio's of the dynamic coefficient to its Taylor value $c_{k,n}^{dyn}/c_{k,n}^{*}$, for the 4^{th} -order linear implicit dynamic finite difference approximation of the skew-symmetric operator $\frac{1}{2}u_j\frac{\partial u_i}{\partial x_j} + \frac{1}{2}\frac{\partial u_j u_i}{\partial x_j}$, as function of time. First, the scheme recovers the asymptotic order of accuracy at the initial stages of the simulation, since $c_{k,n}^{dyn}/c_{k,n}^{*} \to 1$. Further, a sharp increase of the coefficient is observed around $1 \leq t \leq 2$. This stems from the fact that the simulation shifts around that time from DNS-resolution to LES-resolution, although the flow is still laminar. Notice that the coefficients of the different contributions increase independently from each other, due to the anisotropy of the initial Taylor-Green Vortex flow. This clearly illustrates the behaviour of the linear dynamic schemes to seamlessly adapt according to the specific properties of the

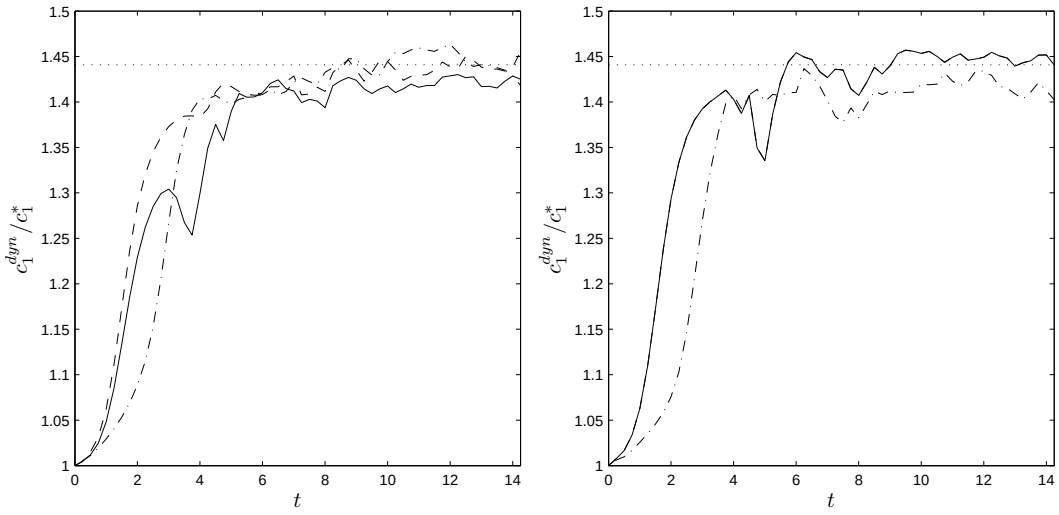

Figure 8.8: A priori results on Taylor-Green Vortex. Ratio of the dynamic coefficient to its Taylor value $c_{k,n}^{dyn}/c_{k,n}^* = c_n^{dyn}/c_n^*$ for the 4^{th} -order explicit linear dynamic approximation of the skew-symmetric operator on the nonlinear term $\frac{1}{2}u_j\frac{\partial u_i}{\partial x_j} + \frac{1}{2}\frac{\partial u_j u_i}{\partial x_j}$. The coefficients for $i = 1$ (**left**) and $i = 3$ (**right**) with $j = 1$ (———), $j = 2$ ($- - -$) and $j = 3$ ($-\cdot-\cdot$) are illustrated. The theoretically obtained coefficient (Table 6.3) for the 4^{th} -order dynamic implicit scheme ($\cdots$), is shown for comparison. Note that due to the symmetry of the Taylor-Green flow some contributions appear to have the same dynamic coefficient, more specific $(i, j) = (1, 1) = (2, 2)$, $(1, 2) = (2, 1)$, $(1, 3) = (2, 3)$ and $(3, 1) = (3, 2)$.

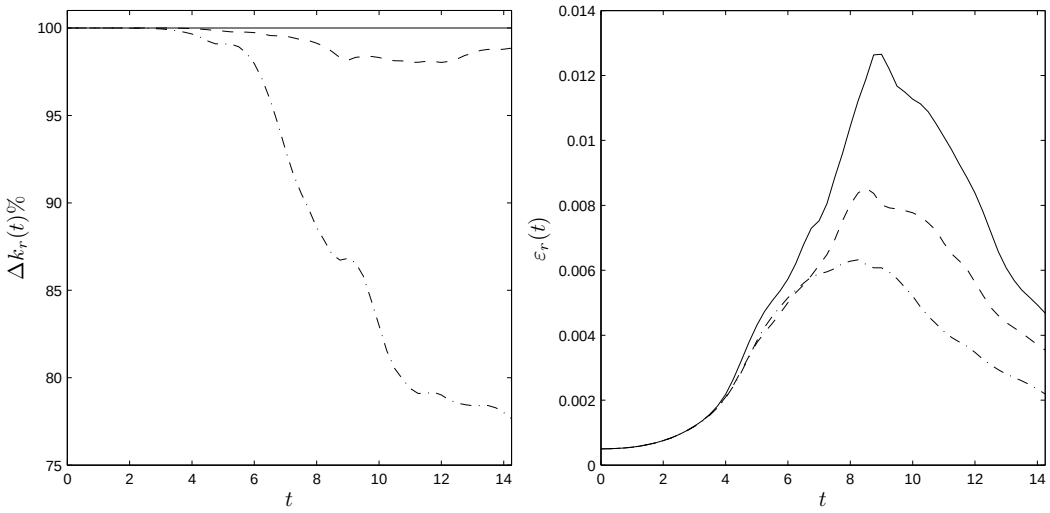

Figure 8.9: A posteriori results on Taylor-Green Vortex. Percentage of resolved kinetic energy $\Delta k_r\,(t)\,\%$ (**left**) and amount of resolved dissipation $\varepsilon_r\,(t)$ (**right**). Distinguish the DNS solution (———), the filtered DNS solution (− − −) and the spectral LES solution obtained with the dynamic Smagorinsky model (−·−·).

flow on the computational grid, including global anisotropy. Hence, such schemes might provide an additional advantage for accurate simulations of more complex anisotropic flows. In the interval $5 \leq t \leq 8$, where the flow goes into transition, the dynamic coefficients seem to reach a plateau. Once the coherent structures break down ($t \approx 8$), the dynamic coefficients $c_{k,n}^{dyn}$ approach the theoretical value found in Table 6.3. Nevertheless, it is observed that some coefficients remain below this value, whereas others rise above this value. Finally, it is mentioned that due to the symmetries of the flow, some of the obtained coefficients for different contributions of the skew-symmetric operator are equal. Therefore, these coefficients are not explicitly shown in Figure 8.8.

8.5 A posteriori study of the Taylor-Green Vortex

The quality assessment on the dynamic finite difference schemes for the Large-Eddy Simulation of the Taylor-Green Vortex flow, using the dynamic Smagorinsky model, is initiated by a verification of Pope's criterion [70] that ideally 80% of the kinetic energy is resolved in a good Large-Eddy Simulation. Figure 8.9 compares the amount of resolved kinetic energy k_r of the filtered DNS solution and the solution of the spectral LES, both on the grid 64^3, to that of the reference DNS on the grid 256^3. Moreover, Figure 8.9 shows the amount of resolved dissipation ε_r. Although the filtered DNS solution indicates that at least 98% of the kinetic energy may ideally be resolved on the 64^3 LES-grid, the spectral LES solution resolves only about 78% of that kinetic energy. Hence, despite the use of a dynamic procedure,

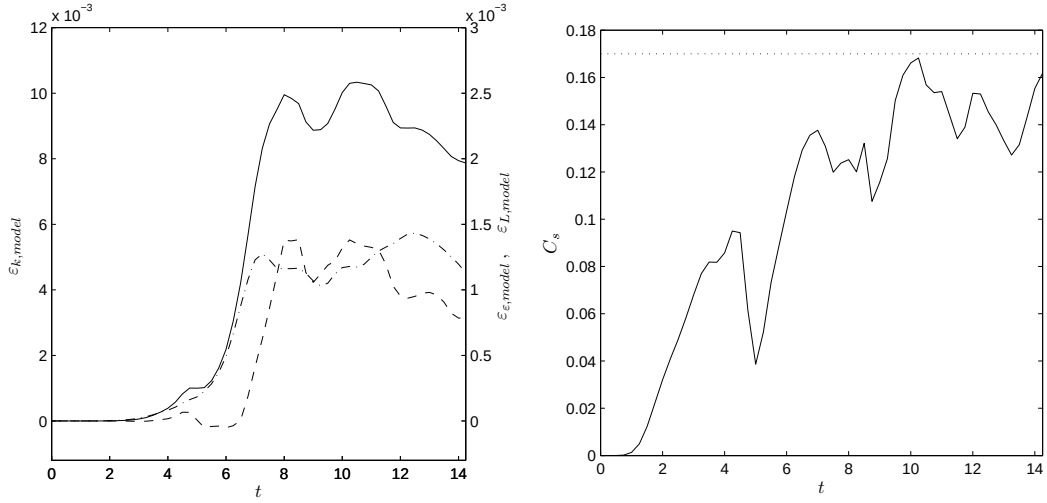

Figure 8.10: A posteriori results on Taylor-Green Vortex. The modeling errors on the global kinetic energy (——), the global dissipation rate (− − −) and the longitudinal integral length scale (−·−·) during the simulation (**left**). The profile of the dynamic Smagorinsky constant C_s (——) for the pseudo-spectral LES as function of time is shown and compared with the theoretical Lilly constant $C_s = 0.17$ ($\cdots$) (**right**).

the Smagorinsky model appears to be too dissipative.
In the following, the modeling error contributions and the numerical error contributions are separated by the decomposition of Vreman *et al.* [87] and Meyers *et al.* [60, 59, 61]. The modeling error on the kinetic energy, the dissipation rate and the longitudinal integral length scale are shown in Figure 8.10. The mainly positive error-profiles confirm that the dynamic Smagorinsky model is too dissipative such that the kinetic energy of the spectral LES solution is smaller than that of the filtered DNS solution. Surprisingly, the dynamic model coefficient C_s of the pseudo-spectral LES, shown in Figure 8.10 remains below the theoretical value $C_s = 0.17$, found by Lilly [52]. This makes sense since the Lilly constant is calibrated for an infinite Reynolds number, whereas the Reynolds number of the current Taylor-Green flow quite low. Hence, the dynamic procedure seems to compensate quite well for this low Reynolds behaviour. It is observed that the dynamic procedure engages the model around $t \approx 1$, although the flow is still laminar. Indeed, the simulation shifts there from DNS-resolution to LES-resolution. Notice that the dynamic Smagorinsky constant in Figure 8.10 displays a very similar behaviour than the dynamic coefficients in the linear dynamic schemes in Figure 8.8.

The quality assessment of the dynamic finite difference approximations is continued by comparing the numerical errors with those of the standard schemes and DRP schemes. Figure 8.11 represents the global magnitude of the numerical er-

rors (related to L_2-norm) on the velocity field $\mathbf{u}(\mathbf{x},t)$ and the pressure field $p(\mathbf{x},t)$. Moreover, Figure 8.12 illustrates the more detailed energy spectrum of the numerical errors at the early stages of the simulation ($t = 1s$) and when the flow is fully turbulent ($t = 9s$). Recall that these mathematics-based error definitions reflect information about the amplitude and the phase of the solution. Apparently, the same conclusion applies for the linear explicit and implicit dynamic schemes, as for the Burgers' study. It is observed that the linear dynamic schemes recover the asymptotic order of accuracy in the early stages of the simulation, i.e $t \leq 2s$, where the flow is still smooth and resolved with DNS-resolution. This is in contrast to the Dispersion-Relation Preserving schemes, which are suboptimal there. As soon as the resolution of the grid becomes inadequate to resolve all scales in the flow (the simulation shifts from DNS-resolution to LES-resolution at $t \approx 2s$), the linear dynamic schemes adapt to the instantaneous solution and achieve an accuracy comparable to that of the Dispersion-Relation Preserving schemes at all times $2 \leq t \leq 14.25$. In particular, the 2^{nd} -order explicit linear dynamic scheme is observed to achieve the accuracy of the 8^{th} -order central scheme, which is better than that of the corresponding 2^{nd} -order static DRP scheme. The latter has a comparable accuracy to that of the standard 6^{th} -order explicit scheme. The 4^{th} -order explicit linear dynamic scheme obtains the same quality as the corresponding DRP scheme, which fluctuates between that of the 8^{th} - and 10^{th} -order standard scheme. In contrast to both explicit dynamic schemes, the quality of the 4^{th} -order dynamic implicit finite difference approximation remains somewhat below the 4^{th} -implicit DRP Padé scheme, although both clearly outperform all other schemes. Looking at Figure 8.12, one can see that in the early stages of the simulation ($t = 1s$), the schemes are clearly adapted to the low-wavenumber content on the computational grid, whereas for the fully developed turbulent flow ($t = 9s$), the schemes are optimized for the inertial range turbulent spectrum.

An explanation for the reduced quality of the 4^{th} -order implicit dynamic scheme compared to the 4^{th} -order implicit DRP scheme, might be found in the optimal value of the blending factor. Although the optimal blending factors f_{opt} were determined assuming a fully developed generic one-dimensional Taylor-Green spectrum for the velocity field (see Section 6.3.4), the corresponding dynamic coefficient, given in Table 6.3, appears to exceed the value of the equivalent coefficient in case of the uniform spectrum, given in Table 6.1. This opposes to the general tendency which indicates that for steeper (negative) slopes of the inertial range spectrum, the dynamic coefficient is expected to be smaller. Moreover, it is observed in Figure 8.8, that some dynamic coefficients may even exceed the theoretical value in Table 6.3 during the simulation. Although this behaviour most likely causes the suboptimal behaviour of the 4^{th} -order implicit dynamic scheme, an exact explanation for the anomalous values of the dynamic coefficient remains unclear at this time. Since some dynamic coefficients may exceed their theoretical value during the simulation, as observed in Figure 8.8, a limitation of the dynamic coefficient to this value might be advantageous in more practical computations. Moreover, a sensitivity study of the blending factor for different schemes may shed a new light to the matter.

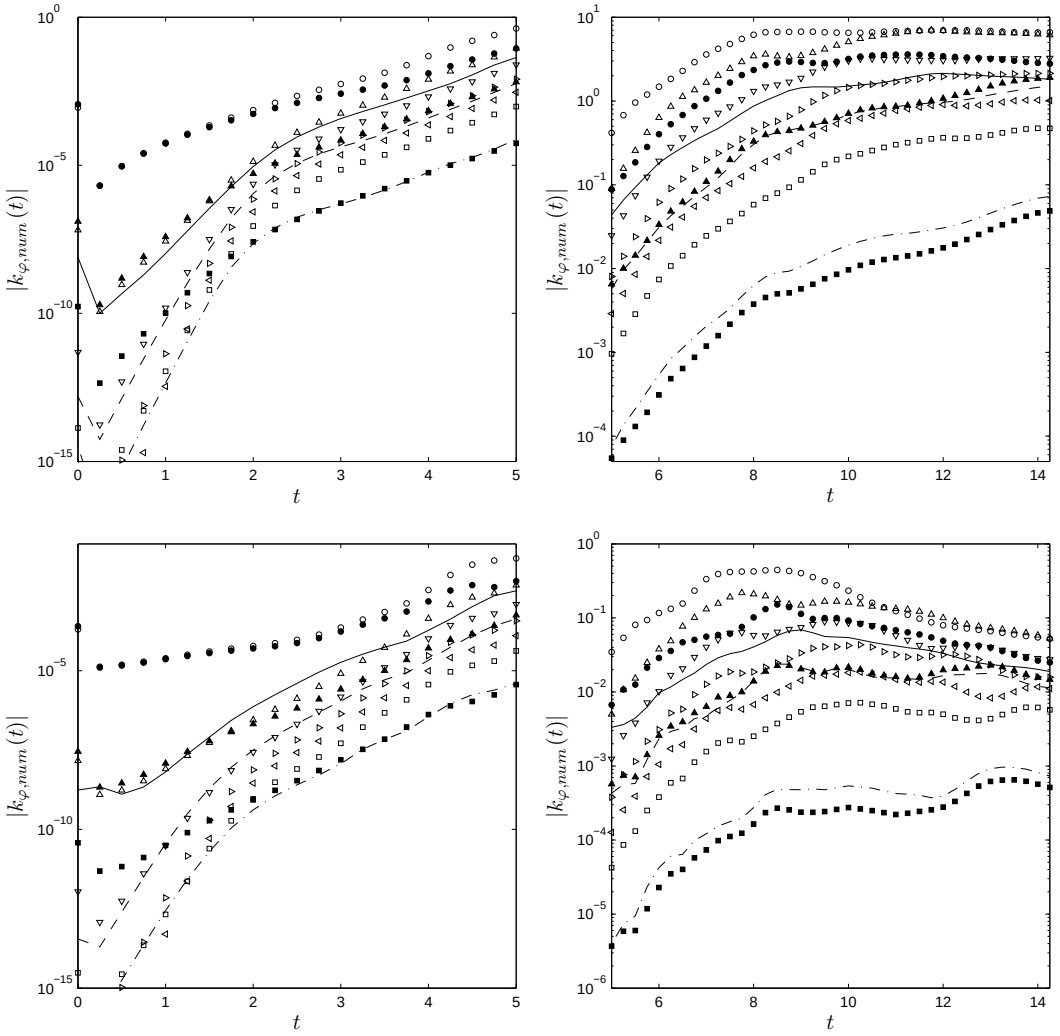

Figure 8.11: A posteriori results on Taylor-Green Vortex. The global magnitude k_φ of the numerical errors on the resolved velocity field, i.e $\varphi = \varepsilon_{\mathbf{u}}$ (**upper**) and the pressure field $\varphi = \varepsilon_p$ (**lower**) of the laminar Taylor-Green Vortex flow, i.e. $0 \leq t \leq 5$ (**left**) and the transitional and turbulent Taylor-Green flow, i.e. $5 \leq t \leq 14.25$ (**right**). (Symbols: see Table 8.1)

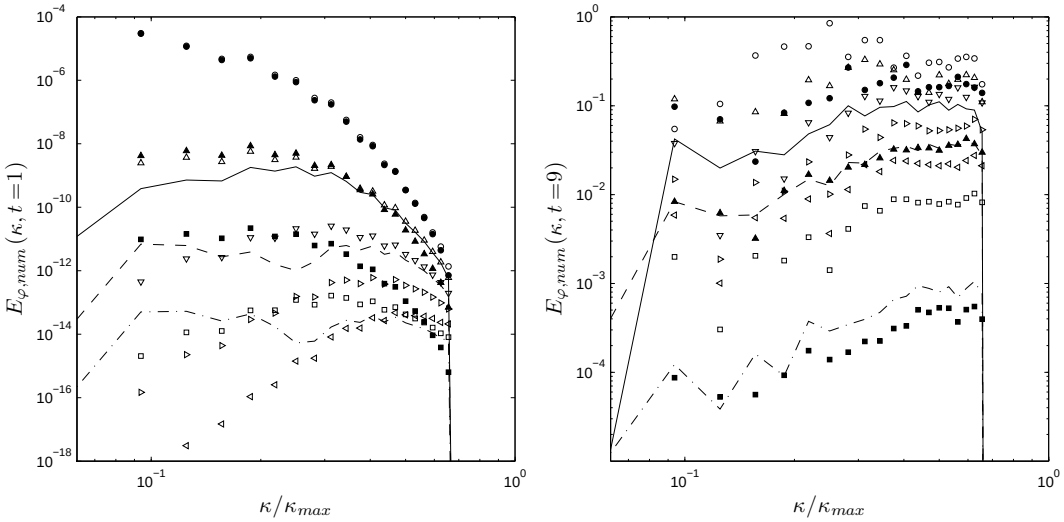

Figure 8.12: A posteriori results on Taylor-Green Vortex. Snapshots of the spectrum $E_\varphi(\kappa, t)$ of the error $\varphi = \varepsilon_u$ of the resolved velocity field of the laminar Taylor-Green Vortex flow at $t = 1s$ (**left**) and the fully turbulent Taylor-Green flow at $t = 9s$ (**right**). (Symbols: see Table 8.1)

The impact of the numerics on the physics-related quantities such as the longitudinal integral length scale, the kinetic energy and the dissipation rate is demonstrated in Figures 8.13-8.15. It is observed that the performance of the finite difference schemes appears to be less clear and less obvious, than for e.g. the Burgers' study. This is mainly due to two factors. First, it is understood from definitions (8.22)-(8.24) that e.g. the error on the longitudinal integral length scale contains more information on the accuracy on the amplitude of the largest resolved scales, whereas the error on the dissipation rate contains more information on the accuracy of the amplitudes on the smallest resolved scales. Secondly, since these physics-based errors are not strictly positive and may cross zero, several local minima are observed in the accuracy plots of the longitudinal integral length scale, the dissipation and the kinetic energy. These rather occasional minima may mask things a little. Nevertheless, in general, the same tendencies are distinguished as in the previous discussion. Focusing on the early laminar stages of the simulation, i.e $0 \leq t \leq 2$, the dynamic finite difference schemes approach the asymptotic order of accuracy as expected. This is reflected by the accuracy on the longitudinal integral length scale, the kinetic energy and the dissipation rate. Further, in the transitional region of the flow, i.e. $5 \leq t \leq 7$ the 2^{nd} -order explicit dynamic scheme and the 2^{nd} -order DRP scheme perform slightly worse than the standard 2^{nd} -order scheme. Focusing on the turbulent regime of the Taylor-Green flow ($9 \leq t \leq 14.25$), the error on the integral length scale clearly shows the good performance of all dynamic schemes and their corre-

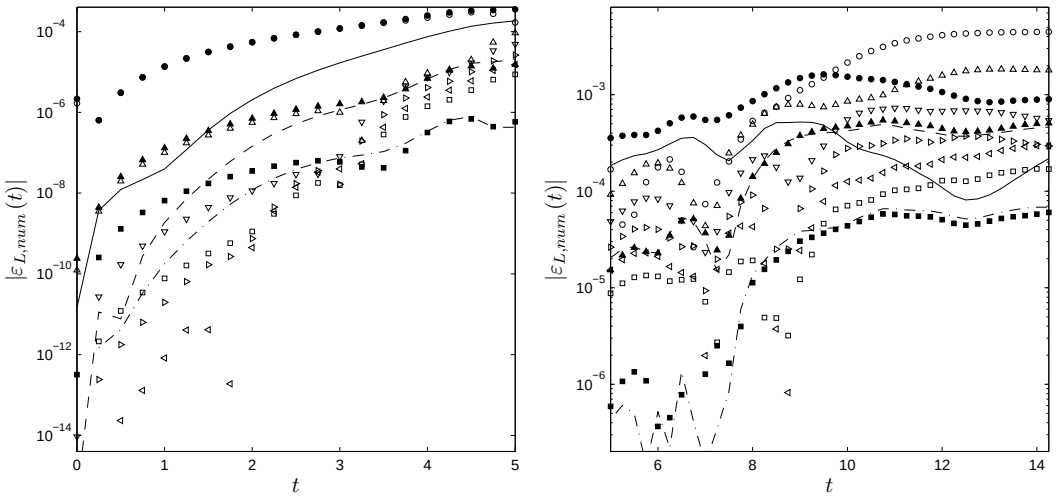

Figure 8.13: A posteriori results on Taylor-Green Vortex. Numerical errors on the longitudinal integral length scale ε_L, in the laminar Taylor-Green Vortex flow, i.e. $0 \leq t \leq 5$ (**left**) and the transitional and turbulent Taylor-Green flow, i.e. $5 \leq t \leq 14.25$ (**right**). (Symbols: see Table 8.1)

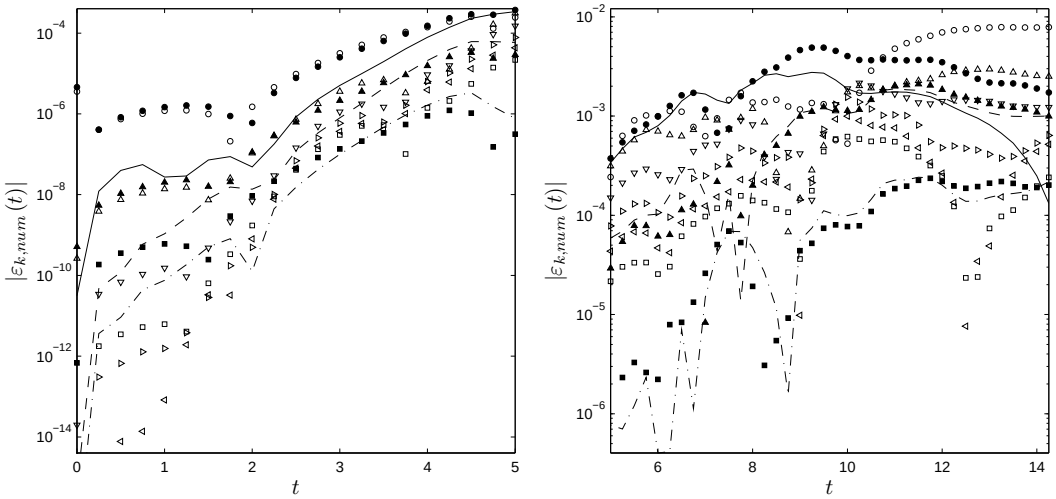

Figure 8.14: A posteriori results on Taylor-Green Vortex. Numerical errors on the kinetic energy ε_k, in the laminar Taylor-Green Vortex flow, i.e. $0 \leq t \leq 5$ (**left**) and the transitional and turbulent Taylor-Green flow, i.e. $5 \leq t \leq 14.25$ (**right**). (Symbols: see Table 8.1)

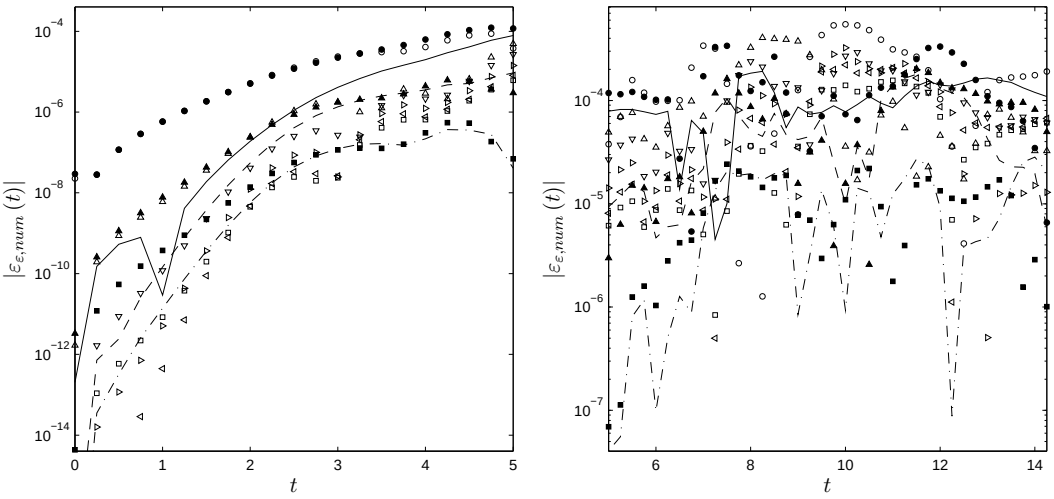

Figure 8.15: A posteriori results on Taylor-Green Vortex. Numerical errors on the dissipation rate ε_ε, in the laminar Taylor-Green Vortex flow, i.e. $0 \leq t \leq 5$ (**left**) and the transitional and turbulent Taylor-Green flow, i.e. $5 \leq t \leq 14.25$ (**right**). (Symbols: see Table 8.1)

sponding static DRP equivalents, compared to the standard asymptotic schemes. While a similar behaviour might be distinguished for the error on the kinetic energy, the largely fluctuating error-results on the dissipation rate remain inconclusive.

As mentioned before, the numerics and modeling are completely entwined in Large-Eddy Simulations, especially when using more advanced subgrid models such as the dynamic model. Although in the previous discussion a clear numerical improvement is shown for more accurate finite difference errors, it does not indicate whether a better numerical approximation of the model will lead to a better overall performance. Therefore, the total numerical errors are investigated, that is the combination of the numerical errors and the modeling errors on the physics-related quantities. The total errors on the longitudinal integral length scale and the kinetic energy for the transitional Taylor-Green flow at $t \geq 5s$ are shown in Figure 8.16. In accordance with the results of Meyers *et al.* [60, 59], contingent cancellation of numerical errors and modeling errors are witnessed for certain finite difference schemes. Nevertheless, these cancellations depend on the specific quantity which is examined. For instance, the 2^{nd} -order standard scheme leads to the largest errors on the longitudinal integral length scale in case the Taylor-Green flow is fully turbulent, whereas it gives the smallest errors for the kinetic energy in that interval. However, both error graphs indicate that the 4^{th} -order scheme produces almost the best results, whereas the implicit standard or Dispersion-Relation Preserving Padé schemes do not perform as well. Therefore, it is unfeasible to draw any sound conclusion from these plots, except that cancellation may occur rather occasionally

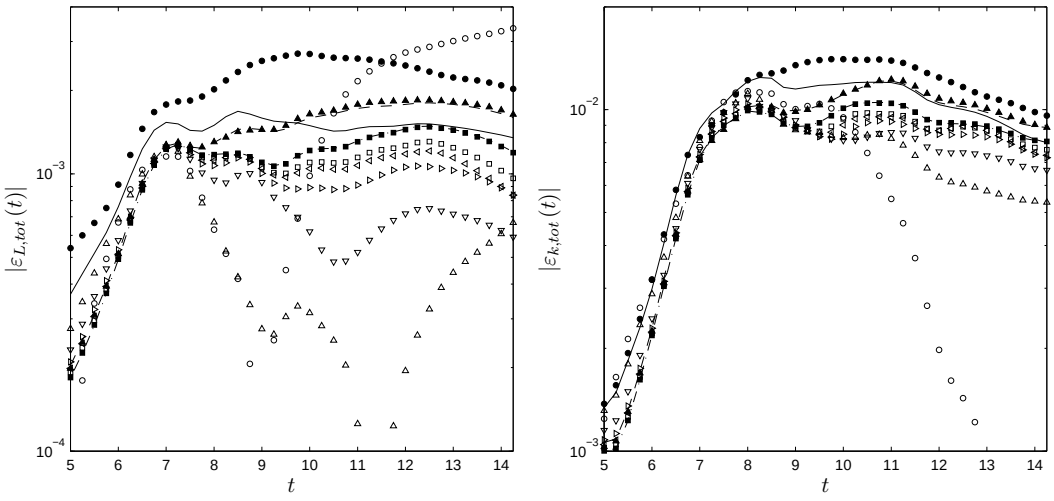

Figure 8.16: A posteriori results on Taylor-Green Vortex. Total errors on the longitudinal integral length scale ε_L (**left**) and the kinetic energy (**right**) ε_k, in the Taylor-Green Vortex flow. (Symbols: see Table 8.1)

than systematically.
Despite the fact that numerical errors and modeling errors interfere, highly accurate numerical schemes for LES are believed to be necessary in order to properly apply the subgrid models that rely on good small scale information, rather than on contingent cancellation of different error sources.

8.6 Computational Cost

Although the results of the linear dynamic finite difference schemes are very promising, the *current implementation* of the method requires the calculation of approximately 42 dynamic coefficients, leading inevitably to a significant computational overhead. It was found for the Large-Eddy Simulation of the Taylor-Green Vortex, that the *total computational time* was about 68% higher for the dynamic schemes in comparison with the DRP schemes and the standard schemes. Despite the very good performance of the dynamic schemes, an overhead of 68% may be considered prohibitive for practical industrial computations. Nevertheless, this premature conclusion must be placed in perspective. In the current work, the dynamic finite difference schemes were implemented straightforwardly and rigorously. This implies that each of the 42 dynamic coefficients were calculated at each Runge-Kutta step, that is 4 times per time step. However, it might sufficient to calculate each dynamic coefficient only once per time step, or even once per few time steps, depending on the time increment Δt. Indeed, since the time scale ratio $\theta = \Delta t/\tau_\eta$ must be chosen sufficiently small in order to avoid numerical dissipation, one can expect that the flow physics do not change much during one time step. Hence, evaluating

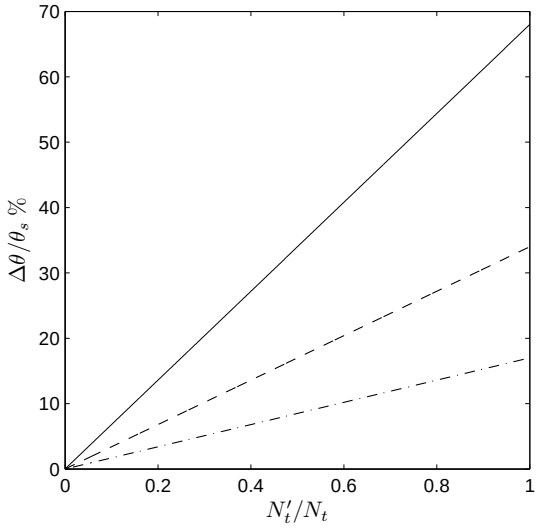

Figure 8.17: Computational overhead for the Large-Eddy Simulation of the Taylor-Green Vortex flow. Reduction of the computational overhead as function of $\frac{N_t'}{N_t}$ for $\frac{q'}{q} = 1$ (——), $\frac{q'}{q} = \frac{1}{2}$ (− − −) and $\frac{q'}{q} = \frac{1}{4}$ (−·−·) assuming $N_c' = N_c$.

the coefficients each θ time steps might be sufficient, e.g. in the current study, every 10 time steps. Moreover, the proposed number of 42 dynamic coefficient may be reduced, saving again some computational cost. These strategies are illustrated hereafter.

Consider the variable θ_s, which indicates the required CPU-time per Runge-Kutta step for a Large-Eddy Simulation, using a finite difference method with *predefined* stencil coefficients. Similarly consider the variable θ_d, which indicates the required CPU-time per Runge-Kutta step for a Large-Eddy Simulation using a finite difference method with *dynamic*, real-time calculated stencil coefficients. Then, $\Delta\theta = \theta_d - \theta_s$ represents the computational overhead for the calculation of N_c dynamic coefficients per Runge-Kutta step. Further, assume a q-stage Runge-Kutta method for the time-integration of the Large-Eddy Simulation over N_t time steps. The computational CPU-time per Runge-Kutta step θ_d can now be expressed as function of θ_s, i.e.

$$\theta_d = \theta_s + \Delta\theta \frac{q'}{q} \frac{N_t'}{N_t} \frac{N_c'}{N_c}, \tag{8.26}$$

where the ratio q'/q determines the number of evaluations per q stages, N_t'/N_t determines the total number of evaluations per N_t time steps, and N_c'/N_c determines the number of coefficients on a total of N_c that are calculated. Figure 8.17 illustrates the reduction of the computational overhead for the Large-Eddy Simulation of the Taylor-Green Vortex flow in the current dissertation with $q = 4$,$N_t = 2850$ and

$N_c = 42$, assuming $N_c' = N_c$. For example, if all dynamic coefficients ($\frac{N_c'}{N_c} = 1$) are evaluated only once every 2 time steps, i.e. $\frac{q'}{q} = \frac{1}{4}$ and $\frac{N_t'}{N_t} = \frac{1}{2}$, the computational overhead is only 8.5%, which is a substantial reduction compared to the original 68%. If all dynamic coefficients are only evaluated every $\theta = 10$ time steps ($\frac{q'}{q} = \frac{1}{4}$ and $\frac{N_t'}{N_t} = \frac{1}{10}$), i.e. after dissipative time scale τ_η, the overhead is only 1.7%. Moreover, if one evaluates only a fraction of the dynamic coefficients and adjust the others as soon as the change of the monitored coefficient becomes significant, then the computational overhead might be reduced even more. Obviously, the various strategies make the dynamic schemes relatively cheap compared to their excellent quality, such that they are competitive with the Dispersion-Relation Preserving schemes. Such strategies will be investigated in more detail in future work.

8.7 Conclusions and Discussion

In the current chapter, the potential of the linear dynamic finite difference approximations was demonstrated for the Large-Eddy Simulation of the Taylor-Green Vortex flow. The main conclusions that were obtained for the Large-Eddy Simulation of Burgers' turbulence also hold for the Large-Eddy Simulation of the more realistic Taylor-Green turbulence. It was observed again that the linear dynamic finite difference approximations seamlessly adapt according to the instantaneous properties of the flow, leading to a quasi-optimal finite difference technique that achieves a significant accuracy improvement compared to the standard asymptotic schemes. More specific, at the early stages of the simulation, the dynamic schemes recover the asymptotic order of accuracy of the standard schemes, which is optimal since the flow is well resolved with DNS-resolution. In contrast, the Dispersion-Relation Preserving schemes are suboptimal if the flow is well-resolved. Once the resolution becomes inadequate to resolve all scales of motion in the (still laminar) flow, the dynamic schemes adapt according to the resolved physics. Moreover, it was shown in the a priori study that the scheme was certainly sensitive to anisotropy in the flow, which could be an additional advantage for the simulation of more complex flows. Once the flow is fully turbulent, the dynamic schemes perform similarly to the Dispersion-Relation Preserving schemes by minimizing the magnitude of the dispersion errors in the flow. These conclusions confirm that the dynamic schemes are certainly viable for numerically accurate Large-Eddy Simulations of turbulent flows. Although the method is still confined to the relatively simple periodic Taylor-Green Vortex flow, it is expected to be useful for more complex flows in more complex geometries. However, for such flows, it might be necessary to limit the value of the dynamic coefficient to a predefined value, in order to prevent possible suboptimal behaviour. Finally, it was observed that the computational overhead of the dynamic finite difference schemes is significant if all dynamic coefficients are evaluated at each Runge-Kutta step. In order to alleviate this problem, a strategy was proposed that could reduce the overhead to only a few percents of the total simulation time. This strategy will be further investigated in future work.

To know that we know what we know, and to know that we do not know what we do not know, that is true knowledge.

Copernicus, Nicolaus

9

Synthesis and Conclusions

In the current dissertation, a novel family of *dynamic* finite difference schemes was developed which allow numerically accurate Large-Eddy Simulations of turbulent flows. The main philosophy behind these dynamic finite difference schemes is to achieve an optimal accuracy for all resolved scales of motion in the flow, rather than focusing only on the asymptotic order of accuracy for the largest resolved scales. This approach implies that the dynamic finite difference approximations minimize the total magnitude of the truncation error and thus preserve the global dispersion relation for all Fourier modes in the entire wavenumber range. The construction of the dynamic finite difference approximations relies on the determination of an optimal value for the preceding coefficient in the discretized leading order truncation term by means of a sampling-based dynamic procedure. Although this procedure was originally proposed in [89, 88, 22, 46] for modeling purposes, it is successfully applied here in a new, alternative way. Indeed, in the new sampling-based dynamic procedure, the Taylor series expansions of any basic finite difference approximation are compared on two different grid resolutions. The method allows to extract a nearly optimal value for the coefficient in the leading order truncation term, provided that a blending factor f is predefined, which regulates the sensitivity of the procedure to the small scales in the resolved flow and can thus be seen as a calibration parameter for the resulting dynamic scheme.

After clarifying the motivation for the current work in Chapter 1, an elaborate discussion on the physical problem definition and the mathematical constraints, which form the basic challenge in this work, was conducted in Chapters 2 and 3. The various standard numerical methods, that are typically used in LES, were in-

troduced in Chapter 4 and an appraisal of these techniques was given. Further, Chapter 5 provided a preliminary investigation into the ability of the new sampling-based dynamic procedure for obtaining higher accuracy. In order to minimize the global magnitude of the truncation error, an optimal dynamic coefficient was determined for each partial differential equation. The proposed approach succeeded in obtaining a significant accuracy improvement for the simple numerical simulation of a two-dimensional laminar cavity flow (Re = 400). Although the results were found to be very promising and encouraging, it was argued that refining the proposed approach, by applying it to each derivative separately instead of to the entire partial differential equation, might be beneficiary. This lead to the development of the dynamic finite difference approximations presented in the subsequent chapters.

Chapter 6 was devoted to the construction of a family of dynamic low-dispersive finite difference approximations for an arbitrary partial derivative. An explicit and implicit family of dynamic low-dispersive finite difference approximations was constructed by combining Taylor series expansions on two different grid resolutions. Moreover, a *linear* and a *nonlinear* variant were derived from the averaging procedure, used in the sampling-based dynamic procedure. The accuracy of the constructed schemes was thoroughly analyzed in Fourier space by means of the modified wavenumbers. Since one of these variants is nonlinear, a multiple-wave Fourier analysis of the transfer function is done in analogy with the work of [27]. The analytically obtained Fourier characteristics clearly revealed the large potential of the linear dynamic finite difference approximations, whereas for the nonlinear variant, the present study indicated some fundamental shortcomings due to the production of spurious scales. The constructed dynamic schemes involve a blending factor f, that regulates the sensitivity of the procedure to the smallest resolved scales and for which an appropriate value must be predefined. By adopting a *generic* energy spectrum of the resolved flow field, a procedure was proposed to retrieve the optimal value of the blending factor. Due to the assumption of the generic energy spectrum for turbulent flows, this optimal value might be considered as applicable for a wide range of Large-Eddy Simulations of turbulent flows.
Although the developed dynamic schemes share similarities with the *prefactored* Dispersion-Relation Preserving schemes of e.g. *Tam et al.* [79], Kim *et al.* [45] and many others [37, 2, 6], their behaviour is more refined. Indeed, the stencil-coefficients of the developed dynamic finite difference approximations are *dynamically adapted* during the simulation through the dynamic coefficient, which is determined according to the characteristics of the resolved flow field. As a consequence, the Fourier characteristics of the dynamic finite difference approximations are adjusted during the simulation such that the global dispersion error for the resolved flow field is minimized. This is in contrast with the prefactored Dispersion-Relation-Preserving schemes, which have predefined Fourier characteristics.

The developed dynamic finite difference approximations, and their numerical

quality, have been extensively investigated for the Large-Eddy Simulation of Burgers' turbulence in Chapter 7 and the Large-Eddy Simulation of the Taylor-Green vortex flow at Re = 1500 in Chapter 8.
The quality assessment on Burgers' turbulence, which is considered as a surrogate model for real turbulence, allowed examining the dynamic schemes rigorously and unambiguously in the context of LES and DNS. Indeed, similarly to Navier-Stokes turbulence, Burgers' turbulence exhibits an inertial range in the energy spectrum, although the small-scale dynamics of Burgers turbulence and real turbulence are substantially different. Nevertheless, Large-Eddy Simulation of such a one-dimensional flow is perfectly suited for the evaluation of the dynamic schemes. Besides the quality-assessment in an a priori study, the performance was examined in an a posteriori study using a perfect subgrid scale model and a dynamic Smagorinsky-like model. The obtained results confirmed the theoretical findings. It was concluded that the excellent performance of the *linear* dynamic schemes might be advantageous for numerically accurate Large-Eddy Simulations of turbulent flows. In contrast, the *nonlinear* dynamic schemes were found to be inappropriate for LES, due to the production of spurious numerical scales. These spurious scales were seen to be distributed along the entire wavenumber range, and strongly affected the accuracy of the solution.
As a consequence of the latter conclusion, only the performance of the *linear* dynamic finite difference approximations was assessed in Chapter 8 for the Large-Eddy Simulation of the three-dimensional Taylor-Green vortex flow at Re = 1500. This flow is considered to describe the fundamental process of transition into turbulence, since the initial laminar large scale vortex grinds down into successively smaller scales, eventually leading to nearly isotropic turbulence. Hence, such a flow is challenging for the quality assessment of the linear dynamic finite difference schemes, since they must continuously adapt to the changing flow. The results were found to be very similar to those obtained in the Burgers' turbulence.

The main conclusions on the quality of the developed *linear* dynamic finite difference schemes for the Large-Eddy Simulation of Burgers' turbulence and the Large-Eddy Simulation of the Taylor-Green vortex flow at Re = 1500 are enlisted below.

i. First it is concluded that the linear dynamic schemes systematically recover their potential asymptotic order of accuracy, regardless of the value of the blending factor f, provided that all scales of motion in the flow field are very well resolved on the computational grid. This implicates that the grid resolution is at least 8 times smaller then the smallest resolved scales in the laminar or turbulent flow field. Hence, the linear dynamic finite difference approximations adapt according to the smooth solution of the flow, focusing on maximum accuracy of the largest resolved scales. Obviously, this is an advantage over the Dispersion-Relation Preserving schemes which remain suboptimal in that case, since they are designed a priori for non-smooth solutions on the computational grid.

ii. Once the resolution becomes inadequate to represent well all scales of motion in the laminar or turbulent flow, the linear dynamic schemes adjust the dynamic coefficient according to the flow solution on the computational grid. The sensitivity with witch the linear dynamic scheme responds to small scale information in the energy spectrum is predefined by the blending factor f. Since the blending factor merely calibrates the linear dynamic scheme to be optimal for a fully developed turbulent flow, characterized by the Kolmogorov inertial range spectrum, it is expected to be applicable for a wide range of turbulent flows. Further, the Fourier characteristics of the dynamic finite difference approximation are adapted such that the global dispersion error in the entire wavenumber range up to the filter cutoff is minimized. This corresponds to the minimization of the magnitude of the Taylor series that determines the entire truncation error.

iii. As soon as the flow is fully turbulent and the energy spectrum exhibits an inertial range, both the linear dynamic finite difference schemes and the Dispersion-Relation Preserving schemes perform very similar. In some cases, the dynamic finite difference schemes tend to perform even better. In order to guarantee the quality, it is recommendable to guard the value of the dynamic coefficient during the simulation such that it does not exceed the coefficient of the static dispersion-relation preserving schemes.

iv. Further, it was observed that the dynamic finite difference scheme is sensitive to the anisotropy of the resolved flow field in the Large-Eddy Simulation of the Taylor-Green vortex. This could be a particularly interesting feature for the Large-Eddy Simulation of more complex and anisotropic flows, or for grids with strongly different resolutions in each direction.

v. Finally, despite the substantial improvement in numerical accuracy obtained by the linear dynamic finite difference schemes and other high-order schemes, these schemes do not necessarily provide a more accurate solution of the Large-Eddy Simulation. Indeed, in comparison with more accurate numerical schemes, less accurate methods can lead to advantageous cancellation between numerical errors and modeling errors, resulting into a reduction of the total errors. These observations confirm the results in [60, 59, 61]. Although it is tempting to resign to application of lower order discretizations in combination with dissipative models, trusting upon contingent cancellation of errors, the present work rather advocates to develop better models in combination with highly-accurate discretizations such that both numerical errors and modeling errors are controlled more systematically.

The former conclusions confirm that the developed family of dynamic finite difference approximations may provide a useful and viable tool for numerically accurate Large-Eddy Simulations of turbulent flows. Although the current implementation required a significant computational overhead, a strategy for reducing the compu-

tational overhead was suggested and illustrated in Chapter 8. The computational overhead of the dynamic schemes in a few illustrated strategies was estimated to be only a few percents larger than the prefactored schemes. Nevertheless, the present work was mainly intended to provide a proof of concept, rather than an assessment on the feasibility of the developed technique in an industrial environment.

It's hard to make predictions, especially about the future.

Bohr, Niels

10 Future Perspectives

Although in this work the quality assessment on the developed dynamic finite difference method was constrained to the relatively simple periodic Burgers' turbulence and Taylor-Green vortex flow, it is expected to be equally accurate and viable for the Large-Eddy Simulation of more complex flows in more complex geometries.[1] However, this requires further research and development on several aspects of the presented method.

First, a following necessary evolution of the current work involves the extension of the dynamic finite difference approximations to non-uniform computational grids. If the computational grid is *structured*, then the method can easily be extended by transforming the Navier-Stokes equations from the non-uniform grid to the uniform grid using the Jacobian transformation $T_{\mathbf{x}\rightarrow\boldsymbol{\xi}}$, $\mathbf{x}, \boldsymbol{\xi} \in \mathbb{R}^3$. This approach, discussed in Section 2.4.1, is often applied to Large-Eddy Simulations [82, 29]. On the other hand, if the computational grid is *unstructured*, so that no such transformation is possible, the construction of the schemes requires direct inclusion of the metrics of the unstructured grid in the stencil definition of the schemes. This inevitably leads to an increased complexity. Note that in principle, the extension of the dynamic schemes toward more general grids is no different than that of traditional prefactored high-order schemes. Moreover, special care must be taken for guaranteeing the conservation properties of the schemes.

[1] Note that these expectations follow from the good results obtained in the laminar lid driven cavity in Chapter 5. Moreover, this test case clearly indicates that the dynamic method is not restricted to Large-Eddy Simulations.

In addition to the previous topic, an appropriate boundary treatment must be defined for the dynamic finite difference approximations in case of non-periodic computational domains. Since the basic stencils of the dynamic schemes are in principle no different than those of prefactored schemes, except for their variable coefficients, the same approaches may be considered as discussed in Section 4.1.5. Only the evaluation of higher derivatives in the expression for the dynamic coefficient at the boundaries may impose some additional difficulties. However, since the constant dynamic coefficients are averaged over the entire domain, it might be sufficient to evaluate them only in the interior domain, away from the boundaries. Nevertheless, such a hypothesis requires further investigation.

Besides these primary research topics described above, it may be interesting and worthwhile to investigate more efficient implementations of the dynamic finite difference schemes, as suggested in Chapter 8. Moreover, evaluation of the constant dynamic coefficient in the conservative formulation of the *linear* dynamic finite difference schemes (see Appendix B), may preclude the need of higher derivatives and thus reduce the complexity and the computational cost.

Les mathématiques comparent les phénomènes les plus divers et découvrent les analogies secrètes qui les unissent.

Fourier, Joseph

A Fourier Transformations

The purpose of this appendix is to provide the definition and the main properties of the general Fourier transformation, which is extensively used in the current dissertation.

A.1 Definition

Consider the continuous function $f(\mathbf{x}), \mathbf{x} \in \mathbb{R}^3$. The the definition of the Fourier transform, adopted in this work,[1] is then given by

$$\widehat{f}(\boldsymbol{\kappa}) = \mathscr{F}\{f(\mathbf{x})\} = \frac{1}{(2\pi)^3} \iiint_{-\infty}^{\infty} f(\mathbf{x})\, e^{-i\boldsymbol{\kappa}\mathbf{x}} d\mathbf{x}, \tag{A.1}$$

where $\boldsymbol{\kappa} \in \mathbb{R}^3$ denotes the wavenumber vector in Fourier space.[2] The inverse Fourier transform is now defined as

$$f(\mathbf{x}) = \mathscr{F}^{-1}\left\{\widehat{f}(\boldsymbol{\kappa})\right\} = \iiint_{-\infty}^{\infty} \widehat{f}(\boldsymbol{\kappa})\, e^{i\boldsymbol{\kappa}\mathbf{x}} d\boldsymbol{\kappa}. \tag{A.2}$$

The functions $f(\mathbf{x})$ and $\widehat{f}(\boldsymbol{\kappa})$ are said to form a Fourier transform pair if the above integrals converge. The exact form of the Fourier transform pair is determined by the properties of the function $f(\mathbf{x})$.

[1] Note that other definitions are possible. However, for further explanation the reader may refer to the work of e.g. Bracewell [7].

[2] The definition of the Fourier transform pair in the time domain $t \in \mathbb{R}$ and the frequency domain $\omega \in \mathbb{R}$ are analogous.

i. If $f(\mathbf{x})$, $\mathbf{x} \in \mathbb{R}^3$ is a *continuous aperiodic* function, then the Fourier transform $\widehat{f}(\boldsymbol{\kappa})$, $\boldsymbol{\kappa} \in \mathbb{R}^3$ is also a *continuous aperiodic* function.

ii. However, if $f(\mathbf{x})$, $\mathbf{x} \in \mathbb{R}^3$ is a *continuous periodic* function with period $\mathscr{L}_j$ in the directions $j = 1, 2, 3$, then the analytical expression of the Fourier transform $\widehat{f}(\boldsymbol{\kappa})$, $\boldsymbol{\kappa} \in \mathbb{R}^3$ consists of an infinite sum of *Dirac* delta-functions. Hence, the Fourier transform corresponds to a *discrete aperiodic* function $\widehat{f}(\boldsymbol{\kappa})$ in which, $\boldsymbol{\kappa} = 2\pi k/\mathscr{L}_j$, $k \in \mathbb{Z}^3$. This property allows to write any *continuous periodic* function $f(\mathbf{x})$ as the infinite sum of discrete waves, called the Fourier series, such that

$$f(\mathbf{x}) = \sum_{\boldsymbol{\kappa}} \widehat{f}(\boldsymbol{\kappa}) e^{i\boldsymbol{\kappa}\mathbf{x}}. \tag{A.3}$$

The former properties were derived under the assumption that $f(\mathbf{x})$ is a *continuous function*. In case $f(\mathbf{x})$ is a *discrete function*, the former conclusions are still valid, except that the Fourier transform $\widehat{f}(\boldsymbol{\kappa})$ is now a *periodic function* instead of an *aperiodic* function. This forms the basis for the *Nyquist-Shannon sampling theorem*, which is thoroughly discussed in Section 2.4.2. Summarizing, an aperiodic (periodic) function corresponds to a continuous (discontinuous) function and vice versa under the Fourier transform.

A.2 PROPERTIES

The most important relations between the functions $f(\mathbf{x})$ and $\widehat{f}(\boldsymbol{\kappa})$ of the Fourier transform pair are summed below.

i. Since $f(\mathbf{x})$ is a real function, $\widehat{f}(\boldsymbol{\kappa})$ has *conjugate symmetry* such that

$$\widehat{f}(\boldsymbol{\kappa}) = \widehat{f}^*(-\boldsymbol{\kappa}). \tag{A.4}$$

ii. The Fourier transform is a *linear operator*, such that

$$\mathscr{F}\{a \cdot f(\mathbf{x}) + b \cdot g(\mathbf{x})\} = a\mathscr{F}\{f(\mathbf{x})\} + b\mathscr{F}\{g(\mathbf{x})\}. \tag{A.5}$$

iii. The Fourier transform pair obeys the following *scaling property*

$$\mathscr{F}\{f(a\mathbf{x})\} = \frac{1}{|a|}\widehat{f}\left(\frac{\boldsymbol{\kappa}}{a}\right). \tag{A.6}$$

iv. The Fourier transform of the n^{th} derivative of a function is defined as

$$\mathscr{F}\left\{\frac{\partial^n f(\mathbf{x})}{\partial x_j^n}\right\} = i^n \kappa_j^n \widehat{f}(\boldsymbol{\kappa}). \tag{A.7}$$

v. *Multiplication property:* the Fourier transform of the product of two functions equals the convolution of the Fourier transforms of the functions, or

$$\mathscr{F}\left\{f\left(\mathbf{x}\right)\cdot g\left(\mathbf{x}\right)\right\}=\mathscr{F}\left\{f\left(\mathbf{x}\right)\right\}*\mathscr{F}\left\{g\left(\mathbf{x}\right)\right\}. \tag{A.8}$$

vi. *Convolution property:* the Fourier transform of the convolution of two functions is equal to the product of $(2\pi)^3$ and the Fourier transform of the functions, i.e.

$$\mathscr{F}\left\{f\left(\mathbf{x}\right)*g\left(\mathbf{x}\right)\right\}=(2\pi)^3\,\mathscr{F}\left\{f\left(\mathbf{x}\right)\right\}\cdot\mathscr{F}\left\{g\left(\mathbf{x}\right)\right\}. \tag{A.9}$$

vii. *Parseval's theorems.* Parseval's *first* theorem, applied to real functions, states that

$$\iiint_{-\infty}^{\infty} f\left(\mathbf{x}\right)g\left(\mathbf{x}\right)d\mathbf{x}=(2\pi)^3\iiint_{-\infty}^{\infty}\widehat{f}\left(\boldsymbol{\kappa}\right)\widehat{g}^{*}\left(\boldsymbol{\kappa}\right)d\boldsymbol{\kappa}. \tag{A.10}$$

The *second* theorem is a specific case of the first theorem and states

$$\iiint_{-\infty}^{\infty} f\left(\mathbf{x}\right)^2 d\mathbf{x}=(2\pi)^3\iiint_{-\infty}^{\infty}\widehat{f}\left(\boldsymbol{\kappa}\right)\widehat{f}^{*}\left(\boldsymbol{\kappa}\right)d\boldsymbol{\kappa}. \tag{A.11}$$

The law of conservation of energy tells us we can't get something for nothing, but we refuse to believe it.

Asimov, Isaac

B

Conservative dynamic finite difference approximations

All linear finite difference schemes, including the linear dynamic scheme, are a priori conservative since they can be rewritten as the discrete divergence of a certain (higher-order) approximation of the velocity field. This approximation $\overline{u}_a$ is then defined in finite difference context as

$$\overline{\frac{\partial^n u}{\partial x^n}}(x) = \frac{\delta^n \overline{u}_a}{\delta x^n} = \frac{\delta^n}{\delta x^n}\left(\overline{u} + c_k \Delta^k \overline{\frac{\delta^k u}{\delta x^k}} + \mathcal{O}\left(\Delta^{k+2}\right)\right) \tag{B.1}$$

in which the central discrete derivate $\frac{\delta^n}{\delta x^n}$ should have the minimal stencil width, corresponding with the 2^{nd} -order central approximation. The conditions for which a compact discretization is achieved by successive discrete differentiation, were already discussed in section 4.3.2. $\overline{u}_a$ is considered a higher-order reconstruction of the velocity field by Taylor series expansion. It is verified that for the linear schemes, the divergence and non-divergence formulations are equal on a discrete level. However, it can be understood that the nonlinear scheme is not written in an a priori conservative formulation because the dynamic coefficient is pointwise varying. This can be remedied by taking the divergence of a low-dispersive dynamic reconstruction definition. Consider the general definition

$$\overline{u}_a(x) = \overline{u} + c_k \Delta^k \overline{\frac{\delta^k u}{\delta x^k}} + \mathcal{O}\left(\Delta^k\right) \tag{B.2}$$

The general dynamic coefficient is now extracted from this definition as

$$c_k^{dyn} = c_k^* \frac{\left\langle \left| \frac{\delta^k \overline{u}}{\delta x^k} \right|^{\Delta^2} - \frac{\alpha^k \left(1-\alpha^2\right)}{1-\alpha^k} f c_k^{**} \Delta^2 \left| \frac{\delta^{k+2} \overline{u}}{\delta x^{k+2}} \right|^{\Delta} \left| \frac{\delta^k \overline{u}}{\delta x^k} \right|^{\Delta} \right\rangle_w}{\left\langle \left(\left| \frac{\delta^k \overline{u}}{\delta x^k} \right|^{\Delta} - \frac{\alpha^k \left(1-\alpha^2\right)}{1-\alpha^k} f c_k^{**} \Delta^2 \left| \frac{\delta^{k+2} \overline{u}}{\delta x^{k+2}} \right|^{\Delta} \right)^2 \right\rangle_w}, \tag{B.3}$$

where the averaging domain is denoted by the parameter w. If the averaging domain w equals the entire computational domain, the coefficient of the linear dynamic finite difference approximation should be recovered. On the other hand, if the averaging domain consists of a box with length Δ, then the nonlinear dynamic coefficient is retrieved as

$$c_k^{dyn} = -\frac{\mathscr{L}}{\mathscr{M}} = \frac{c_k^*}{1 - \frac{\alpha^k \left(1-\alpha^2\right)}{1-\alpha^k} \Delta^2 f c_k^{**} \frac{\left| \frac{\delta^{k+2} \overline{u}}{\delta x^{k+2}} \right|^{\Delta}}{\left| \frac{\delta^k \overline{u}}{\delta x^k} \right|^{\Delta}}}. \tag{B.4}$$

Taking the divergence of this dynamic reconstruction series gives the conservative formulation of the nonlinear dynamic scheme. The constants c_k^* and c_k^{**} remain those of the non-conservative formulation. This way the modified wavenumbers of the conservative and non-conservative formulation are identical, and thus the expected accuracy should be preserved. However, in case of the linear dynamic finite difference approximation, the value of the blending factor f in the conservative or original formulation is not necessarily identical. Remark that calculation of the dynamic coefficient from the conservative formulation is advantageous, since the derivatives have more compact stencils, leading to less computational cost.

Setting an example is not the main means of influencing others, it is the only means.

Einstein, Albert

C

A selection of dynamic finite difference approximations

The present appendix, describes in more detail, a selection of four dynamic finite difference approximations: the 2^{nd} - and 4^{th} -order explicit linear dynamic finite difference approximations, the 2^{nd} -order explicit non-linear finite difference approximations and the 4^{th} -order implicit linear dynamic finite difference approximation. Note that hereafter, the coarse resolution is chosen twice the fine resolution such that $\alpha = 2$.

C.1 Second-order Explicit Dynamic Finite Difference Approximation

C.1.1 The first derivative

The basic expression for both the linear and non-linear dynamic finite difference approximations of the first derivative in a node $\overline{u}(x_i) = \overline{u}_i$ is given by

$$\overline{\frac{\partial u}{\partial x}}(x) = \frac{\delta \overline{u}}{\delta x} + c_1^{dyn} \Delta^2 \frac{\delta^3 \overline{u}}{\delta x^3}. \tag{C.1}$$

n	β_0	$\pm\beta_{\pm1}$	$\pm\beta_{\pm2}$	$\pm\beta_{\pm3}$	$\pm\beta_{\pm4}$	k
1	0	$-c_1^{dyn}+\frac{1}{2}$	$\frac{1}{2}c_1^{dyn}$			2
3	0	-1	$\frac{1}{2}$			2
5	0	$\frac{5}{2}$	-2	$\frac{1}{2}$		2

Table C.1: Explicit 2^{nd} -order dynamic scheme. Explicit 2^{nd} -order dynamic finite difference approximation for the 1^{st} -order derivative ($n = 1$). Note that $\beta_i = -\beta_{-i}$.

For the linear dynamic finite difference approximation, the constant coefficient c_1^{dyn} is calculated with expression (6.20), leading to

$$c_1^{dyn} = c_1^* \frac{\left\langle \left(\frac{\delta^3\overline{u}}{\delta x^3}\right)^2 - 4fc_1^{**}\Delta^2\left(\frac{\delta^5\overline{u}}{\delta x^5}\right)\left(\frac{\delta^3\overline{u}}{\delta x^3}\right)\right\rangle}{\left\langle \left(\frac{\delta^3\overline{u}}{\delta x^3} - 4fc_1^{**}\Delta^2\frac{\delta^5\overline{u}}{\delta x^5}\right)^2\right\rangle}, \tag{C.2}$$

whereas for the non-linear dynamic finite difference approximation, the constant coefficient c_1^{dyn} is calculated with expression (6.21), leading to

$$c_1^{dyn} = \frac{c_1^*}{1 - 4\Delta^2 fc_1^{**}\dfrac{\overline{\dfrac{\delta^5\overline{u}}{\delta x^5}}}{\overline{\dfrac{\delta^3\overline{u}}{\delta x^3}}}}. \tag{C.3}$$

From Taylor expansion the values $c_1^* = -\frac{1}{6}$ and $c_1^{**} = -\frac{1}{4}$ are obtained. The discretization stencil for the basic scheme as well as for the derivatives in the calculation of the dynamic coefficient are given in Table C.1 Note that the current formulation of the non-linear derivatives is not conservative. However, Appendix B describes how to construct a conservative variant of this formulation.

C.1.2 The second derivative

The basic expression for both the linear and non-linear dynamic finite difference approximation of the second derivative in a node $\overline{u}(x_i) = \overline{u}_i$ is given by

$$\overline{\frac{\partial^2 u}{\partial x^2}}(x) = \frac{\delta^2\overline{u}}{\delta x^2} + c_2^{dyn}\Delta^2\frac{\delta^4\overline{u}}{\delta x^4}. \tag{C.4}$$

n	β_0	$\beta_{\pm1}$	$\beta_{\pm2}$	$\beta_{\pm3}$	$\beta_{\pm4}$	k
2	$6c_2^{dyn}-2$	$1-4c_2^{dyn}$	c_2^{dyn}			2
4	6	-4	1			2
6	-20	15	-6	1		2

Table C.2: Explicit 2^{nd} -order dynamic scheme. Explicit 2^{nd} -order dynamic finite difference approximation for the 2^{nd} -order derivative ($n = 2$). Note that $\beta_i = \beta_{-i}$.

For the linear dynamic finite difference approximation, the constant coefficient c_2^{dyn} is calculated with expression (6.20), leading to

$$c_2^{dyn} = c_2^* \frac{\left\langle \left(\frac{\delta^4\overline{u}}{\delta x^4}\right)^2 - 4fc_2^{**}\Delta^2\left(\frac{\delta^6\overline{u}}{\delta x^6}\right)\left(\frac{\delta^4\overline{u}}{\delta x^4}\right)\right\rangle}{\left\langle \left(\frac{\delta^4\overline{u}}{\delta x^4} - 4fc_2^{**}\Delta^2\frac{\delta^6\overline{u}}{\delta x^6}\right)^2\right\rangle}, \tag{C.5}$$

whereas for the non-linear dynamic finite difference approximation, the constant coefficient c_1^{dyn} is calculated with expression (6.21), leading to

$$c_2^{dyn} = \frac{c_2^*}{1 - 4\Delta^2 fc_2^{**}\dfrac{\overline{\dfrac{\delta^6\overline{u}}{\delta x^6}}}{\overline{\dfrac{\delta^4\overline{u}}{\delta x^4}}}}. \tag{C.6}$$

From Taylor expansion the values $c_2^* = -\frac{1}{12}$ and $c_2^{**} = -\frac{1}{6}$ are obtained. The discretization stencil for the basic scheme as well as for the derivatives in the calculation of the dynamic coefficient are given in Table C.2 Note that the current formulation of the non-linear derivatives is not conservative. However, Appendix B describes how to construct a conservative variant of this formulation.

C.2 Fourth-order Explicit Dynamic Finite Difference Approximation

C.2.1 The first derivative

The basic expression for the dynamic finite difference approximation of the first derivative in a node $\overline{u}(x_i) = \overline{u}_i$ is given by

$$\overline{\frac{\partial u}{\partial x}}(x) = \frac{\delta\overline{u}}{\delta x} + c_1^{dyn}\Delta^4\frac{\delta^5\overline{u}}{\delta x^5} \tag{C.7}$$

n	$\pm\beta_{\pm 0}$	$\pm\beta_{\pm 1}$	$\pm\beta_{\pm 2}$	$\pm\beta_{\pm 3}$	$\pm\beta_{\pm 4}$	k
1	0	$\frac{2}{3}+\frac{5}{2}c_1^{dyn}$	$-\frac{1}{12}-2c_1^{dyn}$	$\frac{1}{2}c_1^{dyn}$		4
5	0	$\frac{5}{2}$	-2	$\frac{1}{2}$		2
7	0	-7	7	-3	$\frac{1}{2}$	2

Table C.3: Explicit 4^{th} -order dynamic scheme. Explicit 4^{th} -order dynamic finite difference approximation for the 1^{st} -order derivative ($n = 1$). Note that $\beta_i = -\beta_{-i}$.

in which c_1^{dyn} is calculated with expression (6.20), leading to

$$c_1^{dyn} = c_1^* \frac{\left\langle \left(\frac{\delta^5 \overline{u}}{\delta x^5}\right)^2 - \frac{16}{5} f c_1^{**} \Delta^2 \left(\frac{\delta^7 \overline{u}}{\delta x^7}\right)\left(\frac{\delta^5 \overline{u}}{\delta x^5}\right) \right\rangle}{\left\langle \left(\frac{\delta^5 \overline{u}}{\delta x^5} - \frac{16}{5} f c_1^{**} \Delta^2 \frac{\delta^7 \overline{u}}{\delta x^7}\right)^2 \right\rangle}. \tag{C.8}$$

From Taylor expansion the values $c_1^* = \frac{1}{30}$ and $c_1^{**} = -\frac{1}{3}$ are obtained. The discretization stencil for the basic scheme as well as for the derivatives in the calculation of the dynamic coefficient are given in Table C.3

C.2.2 The second derivative

The basic expression for the dynamic finite difference approximation of the second derivative in a node $\overline{u}(x_i) = \overline{u}_i$ is given by

$$\overline{\frac{\partial^2 u}{\partial x^2}}(x) \quad = \quad \frac{\delta^2 \overline{u}}{\delta x^2} + c_2^{dyn} \Delta^4 \frac{\delta^6 \overline{u}}{\delta x^6} \tag{C.9}$$

in which c_2^{dyn} is calculated with expression (6.20) , leading to

$$c_2^{dyn} = c_2^* \frac{\left\langle \left(\frac{\delta^6 \overline{u}}{\delta x^6}\right)^2 - \frac{16}{5} f c_2^{**} \Delta^2 \left(\frac{\delta^8 \overline{u}}{\delta x^8}\right)\left(\frac{\delta^6 \overline{u}}{\delta x^6}\right) \right\rangle}{\left\langle \left(\frac{\delta^6 \overline{u}}{\delta x^6} - \frac{16}{5} f c_2^{**} \Delta^2 \frac{\delta^8 \overline{u}}{\delta x^8}\right)^2 \right\rangle}. \tag{C.10}$$

From Taylor expansion the values $c_1^* = \frac{1}{90}$ and $c_2^{**} = -\frac{1}{4}$ are obtained. The discretization stencil for the basic scheme as well as for the derivatives in the calculation of the dynamic coefficient are given in Table C.4

n	$\beta_{\pm 0}$	$\beta_{\pm 1}$	$\beta_{\pm 2}$	$\beta_{\pm 3}$	$\beta_{\pm 4}$	k
2	$-\frac{5}{2} - 20c_2^{dyn}$	$\frac{4}{3} + 15c_2^{dyn}$	$-6c_2^{dyn} - \frac{1}{12}$	c_2^{dyn}		4
6	-20	15	-6	1		2
8	70	-56	28	-8	1	2

Table C.4: Explicit 4^{th} -order dynamic scheme. Explicit 4^{th} -order dynamic finite difference approximation for the 2^{nd} -order derivative ($n = 2$). Note that $\beta_i = \beta_{-i}$.

n	α_0	$\alpha_{\pm 1}$	β_0	$\pm\beta_{\pm 1}$	$\pm\beta_{\pm 2}$	$\pm\beta_{\pm 3}$	$\pm\beta_{\pm 4}$	k
1	1	$\frac{1}{4} + \frac{1}{12}\frac{c_1^{dyn}}{c_1^*}$	0	$\frac{3}{4} + \frac{1}{36}\frac{c_1^{dyn}}{c_1^*}$	$\frac{1}{36}\frac{c_1^{dyn}}{c_1^*}$			4
5	1		0	$\frac{5}{2}$	-2	$\frac{1}{2}$		2
7	1		0	-7	7	-3	$\frac{1}{2}$	2

Table C.5: Implicit 4^{th} -order dynamic scheme . Implicit 4^{th} -order dynamic finite difference approximation for the 1^{st} -order derivative ($n = 1$). Note that $\alpha_i = \alpha_{-i}$ and $\beta_i = -\beta_{-i}$.

C.3 Fourth-order Implicit Dynamic Finite Difference Approximation

C.3.1 The first derivative

The basic expression for the 4^{th} -order dynamic implicit finite difference approximation of the first derivative in a node $\overline{u}(x_i) = \overline{u}_i$ can be formulated as

$$\sum_{l=-1}^{1} \alpha_l \left(\frac{c_1^{dyn}}{c_1^*}\right) \overline{\frac{\partial u}{\partial x}}\,(x_{i+l}) = \sum_{j=-2}^{2} \frac{\beta_j}{\Delta} \left(\frac{c_1^{dyn}}{c_1^*}\right) \overline{u}\,(x_{i+j})\,, \tag{C.11}$$

in which c_1^{dyn} is calculated with expression (6.36), leading to

$$c_1^{dyn} = c_1^* \frac{\left\langle \left(\frac{\delta^5 \overline{u}}{\delta x^5}\right)^2 - \frac{16}{5} f c_1^{**} \Delta^2 \left(\frac{\delta^7 \overline{u}}{\delta x^7}\right)\left(\frac{\delta^5 \overline{u}}{\delta x^5}\right) \right\rangle}{\left\langle \left(\frac{\delta^5 \overline{u}}{\delta x^5} - \frac{16}{5} f c_1^{**} \Delta^2 \frac{\delta^7 \overline{u}}{\delta x^7}\right)^2 \right\rangle}. \tag{C.12}$$

From Taylor expansion the values $c_1^* = -\frac{1}{120}$ and $c_1^{**} = -\frac{1}{3}$ are obtained. The discretization stencil for the basic scheme as well as for the derivatives in the calculation of the dynamic coefficient are given in Table C.5 Although the higher derivatives in expression (C.12) can be obtained by implicit finite difference approximations, no

n	α_0	$\alpha_{\pm1}$	β_0	$\beta_{\pm1}$	$\beta_{\pm2}$	$\beta_{\pm3}$	$\beta_{\pm4}$	k
1	1	$\frac{1}{10}+\frac{9}{110}\frac{c_2^{dyn}}{c_2^*}$	$-\frac{12}{5}+\frac{9}{110}\frac{c_2^{dyn}}{c_2^*}$	$\frac{6}{5}-\frac{6}{55}\frac{c_2^{dyn}}{c_2^*}$	$\frac{3}{44}\frac{c_2^{dyn}}{c_2^*}$			4
6	1		-20	15	-6	1		2
8	1		70	-56	28	-8	1	2

Table C.6: Implicit 4^{th} -order dynamic scheme. Implicit 4^{th} -order dynamic finite difference approximation for the 2^{nd} -order derivative ($n = 2$). Note that $\alpha_i = \alpha_{-i}$ and $\beta_i = \beta_{-i}$.

attempt is done in this work. Hence, these derivatives are calculated using standard explicit finite difference approximations.

C.3.2 The second derivative

The basic expression for the 4^{th} -order dynamic implicit finite difference approximation of the second derivative in a node $\overline{u}(x_i) = \overline{u}_i$ can be formulated as

$$\sum_{l=-1}^{1} \alpha_l \left(\frac{c_2^{dyn}}{c_2^*}\right) \overline{\frac{\partial^2 u}{\partial x^2}}\left(x_{i+l}\right) = \sum_{j=-2}^{2} \frac{\beta_j}{\Delta^2} \left(\frac{c_2^{dyn}}{c_2^*}\right) \overline{u}\left(x_{i+j}\right), \tag{C.13}$$

in which c_2^{dyn} is calculated with expression (6.36), leading to

$$c_2^{dyn} = c_2^* \frac{\left\langle \left(\frac{\delta^6 \overline{u}}{\delta x^6}\right)^2 - \frac{16}{5} f c_2^{**} \Delta^2 \left(\frac{\delta^8 \overline{u}}{\delta x^8}\right)\left(\frac{\delta^6 \overline{u}}{\delta x^6}\right) \right\rangle}{\left\langle \left(\frac{\delta^6 \overline{u}}{\delta x^6} - \frac{16}{5} f c_2^{**} \Delta^2 \frac{\delta^8 \overline{u}}{\delta x^8}\right)^2 \right\rangle}. \tag{C.14}$$

From Taylor expansion the values $c_2^* = -\frac{1}{200}$ and $c_2^{**} = -\frac{1}{4}$ are obtained. The discretization stencil for the basic scheme as well as for the derivatives in the calculation of the dynamic coefficient are given in Table C.5 Although the higher derivatives in expression (C.14) can be obtained by implicit finite difference approximations, no attempt is done in this work. Hence, these derivatives are calculated using standard explicit finite difference approximations.

Bibliography

[1] A. Abba, A. Cercignani, and L. Valdettaro, *Analysis of subgrid scale models*, Computers & Mathematics with Applications, 46 (2003), pp. 521–535.

[2] G. Ashcroft and X. Zhang, *Optimized prefactored compact schemes*, J. Comp. Phys., 190 (2003), pp. 459–477.

[3] J. Berland, C. Bogey, and C. Bailly, *Low-dissipation and low-dispersion fourth-order runge-kutta algorithm*, Computers & Fluids, 35 (2006), pp. 1459–1463.

[4] J. Berland, C. Bogey, and C. Bailly, *A study of differentiation errors in large-eddy simulations based on the EDQNM theory*, J. Comp. Phys., 227 (2008), pp. 8314–8340.

[5] G. A. Blaisdell, E. T. Spyropoulos, and J. H. Qin, *The effect of the formulation of nonlinear terms on aliasing errors in spectral methods*, Appl. Numer. Math., 21 (1996), pp. 207–219.

[6] C. Bogey and C. Bailly, *A family of low dispersive and low dissipative explicit schemes for flow and noise computations*, J. Comp. Phys., 194 (2004), pp. 194–214.

[7] R. N. Bracewell, *The Fourier transform and its applications*, Electrical engineering series, McGraw-Hill international editions, Signapore, 3 ed., 2000.

[8] M. Brachet, D. Meiron, S. Orszag, B. Nickel, R. Morf, and U. Frisch, *Small-scale structure of the taylor-green vortex*, J. Fluid. Mech., 130 (1983), pp. 411–452.

[9] T. Brandt, *A priori tests on numerical errors in large eddy simulation using finite differences and explicit filtering*, International Journal for Numerical Methods in Fluids, 51 (2006), pp. 635–657.

[10] T. Brandt, *Study on numerical and modelling errors in LES using a priori and a posteriori*, PhD dissertation, Helsinki University of Technology- Deptartment of Mechanical engineering, P.O. BOX 4400, FI-02015 TKK, 2007. ISBN 978-951-22-8634-8.

[11] J. M. BURGERS, *Application of a model system to illustrate some points of the statistical theory of free turbulence*, in Nederl. Akad. Wetensch. Proc., vol. 43, 1940, pp. 2–12.

[12] J. M. BURGERS, *A mathematical model illustrating the theory of turbulence*, Adv. in Appl. Mech., 1 (1948), pp. 171–199.

[13] D. CARATI AND W. CABOT, *Anisotropic eddy viscosity models*, in Proceedings of the Summer Program 1996, Stanford, 1996, Stanford University and Nasa Ames Research Center, pp. 249–258.

[14] D. CARATI, K. JANSEN, AND T. LUND, *A family of dynamic models for large eddy simulation*, in Proceedings of the Summer Program 1995, 35-40, ed., Stanford, 1995, Stanford University and Nasa Ames Research Center.

[15] D. CARATI AND E. VANDEN EIJNDEN, *On the self-similarity assumption in dynamic models for large eddy simulations*, Physics of Fluids, 9 (1997), pp. 2165–2167.

[16] D. CARATI, G. WINCKELMANS, AND H. JEANMART, *On the modelling of the subgrid-scale and filtered-scale stress tensors in large-eddy simulation*, J. Fluid. Mech., 441 (2001), pp. 119–138.

[17] A. J. CHORIN, *A numerical method for solving incompressible viscous flow problems*, J. Comp. Phys., 135 (1997), pp. 118–125.

[18] A. J. CHORIN, *A numerical method for solving incompressible viscous flow problems*, J. Comput. Phys., 135 (1997), pp. 118–125.

[19] F. K. CHOW AND P. MOIN, *A further study of numerical errors in large-eddy simulations*, J. Comp. Phys., 184 (2003), pp. 366–380.

[20] A. DAS AND R. D. MOSER, *Optimal large-eddy simulation of forced burgers equation*, Phys. Fluids, 14 (2002), pp. 4344–4351.

[21] G. DE STEFANO AND O. VASILYEV, *Sharp cutoff versus smooth filtering in large eddy simulation*, Phys. Fluids, 14 (2002), pp. 362–369.

[22] O. DEBLIQUY, B. KNAEPEN, D. CARATI, AND A. A. WRAY, *Sampling versus filtering in Large-Eddy simulations*, in Proceedings of the Summer Program 2004, P. Moin and N. N. Mansour, eds., Stanford, December 2004, Stanford University and Nasa Ames Research Center, pp. 133–144.

[23] A. DOMARADZKI AND D. CARATI, *An analysis of the energy transfer and the locality of nonlinear interactions in turbulence*, Phys. Fluids, 19 (2007), p. 085112.

[24] A. Domaradzki and D. Carati, *A comparison of spectral sharp and smooth filters in the analysis of nonlinear interactions and energy transfer in turbulence*, Phys. Fluids, 19 (2007), p. 085111.

[25] G. Eyink, *Locality of turbulent cascades*, Physica D, 207 (2005), pp. 91–116.

[26] G. Eyink, *Multi-scale gradient expansion of the turbulent stress tensor*, J. Fluid. Mech., 549 (2006), pp. 159–190.

[27] D. Fauconnier, C. De Langhe, and E. Dick, *The dynamic procedure for accuracy improvement of numerical discretizations in fluid mechanics*, J. Comp. Phys., 224 (2007), pp. 1095–1123.

[28] D. Fauconnier, C. De Langhe, and E. Dick, *The sampling-based dynamic procedure as tool for higher-order discretization*, Int. J. Num. Methods in Fluids, 56 (2008), pp. 1241–1247.

[29] L. Gamet, F. Ducros, F. Nicoud, and T. Poinsot, *Compact finite difference schemes on non-uniform meshes. Application to direct numerical simulations of compressible flows*, International Journal for Numerical Methods in Fluids, 29 (1999), pp. 159–191.

[30] M. Germano, U. Piomelli, P. Moin, and W. H. Cabot, *A dynamic subgrid-scale eddy viscosity*, Phys. Fluids A, 3 (1991), pp. 1760–1765.

[31] B. J. Geurts and D. D. Holm, *Commutator errors in large-eddy simulation*, Journal of Physics A: Mathematical and General, 39 (2006), pp. 2213–2229.

[32] S. Ghosal, *An analysis of numerical errors in large-eddy simulations of turbulence*, J. Comp. Phys., 125 (1996), pp. 187–206.

[33] S. Ghosal and P. Moin, *The basic equations for the large-eddy simulation of turbulent flows in complex geometries.*, J. Comp. Phys., 118 (1995), pp. 24–37.

[34] T. Gotoh and D. Fukayama, *Pressure spectrum in homogeneous turbulence*, Phys. Rev. Lett., 86 (2001), pp. 3775–3778.

[35] J. Gullbrand and F. Chow, *Investigations of numerical errors, subfilter-scale models, and subgrid-scale models in turbulent channel flow simulatons*, in Proceedings of the Summer Program 2002, P. Bradshaw, ed., Stanford, 2002, Stanford University and Nasa Ames Research Center, pp. 87–104.

[36] J. Gullbrand and F. Chow, *The effect of numerical errors and turbulence models in large eddy simulations of channel flow, with and without explicit filtering*, J. Fluid. Mech., 495 (2003), pp. 323–341.

[37] R. Hixon, *Nonlinear comparison of high-order and optimized finite-difference schemes*, International Journal of Computational Fluid Dynamics, 13 (2000), pp. 259–277.

[38] J. Holmen, T. J. R. Hughes, A. A. Oberai, and G. N. Wells, *Sensitivity of the scale partition for variational multiscale large-eddy simulation of channel flow*, Physics of Fluids, 16 (2004), pp. 824–827.

[39] F. Q. Hu, M. Y. Hussaini, and J. L. Manthey, *Low-dissipation and low-dispersion runge-kutta schemes for computational acoustics*, J. Comput. Phys., 124 (1996), pp. 177–191.

[40] T. J. R. Hughes, L. Mazzei, A. A. Oberai, and A. A. Wray, *The multiscale formulation of large eddy simulation: Decay of homogeneous isotropic turbulence*, Physics of Fluids, 13 (2001), pp. 505–512.

[41] T. J. R. Hughes, A. A. Oberai, and L. Mazzei, *Large eddy simulation of turbulent channel flows by the variational multiscale method*, Physics of Fluids, 13 (2001), pp. 1784–1799.

[42] T. J. R. Hughes, G. N. Wells, and A. A. Wray, *Energy transfers and spectral eddy viscosity in large-eddy simulations of homogeneous isotropic turbulence: Comparison of dynamic Smagorinsky and multiscale models over a range of discretizations*, Physics of Fluids, 16 (2004), pp. 4044–4052.

[43] H. Jeanmart and G. Winckelmans, *Comparison of recent dynamic subgrid-scale models in turbulent channel flow*, in Proceedings of the Summer Program 2002, P. Bradshaw, ed., Stanford, 2002, Stanford University and Nasa Ames Research Center, pp. 105–116.

[44] J. Jeong and F. Hussain, *On the identification of a vortex*, Journal of Fluid Mechanics, 285 (1995), pp. 69–94.

[45] J. W. Kim and D. T. Lee, *Optimized compact finite difference schemes with maximum resolution*, AIAA Journal, 34 (1996), pp. 887–893.

[46] B. Knaepen, O. Debliquy, and D. Carati, *Large-eddy simulation without filter*, J. Comp. Phys., 205 (2005), pp. 98–107.

[47] A. Kolmogorov, *Local structure of turbulence in an incompressible fluid at very high reynolds numbers.*, Dokl., 30 (1942).

[48] R. Kraichnan, *Eddy viscosity in two and three dimensions*, Journal of Atmospheric Sciences, 33 (1976), pp. 1521–1536.

[49] A. G. Kravchenko and P. Moin, *On the effect of numerical errors in large-eddy simulations of turbulent flows*, J. Comp. Phys., 131 (1997), pp. 310–322.

[50] S. K. Lele, *Compact finite difference schemes with spectral-like resolution*, J. Comp. Phys., 103 (1991), pp. 16–42.

[51] D. C. Leslie and G. L. Quarini, *The application of turbulence theory to the formulation of subgrid modelling procedures*, J. Fluid. Mech., 91 (1979), pp. 65–91.

[52] D. Lilly, *The representation of small-scale turbulence in numerical simulation experiments.*, in Proceedings of IBM Scientific Computing Symposium on Environmental Sciences, Yorktown Heights, New York, 1967, IBM Data Processing Division, Goldstine H.H., pp. 159–210.

[53] D. K. Lilly, *A proposed modification of the Germano subgrid-scale closure*, Phys. Fluids A, 4 (1992), pp. 633–635.

[54] M. D. Love, *Subgrid modelling studies with burgers'equation*, J. Fluid. Mech., 100 (1980), pp. 87–110.

[55] T. S. Lund, *On the use of discrete filters for large eddy simulation*, annual research briefs, Center for Turbulence Research, Stanford, 1997.

[56] T. S. Lund and H. Kaltenbach, *Experiments with explicit filtering for les using a finite-difference method*, annual research briefs, Center for Turbulence Research, Stanford, 1995.

[57] P. Lynch, *The Emergence of Numerical Weather Prediction: Richardson's Dream*, Cambridge University Press, November 2006. ISBN 0521857295.

[58] C. Meneveau and T. S. Lund, *The dynamic smagorinsky model and scale-dependent coefficients in the viscous range of turbulence*, Physics of Fluids, 9 (1997), pp. 3932–3934.

[59] J. Meyers, *Accuracy of large-eddy simulation strategies*, PhD dissertation, KUL. Faculteit toegepaste wetenschappen. Departement werktuigkunde. Toegepaste mechanica en energieconversie, Leuven, 2004. ISBN 90-5682-473-2.

[60] J. Meyers, B. Geurts, and M. Baelmans, *Database analysis of errors in large-eddy simulation*, Phys. Fluids, 15 (2003), pp. 2740–2755.

[61] J. Meyers, B. Geurts, and M. Baelmans, *Optimality of the dynamic procedure for large-eddy simulations*, Phys. Fluids, 17 (2005), pp. 045–108.

[62] J. Meyers, B. Geurts, and P. Sagaut, *A computational error-assessment of central finite-volume discretizations in large-eddy simulation using a smagorinsky model*, J. Comp. Phys., 227 (2007), pp. 156–173.

[63] J. Meyers, C. Lacor, and M. Baelmans, *On the use of high-order finite-difference discretization for les with double decomposition of the subgrid-scale stress*, Int. J. Num. Methods in Fluids, 56 (2008), pp. 383–400.

[64] J. MEYERS AND P. SAGAUT, *On the model coefficients for the standard and the variational multi-scale Smagorinsky model*, Journal of Fluid Mechanics, 569 (2006), pp. 287–319.

[65] Y. MORINISHI, T. S. LUND, O. V. VASILYEV, AND P. MOIN, *Fully conservative higher order finite difference schemes for incompressible flow*, J. Comput. Phys., 143 (1998), pp. 90–124.

[66] A. MUSCHINSKI, *A similarity theory of locally homogeneous and isotropic turbulence generated by a Smagorinsky-type LES*, J. Fluid. Mech., 325 (1996), pp. 239–260.

[67] S. A. ORSZAG, *On the elimination of aliasing in finite-difference schemes by filtering high-wavenumber components*, Journal of the Atmospheric sciences, 28 (1971), p. 1074.

[68] S. A. ORSZAG, *Numerical simulation of the taylor-green vortex*, in Proceedings of the International Symposium on Computing Methods in Applied Sciences and Engineering, Part 2, London, UK, 1974, Springer-Verlag, pp. 50–64.

[69] N. PARK AND K. MAHESH, *Analysis of numerical errors in large eddy simulation using statistical closure theory*, Journal of Computational Physics, 222 (2007), pp. 194–216.

[70] S. POPE, *Turbulent Flows*, Cambridge University Press, Cambridge, 2000.

[71] G. PUCKETT, *Introduction to "a numerical method for solving incompressible viscous flow problems"*, J. Comput. Phys., 135 (1997), pp. 115–117.

[72] C. RHIE AND W. CHOW, *Numerical study of the turbulent flow past an airfoil with trailing edge separation*, AIAA Journal, 21 (1983), pp. 1525–1532.

[73] L. F. RICHARDSON, *Weather Prediction by Numerical Process*, Cambridge University Press, 1922.

[74] P. SAGAUT, *Large Eddy Simulations for Incompressible Flows*, Springer, Berlin-Heidelberg, 1998.

[75] P. SAGAUT AND V. LEVASSEUR, *Sensitivity of spectral variational multiscale methods for large-eddy simulation of isotropic turbulence*, Physics of Fluids, 17 (2005), p. 035113.

[76] R. SHAH, M. HEIKAL, B. THONON, AND P. TOCHON, *Progress in the numerical analysis of compact heat exchanger surfaces*, Advances in Heat Transfer, 34 (2001), pp. 363–443.

[77] P. N. SHANKAR AND M. D. DESHPANDE, *Fluid mechanics in the driven cavity*, Annu. Rev. Fluid Mech., 32 (2000), pp. 93–136.

[78] J. Smagorinsky, *General circulation experiments with the primitive equations*, Monthly Weather Review, 91 (1963), pp. 99–164.

[79] C. K. W. Tam and J. C. Webb, *Dispersion-relation-preserving finite difference schemes for computational acoustics*, J. Comp. Phys., 107 (1993), pp. 262–281.

[80] G. I. Taylor and A. E. Green, *Mechanism of the Production of Small Eddies from Large Ones*, Royal Society of London Proceedings Series A, 158 (1937), pp. 499–521.

[81] F. van der Bos and B. Geurts, *Commutator errors in the filtering approach to large-eddy simulation*, Phys. Fluids, 17 (2005), p. 035108.

[82] O. V. Vasilyev, *High Order Finite Difference Schemes on Non-uniform Meshes with Good Conservation Properties*, Journal of Computational Physics, 157 (2000), pp. 746–761.

[83] O. V. Vasilyev, T. S. Lund, and P. Moin, *A general class of commutative filters for les in complex geometries*, J. Comp. Phys., 146 (1998), pp. 82–104.

[84] P. R. Voke, *Subgrid-Scale Modelling at Low Mesh Reynolds Number*, Theoretical and Computational Fluid Dynamics, 8 (1996), pp. 131–143.

[85] A. W. Vreman, *The filtering analog of the variational multiscale method in large-eddy simulation*, Physics of Fluids, 15 (2003), pp. L61–L64.

[86] B. Vreman, B. Geurts, and H. Kuerten, *Realizability conditions for the turbulent stress tensor in large-eddy simulation*, Journal of Fluid Mechanics, 278 (1994), pp. 351–362.

[87] B. Vreman, B. Geurts, and H. Kuerten, *Comparison of numerical schemes in large-eddy simulations of the temporal mixing layer.*, Int. J. Num. Methods in Fluids, 22 (1996), pp. 297–311.

[88] G. Winckelmans, L. Bricteux, L. Georges, G. Daeninck, and H. Jeanmart, *The sampling-based dynamic procedure for LES: investigations using finite differences*, in Ercoftac Series - Direct and Large-Eddy Simulations 6, E. Lamballais, R. Friederich, B. Geurts, and O. Métais, eds., Poitiers, September 2005, Ercoftac, Springer, pp. 183–190.

[89] G. Winckelmans, L. Georges, L. Bricteux, and H. Jeanmart, *The Sampling-based dynamic procedure for LES in physical space*, Bulletin of the American Physical Society Division of Fluid Dynamics, 49 (2004). 57th Annual Meeting of the American Physical Society Division of Fluid Dynamics, Seattle, Nov. 2004.

[90] V. Wong and D. Lilly, *A comparison of two dynamic subgrid closure methods for turbulent thermal convection*, Phys. Fluids, 6 (1994), pp. 1016–1023.